MICROSTRUCTURE-PROPERTY DEVELOPMENT IN LINEAR FRICTION WELDING OF NICKEL-BASED SUPERALLOYS

By

JIAN YANG

A Thesis Submitted to
The University of Birmingham
for the Degree of
DOCTOR OF PHILOSOPHY

Department of Metallurgy and Materials
University of Birmingham
October 2014

Abstract

Linear friction welding (LFW) is known as an advanced technique to substitute fusion welding of joining Ni-based superalloys. However, due to the complex microstructural development caused by LFW, some unexplained issues still need to be solved, such as: influence of weld parameters (weld pressure, amplitude of oscillation, and frequency of oscillation) on the development of microstructural, microhardness, texture and residual stresses in LFWed IN718-IN713LC; impact of post-weld heat treatment (PWHT) on the microstructural and microhardness development; influence of rapid thermal cycle on the precipitate dissolution of IN718 and IN713LC; formation mechanisms of alumina inclusions (Al-oxides) on the weld interface. The present work aims to investigate these issues.

Linear friction welds (LFWs) between two Ni-based superalloys, IN718-IN713LC were characterised using optical microscope (OM), scanning electron microscope (SEM), electron backscatter diffraction (EBSD), energy dispersive X-ray (EDX), microhardness, and neutron diffraction. LFWs possess a much narrower heat affected zone (HAZ) than fusion welds, and recrystallisation occurs in the thermo-mechanically affected zone (TMAZ). Large force in LFW causes distortion in IN713LC, and also leaves a weak texture in IN718. As-welded samples show uneven hardness development across the welds, with a hardness trough in IN718 and a hardness increase in IN713LC. The uneven hardness is attributed to the different precipitate distribution, grain size, and stored energy in the two alloys, in which the precipitate distribution is proved to be the main factor. Large tensile residual stress is generated near the weld line with compressive stress in the adjacent area. Weld pressure is the main factor that affects the microstructure-property of welds. The weld time and the area of HAZ reduce with the increase in pressure. The tensile residual stress near the weld line decreases and further changes result in the compressive stress with the increase in the pressure.

A range of PWHTs have been carried out to recover the strength of the LFWs. It has been found that two-stage aging treatment is the most efficient way to recover the hardness of the welds without causing grain growth. Solution treatment plus two-stage aging treatment can generate a homogenous hardness distribution, but may induce grain recrystallisation and rapid coarsening when the solution temperature is too high.

Alumina inclusions are found in high amplitude welds, and the formation mechanism of the alumina is primarily due to the abnormal expulsion of material caused by insufficient ejection of IN713LC flash during oscillation. A reduction in amplitude, an increase in pressure, or an increased upset can produce oxide-free welds. Although oxides can be eliminated by argon shielding, oxidation can still occur, which may be prevented by using sufficient purge times.

The effect of a rapid thermal cycle on precipitate (γ' and δ) dissolution was carried out on a Gleeble thermo-mechanical simulator (GTMS), where the expected influence of heating rate on the rate of precipitate dissolution was observed. A mathematical model was established to predict the rate and the temperature of precipitate dissolution for different thermal cycles, which shows good agreement with the experimental values.

Acknowledgements

First of all, I would like to express my deepest appreciation to my supervisor Prof. Moataz M. Attallah, for his invaluable guidance, support and patience on my PhD research and thesis. Without his help, it is impossible to accomplish what I have achieved today.

Great appreciation goes to Prof. Mike Loretto and Dr. Simon Bray for their assistance and professional advices on the modification of thesis. Also, thanks to Rolls-Royce plc in person of Dr. Andrew Walpole, who provided the materials and technical guidance.

Thanks to the financial support from the Department of Metallurgy and Materials at the University of Birmingham and Rolls-Royce plc.

I would like to thank my colleagues in the department, especially Dr. Tim Doel for helping me with the Gleeble work, and Minshi Wang for his kindly help on the TEM work. Also, I would like to thank the former and present members in the AMPLab group, especially Lakshmi Parimi, Vitthal Konaraddi, and Sheng Li.

I would like to express my love and gratitude to my parents Changjin Yang and Yunxia Wang, for their never-ending support during the hard times in my life so far. To my wife Nannan, who always stands by me through thick and thin. I am so glad that we are on the way to open the new chapter of our lives together.

Finally, best wishes to all the people who give me strength, support, and love. It is my pleasure to meet all of you!

Table of Contents

Table of Figures

List of Tables

Nomenclature

Abbreviation	Description
a	Amplitude of Oscillation
AC	Air Cooling
APB	Anti-Phase Boundary
BC	Band Contrast
BCT	Body-Centred Tetragonal
BF	Bright Field
blisk	Bladed Disk
BSE	Backscattered Electron
CCT	Continuous Cooling Transformation
CDFW	Continuous Drive Friction Welding
CDRX	Continuous Dynamic Recrystallisation
τ_c	Critical Resolved Shear Stress
d	Grain Size
d_0	Strain Free Lattice Spacing
δ	Delta Phase
DDRX	Discontinuous Dynamic Recrystallisation
DRX	Dynamic Recrystallisation
DSC	Differential Scanning Calorimetry
DTA	Differential Thermal Analysis
ε	Strain
$\dot{\varepsilon}$	Strain Rate
E	Young's Modulus
EBSD	Electron Backscatter Diffraction
EBW	Electron Beam Welding
EDM	Electric Discharge Wire Cutting Machine
EDX	Energy Dispersive X-ray
f	Frequency of Oscillation
FCC	Face-Centred Cubic
FSW	Friction Stir Welding
FW	Friction Welding
FZ	Fusion Zone
γ	Gamma Phase
γ'	Gamma Prime Phase
γ''	Gamma Double Prime Phase
GTAW	Gas Tungsten Arc Welding
GTMS	Gleeble Thermo-Mechanical Simulator
HAGB	High Angle Boundary
HAZ	Heat Affected Zone

Abbreviation	Description
HT-CLSM	High-Temperature Confocal Laser Scanning Microscopy
HV	Vickers Hardness
IFW; IFWs	Inertia Friction Welding; Inertia Friction Welds
IPF	Inverse Pole Figure
λ	Wave Length
LAGB	Low Angle Grain Boundary
LFW; LFWs	Linear Friction Welding; Linear Friction Welds
MMGB	Moderately Misoriented Grain Boundary
OM	Optical Microscope
P	Weld Pressure
PDRX	Partially Dynamic Recrystallised Zone
PDZ	Plastically Deformed Zone
PTAW	Plasma Tungsten Arc Welding
PWHT	Post-Weld Heat Treatment
τ_r	Resolved Shear Stress
RF	Recrystallised Fraction
RFW	Rotary Friction Welding
θ	Diffraction Angle
σ	Yield Strength
SADP	Selected Area Diffraction Pattern
SALSA	Strain Analyser for Large and Small Scale Engineering Application
SE	Secondary Electron
SEM	Scanning Electron Microscope
τ	Shear Stress
t	Time
T	Temperature
TCP	Topologically Close-Packed
TEM	Transmission Electron Microscope
TIG	Tungsten Inert Gas Welding
TMAZ	Thermo-Mechanically Affected Zone
TTT	Transformation-Time-Temperature
v	Poisson's Ratio
WAZ	Weld Affected Zone
WQ	Water Quenching
Z	Zener-Hollomon Parameter

Chapter 1. Introduction

1.1. General Introduction and Research Background

Ni-based superalloys are complex alloys that possess high temperature strength and creep resistance, coupled with corrosion resistance at temperatures as high as 1200 °C (90% of their melting points) [1, 2]. Due to this high performance, Ni-based superalloys have been widely used in various applications, including aeroengines, steam turbine power plants, nuclear power systems, chemical and petrochemical industries, even food processing industries. The use of Ni-based superalloys in the manufacturing of jet engines has evolved in the past 60 years, reaching 50% of the total engine weight [3]. As seen in Fig. 1.1, large amounts of Ni-based superalloys are used in the high-pressure compressor and low-to-high pressure turbine in the Rolls-Royce Trent 800 aeroengine, as these areas are maintained at the highest temperature in the engine during operation. Rolls-Royce predicted that in the period of 2012 to 2031, the global market would need 149,000 engines to power 68,000 commercial aircraft and business jets [4].

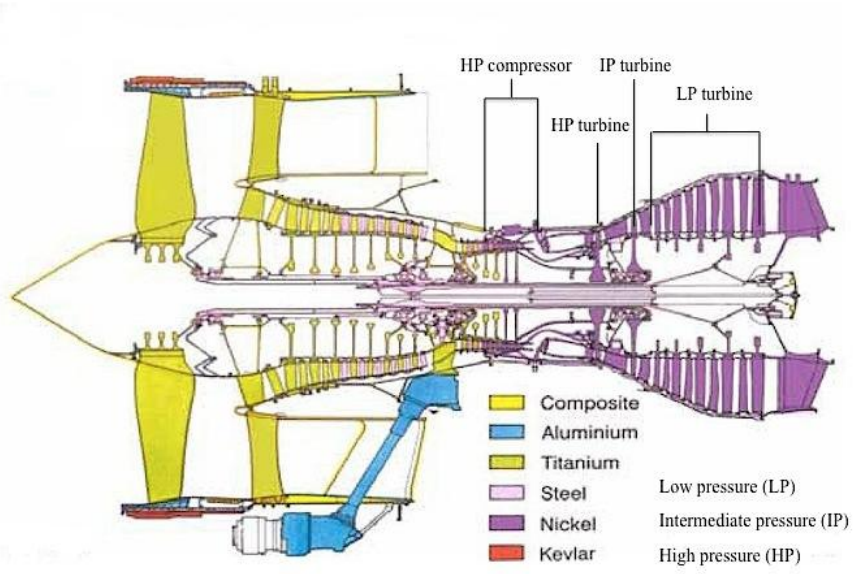

Fig. 1.1. Materials usage in Trent 800 turbine engine [2]

Joining is a critical aeroengine technology, and is required to underpin the use of Ni-based superalloys. The traditional joining methods for Ni-based superalloys include mechanical fastening (for fir-tree blades) and fusion welding. Mechanical fastening has some advantages, including its low cost, low energy, high speed, and ease of operation. However, this process may cause fretting fatigue damage in joining the blade/disk assembly [5] and can be difficult to apply for internal parts. In comparison, fusion welding (e.g. electron or laser beam welding, and gas tungsten arc welding) may solve some of the issues in mechanical fastening, but are associated with new challenges, including constitutional liquation, hot cracking, and chemical segregation [6].

Linear friction welding is a solid-state joining technique that uses frictional heating between two rubbing components to create solid joints, no filler material is required. It has a number of advantages over conventional joining methods, including the fact that it is a solid-state joining method, which avoids melting, grain boundary liquation, and hot cracking. Also, it is a self-cleaning process, typically requiring no gas shielding, since any inclusions, oxides, or impurities can be ejected in the flash. Moreover, it is a fairly rapid welding process, which requires less weld preparation time and is more energy efficient, resulting in a sound weld with a narrower weld affected zone and lower residual stresses, compared to fusion welding. It is also suitable for welding nearly any metal, regardless of the complexity of the geometry, resulting in 30% weight reductions of blade disks (blisks) [7].

1.2. Project Aim and Objectives

This project aims to study the microstructure-property development in linear friction welded IN718-IN713LC (as candidate alloys for a low pressure turbine blisk). A number of challenges might be associated with LFW of Ni-based superalloys, including the development of residual stress, the localised microstructural inhomogeneity across the weld zone, and the influence of the microstructural development during LFW on strength. In this thesis the following aspects have been investigated:

(1) Influence of LFW process parameters (forging pressure, amplitude and frequency of oscillation) on the microstructure, microhardness, texture, and residual stress in LFWed IN718-IN713LC.

(2) To develop a post-weld heat treatment, and assess its impact on the microstructure and hardness in IN718-IN713LC LFW.

(3) Effect of rapid heating on the precipitates (γ' and δ) dissolution kinetics in IN713LC and IN718.

(4) To study the alumina formation mechanism in IN718-IN713LC LFWs and find an elimination method.

1.3. Thesis Structure

This thesis consists of 9 chapters. Chapters 2 and 3 cover the literature review. Chapter 2 summarises the metallurgy of Ni-based superalloys, including the metallurgical phases present, strengthening mechanisms, and microstructural development during thermal and thermo-mechanical processing. The literature review of LFW is presented in Chapter 3,

focusing on the temperature development, the microstructural and residual stress development, and the classification of weld zones in LFWs. A detailed description of the experimental methods is provided in Chapter 4, summarising sample preparation, heat treatment processes, Gleeble thermo-mechanical simulation, microstructural characterisation, residual stress measurement, and hardness testing. Results are divided into 4 chapters. Chapter 5 focuses on IN718-IN713LC LFWs characterisation, specifically the microstructural, microhardness, texture, and residual stress development. The influence of the post-weld heat treatment on the microstructural and hardness development of welds is discussed in Chapter 6. Chapter 7 explores the rapid heating simulations carried out to define the effect of heating rates on the dissolution of precipitates. Chapter 8 discusses the formation mechanisms of alumina in IN718-IN713LC LFWs. Finally, conclusions and future work are summarised in Chapter 9.

1.4. References

[1] T. M. Pollock and S. Tin, "Nickel-based superalloys for advanced turbine engines: chemistry, microstructure and properties," *Journal of Propulsion and Power,* vol. 22, pp. 361-374, 2006.

[2] R. C. Reed, *The Superalloys : Fundamentals and Applications*. Cambridge, Cambridge University Press, 2006.

[3] R. Schafrik and R. Sprague, "Saga of Gas Turbine Materials, Part III," *Advanced Materials & Processes,* pp. 29-33, 2004.

[4] "Nickel-Based Super Alloys," International Nickel Study Group,2013.

[5] M. E. Nunn, "Aero engine improvements through linear friciton welding," presented at the 1st International Conference on Innovation and Integration in Aerospace Sciences, Queen's University, Belfast, Northen Ireland, UK, 2005.

[6] J. N. DuPont, J. C. Lippold, and S. D. Kiser, *Welding Metallurgy and Weldability of Nickel-Base Alloys*. NJ, USA, Wiley, 2009.

[7] X. Lin, M. H. Song, W. W. Zhao, and J. Chen, "Effect of intermediate heat treatment temperature on microstructure and notch sensitivity of laser solid formed Inconel 718 superalloy," *Journal of Wuhan University of Technology-Materials Science Edition,* vol. 26, pp. 908-913, 2011.

Chapter 2. Metallurgy of Ni-based Superalloys

2.1. General Introduction

2.1.1. Classification of Ni-based Superalloys

Ni-based superalloys can be divided into three classes:

(1) Solid-solution-strengthened alloys: The elements Co, Cr, Fe, Mo, W, Ta, and Re dissolve in the Ni matrix, to form solid solution Ni-based superalloys, such as Hastelloy X and IN625. These alloys may derive some additional strengthening from precipitates and/or carbides [1]. They have excellent fabricability and weldability, but moderate mechanical strength at high-temperature, and are used for burners and combustors in gas turbine engines.

(2) Oxide-dispersion-strengthened alloys: The oxide-dispersion-strengthened alloys, IN-MA-754, IN-MA-6000E, Ni-20Cr-2ThO_2, are strengthened by inert dispersoids of Y_2O_3 and/or ThO_2. Yttria-strengthened alloys are more attractive because of the radioactivity in thoriated alloys [1, 2].

(3) Precipitation-strengthened alloys: These alloys are the most important class of Ni-based superalloys. High Ti and/or high Al containing alloys such as IN713LC, Astroloy, Waspaloy, RR1000, Udimet720, and CMSX-4 are strengthened by gamma prime (γ') precipitates. In high Nb plus Ti and/or Al containing alloys, the strengthening precipitates are γ' and gamma double prime (γ''), and are typified by IN718, IN706 and IN909 [1]. Compared with solid-solution-strengthened alloys, precipitation-strengthened alloys not only possess good corrosion and creep resistance, but also have excellent high temperature mechanical strength. They are typically used in turbine blisks, casings, and vanes in aeroengines.

2.1.2. Alloying Elements and Their Effects

Ni-based superalloys are complex alloys, which contain various alloying elements, most of which are transition metals. The majority of the alloys contain large amounts of Cr, Al, Ti and Co, and small amounts of Zr, C and B. Some other alloys may have Fe, Mo, Ru, Nb, V, Re, Ta, W and Hf.

The elements which are added to Ni-based superalloys partition either to the γ, γ′, or to the grain boundaries, are shown in the periodic table (Fig. 2.1). The first group of elements, including Ni, Cr, Fe, Co, V, Ru and Ir, has atomic radii close to that of Ni, hence they can dissolve in the face-centred cubic (FCC) gamma (γ) matrix to stabilise it. The second group includes Al, Ti, Nb and Ta, which have larger atomic radii than Ni, and they tend to form the ordered γ′ phase Ni_3(Al, Ti) and γ″ phase Ni_3(Nb, Ti). In comparison with Ni, a third group of elements, B and C have very different atomic radii and these elements segregate at the grain boundaries [3]. More detailed information of the role of elements and their potential defects are described below in Table 2.1 [1].

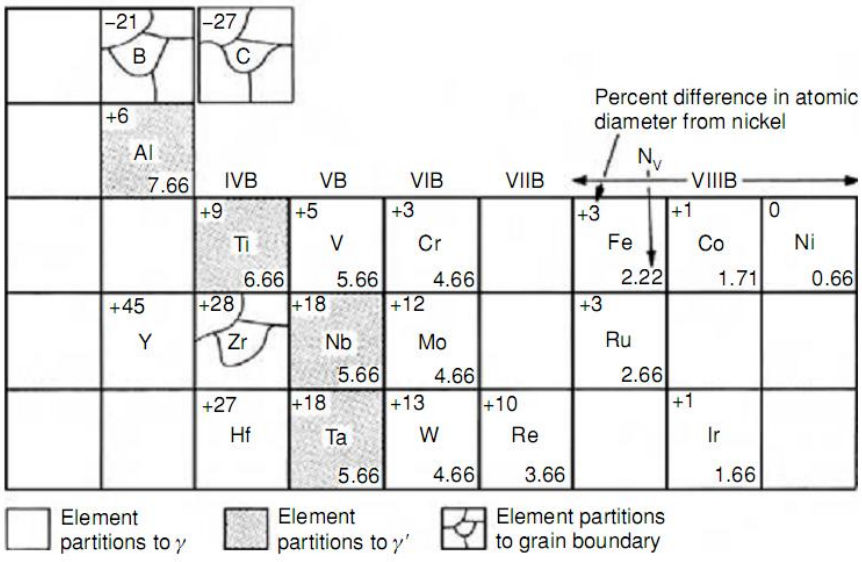

Fig. 2.1. Element partitioning in Ni-based superalloys [3]

Table 2.1. Effect of elements on Ni-based superalloys [1]

Effect	Alloying Elements
Solid-solution strengtheners	Co, Cr, Fe, Mo, W, Ta, Nb, Re
Carbide formers:	
MC	Nb, Ti, Mo, W, Ta, Hf
M_7C_3	Cr
$M_{23}C_6$	Cr, Mo, W
M_6C	Mo, W, Nb
Carbonitrides: M(CN)	C, N
Form γ′ Ni_3(Al,Ti)	Al, Ti
Raise γ′ solvus temperature	Co
Hardening precipitates and/or intermetallics	Al, Ti, Nb
Oxidation resistance	Al, Cr, Y, La, Ce
Hot corrosion resistance	La, Th
Sulfidation resistance	Cr, Co, Si
Improve creep resistance	B, Ta
Increase rupture strength	B*
Grain-boundary refiners/grain size control	B, C, Zr, Hf
Retard γ′ coarsening	Re

*: Borides are formed if B present in large amounts.

2.1.3. Phases Present in Ni-based Superalloys

A summary of the chemical formula, crystal structure, and lattice parameters of the phases present in Ni-based superalloys is shown in Table 2.2. In general, the microstructure of Ni-based superalloys consists of the FCC γ matrix and various secondary phases for controlling properties. Among the secondary phases, γ′ Ni_3(Al, Ti) and γ″ Ni_3Nb are the main strengthening precipitates. Carbides (MC, $M_{23}C_6$, M_6C, and M_7C_3) usually form intergranularly for stabilising grain boundaries. Delta (δ) and eta phases (η) contribute to controlling the microstructure during processing. In addition, small amounts of borides may precipitate at grain boundaries for improving creep-rupture properties. Sigma phase (σ), Mu phase (μ), and Laves are topologically close-packed (TCP) phases, which are detrimental

phases in Ni-based superalloys. Figure 2.2 shows the schematic diagram of the microstructure of Ni-based superalloys [1].

Table 2.2. Phases present in Ni-based superalloys [1]

Phase	Formulae	Crystal Structure	Lattice Parameters (Å)
γ′	Ni_3Al, $Ni_3(Al,Ti)$	FCC (Ll_2)	a=3.561-3.568
γ″	Ni_3Nb	BCT ($D0_{22}$)	a=3.624, c=7.406
MC	TiC, NbC, HfC	Cubic	a=4.3-4.7
$M_{23}C_6$	$Cr_{23}C_6$, $(Cr,Fe,W,Mo)_{23}C_6$	FCC	a=10.5-10.7
M_6C	Fe_3Mo_3C, Nb_3Co_3C, Ta_3Co_3C, Fe_3Nb_3C Fe_3W_3C-Fe_4W_2C	FCC	a=10.85-11.75
M_7C_3	Cr_7C_3	Hexagonal	a=13.98, c=4.523
M_3B_2	Ta_3B_2, Nb_3B_2, V_3B_2, Mo_2FeB_2, $(Mo,Ti,Cr,Ni,Fe)_3B_2$	Tetragonal	a=5.6-6.2, c=3.0-3.3
MN	(Ti,Nb,Zr)(C,N)	Cubic	a=4.24
δ	Ni_3Nb	Orthorhombic	a=5.106-5.11, b=4.21-4.251, c=4.52-4.556
η	Ni_3Ti	HCP ($D0_{24}$)	a=5.093, c=8.276
σ	FeCr, FeCrMo, CrFeMoNi, CrCo,	Tetragonal	a=8.8-9.1, c=4.5-4.8
μ	Co_2W_6, $(Fe,Co)_7(Mo,W)_6$	Rhombohedral	a=4.75, c=25.77
Laves	Fe_2Nb, Fe_2Ti, Fe_2Mo, Co_2Ta, Co_2Ti	Hexagonal	a=4.75-4.95, c=7.70-8.15

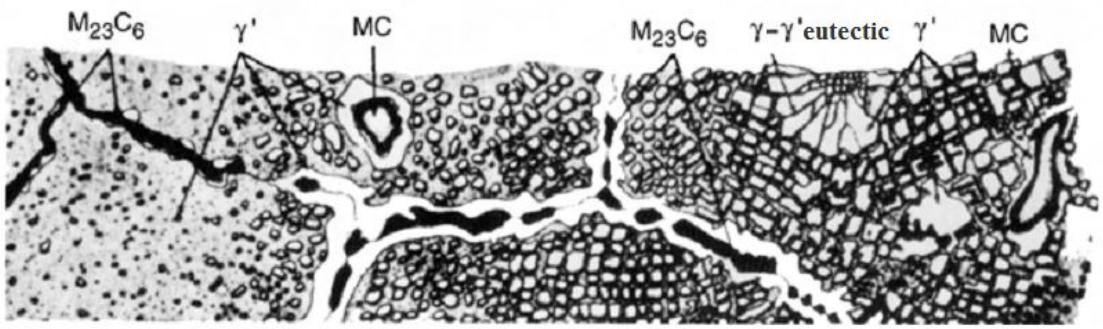

Fig. 2.2. Schematic diagram of the microstructure in Ni-based superalloys [8]

The γ′ can be classified as primary, secondary, and tertiary γ′ based on the formation order (Fig. 2.3) [3]. Primary γ′ precipitates have the largest size (1-10 μm) and the highest solvus temperature among three types of γ′, which are located at grain boundaries for restricting γ-grain growth. Secondary and tertiary γ′ are intragranular particles, typically at particle diameters of around 70-120 nm and 5-50 nm, respectively. This trimodal distribution occurs due to the interplay between the kinetics of γ′ precipitate nucleation, growth and coarsening during isothermal solution and aging treatments. Also, the cooling rate from the solution treatment is important since the γ′ nucleation and growth occurs during cooling. Due to the difference in chemical composition and heat treatment process, not all these types γ′ necessarily form in a given alloy.

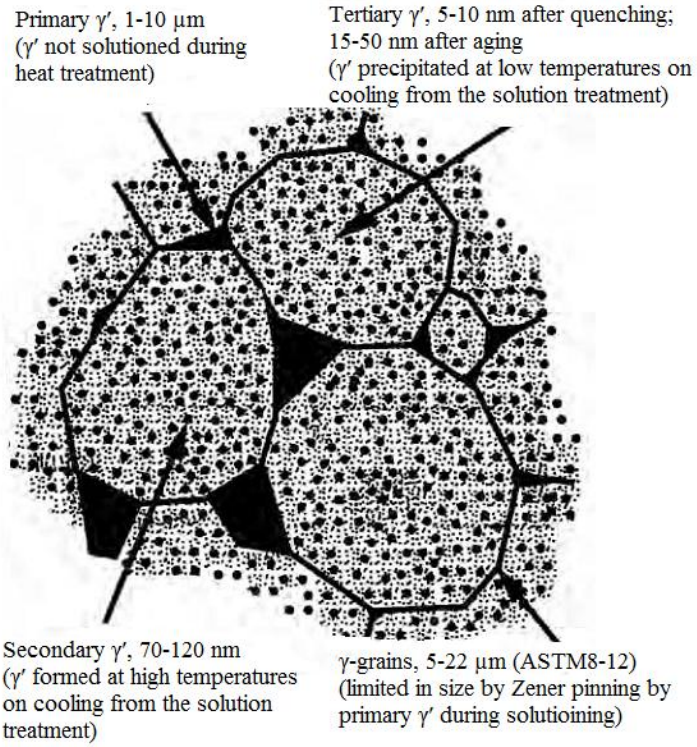

Fig. 2.3. Schematic illustration of the γ′ distribution in Ni-based superalloys [3]

2.2. Wrought IN718 Alloy

IN718 is a precipitation-strengthened Ni-based superalloy, which shows excellent mechanical strength, creep and corrosion resistance at high temperature (~650 °C) [4]. It has been widely used in extremely harsh conditions, especially in aeroengines.

2.2.1. Microstructure of IN718

Wrought IN718 consists of FCC γ matrix, with several types of precipitates. The commercial IN718 has a range of different compositions and heat treatments, which generate different microstructures and precipitate morphology [4-10].

2.2.1.a. Chemical Composition and Precipitates

In general, IN718 contains significant amounts of Ni, Cr, Fe, and Nb, and with small amounts of Mo, Ti, Al, and very little C. The chemical composition is given in Table 2.3.

Table 2.3. Chemical composition of IN718 (wt.%) [14]

Cr	Al	Mo	Nb	Ti	Fe	C	Co	Ni
19.06	0.52	3.04	5.08	0.93	18.15	0.021	0.11	Bal.

Due to the large variety of elements, there are many types of phases in IN718:

γ: γ phase is the matrix phase of IN718. It is an FCC phase, typically formed of Ni, Fe, Cr, Mo, Al, Ti, and Nb.

γ′: γ′ (Ni_3Al) is an FCC phase, with ordered Ll_2 crystal structure (Fig. 2.4). Ti atoms can substitute Al atoms. In IN718, γ′ is the secondary strengthening phase, which is spherical and

occupies a volume percentage of 4-6%. The size of γ′ is ~20 nm, which can be investigated by transmission electron microscope (TEM) dark field micrograph, as shown in Fig. 2.5. The lattice misfit of γ-γ′ is +0.407% which varies with aging [11]. After isothermal long-term aging, the size of γ′ can increase to ~50 nm (Fig. 2.6) [12].

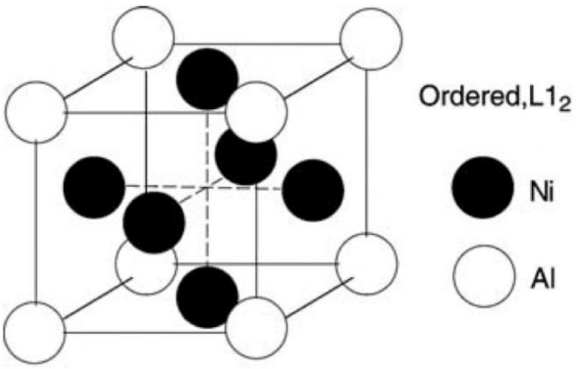

Fig. 2.4. The unit cell of γ′ phase [3]

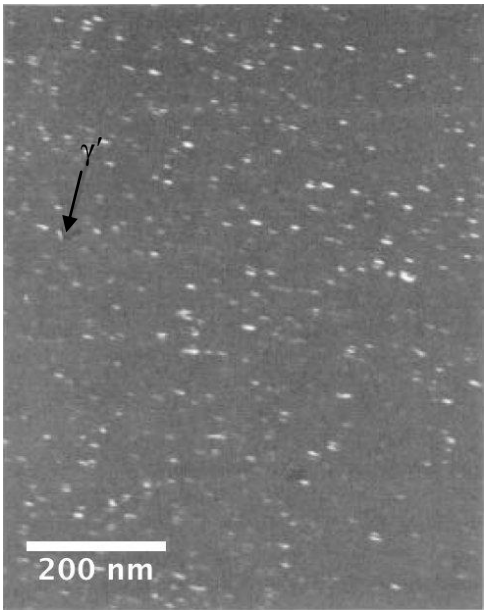

Fig. 2.5. TEM dark field micrograph showing the morphology of the γ′ in forged IN718 after 980 ℃ solution treatment followed by furnace cooling. Diffraction vector 100, beam direction [001] [15]

γ″: DO_{22}-ordered body-centred tetragonal (BCT) γ″ (Ni_3Nb) is the primary strengthening precipitate in IN718. The unit cell is illustrated in Fig. 2.7. Nb atoms can be replaced by Ti atoms. The γ″ particles are disc-shaped ~10 nm thick and ~50 nm length (Fig. 2.8). After long-term aging treatment, the size of γ″ can increase to ~20 nm thick and ~110 nm length (Fig. 2.6). γ″ is coherent with the matrix and the orientation relationship is (001)γ//{001}γ″ and [100]γ//<100>γ″ [13]. The lattice misfit of γ-γ″ is +2.86% which varies with aging [11]. In general, the volume percentage of γ″ is 15-20% in IN718. With decrease in the (Ti+Al)/Nb ratio, γ″ rather than γ′ particles are formed [7].

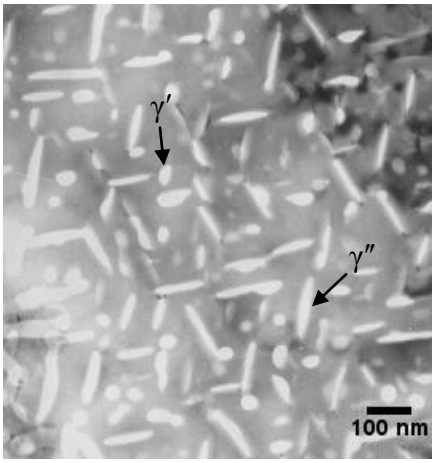

Fig. 2.6. TEM dark field micrograph showing the morphology of the γ′ and γ″ in standard heat treated IN718 after aging at 680 ℃ for 1000 h [12]

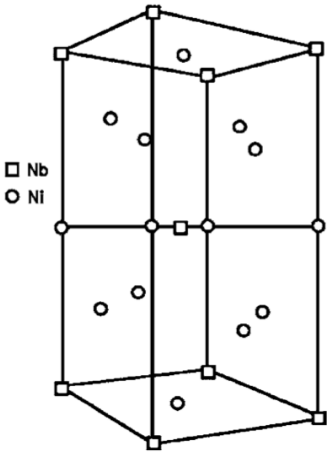

Fig. 2.7. The unit cell of γ″ phase [3]

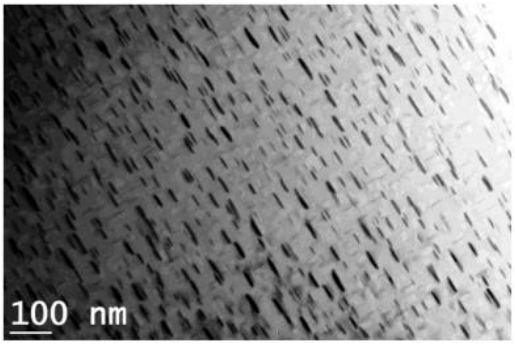

Fig. 2.8. TEM bright field (BF) micrograph showing the morphology of the γ″ in IN718 after standard solution treatment followed by aging [16]

δ: The metastable γ″ phase can transform into δ phase, when long-term exposed to temperature above 650 °C [17]. Needle-shaped δ phase has the same composition as γ″ (Ni_3Nb), and mainly precipitates at the grain boundaries (Fig. 2.9). The DO_a orthorhombic crystal structure δ phase is incoherent with the γ matrix, which does not provide strengthening to the mechanical properties (hardness, toughness, and ductility) [18, 19], and is often the origin of crack nucleation [20]. However, δ phase is stable at high temperatures, which is beneficial to control grain size during manufacturing or high temperature services. δ can also provide grain nucleation sites during forging, and prevents grain boundary migration at high temperature [21].

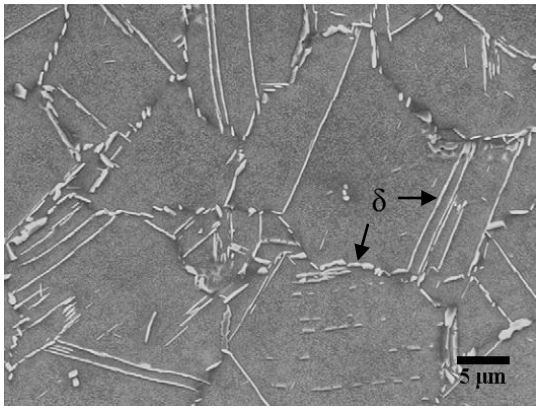

Fig. 2.9. SEM secondary electron (SE) micrograph of δ phase in IN718 heated to 980 ℃, held for 10 min and then cooled at 10 ℃/min [22]

Laves phase: The Laves phase has a hexagonal crystal structure with the composition of $(Ni, Cr, Fe)_2(Nb, Ti, Mo)$. In general, Laves phase often forms during casting, welding and heat treatment, due to the slow cooling rate. It is a brittle phase, which acts as a crack nucleation site. Fig. 2.10 illustrates the morphology of Laves in gas tungsten arc welding (GTAW) of IN718. These are irregular shaped globules, with a high concentration of Nb, which severely degrade the mechanical properties (tensile strength, ductility, fracture toughness) [23]. Solid solution treatment is an effective method to eliminate the Laves phase (at 1090 ℃ for 20 min), but this may result in extensive δ phase precipitation around the Laves phase during treatment [24, 25].

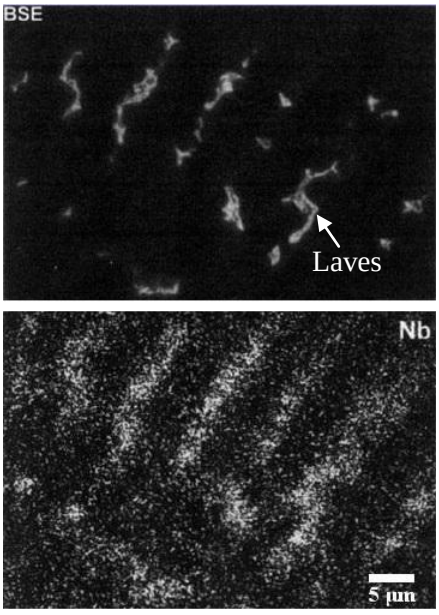

Fig. 2.10. SEM back scattered electron (BSE) micrograph and the corresponding energy dispersive X-ray (EDX) map of Laves phase in GTAW IN718, showing Nb segregation in Laves and interdendritic regions [24]

Carbides: In IN718, carbides are cubic MC (NbC, TiC) and FCC $M_{23}C_6$ (M stands for Cr, Fe, and Mo). Both types of carbides are formed mainly at grain boundaries, where they impede grain growth, thus influencing high-temperature creep properties. $M_{23}C_6$ carbide precipitates

at lower temperatures (~750 °C) and is Cr-rich. During long-time exposure at around 750 ℃, MC dissociates to form the $M_{23}C_6$ via the reaction as follows [3]:

$$MC + \gamma \rightarrow M_{23}C_6 + \gamma'$$

In fact, blocky MC is the major carbide in IN718 (Fig. 2.11), which is stable close to the fusion temperature (1280 °C) [26]. MC carbide is formed at the expense of γ′ and γ" forming elements (Nb, Ti). It has no orientation relationship with the γ matrix, and may act as a crack initiation site. Therefore, large fractions of blocky MC should be avoided in IN718. The main carbide that can be found in commercial IN718 with reduced C content due to vacuum melting is MC type [22], although limited amounts of M_6C can be present in high Si containing IN718 [27].

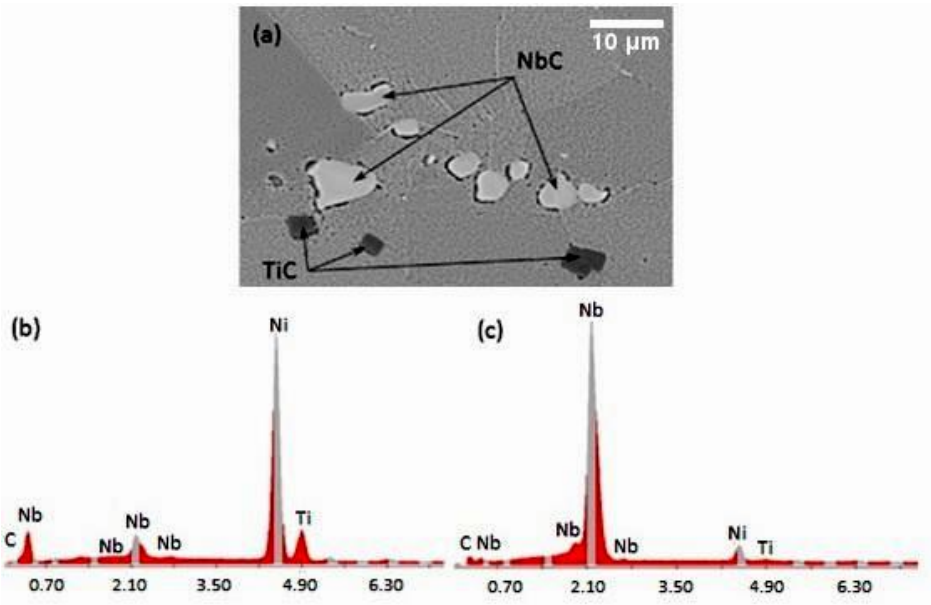

Fig. 2.11. (a) SEM BSE micrograph showing the morphology of the MC carbides in IN718 (solution annealed at 950 ℃ rapid cooling, and aging at 720 ℃ for 8 h), (b) EDX spectrum of TiC, and (c) of NbC [28]

Nitrides: Nitride (MN) is another cubic precipitate in IN718 (Fig. 2.12), where M stands for Ti, Nb, Fe, Ni, and/or Cr. MN phase is rectangular and precipitates at about 1265 °C. As with MC, MN particles improve high-temperature creep properties by preventing grain boundary sliding [3].

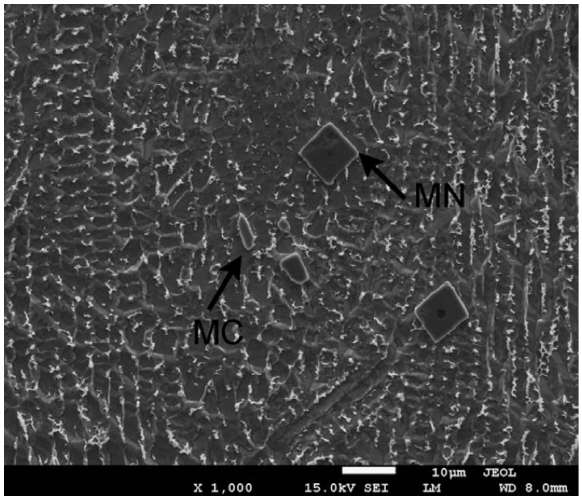

Fig. 2.12. SEM BSE micrograph of the MN and MC carbides in laser clad IN718 coatings [36]

2.2.1.b. Grain Structure

Generally, annealed IN718 possesses equiaxed grains with a large number of annealing twins (Fig. 2.13). The grain size can be varied from a few microns to several hundred microns [8, 9, 30-33]. More information about the role of grain boundaries [34] in Inconel alloys will be described in Section 2.4.3.

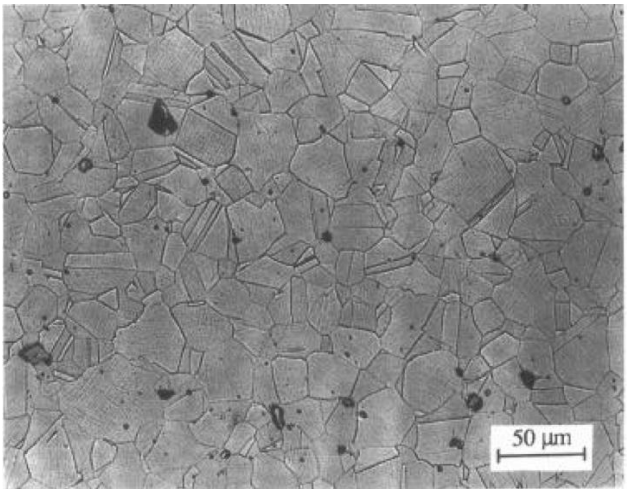

Fig. 2.13. Optical micrograph showing annealed microstructure (with annealing twins) of IN718 with average grain size 23 µm [30]

2.2.2. Phase Transformations in IN718

Thermal analysis and microstructural characterisation are common methods to study the phase transformations of materials. Phase transformations can be divided into isothermal transformations (transformation-time-temperature, TTT) and continuous cooling transformations (CCT). The TTT and CCT diagrams for IN718 are obtained from a large number of experimental results to depict the dissolution and precipitation kinetics of the various phases. The common issue that has been stressed during studies of TTT and CCT diagrams of IN718 is that γ′ and γ″ are too small to be easily identified, which leads to difficulties when determining the precipitation-start and finish-temperatures.

Early work produced conflicting views on the precipitation sequence of γ′ and γ″ phases. Brooks and Bridges [15] reported that γ″ formed before γ′, and drew a TTT diagram with separate γ′ and γ″ curves (Fig. 2.14). Other researchers suggested that at lower temperature (≤680 °C), γ′ precipitation played a dominant role. Slama and Abdellaoui [35] proposed that

γ′ precipitated before γ″ in isothermal aging at 680 °C. To simplify the TTT diagram, Donachie *et al.* [1] merged the γ′/γ″ precipitation process and constructed a new TTT diagram (Fig. 2.15), which is the most reliable TTT diagrams of IN718 and can be used for reference. Niang *et al.* [22] summarised other works on the δ phase solvus and reported that the δ phase solvus is a function of the Nb content (Fig. 2.16). The nose of δ phase TTT curve is in the range of 910 °C to 980 °C [27, 36, 37].

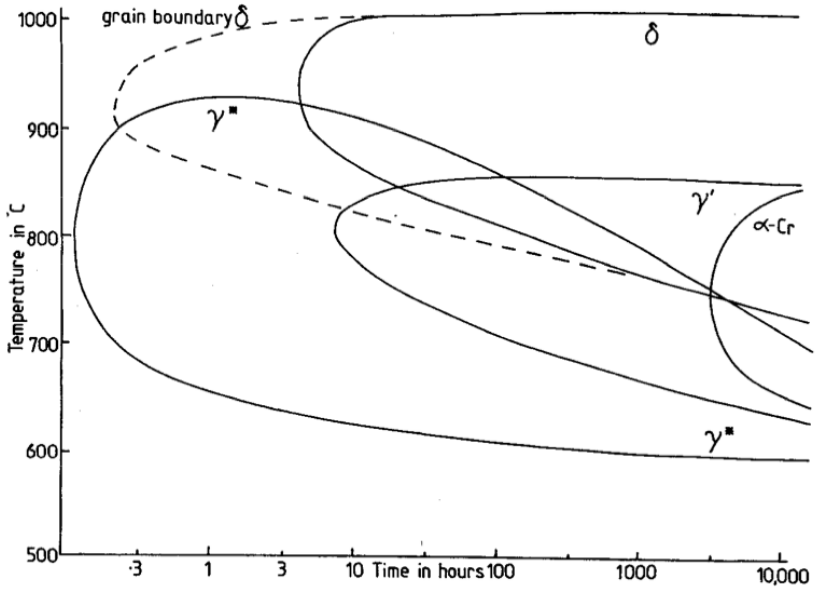

Fig. 2.14. TTT diagram of forged IN718 reported by Brooks and Bridges [15]

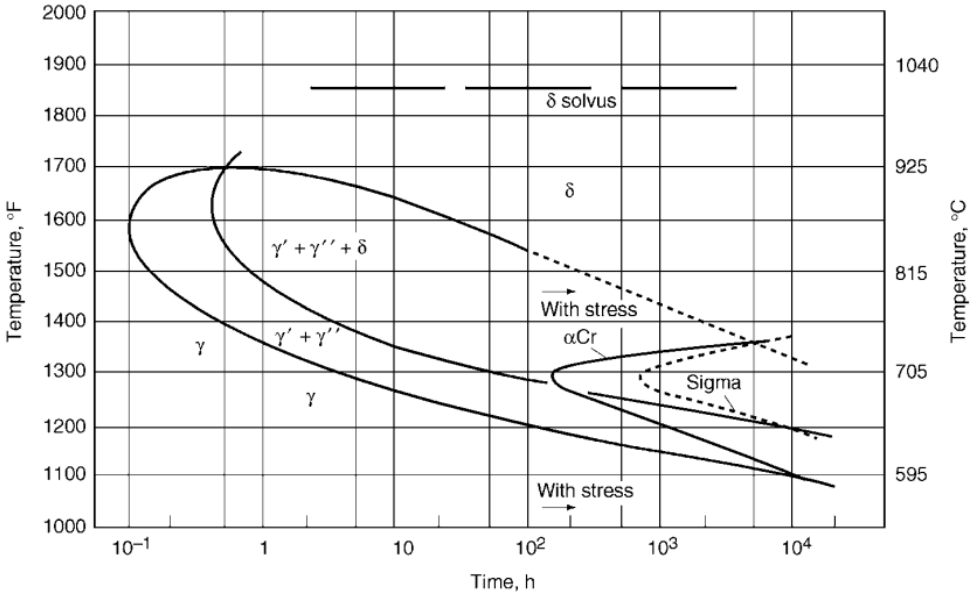

Fig. 2.15. TTT diagram of IN718 reported by Donachie *et al.* [1]

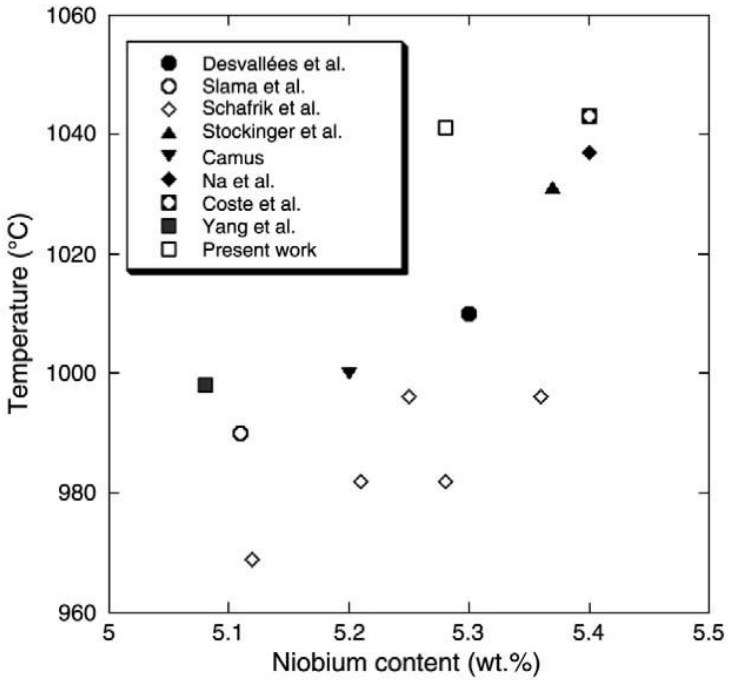

Fig. 2.16. δ phase solvus temperature at different Nb content of forged IN718 [22]

In comparison with TTT data, information concerning CCT diagrams is scarce. Garcia *et al.* [38] used dilatometric analysis and obtained three CCT diagrams from cooling the cast IN718 after holding at 1180 °C for 24, 72, and 90 h. As shown in Fig. 2.17, the transformation start temperature shifts to longer time with the increase in homogenisation time, as the result of the reduction of Nb content at grain boundaries. The lowest critical cooling rate for suppressed γ′/γ″ precipitation is around 10 °C/s, which is about 15 times bigger than that proposed by Geng *et al.* [39] of 0.67 °C/s. For the Laves phase, the critical cooling rate (10 °C/s) is much lower than the value (55.4 °C/s) given by Antonsson and Fredriksson [40]. This discrepancy may be due to the difference of the temperatures from which the samples were cooled or the chemical composition. In addition, Nb is easier to enrich at grain boundaries to form Laves phase when the material solidifies from a liquid state (1430 ℃, in Antonsson and Fredriksson's study) than that in the material cooled from a solid state (1180 ℃, in Garcia *et al*. study). Moreover, the δ phase precipitation reported by Garcia *et al.* appears higher than 1100 °C, which is 80 °C higher than other reports [6, 32, 36]. Later Niang *et al.* [22] drew a new CCT diagram for IN718 based on other works, which will be used as a reference for current study (Fig. 2.18) [38, 41].

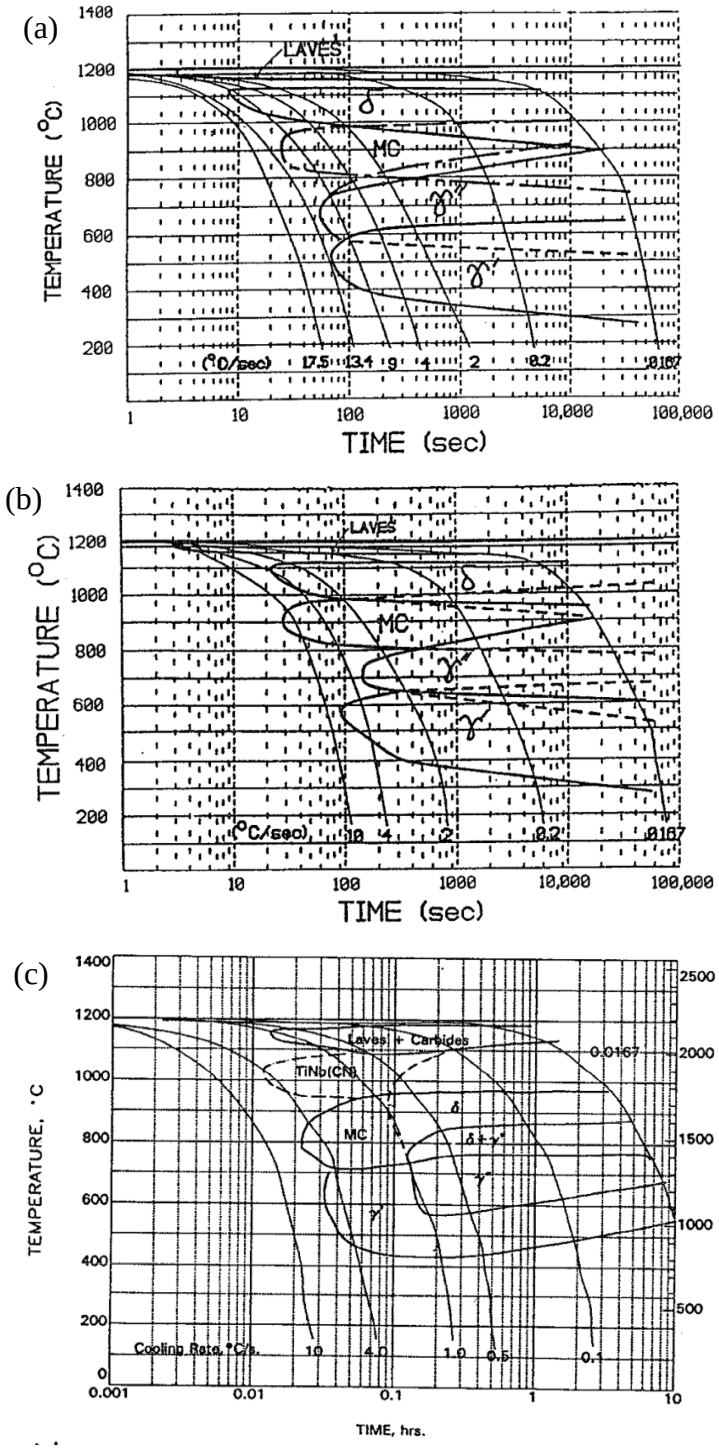

Fig. 2.17. CCT diagrams of IN718 homogenised at 1180 ℃ for (a) 24 h, (b) 72 h, and (c) 90 h [38]

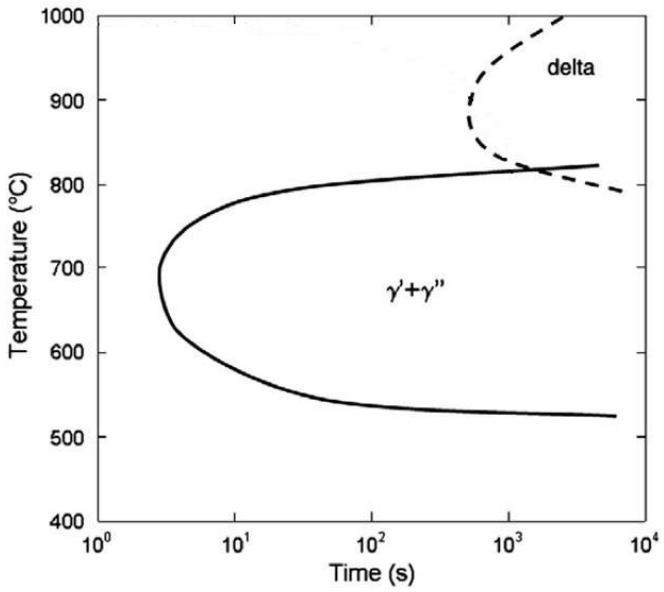

Fig. 2.18. CCT diagram of IN718 reported by Niang *et al.* [22]

DTA curves for wrought IN718 were measured by Dahotre *et al.* [42], as shown in Fig. 2.19. It shows the γ′ starts dissolving at 670 ℃ under heating rate 40 ℃/min which is lower than that of γ″ (838 °C). The forming temperatures for Laves, δ (Ni_3Nb) and γ″ are 1152 ℃, 1098 ℃ and 732 ℃, respectively.

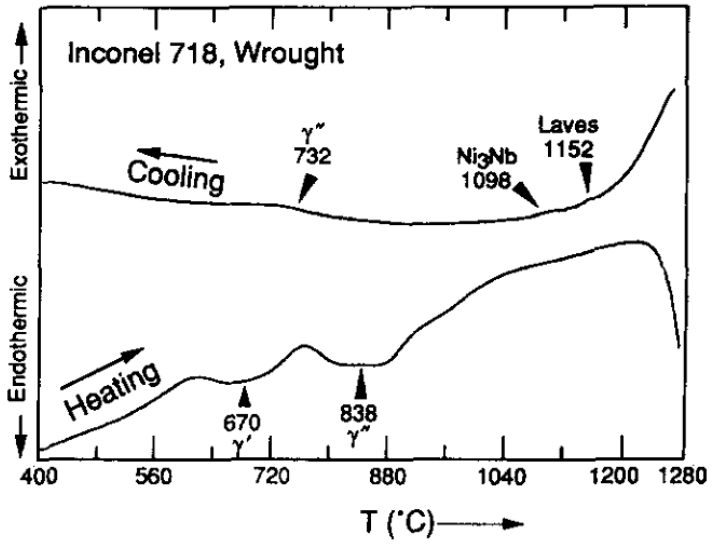

Fig. 2.19. DTA curves for wrought IN718 measured at heating/cooling rate of 40 ℃/min [42]

2.3. Cast IN713LC

Cast IN713LC is a low-carbon Ni-based superalloy, which has excellent high-temperature strength, fatigue, and creep resistance. It has been applied in aeroengines, especially in turbine blades [43]. It was originally produced by air melting the master alloy and followed by argon cast. With the development of vacuum technology, the cast process changes to vacuum melting plus vacuum cast which generates an improvement of high temperature properties [44].

2.3.1. Microstructure of IN713LC

Cast IN713LC consists of a γ matrix, with numbers of intragranular and intergranular precipitates. The chemical heterogeneity is a common issue in cast IN713LC due to the cooling rates in casting. Nb tends to segregate in intradendritic regions, rather than in interdendritic regions [45]. The heterogeneity influences the precipitation behaviour. The typical chemical composition is shown in Table 2.4.

Table 2.4. Chemical composition of IN713LC (wt.%) [45]

Cr	Al	Mo	Nb	Ti	C	Ni
11.94	5.9	4.59	2.24	0.78	0.04	Bal.

2.3.1.a. Phases Present in IN713LC

The main phases in cast IN713LC are the γ matrix, γ′ precipitates, γ-γ′ eutectic and carbides.

γ′: In cast IN713LC, γ′ is the main strengthening phase in the matrix. γ′ phase is coherent with the γ matrix, which can be described as {100}γ//{100}γ′, <010>γ//<010>γ′ cube-cube orientation relationship. As reported by Ricks *et al.* [46], γ′ precipitate appears on the γ matrix {001} facets with <111> growth direction. In general, the value of γ-γ′ misfit exhibits a significant influence on the morphology of the γ′ precipitates (Fig. 2.20). With the increase in aging time at a constant aging temperature, the morphology of γ′ particles evolves from spheres to cubes to arrays of cubes [47]. Hagel and Beattie [48] reported that spherical particles are at γ-γ′ lattice misfit of 0-0.2%, cubes at 0.5-1.0% misfit, and plates at misfits higher than 1.25%. Coarsening of γ′ particles leads to an increase of misfit magnitude and loss of coherency. Lachowicz *et al.* [49] reported that the γ-γ′ lattice misfit of IN713C is in the range of -0.20% to -0.06%. The intragranular γ′ precipitate is cubic, as in Fig. 2.20.b or cubic (arrowed) as in Fig. 2.20.c. In comparison, the grain boundary γ′ particle is mostly in the form of Figs. 2.20.e or f, due to the faster coarsening rate provided by grain boundaries. The morphology of γ′ in light casting IN713LC is cubic, as shown in Fig. 2.21. Some researches show that alloys with negative misfit possess better creep resistance than those of positive misfit [50].

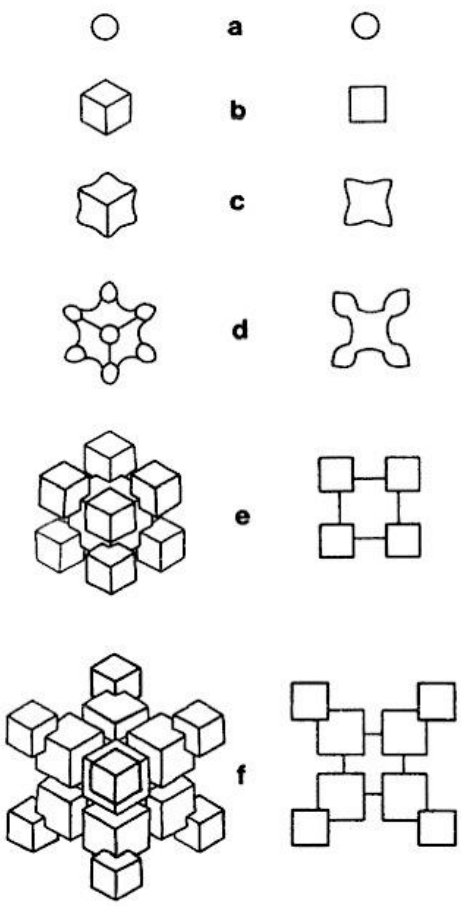

Fig. 2.20. Schematic diagrams displaying the morphology development of strain-induced, faceted γ′ precipitates in <111> (left) and <001> (right) projection [46]

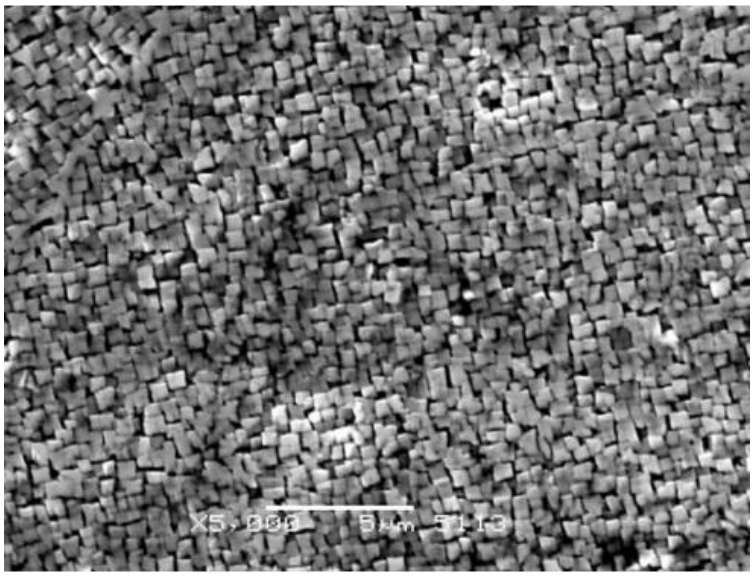

Fig. 2.21. SEM SE micrograph showing the cubic γ′ particles in light cast IN713LC [51]

γ-γ′ eutectic: γ-γ′ eutectic forms at the end of solidification, as a result of supersaturated interdendritic liquid and is rich in γ′-forming elements. As seen in Fig. 2.22, the eutectic is composed of γ′ precipitates (area 1) with embedded thin γ lamellae. The size of the γ-γ′ eutectic is ~10 μm, which is much bigger than the γ′ precipitate. This eutectic is formed during solidification of the casting, consuming large amounts of γ′-forming elements (Al, Ti), which therefore needs to be minimised in casting, or via homogenisation/solution heat treatment.

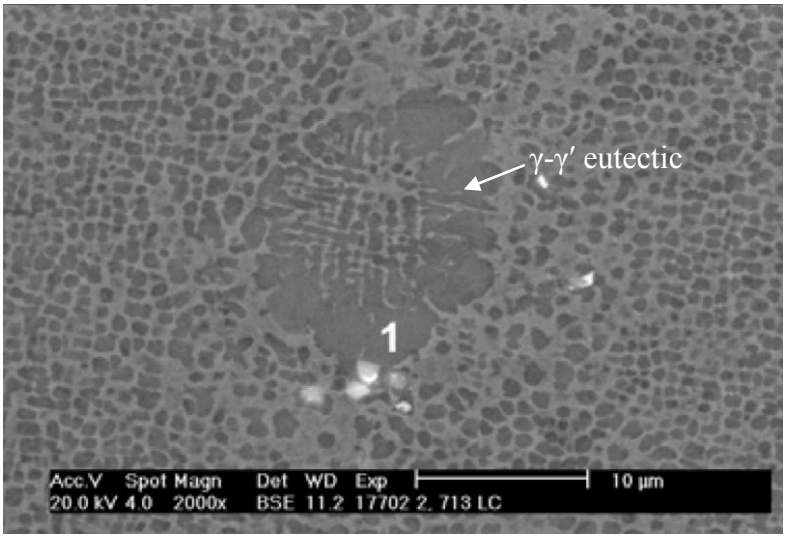

Fig. 2.22. SEM BSE micrograph showing the γ-γ′ eutectic in IN713LC [52]

Carbides: In cast IN713LC, the form of carbides is MC type, where M stands for Nb and Ti in the approximate ratio 8:1 [53]. Podrábský *et al.* [52] reported that M can be replaced by Zr and Mo (Fig. 2.23.a). These blocky MC normally precipitate in interdendritic spaces and grain boundaries, as seen in Fig. 2.23.b. The role of carbides is to improve high-temperature creep properties by the inhibition of grain boundary sliding.

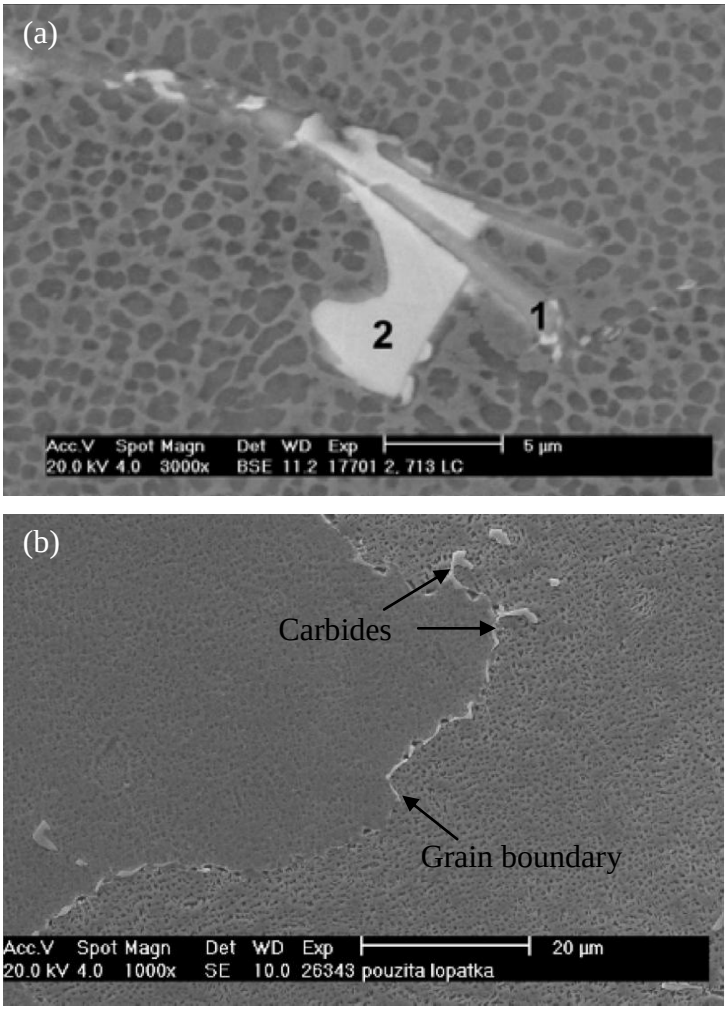

Fig. 2.23. SEM micrographs showing the morphology of carbides in cast IN713LC, (a) area 1 contains Nb and Mo, and area 2 contains Nb, Zr, and Mo (BSE micrograph) [52], and (b) grain boundary carbides (SE micrograph) [54]

2.3.1.b. Grain Structure

Cast polycrystalline IN713LC exhibits very coarse grains (Fig. 2.24). The grain size is in the range of 0.5-2 mm depending on the cooling rate.

Fig. 2. 24. Optical micrograph showing the structure of cast IN713LC [52]

2.3.2. Phase Transformations in IN713LC

In contrast to IN718, there is very limited data on the phase transformations in IN713LC. Zl á *et al.* [55] studied the phase transformation temperatures of cast IN713LC using differential thermal analysis (DTA). The phase transformation sequence during heating was reported following as γ′ dissolution, γ/γ′ eutectic dissolution, carbides dissolution, and γ matrix fully melted (Fig. 2.25.a). Variation of transformation temperatures with changing of the heating/cooling rates in DTA are shown in Tables 2.5 and 2.6. The γ′ solvus rises with the increase in heating/cooling rate. It is reasonable that the γ′ solvus shifts to higher temperature due to the higher heating rate. However, the reported increase in the γ′ solvus with increase of cooling rate is not expected. The expectation is that the increase in cooling rate generates higher undercooling which would suppress γ′ precipitation, and therefore reduce the γ′ solvus [56]. The γ′ solvus temperature at equilibrium (1205 ℃) was obtained from a zero heating rate by extrapolation. However, as seen in Fig. 2.25, it can be difficult to precisely identify some of dissolution/precipitation temperatures (e.g. γ′ initial dissolution temperature, γ′ final precipitation temperature, γ/γ′ eutectic dissolution/precipitation temperatures). It is

reasonable to assume that determination of phase transformations of IN713LC by thermal analysis is not sufficient, additional microstructural analysis would be required.

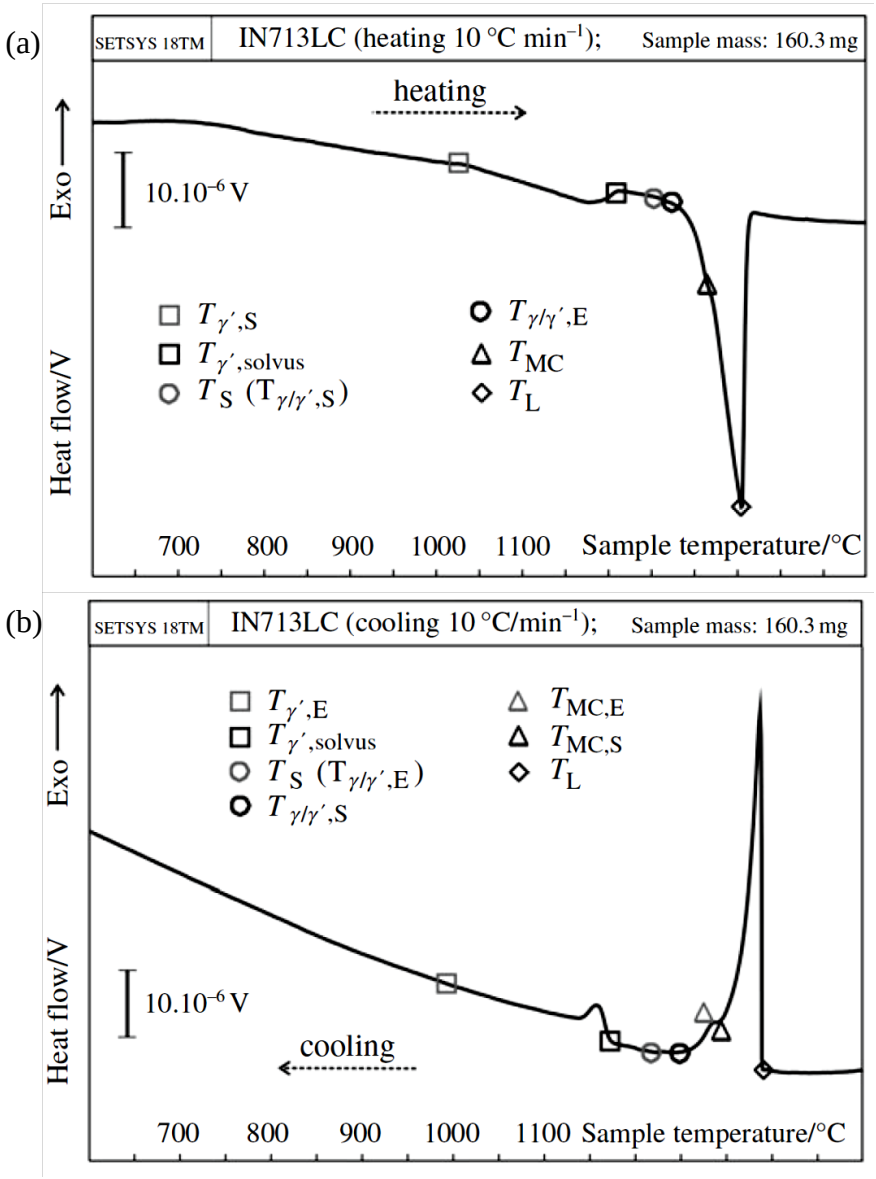

Fig. 2.25. DTA curves of cast IN713LC, (a) heating rate 10 ℃/min, $T_{\gamma',S}$: γ′ initial dissolution temperature (T) ; $T_{\gamma',solvus}$: γ′ solvus T (γ′ final dissolution T); T_S ($T_{\gamma/\gamma',S}$): solidus T (γ/γ′ eutectic initial dissolution T); $T_{\gamma/\gamma',E}$: γ/γ′ eutectic final dissolution T; T_{MC}: MC carbides dissolution T; T_L: liquidus T, and (b) cooling rate 10 ℃/min, $T_{\gamma',E}$: γ′ final precipitation T; $T_{\gamma',solvus}$: γ′ solvus T (γ′ initial precipitation T); T_S ($T_{\gamma/\gamma',E}$): solidus T (γ/γ′ eutectic final precipitation T); $T_{\gamma/\gamma',S}$: γ/γ′ eutectic initial precipitation T; $T_{MC,E}$: MC carbides final precipitation T; $T_{MC,S}$: MC carbides initial precipitation T; T_L: liquidus T [55]

Table 2.5. Phase transformation temperatures of IN713LC at various heating rates. $T_{\gamma',S}$: γ′ initial dissolution temperature, $T_{\gamma',solvus}$: γ′ solvus temperature, T_S ($T_{\gamma/\gamma',S}$): solidus temperature (γ/γ′ eutectic initial dissolution temperature), $T_{\gamma/\gamma',E}$: γ/γ′ eutectic final dissolution temperature, T_{MC}: MC carbides dissolution temperature, T_L: liquidus temperature [55]

Heating rate (℃ min^{-1})	Temperature of phase transformation (℃)					
	$T_{\gamma',S}$	$T_{\gamma',solvus}$	T_S ($T_{\gamma/\gamma',S}$)	$T_{\gamma/\gamma',E}$	T_{MC}	T_L
50	987	1226	1252	1268	1325	1370
20	1003	1215	1253	1270	1322	1359
10	1029	1210	1253	1271	1319	1354
5	1101	1208	1248	1286	1318	1251
1	1133	1204	1248	1289	1316	1349
0 (calc.)	1094	1205	1250	1283	1317	1349

Table 2.6. Phase transformation temperatures of IN713LC at various cooling rates. T_L: liquidus temperature, $T_{MC,S}$: MC initial precipitation temperature, $T_{MC,E}$: MC final precipitation temperature, $T_{\gamma/\gamma',S}$: γ/γ′ eutectic initial precipitation temperature, T_S ($T_{\gamma/\gamma',E}$): γ/γ′ eutectic final precipitation temperature, $T_{\gamma',solvus}$: γ′ solvus temperature (γ′ initial precipitation temperature), $T_{\gamma',E}$: γ′ final precipitation temperature [55]

Cooling rate (℃ min^{-1})	Temperature of phase transformation (℃)						
	T_L	$T_{MC,S}$	$T_{MC,E}$	$T_{\gamma/\gamma',S}$	T_S ($T_{\gamma/\gamma',E}$)	$T_{\gamma',solvus}$	$T_{\gamma',E}$
50	1324	1262	1249	1223	1193	1183	925
20	1329	1283	1270	1238	1213	1182	953
10	1338	1289	1286	1238	1219	1175	996
5	1339	1294	1290	1251	1227	1178	1084
1	1346	1341	1295	1262	1233	1167	1114
0 (calc.)	1343	1314	1294	1254	1230	1172	1074

Due to the lack of CCT diagram for IN713LC, it is reasonable to use the CCT of another alloy which contains a similar chemical composition and γ′ volume fraction for reference. Grosdidier *et al.* [57] studied the influence of cooling rate on the precipitation of γ′, and created a CCT diagram for CMSX-2 (70% γ′ volume fraction). As seen in Fig. 2.26, the

morphology of precipitated γ′ changes with the cooling rates. At a cooling rate of 100 ℃/s, γ′ particles are around 100 nm spheres or cubes. However, with the decrease in cooling rate to 0.2 ℃/s, γ′ particles grow to form 700 nm cubes. When the cooling rate reaches 0.02 ℃/s, γ′ particles coarsen to plates of several microns.

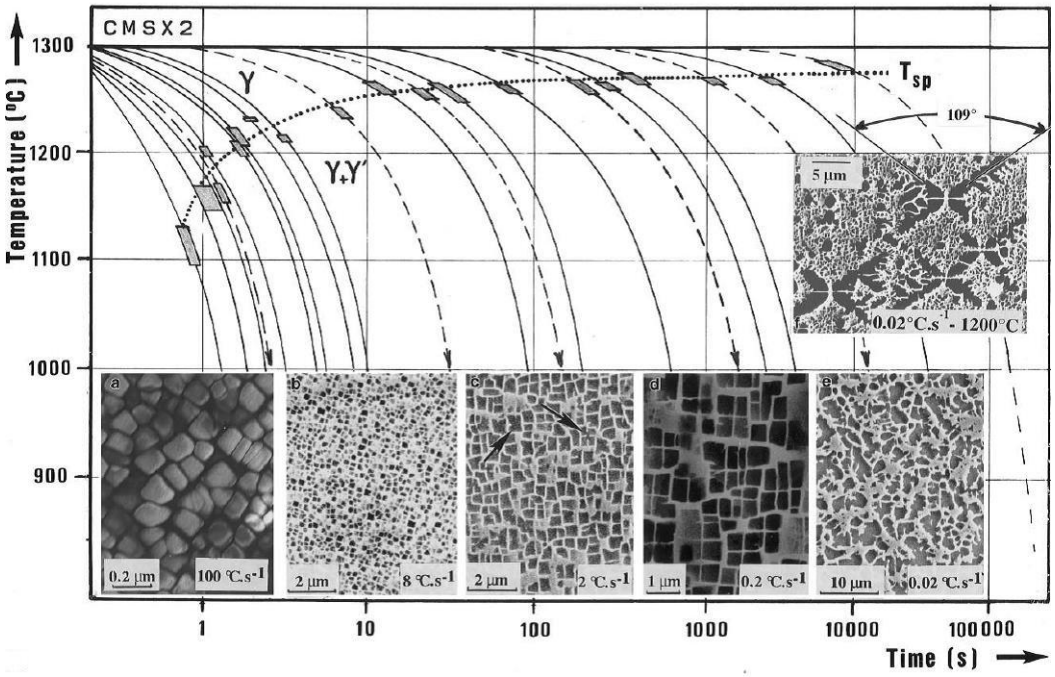

*T_{sp}: temperature for γ′ starting precipitation

Fig. 2.26. CCT diagram of CMSX-2, homogenised at 1300 ℃ for 3 h, and SEM micrographs showing the microstructures at various cooling rates [57]

2.4. Strengthening Mechanisms in Ni-based Superalloys

There are several strengthening mechanisms in Ni-based superalloys, which can be classified into: precipitation strengthening, solid solution strengthening, and grain boundary strengthening.

2.4.1. Precipitation Strengthening

Precipitation strengthening is the main strengthening mechanism in precipitation-strengthened Ni-based superalloys (e.g. IN718 and IN713LC), due to the large volume fraction of γ′/γ″ precipitates in the matrix.

2.4.1.a. Coherency Strain Hardening

γ′ and γ″ are coherent with the γ matrix, and as such would induce coherency strain hardening. When the precipitates are sheared, the dislocations must glide in pairs to maintain ordered atomic arrangements within the precipitates. There are two different couplings: weak-pair coupling and strong-pair coupling. The weak-pair coupling works on small precipitates (small γ″ or tertiary γ′), i.e. when the leading dislocation exits the sheared precipitates, the trailing dislocation is still outside these precipitates. When the precipitates reach a critical size, the pair of dislocations shears the precipitates together, which is referred to as strong-pair coupling (Fig. 2.27).

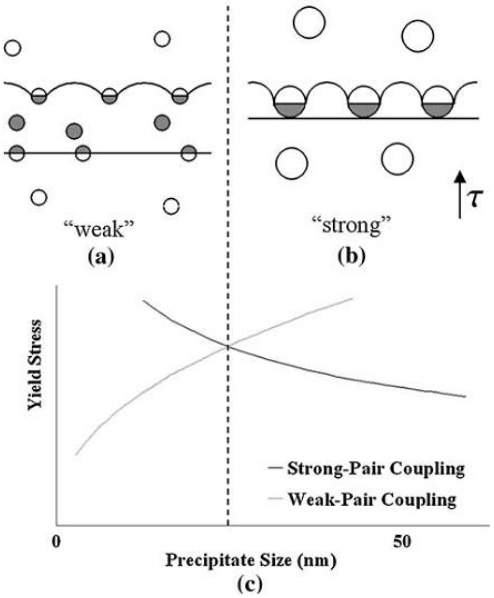

Fig. 2.27. Schematic diagram of dislocations shearing precipitates, (a) weak-pair coupling, (b) strong-pair coupling, and (c) yield stress vs. precipitate size in two coupling situations [58]

Sundararaman *et al.* [59] , and Chaturvedi and Han [11] suggested that the yield strength of IN718 can be accounted for mainly by the this coherency hardening mechanism. Sundararaman *et al.* [59] reported that the critical size from weak-pair coupling to strong-pair coupling in IN718 is 10 nm. Because of this, strong-pair coupling mainly operates within secondary γ′. It should be noted that the anti-phase boundary (APB) is the strengthening increment in both situations. The critical resolved shear stress (τ_c) required for cutting weak-pair and strong-pair couplings proposed by Reed [3] are as follows:

Weak-pair coupling $$\tau_c = \frac{\gamma_{APB}}{2b}\left[\left(\frac{6\gamma_{APB} fr}{\pi T}\right)^{1/2} - f\right] \quad (2.1)$$

Strong-pair coupling $$\tau_c = \sqrt{\frac{3}{2}}\left(\frac{Gb}{r}\right) f^{1/2} \frac{w}{\pi^{3/2}} \left(\frac{2\pi\gamma_{APB} r}{wGb^2} - 1\right)^{1/2} \quad (2.2)$$

where γ_{APB} is the APB energy, f is the volume fraction of strengthening particles, r is the average radius of strengthening particles, b is the Burgers vector, T is approximately $\frac{1}{2}Gb^2$, and w is a dimensionless constant. Several modified equations were proposed to satisfy more specific alloys [58, 60].

2.4.1.b. Cross-slip-induced hardening

Thermally activated cross-slip pinning is another strengthening mechanism, which operates in primary and large secondary γ′ precipitates (>300 nm) [58]. There is a critical γ′ precipitate size for thermally activated cross-slip pinning events, while the size is smaller than the critical size, no cross-slip-induced hardening occurs. The quantitative analyses reported by Kozar *et al.* [58] illustrates that for IN100, the critical size is 300 nm and in the range of 100-900 nm, the larger the precipitates, the more thermally activated cross-slip occurs. The cross-slip-induced hardening, Δσ, is given as [58]:

$$\Delta\sigma = f\left[\sigma(T)_{Ni_3Al} + \sum_i\left(\frac{d\sigma}{dC_i}C_i\right)\right] \quad (2.3)$$

where f is the fraction of γ' subject to cross-slip-induced hardening, $\sigma(T)_{Ni_3Al}$ is the temperature dependent strength of Ni_3Al, C_i is the concentration of alloying elements, and $\frac{d\sigma}{dC_i}$ is the cross-slip-induced hardening constants for alloying elements to γ', as shown in Table 2.7.

Table 2.7. Cross-slip-induced hardening constants for alloying elements to γ' [58]

	Al	Cr	Co	Mo	Ti	V
Constant (MPa/pct)	0	7	0	16.8	25	8.2

2.4.1.c. Orowan Strengthening

Orowan strengthening (Orowan bowing mechanisms) occurs when the precipitates are larger than a critical size (typically ~17 μm), which leads to dislocations bypassing precipitates forming dislocation loops (Fig. 2.28).

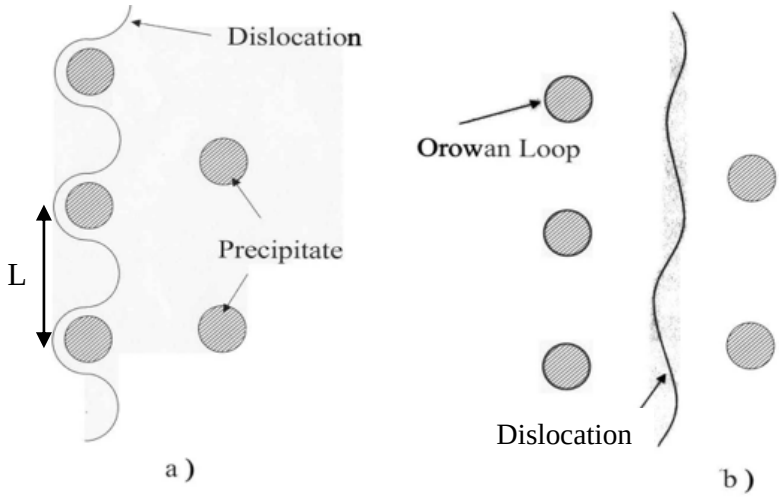

Fig. 2.28. Configuration of Orowan mechanism, (a) dislocation bowing between adjacent precipitates, (b) dislocation bypassing precipitates leaving Orowan loops near precipitates [61]

This is because the stress required for dislocations to cut precipitates is bigger than the stress needed for them to bow between precipitates. The Orowan bowing stress (τ) is equal to Equation 2.4, where *G* is shear modulus, *b* is Burgers vector, *r* is precipitate radius, and *L* is the distance between pinning points. Reed [3] claimed that the Orowan bowing mechanism is unlikely to be the main strengthening mechanism in Ni-based superalloys at room temperature, because the shear stress calculated from Equation 2.2 required for dislocations cutting precipitates is much lower than the Orowan bowing stress.

$$\tau = \frac{Gb}{L-r} \tag{2.4}$$

2.4.2. Solid Solution Strengthening

In general, there are two solid solution mechanisms, i.e. interstitial solid solution and substitutional solid solution. The latter is dominant in Ni-based superalloys, by replacing solvent atoms with substitutional atoms, which causes stress fields surrounding solute atoms. The theory for solid solution strengthening of Ni-based superalloys is deduced from a model proposed by Gypen and Deruyttere [62]. The solute spacing is proportional to the square root of the concentration, thus the solid solution strengthening, $\Delta\sigma_{SSS}$, is expressed as:

$$\Delta\sigma_{SSS} = \sum_i \left(\frac{d\sigma}{\sqrt{dC_i}}\sqrt{C_i}\right) \tag{2.5}$$

where $\sqrt{C_i}$ is the concentration for solute *i*, and $\frac{d\sigma}{\sqrt{dC_i}}$ is the strengthening constant of solute *i*. Roth *et al.* [63] reported the strengthening constants ($k_i = \frac{d\sigma}{\sqrt{dC_i}}$) of alloying additions in Ni, which are listed in Table 2.8.

Table 2.8. Strengthening constants of alloying elements for solid solution strengthening in Ni-based superalloys [63]

Alloying Element	Strengthening Constant, k_i (MPa At. Fraction$^{-1/2}$)
Al	225
Si	275
Zn	386
Ga	310
Ge	332
In	985
Sn	1225
Sb	960
Ti	775
V	408
Zr	2359
Hf	1401
Nb	1183
Ta	1191
Cr	337
Mo	1015
W	977
Mn	448
Fe	153
Ru	1068
Co	39.4
Rh	520
Cu	86.7
C	1061
Pd	492

2.4.3. Grain Boundary Strengthening

According to the Hall-Petch relation [64], the yield strength (σ) of polycrystalline material is inversely proportional to the square root of grain size (d), which is given by:

$$\sigma = \sigma_o + k_y d^{-1/2} \tag{2.6}$$

where σ_o is the friction stress and k_y is the Hall-Petch slope.

For precipitation hardening materials, the Hall-Petch relation is rarely used. Values of k_y for IN100 and Nimonic 105 were reported 750 MPa·μm$^{-1/2}$ and 700 MPa·μm$^{-1/2}$, respectively [58, 65]. Mangen and Nembach's work on Nimonic PE16 showed that the value of Hall-Petch slope varies greatly with the change of the size, volume fraction and distribution of γ′. In γ′-free matrix, the σ_o and k_y are 153 MPa and 371 MPa·μm$^{-1/2}$, respectively [66].

In precipitation hardened Ni-based superalloys, grain boundary strengthening is obtained by refined grains, associated with grain boundary particles impeding grain boundary sliding at high temperature. In IN718, δ phase precipitates at grain boundaries, and prevents grain coarsening. However, if there is too much δ phase, the mechanical properties (tensile strength, fracture toughness, ductility) are degraded.

2.5. Thermal and Thermo-Mechanical Processing of Ni-based Superalloys

Thermal and thermo-mechanical processes cover solution treatment, aging treatment, hot deformation, welding, etc.. The microstructural and the mechanical properties development are influenced by thermal and thermo-mechanical processing. A number of experimental and modelling studies have been focused on this area.

2.5.1. Influence of Rapid Heating on Precipitates Dissolution

Investigation of the dissolution mechanisms of precipitates in Ni-based superalloys is essential, in order to understand the influence of phase transformations during thermal or thermo-mechanical processing on mechanical properties. Payton *et al.* [67] pointed out that measurement of the dissolution kinetics is difficult, especially in the supersolvus temperature-range, due to the rapidly varying volume fraction of precipitates. To obtain kinetic constants, a heat transfer analysis was incorporated into experimental data. Under rapid heating rates, the precipitates dissolution behaviour is different from equilibrium dissolution. Tancret [68] demonstrated that if the temperature reaches the γ′ melting point before full dissolution, liquid occurs as a form of γ′ liquation. This is due to the limited time for diffusion leading to a high concentration of Al located at γ′ particles, which reduces the melting point to below that of the matrix, so that these Al-rich regions dissolve below the melting temperature of the matrix. There is a critical heating rate (V_c) for γ′ liquation proposed by Tancret [68], which is plotted in Fig. 2.29, following the equation:

$$V_c = \frac{A}{r^2} \tag{2.7}$$

where r is the initial particle size and A = 280 K ·μm^{2}s^{-1}.

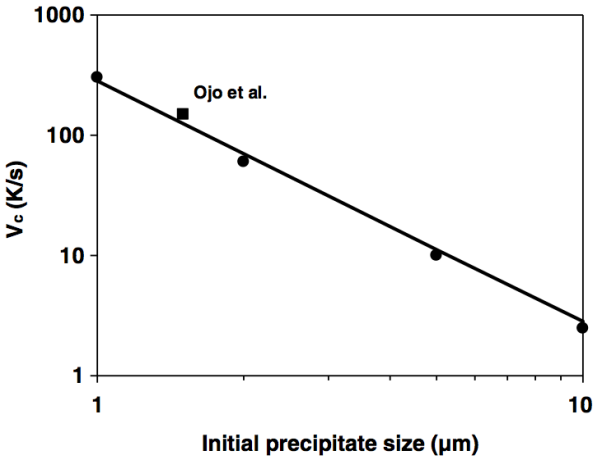

Fig. 2.29. The relationship between the initial precipitate size and the critical heating rate for γ′ liquation in IN738 [68]

Ojo *et al*. [69-71] reported a critical heating rate of 150 K/s for the size of 1.5 μm γ′ particles in IN738, which is in agreement with Equation 2.7. Similar liquation of primary γ′ (~2 μm) in RR1000 at heating rate 5 K/s was observed by Attallah *et al.* [72] using the High-Temperature Confocal Laser Scanning Microscopy (HT-CLSM). The measured heating rate (5 K/s) is much lower than the value predicted by Tancret's equation (70 K/s). Attallah *et al.* argued that is due to the complexity of γ′ constitutional liquation phenomenon. The liquation is formed through γ-γ′ reaction including diffusion, rather than the melting of γ′. This argument is based on Ojo and Tancret's paper [73], which clarified Tancret's previously published work [68]. Ojo and Tancret [73] explained that the liquation in Tancret's [68] study was due to γ-γ′ eutectic reaction, rather than the melting of γ′. This eutectic reaction is called constitutional liquation, which was first introduced by Pepe and Savage [74], as illustrated in a Ni-Al phase diagram Fig. 2.30. During rapid heating an alloy with a composition X, for kinetic reasons, γ′ precipitates may not have enough time to fully dissolve before the temperature reaches the eutectic temperature T_E. Hence, the rest of γ′ precipitates reacts with the γ matrix as a form of eutectic reaction to form a liquid phase L. This type of phenomenon is known as constitutional liquation. This liquation concept is more pertinent than exclusive melting of γ′, because γ and γ′ are highly reactive at high temperatures.

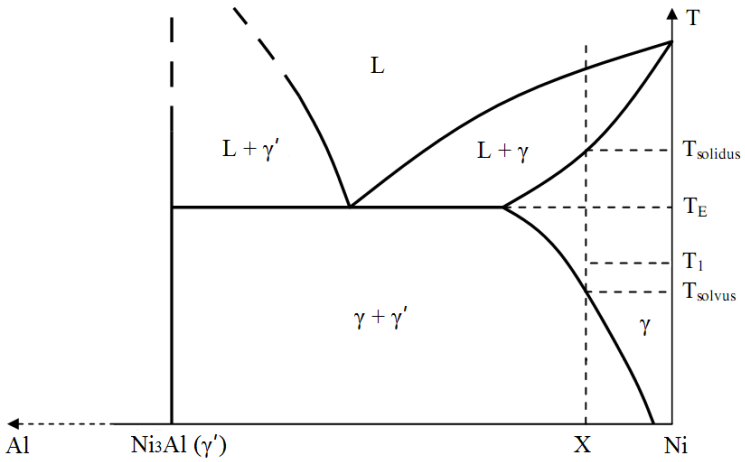

Fig. 2.30. Ni-Al phase diagram illustrating the constitutional liquation between γ and γ′ [73]

It is generally agreed [67, 68, 75] that the dissolution of precipitates depends on the heating rate, the size and shape of precipitates, and the distribution of precipitate. Soucail and Bienvenu [75] presented experimental values of γ′ dissolution for Astroloy (45% γ′ volume fraction) at equilibrium and at rapid heating rates. They proposed a model for γ′ phase dissolution based on Al diffusion length and geometric parameters. The equation for expressing the volume fraction of γ′ at equilibrium $f_{\gamma'}(T)$ is given by:

$$f_{\gamma'}(T) = \frac{X_{0,Al} - X_{Al,\gamma}(T)}{X_{Al,\gamma'} - X_{Al,\gamma}(T)} \tag{2.8}$$

where $X_{0,Al}$ and $X_{Al,\gamma'}$ are the atomic fraction of Al in alloy and γ′ phase respectively, and $X_{Al,\gamma}(T)$ refers to the atomic fraction of Al in γ phase at temperature *T*. For a rapid heating model, the time-temperature equivalence concept was introduced to replace the rapid thermal cycle with a holding time of t_e at the equivalent temperature T_e, as shown in Fig. 2.31.

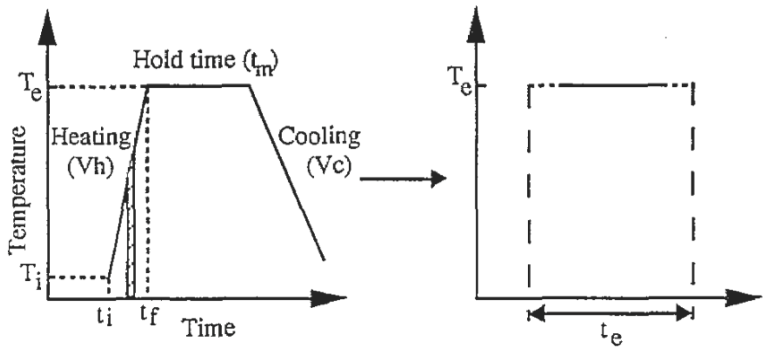

Fig. 2.31. The replacement of thermal cycle with time-temperature equivalence [75]

Soucail and Bienvenu model was applied to the calculation of the γ′ solvus for different thermal cycles, to the prediction of γ′ volume fraction under thermal cycling for different γ′ sizes, and also was validated by prediction of the maximum temperature reached at a certain distance in a friction welded sample. The dissolution follows the Arrhenius equation:

$$D = D_0 exp(-Q/RT) \quad (2.9)$$

where D is the diffusion coefficient at temperature T, D_0 is the diffusion coefficient at a reference temperature, Q is the diffusion activation energy, and R is the gas constant.

2.5.2. Growth Behaviour of Precipitates

During aging treatment, the coarsening of γ′ and γ″ particles is based on the theory of Lifshitz, Slyosov and Wagner (LSW theory) [76, 77]. The particle size can be written as:

Spherical γ′ $$\bar{r}^3 - \bar{r}_0^3 = Kt \quad (2.10)$$

Disc-shaped γ″ $$\bar{d}^3 - \bar{d}_0^3 = Kt \quad (2.11)$$

where $\bar{r}$ is the average radius of γ′ at time t, $\bar{r}_0$ is the initial average radius of γ′, $\bar{d}$ is the mean diameter of γ″ at time t, $\bar{d}_0$ is the initial mean diameter of γ″, and K is a temperature dependent rate constant. For cuboidal particles, $\bar{r}$ and $\bar{r}_0$ are replaced by $\bar{a}/2$ and $\bar{a}_0/2$ respectively, where $\bar{a}$ is the average cube edge length at time t, and $\bar{a}_0$ is the initial cube edge length [78]. Han *et al.* [77] proposed that K for IN718 is defined as:

Spherical γ′ $$K = \frac{8\gamma D C_e V_m^2}{9RT} \quad (2.12)$$

Disc-shaped γ″ $$K = \frac{128\gamma^P q D C_e V_m^2}{9\pi RT} \quad (2.13)$$

where γ is the interfacial free energy of γ-γ′ interface, γ^P is the interfacial energy of γ-γ″ interface, C_e is the concentration of solute atoms in equilibrium with a γ′ of infinite radius, V_m is the molar fraction of γ′ or γ″, R is the gas constant, T is the absolute temperature of growth, q is d/h where h is the thickness of γ″, and D is the diffusion coefficient of the solute atoms in γ matrix, $D = D_0 \exp(-Q/RT)$, where Q is the activation energy of growth. Table 2.9 shows the K values of γ′ and γ″ at different temperatures. The activation energy Q of γ′ and γ″ growth are calculated from K, as $Q_{\gamma'}$ and $Q_{\gamma''}$ are 271 and 298 kJmol^{-1} [77]. Table 2.10 lists

the activation energies for γ′ and γ″ growth in various Ni-based superalloys. All work illustrates that the activation energy is a constant value independent of temperature and volume fraction of particles, and the growth rates of particles accelerate at high temperature. The activation energies for γ′ and γ″ growth are close to the activation energies for the diffusion of Al in Ni (269.4 $kJmol^{-1}$) or Ti in Ni (256.9 $kJmol^{-1}$) or Nb in Ni-Fe-Nb system (264 $kJmol^{-1}$) [76, 77, 79]. This suggests that the growth of γ′ and γ″ particles follows the diffusion-controlled growth mechanism.

Table 2.9. *K* values of γ′ and γ″ growth at different temperatures [77]

Temperature (K)	$K_{\gamma'}$ ($Å^3s^{-1}$)	$K_{\gamma''}$ ($Å^3s^{-1}$)
973	0.213×10^2	1.26×10^2
998	0.627×10^2	5.28×10^2
1023	1.043×10^2	6.94×10^2

Table 2.10. Activation energy of γ′ and γ″ growth in various Ni-based alloys

Materials	Particles	Activation energy ($kJmol^{-1}$)	Researchers
Udimet 700	38% γ′	269.9	Van Der Molen *et al.* [76]
Udimet 700	32% γ′	265	Monajati *et al.* [80]
Nimonic 105	35% γ′	266	Kusabiraki *et al.* [81]
N/A	60% γ′	268	MacKay and Nathal [82]
IN718	4.4% γ′	271	Han *et al.* [77]
IN718	13.1% γ″	298	Han *et al.* [77]

2.5.3. Dynamic Recrystallisation

Dynamic recrystallisation (DRX) is a common phenomenon in thermo-mechanical processes. It involves grain boundary migration, dislocation formation and annihilation, subgrain and

new fine grain generation. DRX therefore influences the microstructural and mechanical properties of materials.

Generally, DRX involves either continuous or discontinuous behaviour [83, 84]. Continuous dynamic recrystallisation (CDRX) is usual in high stacking fault energy materials (e.g. Al, Zr), new grains are formed by the progressive accumulation of dislocations formed low-angle boundary subgrains. Whereas, in discontinuous dynamic recrystallisation (DDRX) new grains nucleate and grow by the migration and bulging of initial high-angle boundaries, which normally occurs in low or intermediate stacking fault energy materials (e.g. Ni, Cu, austenitic steel [85]).

During hot deformation of polycrystalline Ni-based superalloys, when the deformation reaches a critical value, dynamic recrystallised (DRXed) equiaxed fine grains are generated at grain boundaries and form a necklace-like structure (Fig. 2.32). Continued deformation will gradually give rise to a fully recrystallised structure with a constant grain size.

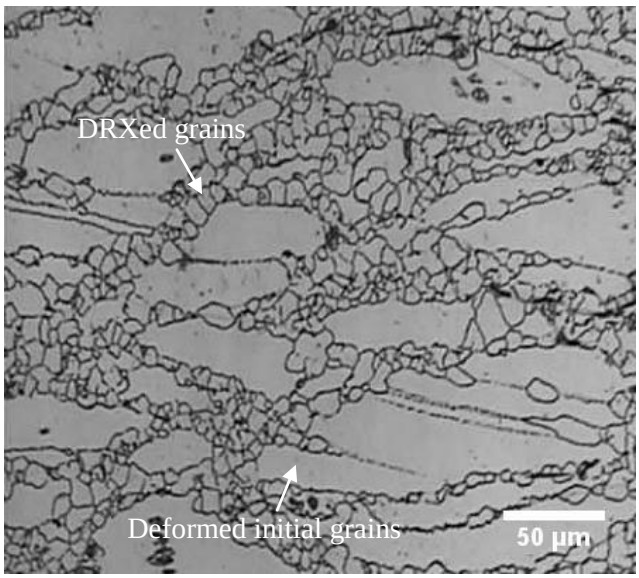

Fig. 2.32. Optical micrograph showing the necklace structure in dynamically recrystallised IN718 deformed with a strain rate of 1 s^{-1} to strain of 0.76 at 1060 ℃ [17]

In general, DRX occurs when the critical strain reaches 0.5-0.8 times the peak strain in the true strain-true stress curve [86, 87]. Two mathematical models of the critical strain for IN718 DRX were proposed by Na *et al.* [88] as follow:

$$\dot{\varepsilon} \geq 0.01s^{-1} \qquad \varepsilon_c = 8.87 \times 10^{-4} d_0^{0.2} Z^{0.099} \tag{2.14}$$

$$\dot{\varepsilon} < 0.01s^{-1} \qquad \varepsilon_c = 9.57 \times 10^{-6} d_0^{0.196} Z^{0.167} \tag{2.15}$$

where ε_c is the critical strain, $\dot{\varepsilon}$ is the strain rate, d_0 is the initial grain size, and Z is the Zener-Hollomon parameter. The Zener-Hollomon parameter is defined as:

$$Z = \dot{\varepsilon} \exp\left(Q/RT\right) \tag{2.16}$$

where $\dot{\varepsilon}$ is the strain rate, Q is the activation energy of deformation, R is the gas constant, and T is the temperature.

The values of the activation energy of deformation (Q) for IN718 were reported by several researches, as seen in Table 2.11. As can be seen from Equations 2.14 and 2.15, the critical strain is mainly dependent on the Z parameter and the initial grain size. If under the same initial grain size, the critical strain is proportional to the strain rate and inversely proportion to the temperature. Most of the studies were based on solution treated IN718 without δ phase, rare studies focused on the dynamic recrystallisation of IN718 involving δ phase. Yuan and Liu [17] reported that in the case of IN718 with a large amount of δ phase, the activation energy only slightly increases from 443 to 458 kJmol^{-1}.

Table 2.11. Activation energy of deformation for IN718

Researches	Activation energy of deformation in IN718, Q (kJmol^{-1})
Medeiros *et al.* [89]	400
Weis *et al.* [90]	423
Yuan and Liu [17]	443
Wang *et al.* [33]	443.2

The nucleation mechanisms of DRXed grains in IN718 are still controversial. Wang *et al.* [8, 33] reported that the nucleation mechanisms of DRX are strongly dependent on the Z parameter. At low Z (1000 °C and 10^{-3} s^{-1}), DDRX is the dominant mechanism, in which the DRX grains are formed by the bulging of initial grain boundaries. The twins generated at the initial grain boundary accelerate the nucleation and development of DRX grains. At high Z (950 °C and 0.1 s^{-1}), CDRX is proved to be the main mechanism. Wang *et al.* [91] proposed that the DRX nucleation mechanism under hot deformation (1000 °C and 0.1 s^{-1}) involves the coalescence of dislocations, reconfiguration of subgrains formed along the original grain boundary, rather than a grain boundary bulging mechanism, because the grain boundary carbides impede the migration of grain boundaries. This explanation is unconvincing because the low percentage of carbides (0.15 wt.%) is insufficient to prevent the large area of grain boundaries migrating. Wang *et al.* results strongly suggested that CDRX is the primary DRX mechanism at high *Z*.

Defu *et al.* [92] suggested that the sizes of DRXed grains are defined irrespective of the deformation strain. Conversely, Wang *et al.* [33] reported that during hot deformation of IN718 at a constant strain, the volume fraction of DRXed grains increases with increase of deformation temperature and decrease of strain rate, and the DRXed grain size (d_{DRX}) is determined as:

$$d_{DRX} = 3 \times 10^5 Z^{-0.27} \tag{2.17}$$

where $Z = \dot{\varepsilon}\exp(Q/RT)$, which demonstrates that the DRXed grain size is proportional to the temperature and inversely proportional to the strain rate.

Other work by Zhao and Chaudhury [30] reported that the fraction of dynamic recrystallisation is also dependent on the initial grain size. At a strain rate of 0.001 s^{-1}, a fine grain alloy requires a higher temperature to complete recrystallisation than a coarse grain

alloy. Because small grains have more grain boundaries than large grains, this character allows small grains to accommodate more strain by grain boundary sliding than large grains, resulting in lower stored strain energy facilitating dynamic recrystallisation.

Some researchers reported that the dynamic recrystallisation behaviour is different in rapid thermal cycle hot deformation of Al-alloy, Al-Mg alloy, pure iron, low and ultra-low carbon steel [93-97]. Ferry and Jones [97] reported that both the recrystallised grain size and the recrystallisation end temperature decrease with the increase in the heating rate for particle-containing Al-alloys, and are more pronounced in single-phase Al-alloys. However, Muljono *et al.* [94] found that in low and ultra-low carbon steel, increasing heating rate in the range of 50-1000 °C/s results in an increase in the recrystallisation initial temperature and a decrease in the recrystallised grain size, which is opposite to Ferry and Jones' results. Moreover, Muljono *et al.* proposed a {111}//ND (normal direction) recrystallisation texture increases at heating rates up to 200 °C/s and remains constant at higher rates due to enhanced nucleation sites at grain boundaries. It is certain that the rapid thermal cycle affects the recrystallisation by varying the nucleation and grain growth processes, but the specific mechanisms are not understood and no related report has been focused on Ni-based superalloys.

2.5.4. Grain Growth

Grain growth occurs during isothermal or anisothermal processes, e.g. welding, hot deformation cooling processes or heat treatment. Grain growth-induced grain size variation can influence the strength of material. Some publications have focused on modelling grain

growth of polycrystalline austenite alloys. Sellars *et al.* [98] and Anelli [99] proposed two different models:

$$d^n = d_0^n + A \cdot t \cdot exp(-Q/RT) \tag{2.18}$$

$$d = Bt^m exp(-Q/RT) \tag{2.19}$$

where d is the final grain size, d_0 is the initial grain size, t is the holding time, T is the temperature, R is the gas constant, Q is the activation energy for grain growth, and A, B, n, m are experimental constant.

The differences of these two equations are that Equation 2.18 does not consider the time exponent, and Equation 2.19 does not include the initial grain size. Considering the two models are based on experimental results, Liu *et al.* [100] proposed a new model which combines these two models:

$$d^n = d_0^n + At^m exp(-Q/RT) \tag{2.20}$$

Liu *et al.* applied this model on isothermal and anisothermal heat treatment of IN718 and gave grain growth equations based on experimental work:

Isothermal:

$$d^{2.682} = d_0^{2.682} + 4.733 \times 10^{18} t^{1.313} exp(-405599/RT) \tag{2.21}$$

Anisothermal:

$$d_{i+1}^{2.682} = d_0^{2.682} + 4.733 \times 10^{18} (\bar{t}_i + \Delta t)^{1.313} exp(-405529/RT_i) \tag{2.22}$$

$$\bar{t}_i^{\,1.313} = \frac{1}{4.733 \times 10^{18}} (d_i^{2.682} - d_0^{2.682}) exp(405529/RT_i) \tag{2.23}$$

where Δt is the time between t_i and t_{i+1}, T_i is the temperature at t_i, d_i and d_{i+1} are the grain size at t_i and t_{i+1}, and $\bar{t}_i$ is the time of grain growth from d_0 to d_i under isothermal condition. Because Δt is a very short time, the grain growth during Δt can be seen as isothermal process. These models are based on average grain size 10.1 μm, thus they are suitable for modelling grain growth of IN718 with grain size no less than this value.

2.6. Summary: Key Findings and Areas of Research

This chapter summarises the metallurgy of Ni-based superalloys, including strengthening mechanisms, microstructure, phase transformations, and the influence of thermal and thermo-mechanical processes. The most relevant aspects of Ni-based superalloys behaviour in response to welding, of those which have been discussed in this brief review are listed below:

1. Ni-based superalloys are a group of complex alloys, which have excellent high temperature mechanical properties and creep resistance. Compared with as-cast Ni-superalloys, forged Ni-superalloys have more homogeneous microstructure and chemical composition. Heat treatment can homogenise the microstructure and modify the formation of preferred precipitates to enhance the mechanical properties. Phase transformations of IN718 and IN713LC have been studied, and TTT and CCT diagrams of IN718 have been established. However, no TTT or CCT diagram relates to IN713LC, only DTA data is available. The results show that the phase transformation temperatures vary with the difference of the alloy chemical composition. For the same alloy, different heating rates induce different transformation temperatures. In addition, the cooling rate dramatically influences the microstructure of precipitates. However, quantitative studies about the influence of rapid heating on the phase transformations of IN718 and IN713LC are limited.
2. There are several strengthening mechanisms in Ni-based superalloys: precipitation strengthening, solid solution strengthening, and grain boundary strengthening. Precipitation strengthening (γ'/γ'' strengthening) is the primary agent in aging heat treatment condition, whereas in solution treatment condition, the solid solution strengthening is the dominant factor. Grain boundary strengthening follows the Hall-Petch relation and plays an equally important role in both conditions. The

theoretical models for different mechanisms have been established, and quantitative researches have been focused on associating strengthening mechanisms with yield strength. However, due to the complexity of various strengthening contributions, it is difficult to quantify the mechanical properties by the theoretical modelling of strengthening mechanisms. Thermal and thermo-mechanical processes change the microstructure of material, and thus influence the mechanical properties. At equilibrium, the microstructural developments (precipitates dissolution, dynamic recrystallisation, precipitates and grain growth) follow a diffusion-controlled mechanism. In contrast, at non-equilibrium conditions (rapid heating/cooling), the microstructure varies in a different manner, where the dissolution temperatures of precipitates and the recrystallised grain size are affected by different heating/cooling rates. However, the influence of rapid thermal cycles on the microstructure of IN718 and IN713LC has not been investigated.

The work in this dissertation studies the microstructure-property development of LFW IN718-IN713LC. The following areas have been focused on for further investigation:

1. Phase transformation temperatures of IN718 and IN713LC used in this dissertation.
2. Influence of rapid heating on the microstructural development of IN718 and IN713LC:
    - Measuring the solvus temperatures of particles at different heating rates.
    - Quantifying and modelling the volume fraction variation of particles.
    - Modelling the peak temperature at the weld zone.
    - Investigating and predicting the constitutional liquation in IN713LC.

2.7. References

[1] M. J. Donachie, *Superalloys: A Technical Guide*, American Welding Society International, 2002.

[2] J. D. Whittenberger, "Creep and tensile properties of several oxide dispersion strengthened nickel base alloys," *Metallurgical Transactions A*, vol. 8, pp. 1155-1163, 1977.

[3] R. C. Reed, *The Superalloys: Fundamentals and Applications*. New York, Cambridge University Press, 2006.

[4] R. B. Li, M. Yao, W. C. Liu, and X. C. He, "Isolation and determination for δ, γ′ and γ″ phases in Inconel 718 alloy," *Scripta Materialia*, vol. 46, pp. 635-638, 2002.

[5] S. H. Chang, "In situ TEM observation of γ′, γ″ and δ precipitations on Inconel 718 superalloy through HIP treatment," *Journal of Alloys and Compounds*, vol. 486, pp. 716-721, 2009.

[6] S. Azadian, L. Y. Wei, and R. Warren, "Delta phase precipitation in Inconel 718," *Materials Characterization*, vol. 53, pp. 7-16, 2004.

[7] R. Cozar and A. Pineau, "Morphology of Y' and Y" Precipitates and Thermal-Stability of Inconel 718 Type Alloys," *Metallurgical Transactions*, vol. 4, pp. 47-59, 1973.

[8] Y. Wang, W. Z. Shao, L. Zhen, and X. M. Zhang, "Microstructure evolution during dynamic recrystallization of hot deformed superalloy 718," *Materials Science and Engineering A*, vol. 486, pp. 321-332, 2008.

[9] F. L. Sui, L. X. Xu, L. Q. Chen, and X. H. Liu, "Processing map for hot working of Inconel 718 alloy," *Journal of Materials Processing Technology*, vol. 211, pp. 433-440, 2011.

[10] J. F. Radavich, "The physical metallurgy of cast and wrought alloy 718," *Superalloy 718—Metallurgy and Applications*, pp. 229-240, 1989.

[11] M. C. Chaturvedi and Y. F. Han, "Strengthening mechanisms in Inconel 718 superalloy," *Metal Science*, vol. 17, pp. 145-149, 1983.

[12] J. H. Du, X. D. Lu, Q. Deng, J. L. Qu, J. Y. Zhuang, and Z. Y. Zhong, "High-temperature structure stability and mechanical properties of novel 718 superalloy," *Materials Science and Engineering A*, vol. 452, pp. 584-591, 2007.

[13] A. Devaux, L. Naze, R. Molins, A. Pineau, A. Organista, J. Y. Guedou, J. F. Uginet, and P. Heritier, "Gamma double prime precipitation kinetic in Alloy 718," *Materials Science and Engineering A*, vol. 486, pp. 117-122, 2008.

[14] A. Thomas, M. El-Wahabi, J. M. Cabrera, and J. M. Prado, "High temperature deformation of Inconel 718," *Journal of Materials Processing Technology*, vol. 177, pp. 469-472, 2006.

[15] J. W. Brooks and P. J. Bridges, "Metallurgical stability of Inconel alloy 718," *Superalloys*, vol. 88, pp. 33-42, 1988.

[16] R. Damodaram, S. Raman, and K. P. Rao, "Microstructure and mechanical properties of friction welded alloy 718," *Materials Science and Engineering: A*, vol. 560, pp. 781-786, 2013.

[17] H. Yuan and W. C. Liu, "Effect of the δ phase on the hot deformation behavior of Inconel 718," *Materials Science and Engineering A*, vol. 408, pp. 281-289, 2005.

[18] L. C. M. Valle, L. S. Araújo, S. B. Gabriel, J. Dille, and L. H. de Almeida, "The effect of δ phase on the mechanical properties of an Inconel 718 superalloy," *Journal of Materials Engineering and Performance*, vol. 22, pp. 1512-1518, 2013.

[19] G. Smith and S. Patel, "The role of niobium in wrought precipitation-hardened nickel-base alloys," in *Superalloys 718, 625, 706 and Various Derivatives*, Pittsburgh, USA, pp. 135-154, 2005.

[20] S. Q. Li, J. Y. Zhuang, J. Y. Yang, Q. Deng, J. H. Du, X. S. Xie, B. Li, Z. C. Xu, Z. Cao, and Z. Q. Su, "The effect of phase on crack propagation under creep and fatigue conditions in alloy 718," in *Superalloys 718, 625, 706 and Various Derivatives*, Pittsburgh, USA, pp. 545-555, 1994.

[21] S. J. Patel and G. D. Smith, "The role of niobium in wrought superalloys," in *International Symposium on Niobium 2001*, Orlando, USA, pp. 1081-1108, 2001.

[22] A. Niang, B. Viguier, and J. Lacaze, "Some features of anisothermal solid-state transformations in alloy 718," *Materials Characterization*, vol. 61, pp. 525-534, 2010.

[23] J. J. Schirra, R. H. Caless, and R. W. Hatala, "The effect of laves phase on the mechanical properties of wrought and cast + HIP Inconel 718," in *Superalloys 718, 625, 706 and Various Derivatives*, Pittsburgh, USA, pp. 375-388, 1991.

[24] G. D. Janaki Ram, A. Venugopal Reddy, K. Prasad Rao, and G. Madhusudhan Reddy, "Control of laves phase in Inconel 718 GTA welds with current pulsing," *Science and Technology of Welding & Joining*, vol. 9, pp. 390-398, 2004.

[25] C. H. Radhakrishna and K. P. Rao, "The formation and control of Laves phase in superalloy 718 welds," *Journal of Materials Science,* vol. 32, pp. 1977-1984, 1997.

[26] G. P. Sabol and R. Stickler, "Microstructure of Nickel-Based Superalloys," *Physica Status Solidi,* vol. 35, pp. 11-52, 1969.

[27] A. Oradei-Basile and J. F. Radavich, "A current TTT diagram for wrought alloy 718," in *Superalloys 718, 625, 706 and Various Derivatives*, Pittsburgh, USA, pp. 325-335, 1991.

[28] J. M. Zhou, V. Bushlya, and J. E. Stahl, "An investigation of surface damage in the high speed turning of Inconel 718 with use of whisker reinforced ceramic tools," *Journal of Materials Processing Technology,* vol. 212, pp. 372-384, 2012.

[29] Y. C. Zhang, Z. G. Li, P. L. Nie, and Y. X. Wu, "Carbide and nitride precipitation during laser cladding of Inconel 718 alloy coatings," *Optics & Laser Technology,* vol. 52, pp. 30-36, 2013.

[30] D. Zhao and P. K. Chaudhury, "Effect of starting grain size on as-deformed microstructure in high temperature deformation of alloy 718," in *Superalloys 718, 625, 706 and Various Derivatives*, Pittsburgh, USA, 1994.

[31] J. M. Zhang, Z. Y. Gao, J. Y. Zhuang, and Z. Y. Zhong, "Grain growth model of IN718 during holding period after hot deformation," *Journal of Materials Processing Technology,* vol. 101, pp. 25-30, 2000.

[32] C. Mary and M. Jahazi, "Multi-scale analysis of IN-718 microstructure evolution during linear friction welding," *Advanced Engineering Materials*, vol. 10, pp. 573-578, 2008.

[33] Y. Wang, W. Z. Shao, L. Zhen, L. Yang, and X. M. Zhang, "Flow behavior and microstructures of superalloy 718 during high temperature deformation," *Materials Science and Engineering A,* vol. 497, pp. 479-486, 2008.

[34] D. L. Coffey, W. B. Cartmill, and C. E. Burgan, "A Welding Defect Related to the Aluminum Content in a Nickel-Base Alloy," *American Welding Society,* pp. 29-30, 1972.

[35] C. Slama and M. Abdellaoui, "Structural characterization of the aged Inconel 718," *Journal of Alloys and Compounds,* vol. 306, pp. 277-284, 2000.

[36] V. Beaubois, J. Huez, S. Coste, O. Brucelle, and J. Lacaze, "Short term precipitation kinetics of delta phase in strain free Inconel 718 alloy," *Materials Science and Technology,* vol. 20, pp. 1019-1026, 2004.

[37] W. J. Boesch and H. B. Canada, "Precipitation reactions and stability of Ni3Cb in Inconel alloy 718," *Journal of Metals*, pp. 34-38, 1969.

[38] C. I. Garcia, A. K. Lis, E. A. Loria, and A. J. Deardo, "Thermomechanical processing and continuous cooling transformation behavior of IN-718," *Superalloys 1992*, pp. 527-536, 1992.

[39] L. Geng, Y. S. Na, and N. K. Park, "Continuous cooling transformation behavior of Alloy 718," *Materials Letters*, vol. 30, pp. 401-405, 1997.

[40] H. Fredriksson, "The effect of cooling rate on the solidification of INCONEL 718," *Metallurgical and Materials Transactions B*, vol. 36, pp. 85-96, 2005.

[41] C. Slama and G. Cizeron, "Etude du comportement structural de l'alliage NC19FbNb (Inconel 718)," *Joural de Physique III*, pp. 665-688, 1997.

[42] N. B. Dahotre, M. H. McCay, T. D. McCay, C. R. Hubbard, W. D. Porter, and O. B. Cavin, "Effect of grain structure on phase transformation events in the Inconel 718," *Scripta Metallurgica et Materialia*, vol. 28, pp. 1359-1364, 1993.

[43] C. N. Wei, H. Y. Bor, C. Y. Ma, and T. S. Lee, "A study of IN-713LC superalloy grain refinement effects on microstructure and tensile properties," *Materials Chemistry and Physics*, vol. 80, pp. 89-93, 2003.

[44] J. J. Schirra, R. H. Caless, and R. W. Hatala, "Mechanical property and microstructural characterization of vacuum die cast superalloy materials," *Superalloys 2004*, pp. 553-561, 2004.

[45] T. Podrábský, K. Stránský, S. Pospíšilová, A. Rek, J. Dobrovská, and M. Juliš, "Heterogeneity alloy of Inconel 713LC," *Acta Metallurgica Slovaca*, vol. 11, pp. 68-73, 2005.

[46] R. A. Ricks, A. J. Porter, and R. C. Ecob, "The growth of γ′ precipitates in nickel-base superalloys," *Acta Metallurgica*, vol. 31, pp. 43-53, 1983.

[47] W. Betteridge and J. Heslop, *The Nimonic Alloys*. London, Edward Arnold, 1974.

[48] W. C. Hagel and H. J. Beattie, *Iron and Steel Institute Special Report*, vol. 64, pp. 98-107, 1964.

[49] M. Lachowicz, W. Dudziński, and M. Podrez-Radziszewska, "TEM observation of the heat-affected zone in electron beam welded superalloy Inconel 713C," *Materials Characterization*, vol. 59, pp. 560-566, 2008.

[50] H. Harada and H. Murakami, "Design of Ni-base superalloys," in *Computational Materials Design*, ed: Springer, 1999, pp. 39-70.

[51] J. Zýka, I. Andršová, B. Podhorná, and K. Hrbáček, "Mechanical properties and microstructure of IN713LC nickel superalloy castings," *METAL 2013,* pp. 15-17, 2013.

[52] T. Podrábský, Z. Jonšta, K. Hrbáček, and K. Němec, "The microstructural analysis of turbine blade from alloy Inconel 713LC," *Acta Metallurgica Slovaca,* vol. 9, pp. 198-202, 2003.

[53] P. Jonšta, Z. Jonšta, J. Sojka, L. Čížek, and A. Hernas, "Structural characteristics of nickel superalloy Inconel 713LC after heat treatment," *Journal of Achievement in Materials and Manufacturing Engineering,* vol. 21, pp. 33-36, 2007.

[54] T. Podrábský, M. Juliš, S. Pospíšilová, K. Němec, K. Hrbáček, A. Rek, and Z. Jonšta, "Changes in microstructure of turbine wheel made of Inconel 713LC," *Acta Metallurgica Slovaca,* vol. 11, pp. 62-67, 2005.

[55] S. Zlá, B. Smetana, M. Žaludová, J. Dobrovská, V. Vodárek, K. Konečná, V. Matějka, and H. Francová, "Determination of thermophysical properties of high temperature alloy IN713LC by thermal analysis," *Journal of Thermal Analysis and Calorimetry,* vol. 110, pp. 211-219, 2012.

[56] R. J. Mitchell, M. Preuss, S. Tin, and M. C. Hardy, "The influence of cooling rate from temperatures above the γ′ solvus on morphology, mismatch and hardness in advanced polycrystalline nickel-base superalloys," *Materials Science and Engineering A,* vol. 473, pp. 158-165, 2008.

[57] T. Grosdidier, A. Hazotte, and A. Simon, "Precipitation and dissolution processes in γ/γ′ single crystal nickel-based superalloys," *Materials Science and Engineering A,* vol. 256, pp. 183-196, 1998.

[58] R. Kozar, A. Suzuki, W. Milligan, J. Schirra, M. Savage, and T. Pollock, "Strengthening mechanisms in polycrystalline multimodal nickel-base superalloys," *Metallurgical and Materials Transactions A,* vol. 40, pp. 1588-1603, 2009.

[59] M. Sundararaman, P. Mukhopadhyay, and S. Banerjee, "Deformation behaviour of γ" strengthened Inconel 718," *Acta Metallurgica,* vol. 36, pp. 847-864, 1988.

[60] J. K. Tien and R. P. Gamble, "Effects of stress coarsening on coherent particle strengthening," *Metallurgical Transactions,* vol. 3, pp. 2157-2162, 1972.

[61] A. Chamanfar, M. Jahazi, J. Gholipour, P. Wanjara, and S. Yue, "Modeling grain size and strain rate in linear friction welded Waspaloy," *Metallurgical and Materials Transactions A,* vol. 44A, pp. 4230-4238, 2013.

[62] L. A. Gypen and A. Deruyttere, "Multi-component solid solution hardening," *Journal of Materials Science,* vol. 12, pp. 1028-1033, 1977.

[63] H. A. Roth, C. L. Davis, and R. C. Thomson, "Modeling solid solution strengthening in nickel alloys," *Metallurgical and Materials Transactions A,* vol. 28, pp. 1329-1335, 1997.

[64] L. L. Shaw, A. L. Ortiz, and J. C. Villegas, "Hall–Petch relationship in a nanotwinned nickel alloy," *Scripta materialia,* vol. 58, pp. 951-954, 2008.

[65] M. Preuss, P. J. Withers, J. W. L. Pang, and G. J. Baxter, "Inertia welding nickel-based superalloy: Part I. Metallurgical characterization," *Metallurgical and Materials Transactions A,* vol. 33, pp. 3215-3225, 2002.

[66] W. Mangen and E. Nembach, "The effect of grain size on the yield strength of the γ′-hardened superalloy NIMONIC PE16," *Acta Metallurgica,* vol. 37, pp. 1451-1463, 1989.

[67] E. J. Payton, T. A. Wynn, and M. J. Mills, "Experimental measurement of the kinetics of gamma prime dissolution during supersolvus heat treatment of powder metallurgical Ni-based disk superalloys," *Journal of Materials Science,* vol. 47, pp. 7305-7311, 2012.

[68] F. Tancret, "Thermo-Calc and Dictra simulation of constitutional liquation of gamma prime (γ′) during welding of Ni base superalloys," *Computational Materials Science,* vol. 41, pp. 13-19, 2007.

[69] O. A. Ojo, N. L. Richards, and M. C. Chaturvedi, "Contribution of constitutional liquation of gamma prime precipitate to weld HAZ cracking of cast Inconel 738 superalloy," *Scripta Materialia,* vol. 50, pp. 641-646, 2004.

[70] O. A. Ojo, N. L. Richards, and M. C. Chaturvedi, "Liquid film migration of constitutionally liquated γ′ in weld heat affected zone (HAZ) of Inconel 738LC superalloy," *Scripta Materialia,* vol. 51, pp. 141-146, 2004.

[71] O. A. Ojo and M. C. Chaturvedi, "On the role of liquated γ′ precipitates in weld heat affected zone microfissuring of a nickel-based superalloy," *Materials Science and Engineering A,* vol. 403, pp. 77-86, 2005.

[72] M. M. Attallah, H. Terasaki, R. J. Moat, S. E. Bray, Y. Komizo, and M. Preuss, "In-Situ observation of primary γ′ melting in Ni-base superalloy using confocal laser scanning microscopy," *Materials Characterization,* vol. 62, pp. 760-767, 2011.

[73] O. A. Ojo and F. Tancret, "Clarification on “Thermo-Calc and Dictra simulation of constitutional liquation of gamma prime (γ′) during welding of Ni-base superalloys”," *Computational Materials Science,* vol. 45, pp. 388-389, 2009.

[74] J. J. Pepe and W. F. Savage, *Welding Journal,* vol. 46, pp. 411-422, 1967.

[75] M. Soucail and Y. Bienvenu, "Dissolution of the γ′ phase in a nickel base superalloy at equilibrium and under rapid heating," *Materials Science and Engineering A,* vol. 220, pp. 215-222, 1996.

[76] E. H. Van Der Molen, J. M. Oblak, and O. H. Kriege, "Control of γ′ particle size and volume fraction in the high temperature superalloy Udimet 700," *Metallurgical Transactions,* vol. 2, pp. 1627-1633, 1971.

[77] Y. F. Han, P. Deb, and M. C. Chaturvedi, "Coarsening behaviour of γ″- and γ′-particles in Inconel alloy 718," *Metal Science,* vol. 16, pp. 555-562, 1982.

[78] A. J. Ardell, "The mechanism of phase transformation in crystalline solids," in *Proceedings of an International Symposium*, Manchester, UK, pp. 111-116, 1968.

[79] R. A. Swalin and A. Martin, "Solute diffusion in nickel-base substitutional solid solutions," *Transactions of the American Institute of Mining, Metallurgical, and Petroleum Engineers,* vol. 206, pp. 567-572, 1956.

[80] H. Monajati, M. Jahazi, R. Bahrami, and S. Yue, "The influence of heat treatment conditions on γ′ characteristics in Udimet 720," *Materials Science and Engineering A,* vol. 373, pp. 286-293, 2004.

[81] K. Kusabiraki, X. Zhang, and T. Ooka, "The growth of γ′ precipitates in a 53Ni-20C0-15Cr superalloy," *The Iron and Steel Institute of Japan International,* vol. 35, pp. 1115-1120, 1995.

[82] R. A. MacKay and M. V. Nathal, "γ′ coarsening in high volume fraction nickel-base alloys," *Acta Metallurgica et Materialia,* vol. 38, pp. 993-1005, 1990.

[83] A. Belyakov, K. Tsuzaki, H. Miura, and T. Sakai, "Effect of initial microstructures on grain refinement in a stainless steel by large strain deformation," *Acta Materialia,* vol. 51, pp. 847-861, 2003.

[84] H. J. McQueen, "Development of dynamic recrystallization theory," *Materials Science and Engineering A,* vol. 387, pp. 203-208, 2004.

[85] V. Randle, "Mechanism of twinning-induced grain boundary engineering in low stacking-fault energy materials," *Acta Materialia,* vol. 47, pp. 4187-4196, 1999.

[86] H. J. McQueen, "Initiating nucleation of dynamic recrystallization, primarily in polycrystals," *Materials Science and Engineering: A,* vol. 101, pp. 149-160, 1988.

[87] G. Krauss, *Deformation, Processing, and Structure*. St. Louis, Missouri, USA, American Society for Metals, 1984.

[88] Y. S. Na, J. T. Yeom, N. K. Park, and J. Y. Lee, "Simulation of microstructures for alloy 718 blade forging using 3D FEM simulator," *Journal of Materials Processing Technology,* vol. 141, pp. 337-342, 2003.

[89] S. C. Medeiros, Y. V. R. K. Prasad, W. G. Frazier, and R. Srinivasan, "Microstructural modeling of metadynamic recrystallization in hot working of IN 718 superalloy," *Materials Science and Engineering A,* vol. 293, pp. 198-207, 2000.

[90] M. J. Weis, M. C. Mataya, S. W. Thompson, and D. K. Matlock, "The hot deformation behavior of an as-cast alloy 718 ingot."

[91] S. Wang, L. Wang, and Y. Liu, "A novel approach to dynamic recrystallization nucleation for a nickel-base superalloy," *Acta Metallurgica Sinica (English Letters),* vol. 24, pp. 295-300, 2011.

[92] D. F. Li, Q. M. Guo, S. L. Guo, H. J. Peng, and Z. J. Wu, "The microstructure evolution and nucleation mechanisms of dynamic recrystallization in hot-deformed Inconel 625 superalloy," *Materials & Design,* vol. 32, pp. 696-705, 2011.

[93] M. Atkinson, "On the credibility of ultra rapid annealing," *Materials Science and Engineering A,* vol. 354, pp. 40-47, 2003.

[94] D. Muljono, M. Ferry, and D. P. Dunne, "Influence of heating rate on anisothermal recrystallization in low and ultra-low carbon steels," *Materials Science and Engineering A,* vol. 303, pp. 90-99, 2001.

[95] M. M. Attallah, M. Strangwood, and C. L. Davis, "Influence of the heating rate on the initiation of primary recrystallization in a deformed Al–Mg alloy," *Scripta Materialia,* vol. 63, pp. 371-374, 2010.

[96] M. Atkinson, "Bifurcation of thermal restoration processes in deformed iron and steel," *Materials Science and Engineering A,* vol. 262, pp. 33-38, 1999.

[97] M. Ferry and D. Jones, "High-rate annealing of single-phase and particle-containing aluminium alloys," *Scripta Materialia,* vol. 38, pp. 177-183, 1997.

[98] C. Sellars and J. Whiteman, "Recrystallization and grain growth in hot rolling," *Metal Science,* vol. 13, pp. 3-4, 1979.

[99] E. Anelli, "Application of mathematical modelling to hot rolling and controlled cooling of wire rods and bars," *The Iron and Steel Institute of Japan International,* vol. 32, pp. 440-449, 1992.

[100] L. Q. Chen, F. L. Sui, and X. H. Liu, "Grain growth model of Inconel 718 alloy forged slab in reheating process prior to rough rolling," *Acta Metallurgica Sinica (Chinese Edition)*, vol. 45, pp. 1242-1248, 2009.

Chapter 3. Linear Friction Welding of Ni-based Superalloys

3.1. General Introduction to Welding Ni-based Superalloys

Welding is a fabrication technique used to join similar or dissimilar materials by the application of heat. Many kinds of heat sources can be used in welding, including gas flame, electric arc, laser beam, electron beam, ultrasound, and friction. There are more than forty different welding techniques, in general, classified into two broad categories: fusion welding and solid-state welding.

3.1.1. Fusion Welding

Fusion welding refers to joining materials by melting and re-solidification of the base metal with or without a filler. The classification of fusion welding relies upon the type of energy source, thermal source, mechanical loading, and shielding. Some frequently-used processes for Ni-based superalloys include tungsten inert gas welding (TIG), electron beam welding (EBW), and plasma tungsten arc welding (PTAW) [1-6].

Panyawat *et al.* [2] and Su *et al.* [6] reported TIG and PTAW were used to repair cast IN738 and IN738LC turbine blades, respectively. Henderson *et al.* [5] proposed that TIG and EBW could be used for welding Ni-based superalloys components in industrial gas turbines, such as combustor liners, exhaust exit casings and transition ducts. The filler alloys normally consist of parent material to minimise the risk of cracking and porosity.

3.1.2. Issues in Fusion Welding

As a result of the large heat affected zone (HAZ) and the rapid heating/cooling rates from above super-liquidus temperatures in fusion welding, many imperfections or defects can occur, including porosity, microfissuring, oxide inclusions, and lack of inter-run fusion, especially in welding of precipitation strengthened alloys, such as IN718, IN738, IN939, Waspaloy, and CMSX-4 [7]. These imperfections cause some common issues in fusion welding of Ni-based superalloys, including grain boundary liquation cracking, solidification cracking, and strain age cracking, which will be discussed in the following section.

3.1.2.a. Grain Boundary Liquation Cracking

Grain boundary liquation cracking (heat affected zone fissuring) usually occurs in the HAZ of Ni-based superalloys, as a result of either local liquation of grain boundary particles (MC carbides, Laves phase), or the melting of low melting point elements segregated at the grain boundaries during casting. The melted particles form a thin liquid film at the grain boundary, creating a crack under the high tensile stresses generated in the HAZ [8-11].

In wrought alloys, HAZ cracking caused by grain boundary liquation is a common defect [12-14]. The susceptibility to HAZ cracking depends on the alloy composition (boron, carbon, sulphur, and phosphorus), grain size, weld traverse speed, and heat input. In general, a larger grain size increases the amount of grain boundary segregation by decreasing the grain boundary area per unit volume. Higher weld traverse speeds induce larger thermal stresses in the HAZ, which tend to result in more HAZ cracking. For IN718, both Chen *et al.* [14] and Chaturvedi *et al.* [15] reported that a high boron concentration induced larger susceptibility to

HAZ cracking. The melting/resolidification temperatures of boron-segregated grain boundaries was 100-200 ℃ lower than that of constitutional liquation of NbC (Fig. 3.1).

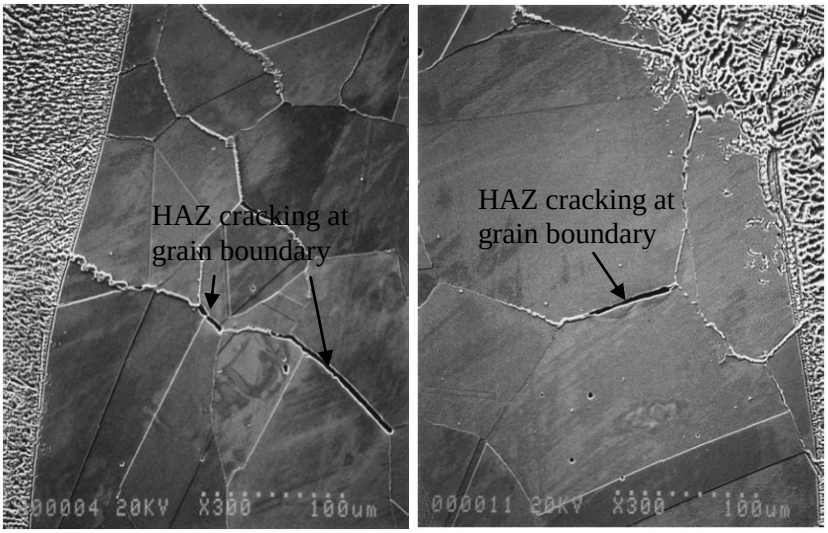

(a) (b)

Fig. 3.1. SEM secondary electron micrographs showing the effect of boron concentration on the susceptibility to HAZ cracking in IN718, (a) high boron alloy (B = 0.0043 wt.%) and (b) low boron alloy (B = 0.0011 wt.%) [14]

It has been shown that it is possible to eliminate or avoid HAZ cracking for some fine grained alloys, such as IN718 and Waspaloy, by controlling the alloy composition, refining grain size, and adjusting weld traverse speed and heat input. However, it is impossible to avoid HAZ cracking in fusion welding for many alloys, particularly some kinds of cast high γ′ Ni-superalloys, such as IN738, IN713LC and IN100 [9, 12].

3.1.2.b. Solidification Cracking

Solidification cracking (hot cracking) refers to the cracks formed in a weld bead during metal resolidification. It originates in the final stage of solidification (when the solid fraction of metal reaches 90%), when the liquid is restricted to flow into the interdendritic region. The

shrinkage strain, generated behind the weld bead, tears the weld bead with the formation of cracks in the weld metal (Fig. 3.2.a). The types of crack include main longitudinal cracks and transverse cracks (Fig. 3.2.b). Yongsoo *et al.* [16] reported the solidification cracks formed at the grain boundary, γ/NbC, and γ/Laves eutectic phases in IN718 and IN625 PTAW.

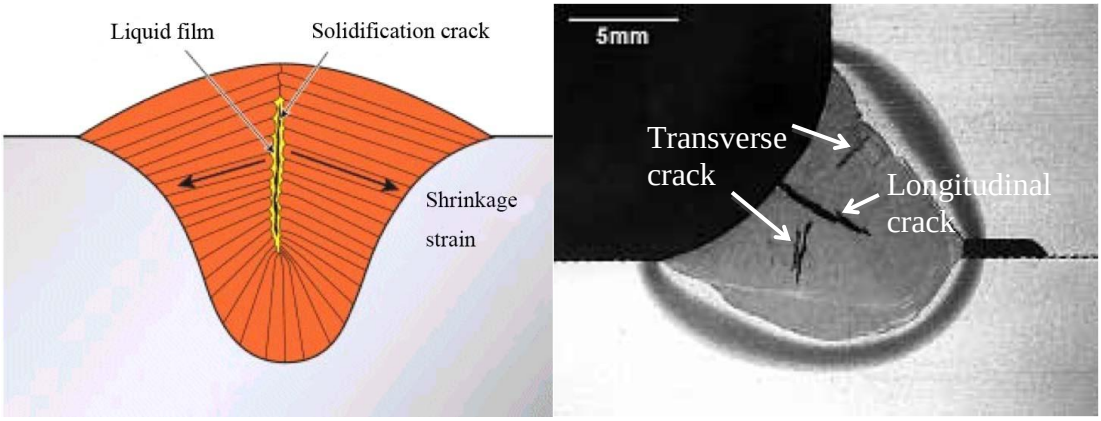

(a) (b)

Fig. 3.2. Solidification cracking in fusion welding, (a) schematic diagram of crack formation, and (b) optical micrograph showing typical solidification cracks [17]

3.1.2.c. Strain-Age Cracking

In precipitation-strengthened Ni-based superalloys, strain-age cracking (post-weld heat treatment cracking) occurs as intergranular microfissuring predominantly in the HAZ, and sometimes in the fusion zone (FZ), either during post-weld heat treatment (mostly), the welding cycle or high temperature service. Figure 3.3 shows strain-age cracks that occurred at the grain boundaries in the HAZ of laser welded Haynes 282 (HY 282) after solution heat treatment [18].

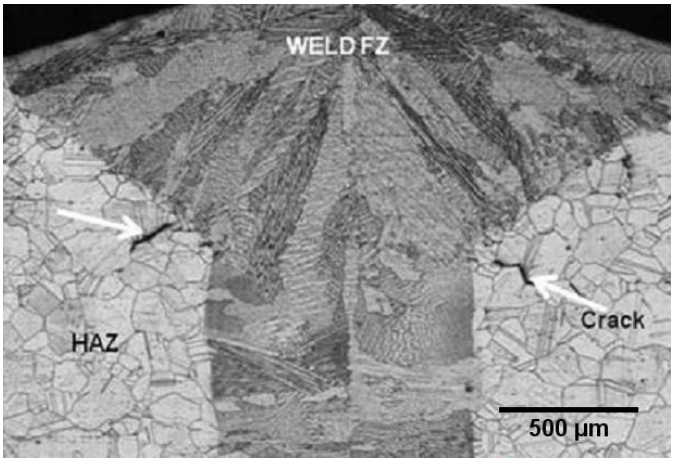

Fig. 3.3. Optical micrograph of the weld cross-section of laser welded HY 282 alloy showing strain-age cracking in the HAZ close to the FZ after solution heat treatment [18]

PWHT is often used to relieve the residual stresses and develop the maximum strength for the welds [19]. Figure 3.4 shows the development mechanism of strain-age cracking in Ni-based superalloys. The γ′ precipitation temperature is in the range of T_1 to T_2 (Fig. 3.4.a). The PWHT process consists of solution treatment and aging. To relieve the residual stresses after welding, the sample is heated to the solution temperature (Fig. 3.4.b). Since the solution temperature is above the γ′ precipitation temperature, this may result in the precipitation of γ′ before the residual stresses are relieved. Unless the heating rate is rapid enough to avoid intersecting the γ′ precipitation C-curve (Fig. 3.4.c), precipitation and hence cracking will occur in the welds as a combined result of the intrinsic stresses caused by γ′ precipitation and the weld residual stresses. The microstructural developments in the HAZ are illustrated in Figs. 3.4.d and e.

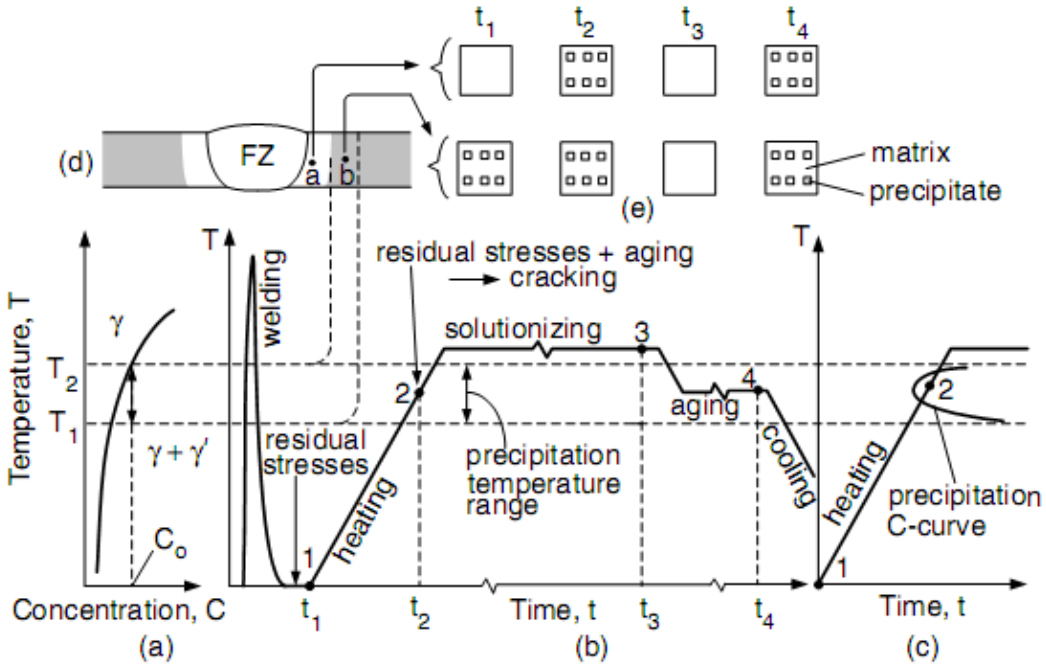

Fig. 3.4. The mechanism for strain-age cracking in Ni-based superalloys: (a) phase diagram, (b) thermal cycles during welding and heat treatment, (c) γ′ precipitation C-curve, (d) weld cross-section, and (e) development of microstructure in HAZ of areas a and b [19]

The effect of Al and Ti contents on strain-age cracking in a variety of Ni-superalloys is shown in Fig. 3.5 where it is clear that high addition of Al or Ti increases the tendency for strain-age cracking. As shown, IN718 is resistant to strain age cracking, which is due to the sluggish precipitation kinetics of γ″. During PWHT, the relief of residual stresses in the welds precedes the γ″ precipitation, leading to IN718 free of strain-age cracks [20]. The resistance to strain-age cracking in IN718 is also attributed to the low concentration of Al and Ti. However, because of the high Al content in IN713C, strain-age cracking is hard to avoid on fusion welding.

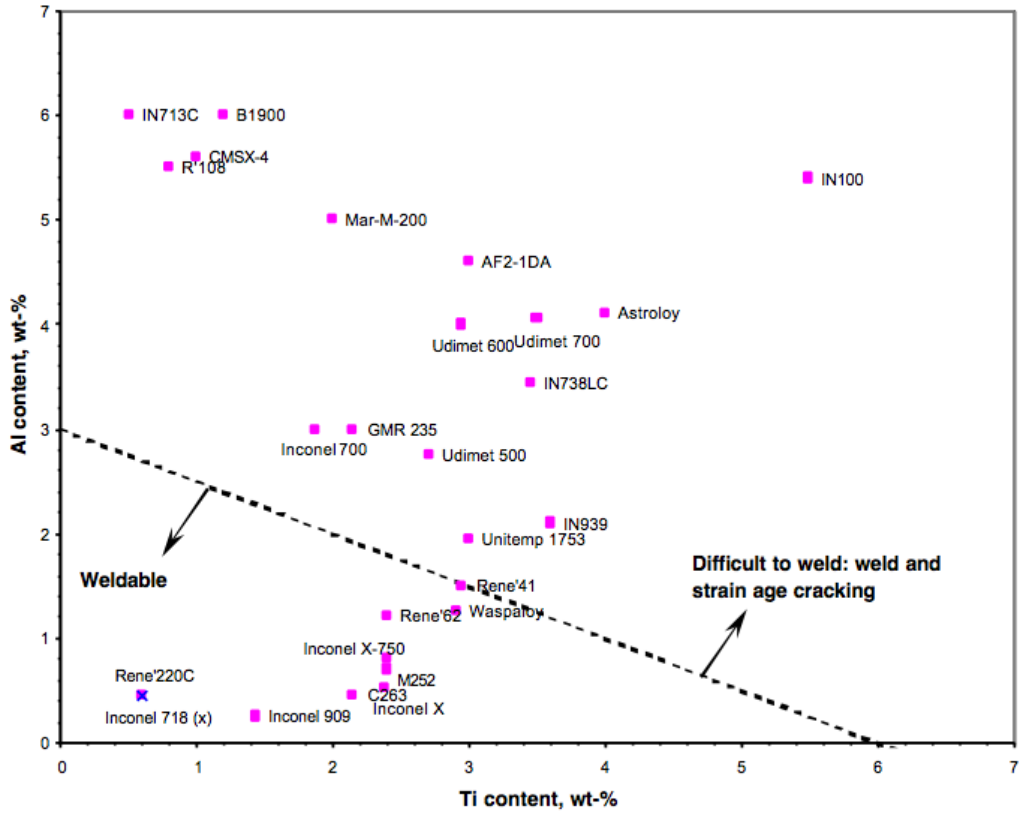

Fig. 3.5. The weld and strain-age cracking susceptibility of selected Ni-based superalloys [21]

3.1.3. Solid-State Welding

Solid-state welding refers to a group of welding techniques in which materials are joined at temperatures below their melting points. Solid-state welding produces welds with a narrower HAZ, and lower thermal stresses than those generated during fusion welding. The welding time can be reduced, which improves welding efficiency.

Solid-state welding is classified by the energy source, including electrical, chemical, and mechanical, and is further divided into various techniques, such as friction welding, friction stir welding, diffusion welding and explosion welding (Fig. 3.6).

In the group of welding techniques that uses mechanical energy, friction welding (FW) is a novel technology to manufacture precise defect-free components, and is suitable for welding high γ′ volume fraction Ni-based superalloys. FW generates heat purely through the relative movement of two components with no need for additional fillers. The joining mechanisms are diffusion, bonding, shearing, and recrystallisation between the two pieces being joined. The influence of both the oxide contamination and the roughness of metal surface on limiting joining are virtually eliminated during FW, because the high pressure exerted expels the oxide within the plasticised material in the flash. This results in intimate contact between the two clean metal surfaces, which is referred to as a self-cleaning process. The high temperature generated by friction increases diffusivity across the interface.

The FW processes can be classified into rotary friction welding (RFW), orbital friction welding, angular friction welding, friction stir welding (FSW), and linear friction welding (LFW), based on their different friction mode. Due to the different spin pattern, RFW can be divided into inertia friction welding (IFW), continuous drive friction welding (CDFW), and radial friction welding, in which IFW and CDFW will be discussed in this section due to their similarity to LFW.

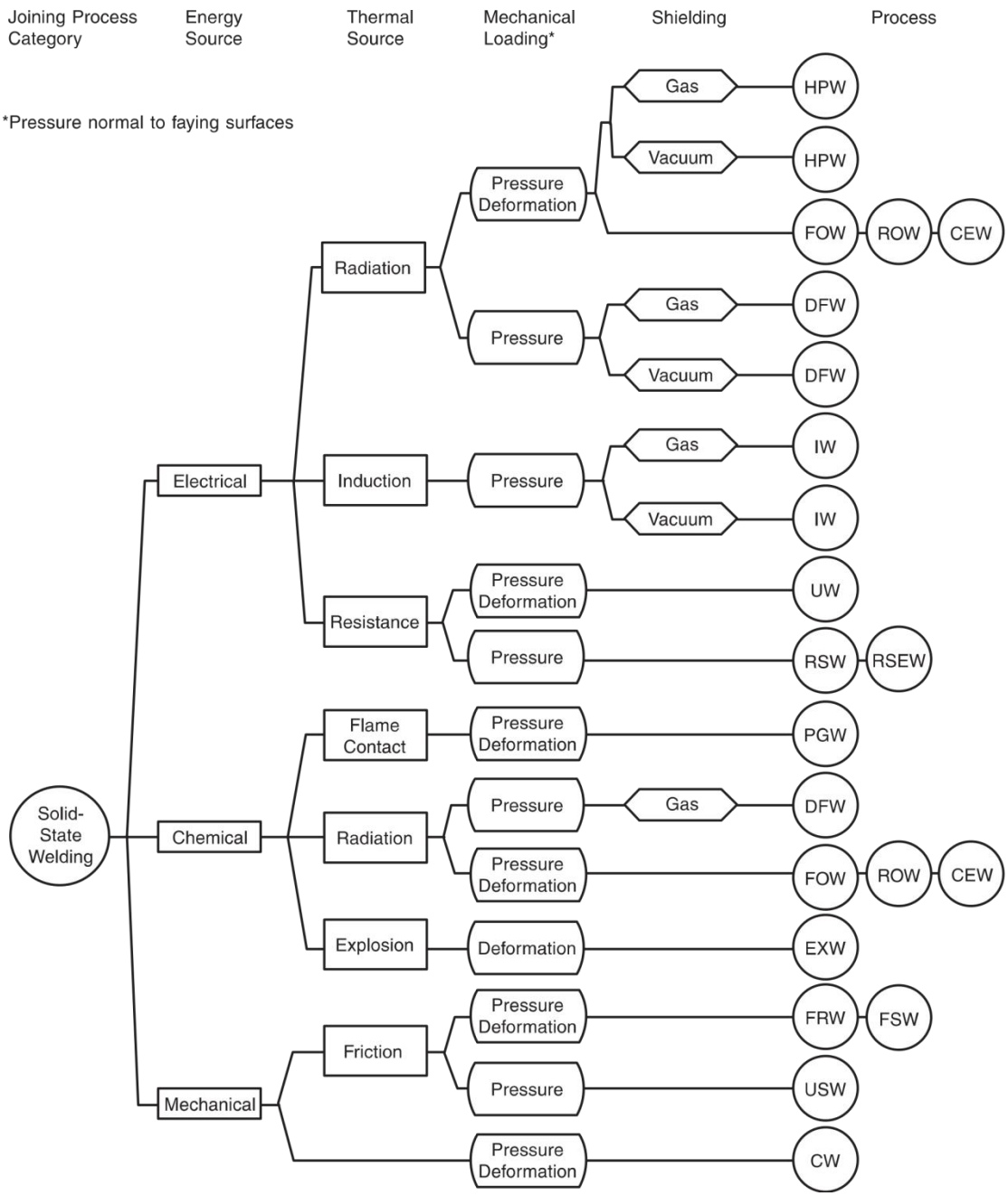

Designation	Welding Process	Designation	Welding Process	Designation	Welding Process
CEW	coextrusion welding	FRW	friction welding	RSEW	resistance seam welding
CW	cold welding	FSW	friction stir welding	RSW	resistance spot welding
DFW	diffusion welding	HPW	hot pressure welding	ROW	roll welding
EXW	explosion welding	IW	induction welding	USW	ultrasonic welding
FOW	forge welding	PGW	pressure gas welding	UW	upset welding

Fig. 3.6. Classification of solid-state welding process [22]

3.1.3.a. Inertia Friction Welding and Continuous Drive Friction Welding

In both IFW and CDFW, the rotational kinetic energy is converted to thermal energy via friction. The joint interfaces can be circular, annulus, or a non-circular surface.

In IFW, a work piece is clamped to a flywheel, and the other work piece is clamped to a non-rotating vise. During welding, an electric motor is used to rotate the flywheel to a preset speed before the motor is decoupled. Then, the non-rotating work piece is pushed by a hydraulic cylinder towards the rotating work piece. When the interfaces rub against each other, the rotational energy transforms into frictional heat with the deceleration in flywheel speed, which causes the rapid increasing of temperature and generates a plasticised layer at the interface. The pressure ejects the plasticised material outside the joint forming a consolidated weldment with flash around the weld line [23]. The schematic diagrams for the set-up and the parameter traces of IFW are shown in Figs. 3.7.a. and 3.8.a [24].

The braking mechanism of CDFW differs from IFW. In IFW, braking occurs gradually with the dissipation of the energy stored in the flywheel. However in CDFW, braking is performed by declutching the spindle from the electric motor, followed by applying a brake to stop the spindle rotation. In CDFW, one work piece is stationary whilst the other work piece is placed onto a spindle which continuously rotates at a preset speed driven by an electric motor. The stationary work piece is then moved by a hydraulic cylinder at a pressure towards the rotating work piece. When the two pieces rub against each other, heat is generated at the weld interface, causing the softened material to be ejected into flash. Once either the pre-determined axial shortening (upset) or pre-defined time has been reached, a brake will be applied along with the motor disengaged. Compared with IFW, CDFW is mainly used to join small components because continuous driving of a large component would require very high

power. The schematic diagrams for the set-up and the parameter traces of CDFW are shown in Figs. 3.7.b. and 3.8.b [24].

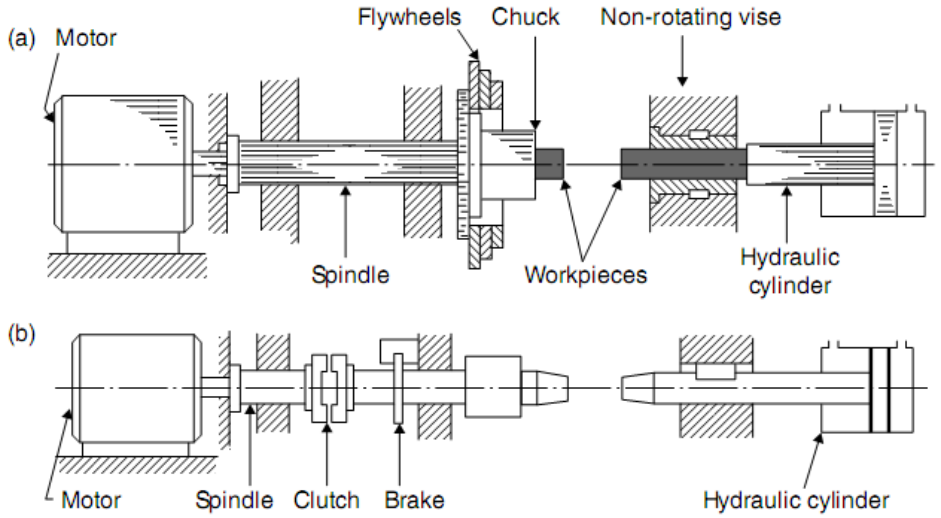

Fig. 3.7. Schematic diagrams for the set-up of (a) IFW and (b) CDFW [24]

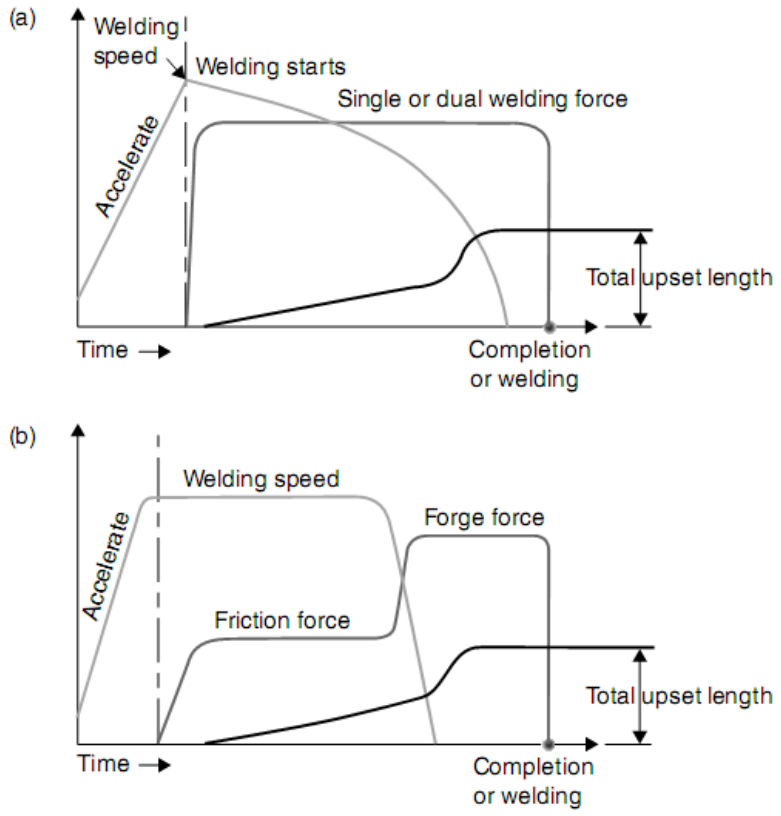

Fig. 3.8. Schematic diagrams of the parameter traces for (a) IFW and (b) CDFW [24]

IFW has successfully been used to join Ni-based superalloys. Preuss *et al.* [25] investigated IFW of IN718, Udimet 720Li, and RR1000. Generally, IFW produced a narrow HAZ (7-8 mm out of 100 mm long weld), which was measured using microhardness. However, high tensile residual stresses were measured near the weld line of all the welds using hole-drilling or diffraction techniques. The stresses were found to increase with the increase in γ′ volume fraction. PWHT at the standard maximum aging temperature (732 ℃) reduced the residual stresses to about half of their initial value. The development of residual stresses will be further discussed in Section 3.3.3.

3.2. Process of LFW

LFW is a solid-state joining process, which has been used to join similar or dissimilar materials to produce components, such as compressor blisks [26], gears [27], and chain links [28]. Above all, LFW is a novel technology to fabricate high strength turbine blisks in gas turbine engine. A schematic of linear friction welding is shown in Fig. 3.9.

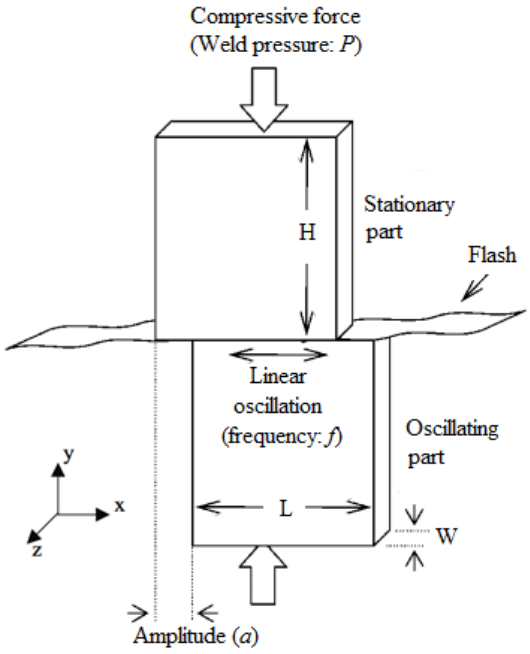

Fig. 3.9. Schematic diagram of LFW; L: length, W: width, and H: height [31]

During LFW, a stationary part is rigidly clamped and forced under a compressive force against an oscillating part that is reciprocating in a linear manner. The frictional heat generates at the interface, which causes material to soften and plastically deform. The plasticised material is expelled from the interface forming flash layers close to the weld line. The weld is consolidated by a forging force after the relative motion. LFW is a self-cleaning process, the surface oxides and other contaminations are removed from the weld interface along with the ejection of the plasticised material [29]. LFW solves the problem of fretting fatigue damage due to mechanical joining of fir-tree blades and brings 30% weight saving by reducing the size of the joint [30]. Nevertheless, high residual stresses may be generated at the weld line due to the steep thermal gradient and large weld pressure.

3.2.1. Phases and Process Parameters

In general, there are four distinct phases in LFW, including contact phase, conditioning phase, burn-off phase, and forging phase [22-24]. Schematic diagrams of the four phases are shown in Fig. 3.10.

Phase I: Contact phase

The frictional heat is generated from two rubbing components in a reciprocating linear manner under compressive pressure. The interface contact area increases throughout this stage due to surface wear. The shear force slightly rises to a roughly constant value as the temperature rises, and the yield stress decreases which compensates for the increase of contact area. Sufficient heat input in this phase is essential for attaining 100% contact area and forming a layer of plasticised material, which is critical for the rest of process to proceed.

Phase II: Conditioning phase

Softening causes large particles to be expelled from the interface if enough heat is generated in the contact phase. The HAZ expands and when the softened layer is unable to support the axial force, permanent plastic deformation occurs.

Phase III: Burn-off phase

The local stress, with the addition of the oscillatory movement, expels the softened material from the interface to the ends of weld line as a form of flash, thus causing axial shortening. The peak temperature is reached in this phase, but is still below the melting point.

Phase IV: Forging phase

When the pre-determined upset is reached, the oscillation stops within a fraction of a second. The forging pressure is maintained to enhance the consolidation of the weld, in which the forging pressure can be increased if necessary.

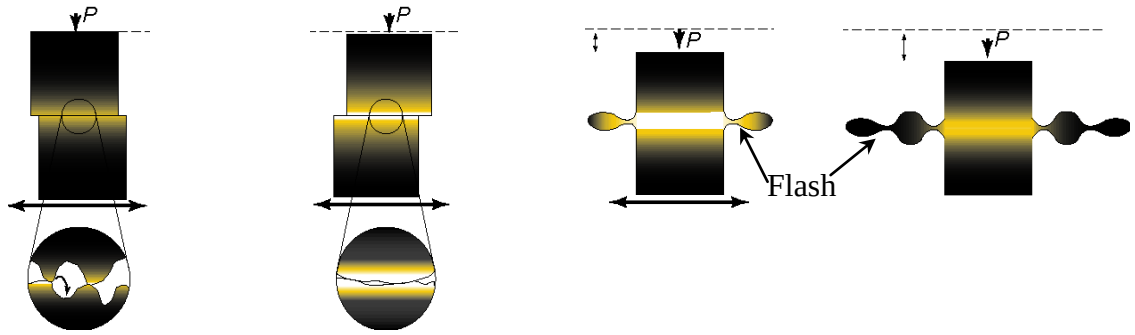

(a) Contact (b) Conditioning (c) Burn-off (c) Forging

Fig. 3.10. Classification of phases in LFW process; P: weld pressure, Double arrow: vibrating direction [32]

Figure 3.11 shows the process parameter traces of MTS Process Development System (MTS-PDS) LFW. The key process parameters in LFW are:

- Weld pressure (friction pressure): pressure applied during the frictional phase, which is calculated from the forging force.
- Amplitude: maximum displacement of the oscillating sample from the equilibrium position.
- Frequency: number of the oscillating cycles per second.

There are also some other important parameters that can be further controlled in modern LFW systems:

- Ramp-up time: time taken for the parameters to reach the required steady state level.
- Decay time: time taken for the amplitude to be reduced to zero.
- Forging pressure: pressure applied during the forging phase to consolidate welds, which could differ from the pressure at the initial stages.
- Forge hold time: total amount of time that the forging pressure is applied.
- Upset: the axial shortening of material, which is typically set up to a fixed value to avoid over-burning of the weld stub.
- In-plane force: force parallel to the oscillatory direction.
- Weld time: time spent on four phases.

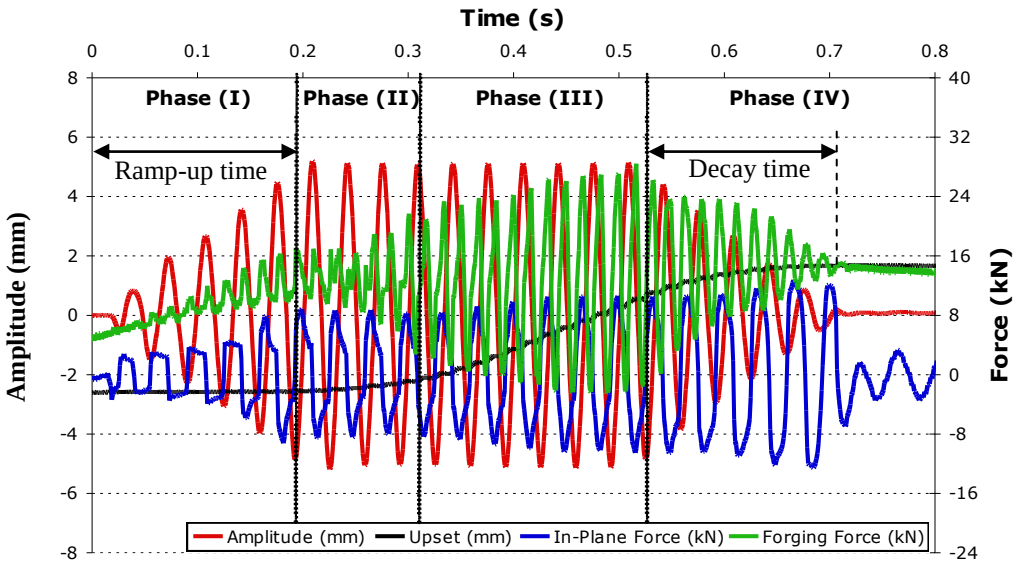

Fig. 3.11. MTS-PDS weld parameter traces (P = 150 MPa, a = 5 mm, f = 30 Hz) [32]

3.2.2. Temperature Distribution

LFW, as a thermo-mechanical joining process, results in an extremely rapid thermal cycle and high strain rate. It is necessary to investigate the temperature distribution in order to understand the microstructural variation and to develop thermo-mechanical simulations. The study of temperature distribution in LFW has been carried out by in-situ thermocouple measurement and infrared imaging.

Because of experimental difficulties, limited work has been published on direct measurement of the temperature during LFW. Vairis and Frost [33] measured the thermal cycle of Ti-6Al-4V LFW by embedding K-type thermocouples at 0.7 mm from the weld interface. As seen in Fig. 3.12, in phase I, the temperature rapidly increases in the first 20 seconds and slowly rises to 630 ℃. The temperature further increases in phase II due to the increase of friction pressure, until it reaches a maximum temperature (T_{max}) of 840 ℃ in phase III,

beyond which the temperature starts to decrease. These measurements reflected some flaws of in-situ thermocouple measurements during LFW. The fluctuation of temperature in 8 s to 18 s could be associated with the unstable contact between the thermocouple and the weld piece. Beyond that, due to the heat dissipation during flash extrusion, the temperature may be underestimated.

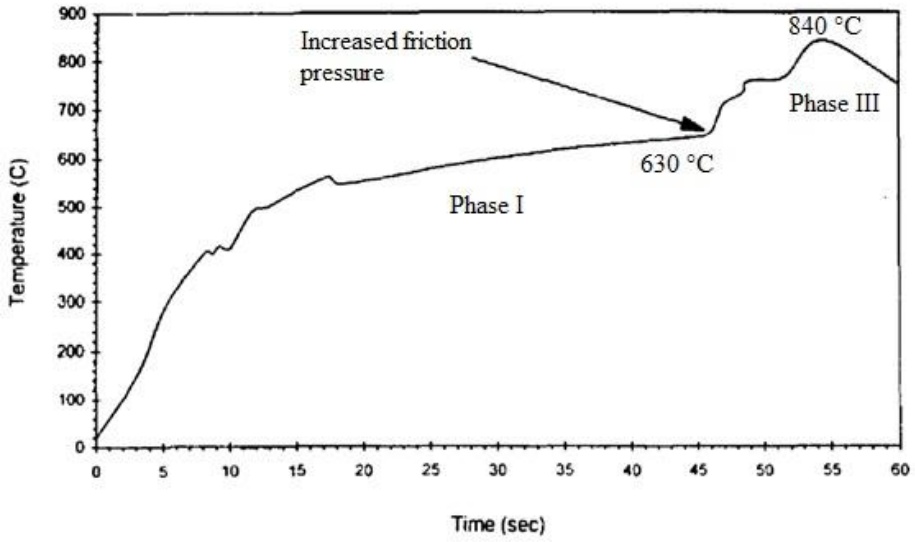

Fig. 3.12. The thermal cycle during LFW of Ti-6Al-4V at 0.7 mm away from interface (P = 32.9 MPa, a = 3 mm, f = 10 Hz) [33]

Mary and Jahazi [35] performed in-situ thermocouple measurements for LFW IN718 (Fig. 3.13.a). They observed that the form of thermal cycle is similar to that found by Vairis and Frost, with the temperature rising steeply (280 ℃/s) in the first 3 s to 4 s due to the large amount of frictional heating. At the end of phase I, the increase rate of temperature decreases until it reaches a plateau. In the beginning of the burn-off phase (phase III), the temperature reaches a peak. Mary and Jahazi also measured the plateau and peak temperatures at different locations (Fig. 3.13.b). The temperature data reflects a linear relation between temperatures and distance from the interface, and the extrapolated T_{max} is 1200 ℃ at the interface. This

temperature is ~0.9 of the melting point (T_m) of the alloy, which confirms the LFW is a hot working thermo-mechanical process.

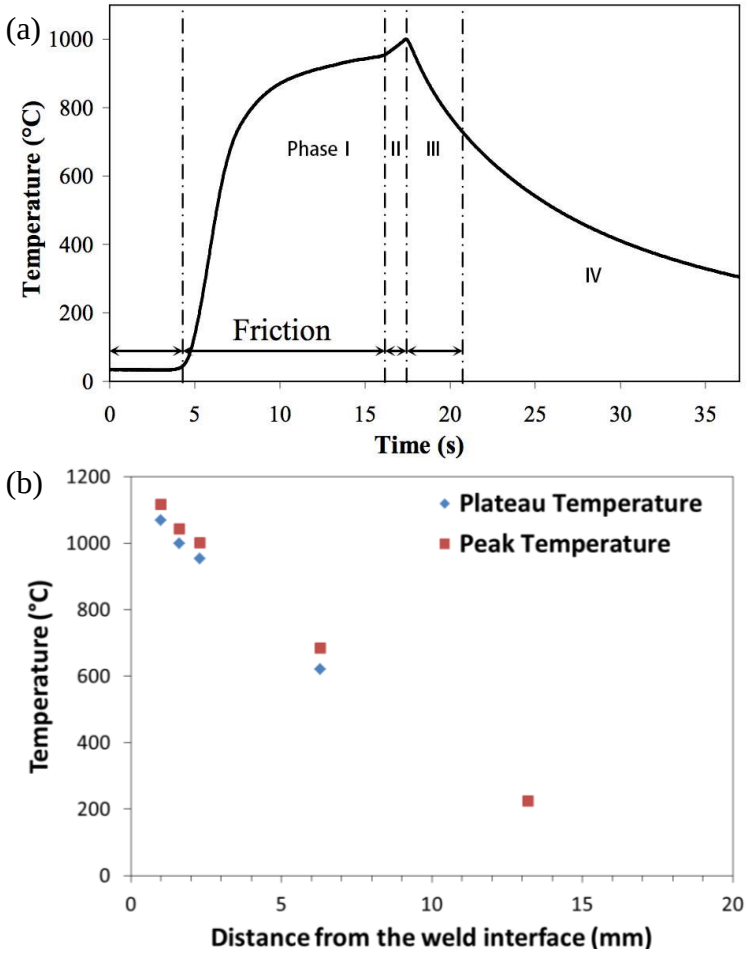

Fig. 3.13. (a) The thermal cycle during LFW of IN718 at 2.3 mm from the weld interface, (b) temperatures as a function of distance from the weld interface (P = 70 MPa, a = 2 mm, f = 80 Hz) [35]

Similarly, Chamanfar *et al.* [31] used thermocouples to measure the thermal cycles during LFW of Waspaloy at different locations from the weld interface (Fig. 3.14). The temperature plot shows the same tendency as Mary and Jahazi's results, with the heating rate increasing closer to the weld interface. The extrapolated interface temperature is 1280 ℃, which is 50 ℃ below the solidus temperature. Chamanfar *et al.* [31] also estimated the interface peak temperature is 1266 ℃ by one-dimensional transient-heat-conduction analysis, which is very

close to the extrapolated value (Fig. 3.14.b). More detailed temperature information is listed in Table 3.1 [31], where the highest heating rate was found to be 643 ℃/s at 1.5 mm with a cooling rate 63 ℃/s, which meant the heating/cooling rates at the interface are even larger than this value.

It should be noted that the weld interface temperature obtained by the back-extrapolation method may not be very precise due to the difference of the thermal cycles and material flow between the weld interface and other places in welds. Moreover, the error of thermocouple measurement need be considered.

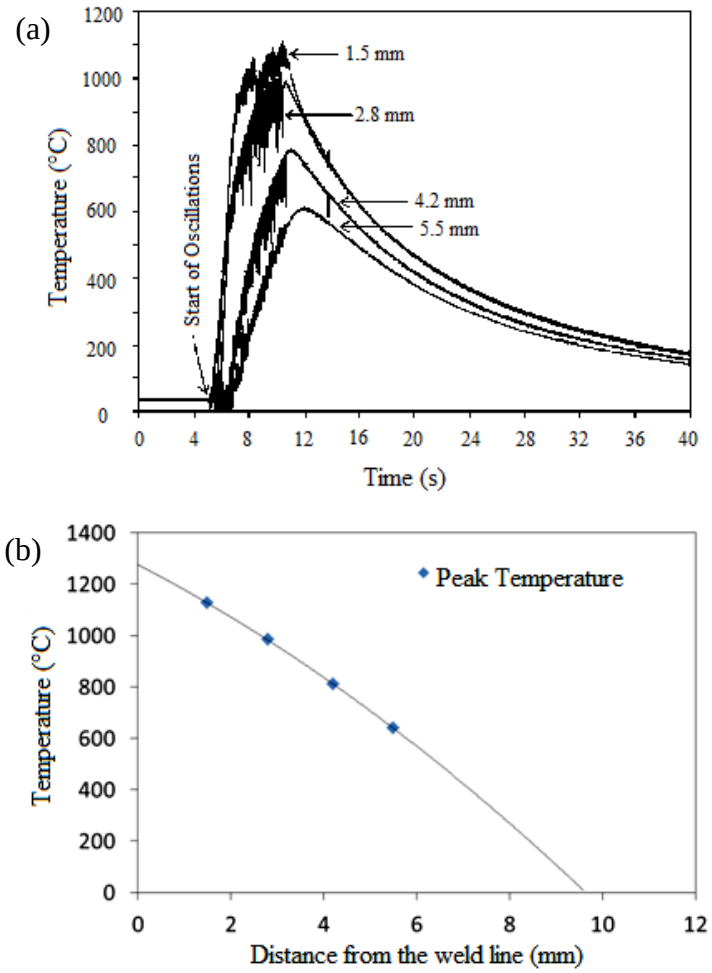

Fig. 3.14. (a) Thermal cycles during LFW of Waspaloy at different locations from the weld line, (b) temperature as a function of distance from the weld line (P = 90 MPa, a = 3 mm, f = 80 Hz) [31]

Table 3.1. Temperature data of Waspaloy LFWs [31]

Initial location from interface (mm)	Maximum heating rate (°C/s)	Peak temperature (°C)	Average cooling rate from peak temperature to 500 °C (°C/s)
Interface	–	1280	–
1.5	643 ± 107	1126 ± 9	63 ± 16
2.6	459 ± 241	1010 ± 33	56 ± 12
4.2	165 ± 19	810 ± 30	40 ± 8
5.5	95 ± 4	640 ± 35	19 ± 2

Finally, Damodaram *et al.* [36] measured the temperature of IN718 FWs by infrared imaging. They reported that the peak temperature is 1118 ℃ at the weld zone. Because the infrared thermometer can only record the surface temperature, the real peak temperature at the centre of the weld zone is probably higher than this value.

In comparison, in-situ thermocouple measurements record more precise temperature evolution during LFW than infrared imaging, since infrared imaging can only measure the surface temperature of the welds. Nonetheless, the thermocouple may shift during the welding process due to the oscillating movement. In addition, thermocouples cannot be used to measure the weld interface temperature. The T_{max} in LFW of Ni-based superalloys measured by thermocouple was found to be below the T_m, and the temperature varies with the difference in the weld geometry and changes in the welding process parameters. The T_{max} in LFW is still higher than the solvus of the some secondary phases in Ni-based superalloys. The dissolution of the strengthening and secondary phases (γ′/γ″, δ, and NbC) and grain boundary liquation may still occur during LFW, and therefore may reduce the mechanical properties of the welds.

3.2.3. Strain Rate

The material experiences severe thermomechanical deformation during LFW due to the high stress and temperature in the weld line. The investigation of strain rate is essential to predict the grain size near the weld interface or to simulate the material flow behaviour.

The first expression for strain rate was proposed by Vairis and Frost [33], where was it given as:

$$\dot{\varepsilon} = af/L \tag{3.1}$$

where a is the amplitude of oscillation, f is the frequency and L is the length of specimen in the oscillating direction.

According to this expression, Vairis [37] established an analytical model which predicted the strain rate as a function of the distance from the weld interface (Fig. 3.15). The analytical model indicated that the strain rate accelerates with increase of frequency or with shortening of the oscillating distance (zz < xx). The predictions were simplified by assuming that the deformation is homogeneous.

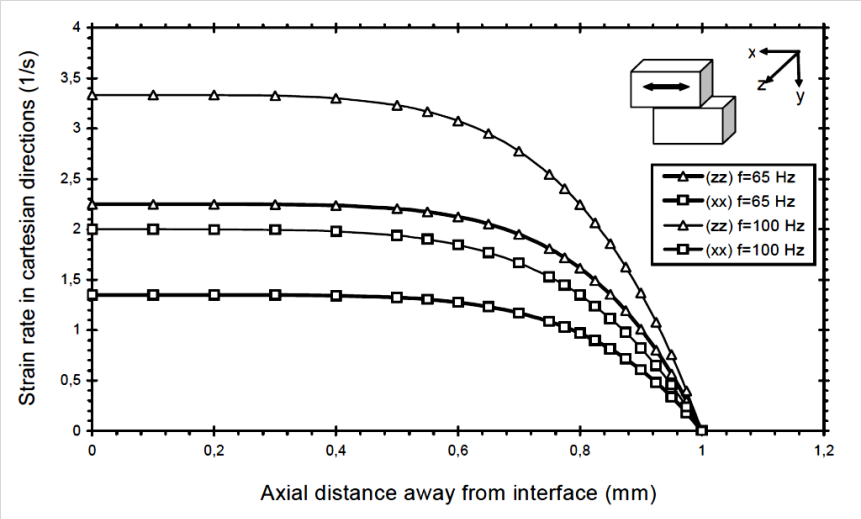

Fig. 3.15. Prediction of the strain rate at different locations using Vairis's model under different frequency and oscillating directions [37]

However, it has been argued that the Vairis's equation greatly underestimated the strain rate. Turner *et al.* [38] predicted the strain rate at different amplitudes by finite element modelling, which suggested that higher strain rates occur with increasing oscillating amplitude. The maximum strain rate was predicted to be over 2500 s^{-1} at an amplitude of 5 mm, which is much larger than the value calculated by Vairis's expression (1 s^{-1}). Chamanfar *et al.* [39] further correlated the predicted strain rate of the two models with recrystallised grain size in LFW of Waspaloy, based on the Zener-Hollomon parameter which was introduced in Section 2.5.3. The results showed that the strain rate is in the range of 1325 s^{-1} which corresponds with the high strain rate predicted by Turner *et al.* [38] in Ti-6Al-4V LFW.

3.3. Microstructure-Property Development of LFWed Ni-based Superalloys

Studies of the microstructure and properties of LFW Ni-based superalloys are essential to understand the influence of welding process parameters on the welds. Table 3.2 lists most of the publicly available research on LFW or IFW of Ni-based superalloys. IFW research was included due to its similarity to LFW.

Table 3.2. Studies on LFW and IFW of Ni-based superalloys in the literature

Material & Process	Sample Dimensions	Weld Parameters	Microstructure	Mechanical Properties	Sources
Waspaloy (AW*/PWHT) LFW	L = 13 mm, W = 11 mm, H = 18 mm	*f* = 40-80 Hz, *a* = 2-3 mm, *P* = 40-360 MPa	Macro/OM/ SEM/EDX/ EBSD/TEM	Hardness/Tensile	Chamanfar *et al.*, Canada [31, 40, 41]
IN718 LFW	L = 26 mm, W = 12 mm, H = 35 mm	*f* = 60-100 Hz, *a* = 2-3 mm, *P* = 50-110 MPa	Macro/OM/ SEM/EDX	Hardness	Jahazi and Mary, Canada [42]
718 Plus (AW/PWHT) LFW	L = 12.8 mm, W = 11.1 mm, H = 17.7 mm	*f* = 100 Hz, *a* = 2 mm, *P* = 90 MPa	OM/SEM/EDX	-	Vishwakarna *et al.*, Canada [43]
IN738 LFW	L = 12.8 mm, W = 11.1 mm, H = 17.7 mm	*f* = 100 Hz, *a* = 2 mm, *P* = 90 MPa	OM/SEM/ EBSD	-	Ola *et al.*, Canada [44]
IN738LC LFW	L = 12.8 mm, W = 11.1 mm, H = 17.7 mm	*f* = 100 Hz, *a* = 2 mm, *P* = N/A	OM/SEM/ EDX/EBSD	Hardness	Amegadize, Canada [45]
CMSX-486 LFW	L = 11 mm, W = 11 mm, H = 17 mm	*f* = 100 Hz, *a* = 2 mm, *P* = 90 MPa	OM/SEM/ EDX/EBSD	-	Ola *et al.*, Canada [46]
CMSX4-RR1000 LFW	N/A	N/A	SEM/TEM	-	Karadge *et al.*, UK [47]
720Li - IN718 LFW	Cross-section = 12 mm × 6mm	*P* = 250 MPa, 400 MPa, 500 MPa	OM/SEM	Hardness/Residual stress	Frankel, UK [48]
720Li - IN718 (AW/PWHT) IFW	Outer diameter = 143 mm, thickness is 25 mm for 720Li, and 20 mm for IN718	N/A	SEM/EDX/ EBSD/TEM	Hardness	Huang *et al.*, UK [23]
720Li/IN718/ RR1000 (AW /PWHT) IFW	Outer diameter = 143 mm, wall thickness 10-11 mm, L = 50 mm	N/A	-	Hardness/Residual stress/Tensile	Preuss *et al.*, UK [25]
RR1000 (AW/PWHT) IFW	Outer diameter = 143 mm, wall thickness = 11 mm, L = 50 mm	N/A	SEM/EBSD/ TEM	Hardness/Residual stress	Preuss *et al.*, UK [49, 50]
IN718 (AW/PWHT) IFW	N/A	Friction pressure = 300 MPa, Upset pressure = 600 MPa, Burn off length = 4 mm, Speed = 1500 rpm	SEM/EBSD/ TEM	Hardness/Tensile	Damodaram *et al.*, India [51]

*AW: as-welded condition; PWHT: post-weld heat treated condition

3.3.1. Microstructural Development

The high temperature and severe thermo-mechanical deformation in the LFW process lead to significant changes in the microstructure associated with phase transformations and recrystallisation. These changes in microstructure cause changes in mechanical properties of welds. Therefore, understanding of the microstructural variation is important for optimising the weld process parameters and enhancing weld properties.

3.3.1.a. Precipitate Dissolution and Reprecipitation

The high dissolution temperatures of the main strengthening precipitates γ′/γ″ were reported on LFW of Ni-based superalloys. The dissolution of primary and secondary γ′ phase in the TMAZ of the Waspaloy LFWs is shown in Fig. 3.16 [31]. In the base metal, the volume fraction of primary γ′ and secondary γ′ are 6% and 27%, respectively, with average diameter of 250 nm and 43 nm, respectively. At 1.5 mm from the weld interface, the volume fraction of secondary γ′ decreases as a result of high temperature dissolution, but the size of the primary γ′ is almost the same as the initial value, because primary γ′ has a higher solvus temperature than that of secondary γ′. At the weld interface, both primary and secondary γ′ particles are fully dissolved as the temperature reached is above the primary γ′ solvus. The full dissolution of γ′ and γ″ at the weld line was also proposed in IN718, 718 Plus, IN738, and CMSX-486 LFWs [35, 43, 44, 46, 52].

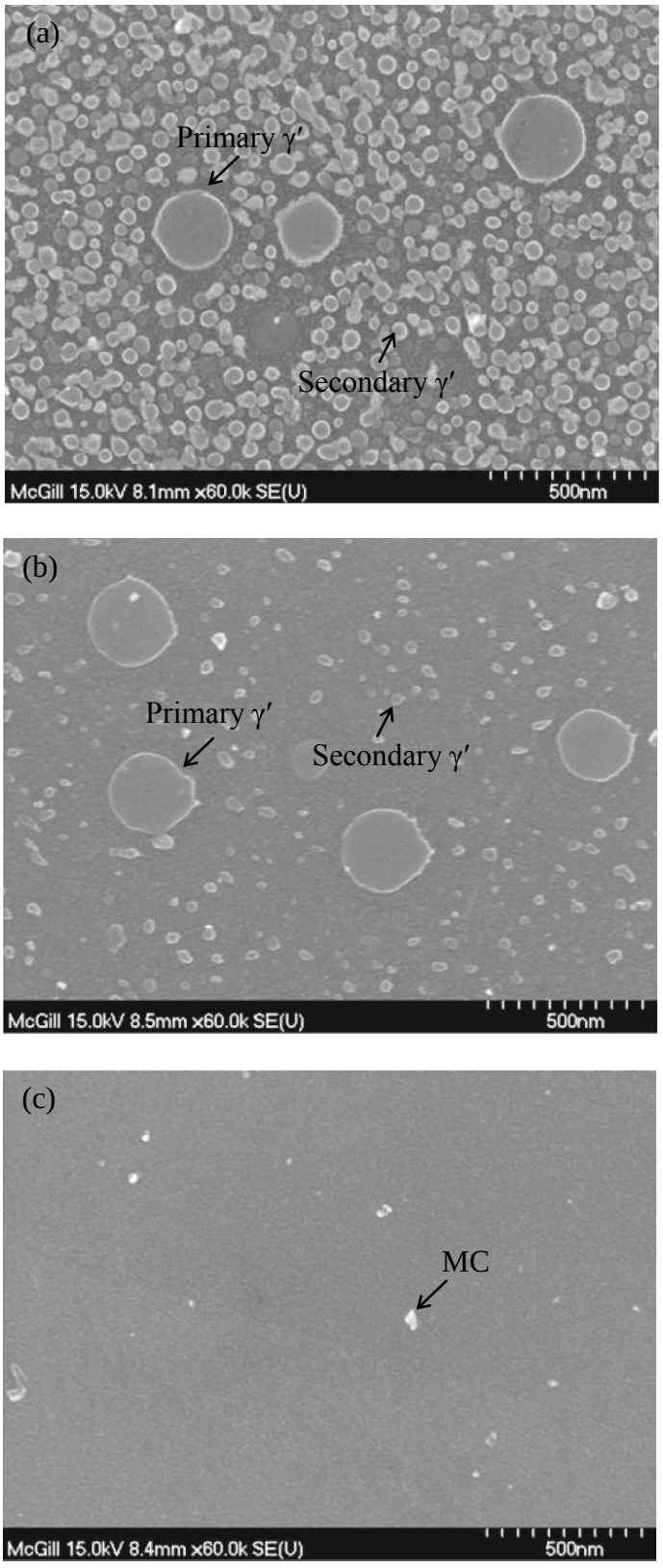

Fig. 3.16. SEM SE micrographs of γ′ in Waspaloy LFWs at (a) base metal, (b) 1.5 mm from weld interface, and (c) weld interface (P = 90 MPa, a = 3 mm, f = 80 Hz) [31]

In addition to γ′ and γ″, Mary and Jahazi [35] reported the dissolution of another important precipitate in IN718, the δ phase. Loss of crystal recovery and recrystallisation restraint can be caused by the loss of δ phase in the weld zone.

Although IFW is different from LFW in the mode of operation and parameters, studying the weld microstructure can give an insight into the changes that could happen due to frictional heating. Huang *et al.* [23] studied dissimilar LFW of 720Li-IN718 using SEM and TEM, which provided more convincing proof of the dissolution and reprecipitation of γ′/γ″ precipitates at the vicinity of the weld region. As seen in Fig. 3.17, the γ′ precipitates fully dissolve at the weld interface, however due to the high γ′ volume fraction (~40%) of 720Li, 25% volume fraction of the γ′ reprecipitate during the cooling process, with average size 9.4 nm. The fraction of reprecipitated γ′ precipitates reduces with increase of distance from the weld interface until no reprecipitated γ′ forms at 2.5 mm. Work from Preuss *et al.* [49] also confirmed that reprecipitated fine γ′ particles form during air cooling of IFWed RR1000 (which contains a similar volume fraction of γ′ as IN713LC).

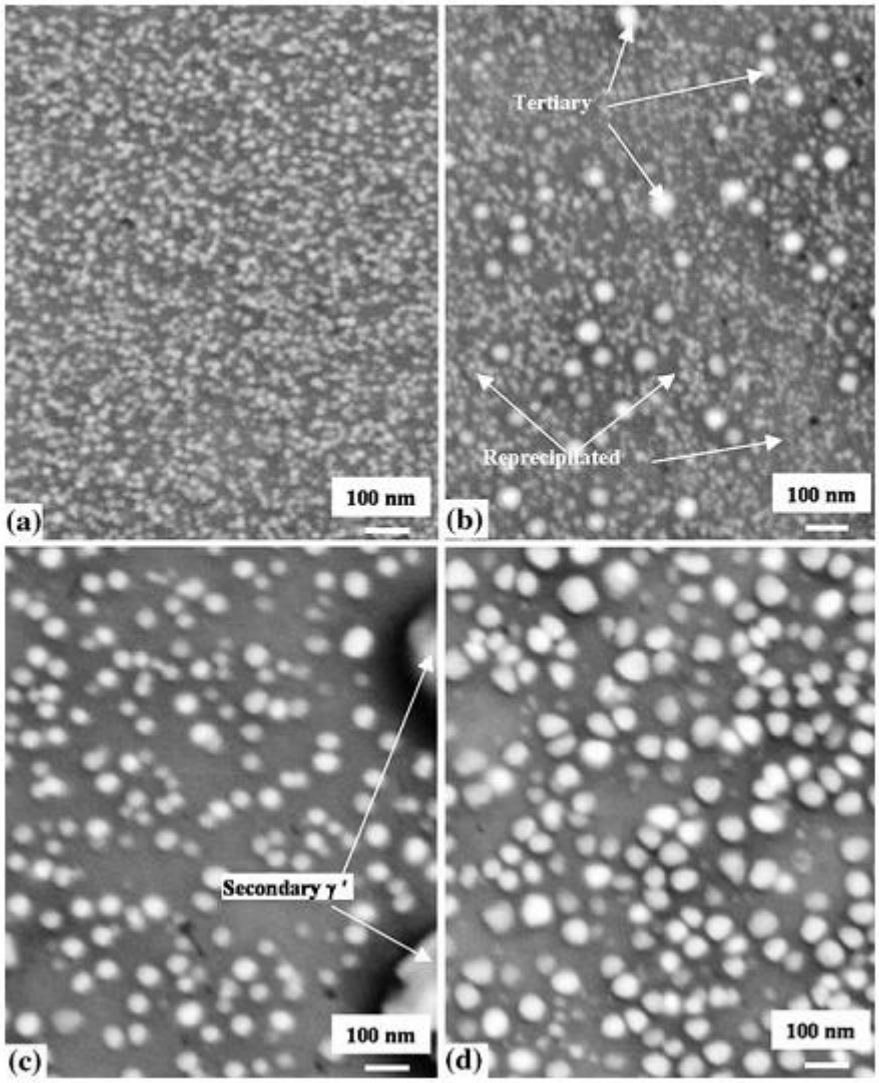

Fig. 3.17. SEM SE micrographs showing γ′ in 720Li IFWs at (a) the weld interface, (b) 1.75 mm, (c) 2.5 mm, and (d) 6 mm from the weld interface [23]

In the work of Huang *et al.* [23], TEM bright field (BF) micrographs together with selected area diffraction patterns (SADPs) along an $<001>_{\gamma}$ zone axis does not show superlattice reflections, showing that the γ′ and γ″ are fully dissolved at the weld interface up to 2.1 mm from the weld interface (Figs. 3.18.a-c). No re-precipitated γ′ or γ″ are detected in the weld line as a result of the low concentration of γ′/γ″ forming elements in IN718 and fast cooling rate after welding. Moreover, as can be seen in Figs. 3.18.a-c, as a result of the loss of γ′/γ″ strengthening in the weld line, dislocations can be easily generated and cut the fine

precipitates during loading. At 4 mm from the weld interface, the TEM BF micrograph and diffraction pattern show fine γ″ precipitates in γ matrix (Fig. 3.18.d). This is due to the fact that the temperature at this location is being lower than towards the weld interface, which does not fully dissolve γ″ precipitates.

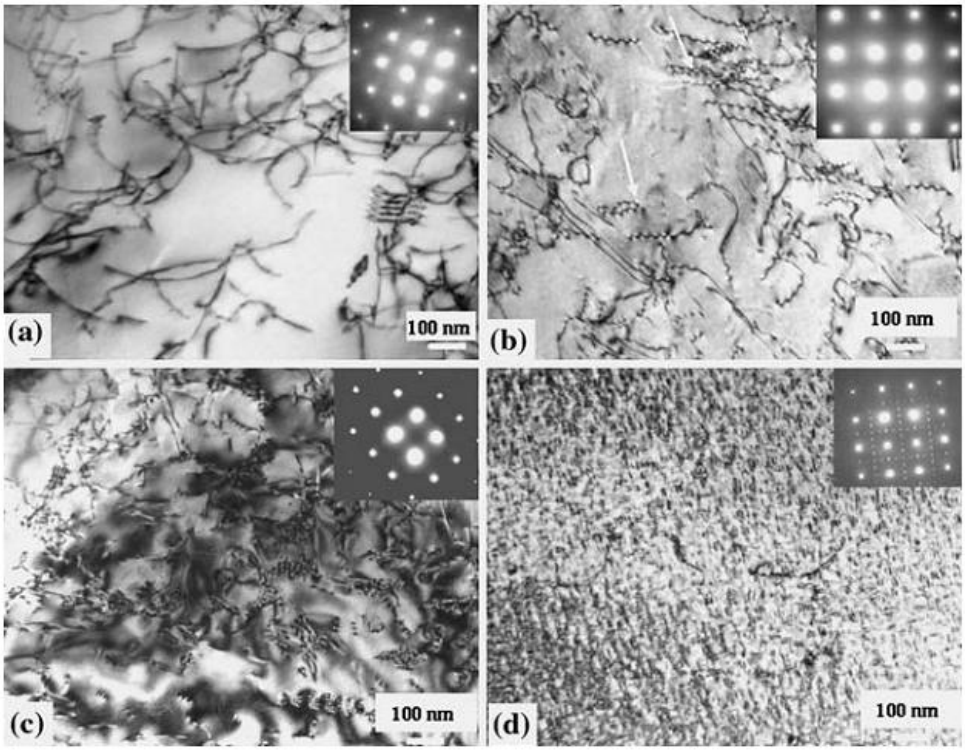

Fig. 3.18. TEM BF micrographs showing microstructures and diffraction patterns of IN718 IFWs at (a) 0.2 mm, (b) 0.7 mm, (c) 2.1 mm, and (d) 4 mm from the weld interface [23]

3.3.1.b. Grain Structure

The high temperature and thermo-mechanical deformation result in recrystallisation in the weld line. Studies have been reported on the grain structures, involving grain size, grain boundaries, morphology, and orientation relationships. Optical microscopy is convenient and

is suitable to measure grain size larger than 3 μm, but to detect finer grains SEM and EBSD are typically required.

Mary and Jahazi [42] investigated the grain size variation in IN718 LFWs (Fig. 3.19). The micrograph showed equiaxed fine recrystallised grains within 3 mm from the weld interface. The smallest grain size is 5.6 μm at 1 mm away from the weld interface. The larger grain size at the weld line was inferred to be due to the high temperature (~1200 ℃), which induced grain growth.

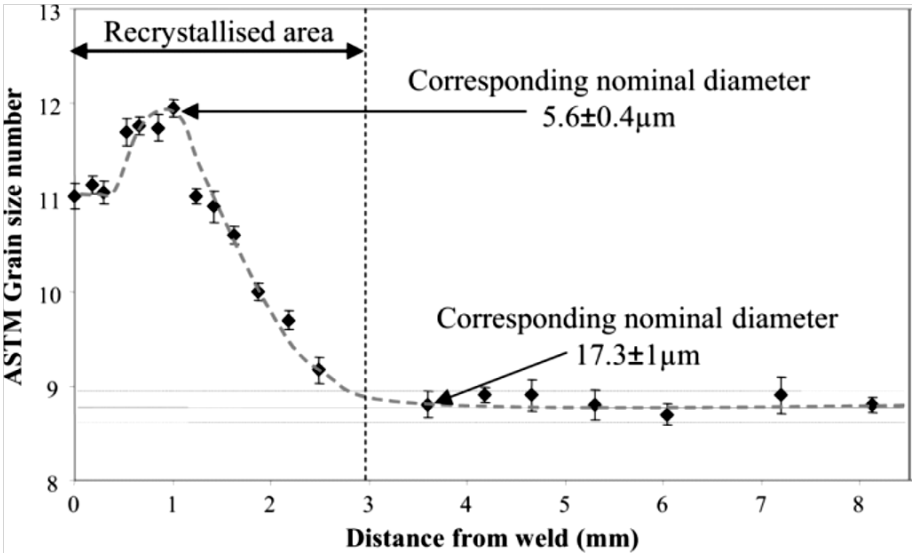

Fig. 3.19. The ASTM grain size variation of IN718 LFWs as a function of the distance from the weld interface (P = 70 MPa, a = 2 mm, f = 80 Hz) [42]

Chamanfar *et al.* [31] used EBSD to measure the grain size in Waspaloy LFWs represented by the average diameter of grains (Fig. 3.20). Similar to Mary and Jahazi's results, fine recrystallised grain formed near the weld line of Waspaloy LFWs. In contrast with Mary Jahazi's results, Chamanfar *et al.* found that the grain size decreases almost linearly until

reaching the finest size at the weld interface, and no larger grains occur near the weld line. This could be due to the difference of welding parameters and alloy type.

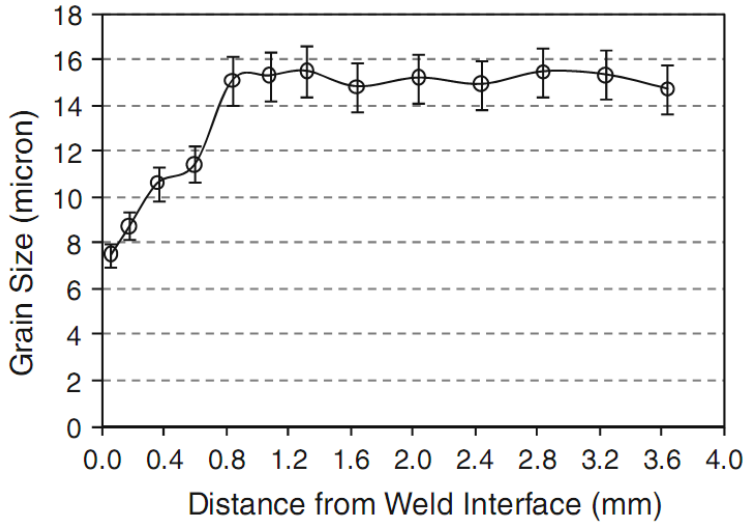

Fig. 3.20. Grain size variation of Waspaloy LFWs as a function of the distance from the weld interface (P = 90 MPa, a = 3 mm, f = 80 Hz) [31]

Reports about the nature of grain boundaries in Ni-based superalloys LFWs are limited. According to the work of Ola *et al.* [44] on LFW of cast IN738, the recrystallised grain boundaries in the thermo-mechanically affected zone (TMAZ) tend to form at prior grain boundaries and are mainly formed as high angle boundaries (HAGBs) with the degree of fit $\sum > 29$, implying a high degree of disorder (Fig. 3.21).

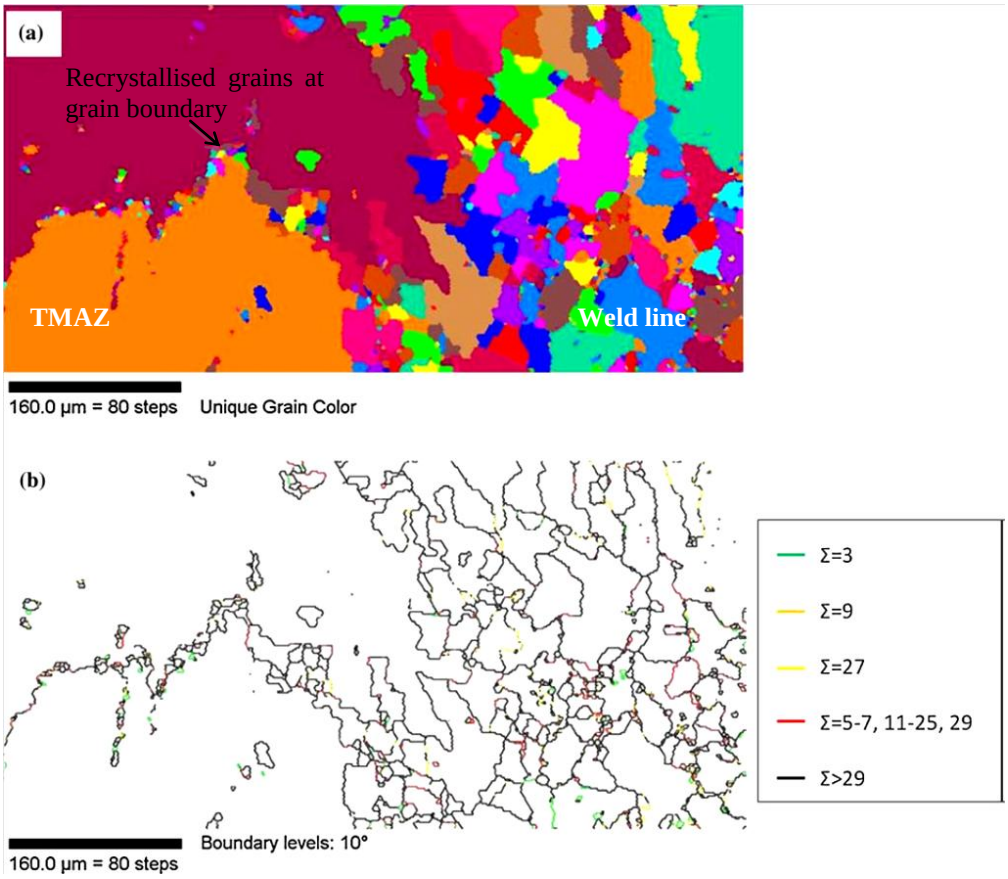

Fig. 3.21. EBSD maps showing partial recrystallisation of IN738 LFWs (a) grain structure between the weld line and TMAZ, and (b) the characters (∑ values) of grain boundaries (P = 90 MPa, a = 3 mm, f = 100 Hz) [44]

Another work by Damodaram *et al.* [51] investigated the grain structure variation of forged IN718 IFWs. As seen in Fig. 3.22, EBSD inverse pole figure (IPF) map shows fine recrystallised grains in weld zone, and partially recrystallised grains localised at prior grain boundaries in TMAZ. Due to the large compressive force, the grains in TMAZ are dramatically elongated.

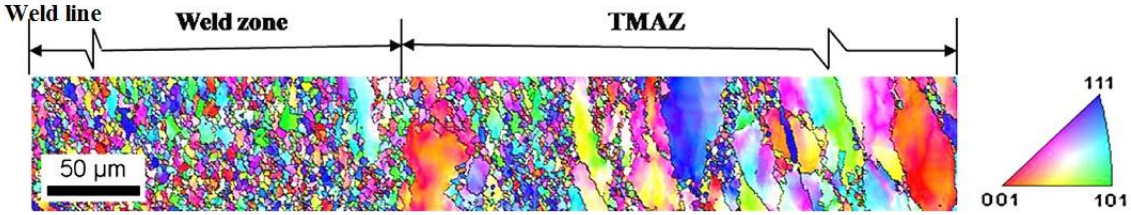

Fig. 3.22. EBSD IPF map showing weld zone and TMAZ of IN718 IFWs [51]

Further investigation on grain boundaries indicated enormous changes in the distributions of misorientation angle (Fig. 3.23). More than 90% boundaries in base metal are HAGBs (misorientation angle ≥ 15°), including a large fraction of annealing twin boundaries (misorientation angle = 60°). Whereas, in dynamically recrystallised regions (HAZ and TMAZ), grain boundaries possess HAGBs with more random misorientations and also consist of a large fraction of low angle grain boundaries (LAGBs, misorientation angle < 5°). It is because the plastic deformation induces the formation of large amounts of subgrains in old grains, and these subgrains consist of large numbers of LAGBs. However, the large fraction of LAGBs in HAZ is abnormal, as subgrains are not supposed to form in strain-free zones. The reason for the large fraction of LAGBs in HAZ was not demonstrated. It is worth mentioning that this study has not considered the angular resolution of EBSD (typically 1-2°) [53]. The misorientation angles between 0-2° were not removed, which might greatly increase the fraction of LAGBs. In some cases, the threshold value was set to 5° to obtain a more precise data [54].

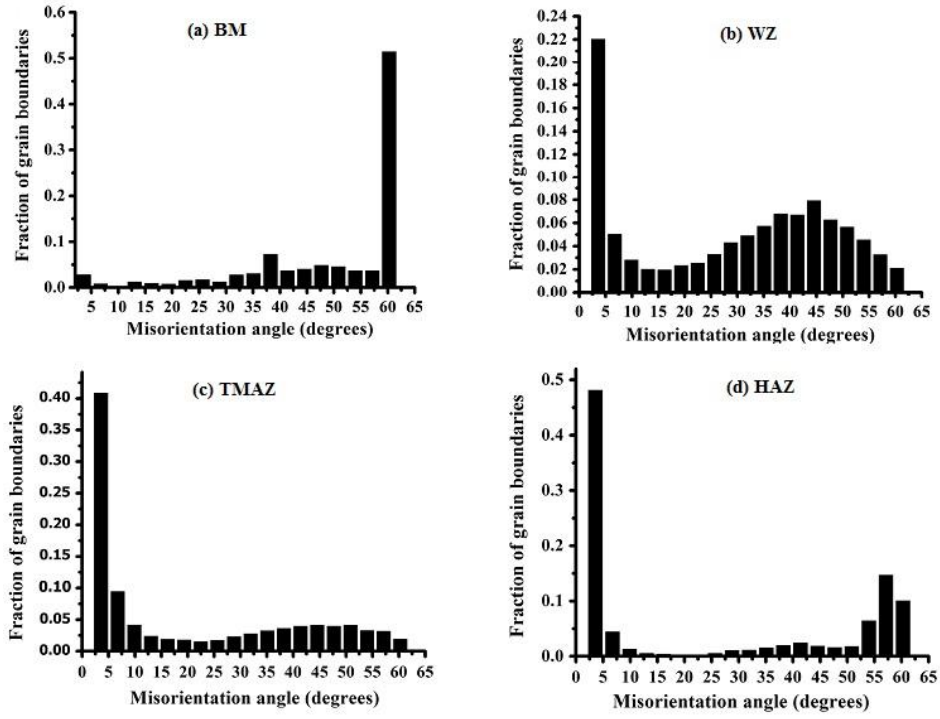

Fig. 3.23. Grain boundary misorientation distribution of (a) base metal, (b) weld zone, (c) TMAZ, and (d) HAZ of IN718 IFWs [51]

3.3.2. Microhardness Development

Mary and Jahazi [35] investigated the microhardness development in IN718 LFWs, as shown in Fig. 3.24.a. The hardness drops in the weld zone are due to the loss of strengthening precipitates, γ′ and γ″. The two hardness peaks at around ±1.5 mm are attributed to the strengthening via the fine grain size, which corresponds to Fig. 3.19. The same tendency of hardness profile was found in Waspaloy LFWs [31], with slight hardness increase at ±0.9 mm (Fig. 3.24.b). Chamanfar *et al.* [31] concluded that the small hardness rise is caused by the formation of re-precipitated fine γ′ and the increase of carbide precipitation.

Preuss *et al.* [25] measured the microhardness development of 720Li, RR1000, IN718 IFWs (Fig. 3.25). IN718 hardness profile shows a loss of hardness in the weld zone, as seen in IN718 LFWs. However, the profiles of 720Li and RR1000 show very limited hardness loss or even a slight increase in the weld zone, which is attributed to the strengthening by reprecipitated γ′. It is reasonable to infer that this reinforcement phenomenon occurs in high γ′ volume fraction LFWs.

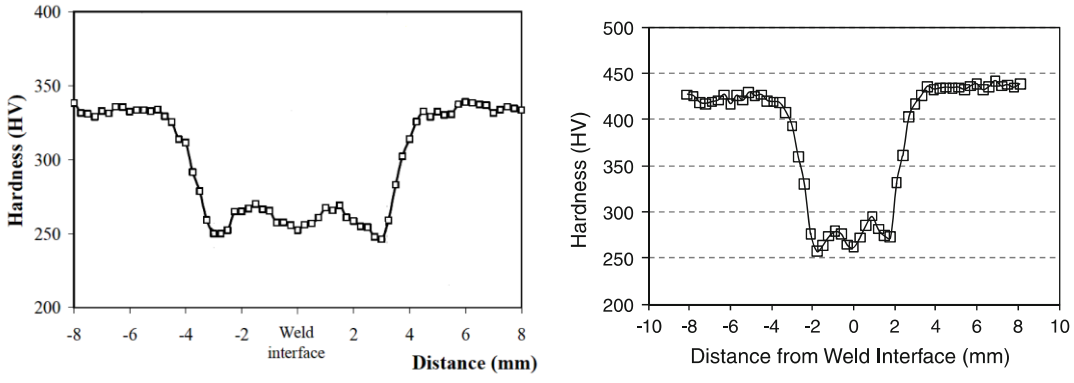

(a) (b)

Fig. 3.24. Microhardness development of LFWed (a) IN718 (P = 70 MPa, a = 2 mm, f = 80 Hz) [35], and (b) Waspaloy (P = 90 MPa, a = 3 mm, f = 80 Hz) [31]

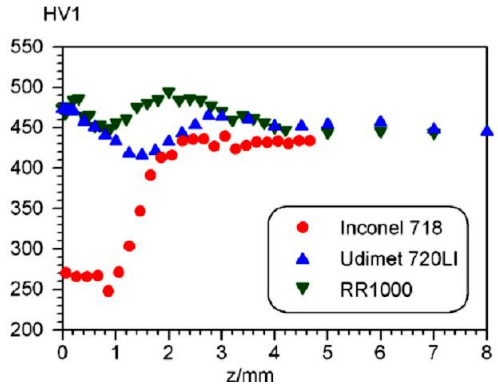

Fig. 3.25. Microhardness development of IFWed IN718, 720Li and RR1000. *x*-axis: distance from the weld interface, *y*-axis: Vickers hardness [25]

Post-weld heat treatment (PWHT) is an effective way to recover the strength of Ni-based LFWs by reprecipitating γ′ and γ″ particles [23, 40]. Huang *et al.* [23] investigated the influence of aging time on microhardness development of 720Li-IN718 IFWs (Fig. 3.26). They showed that the PWHT at 760 ℃ increases the microhardness of the weld zone to levels even higher than that of the base metal. Moreover, 2 h aging time provides the largest hardness increase, as the occurrence of overaging reduces the hardness, which is more pronounced in IN718 beyond 4 h.

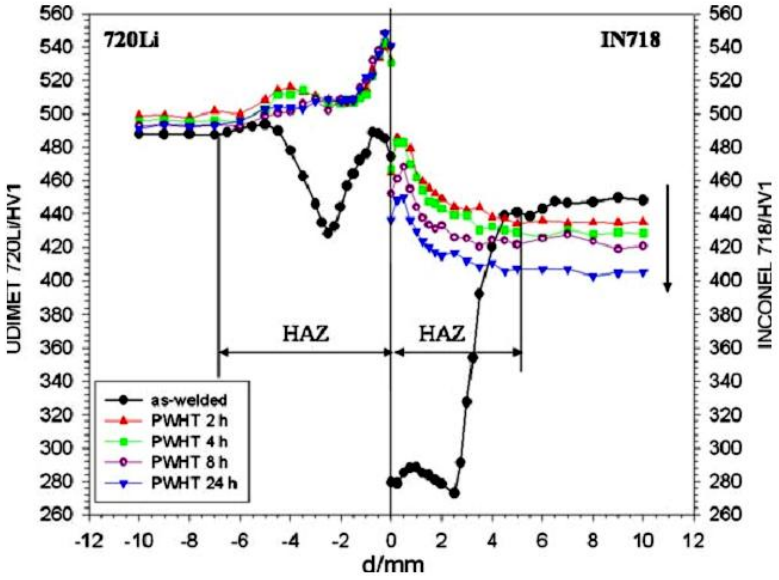

Fig. 3.26. Microhardness development of 720Li-IN718 IFWs in as-welded and PWHTed conditions. *x*-axis: distance from the weld interface, *y*-axis: Vickers hardness [23]

3.3.3. Residual Stress Development

Residual stresses are internal forces existing in material when there is no external force. Studies on residual stress are important because residual stress can combine with applied stress to cause structural failure. On the other hand, compressive stress may be introduced deliberately to improve fatigue resistance. Residual stresses are classified into three types: (I) macrostress, (II) intergranular stress, and (III) atomic stress [55]. The common methods for residual stress measurement include mechanical approaches, diffraction and other methods. The mechanical methods consist of hole drilling, contour method, curvature and compliance methods, which are low cost destructive methods for measuring macrostress, but they are limited by their poor accuracy and low penetration.

To achieve high accuracy and deep penetration non-destructively, diffraction is the most reliable approach. The principle is to detect elastic strain by measuring the changes in interplanar spacing based on Bragg's law [56]:

$$\lambda = 2d\ sin\ \theta \tag{3.2}$$

where λ is the incident wavelength, θ represents the diffraction angle defined by the lattice plane spacing d. The changes in the lattice plane spacing can be recorded as angular shifts $\Delta\theta$ in the diffraction peak position, thus the strain ε can be calculated by [56]:

$$\varepsilon = (d - d_0)/d_0 = -\cot\theta\,\Delta\theta \tag{3.3}$$

where d, d_0, θ correspond to deformed lattice spacing, strain free lattice spacing and strain-free diffraction angle. The residual stress can be converted from strain results by Equation 4.7.

There are many diffraction sources: neutrons, electron beams, laboratory X-rays, and synchrotron (hard) X-rays. Among them, neutron diffraction possesses the highest penetration depth (exceeding several centimetres for most metals) [57] with relatively high

spatial resolution and accuracy, which has been used to detect the residual stress in welded Ni-superalloys. In contrast, synchrotron radiation provides smaller penetration depth, but offers the finest spatial resolution.

Youtsos and Ohms [58] reported that residual stress of Waspaloy LFWs measured by neutron and X-ray diffraction are in good agreement (Fig. 3.27). The stresses profile showed a 'W' shape, with high tensile stress near the weld line (±3 mm) and moderate compressive stress in the adjacent region. The highest tensile and compressive stresses are 900 MPa at the weld interface and 320 MPa at 5 mm from the weld interface. The d_0 measurement was not carried out in this work, therefore the measured residual stresses may not be very accurate.

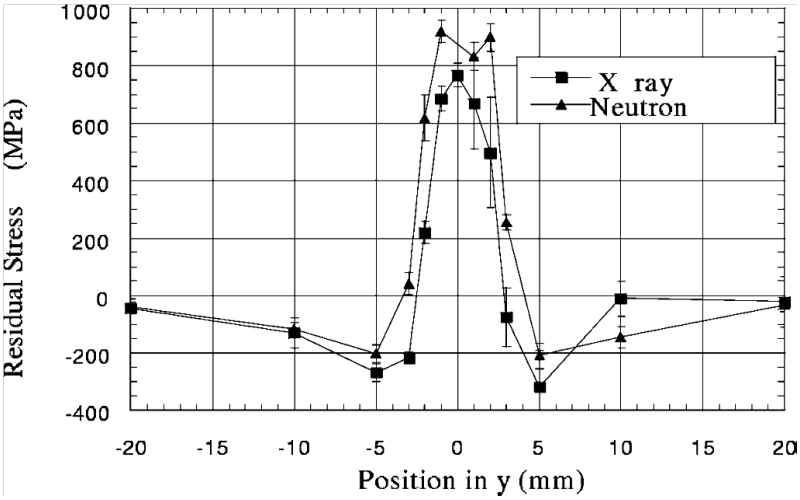

Fig. 3.27. Comparison between neutron diffraction and X-ray diffraction for measuring residual stress in Waspaloy LFWs [58]

Frankel [48] reported the residual stress profiles in IN718-720Li LFWs calculated from mid-thickness-mid-width measurements using neutron diffraction. A single far-field d_0 for each alloy has been applied to calculate the residual stresses across the welds, as shown in Fig. 3.28, which reflects the same trend as Waspaloy LFWs (Fig. 3.27). The highest tensile

stress (~960 MPa) was found at 1 mm from the weld line in IN718, in the *x*-direction of the sample welded under 250 MPa. This tensile stress reaches about 93% of the yield strength of standard heat treated IN718 (1034 MPa) [17]. The intensity of the tensile stresses near the weld line reduces with the increase in weld pressure, and changes the stress levels from tensile to compressive stresses in the *y* and *z*-directions.

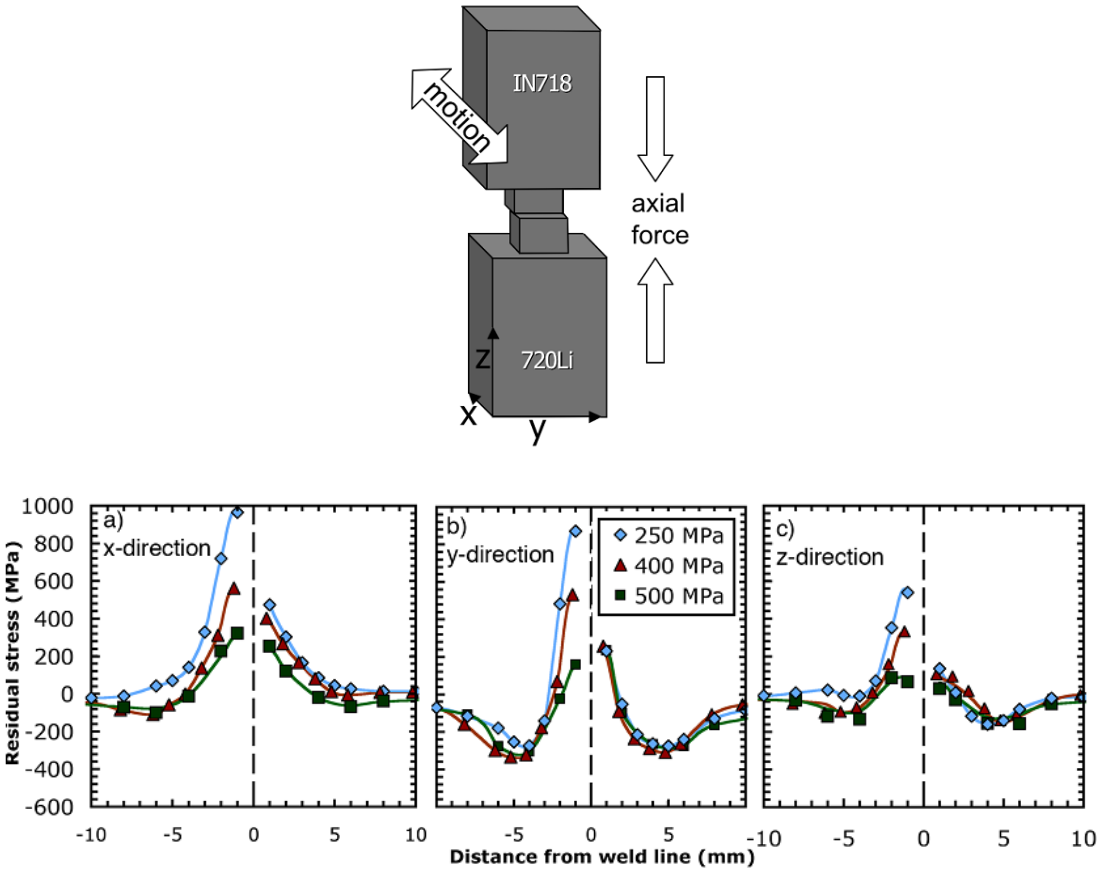

Fig. 3.28. Schematic and residual stress development of LFWed IN718 (left)-720Li (right) under different weld pressure calculated by far-field d_0 [48]

The variation of d_0 values across the welds is shown Fig. 3.29, as determined for the (311) diffraction peak. All the samples exhibit an increase in d_0 from 4 mm towards the weld line. The variation of d_0 is believed to be related to the dissolution of precipitates (γ' for 720Li, and γ', γ'' and δ phases for IN718). During LFW, precipitates dissolve as the alloys are heated,

increasing the concentration of Al, Ti, and Nb in the matrix, and forcing the lattice spacing to become larger, since the atomic radii of Al, Ti, and Nb are larger than that of Ni. Since temperature increases from the base metal towards the weld line during LFW (as discussed in Section 3.2.2), a higher fraction of precipitates is dissolved near the weld line, which causes a larger d_0 in this area due to the presence of more Ti, Al and Nb elements in the matrix.

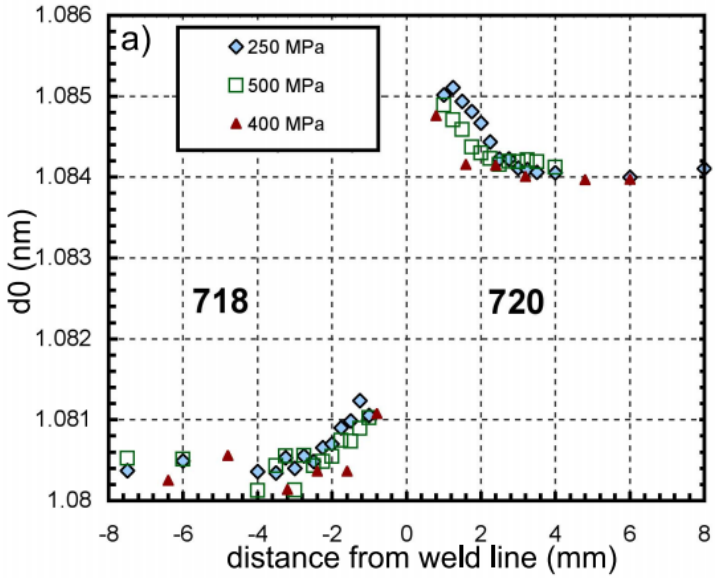

Fig. 3.29. Variation of d_0 values across the IN718-720Li LFWs under different weld pressure [48]

Figure 3.30 shows the residual stress development in IN718-720Li LFWs after d_0 correction. Compared Fig. 3.30 to Fig. 3.28, it is apparent that accounting for the d_0 variation has a significant effect on the magnitude of the calculated residual stresses. The tensile stresses are reduced up to 500 MPa by this adjustment. The highest tensile stress (up to 400 MPa) remains in the *x*-direction for the weld pressure 250 MPa. Similar to the residual stress measured using far-field d_0, the magnitude of the stress reduces with increase in weld pressure.

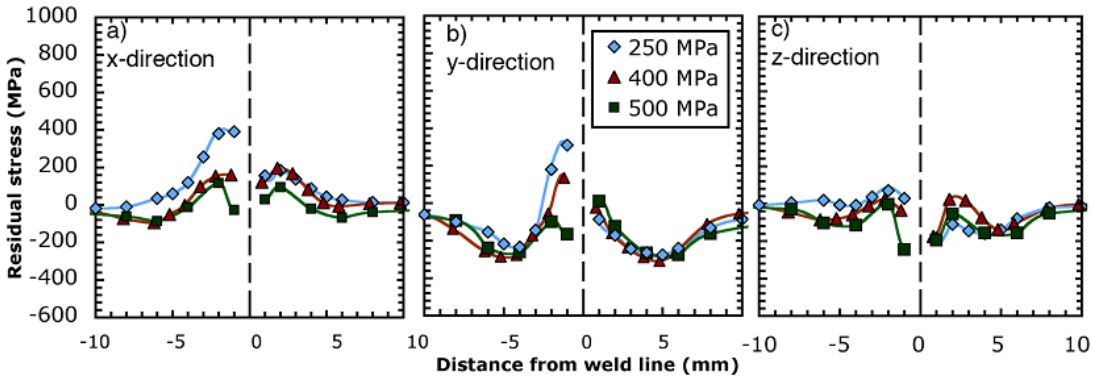

Fig. 3.30. Residual stress development of the IN718 (left)-720Li (right) LFWs under different weld pressure after d_0 correction [48]

Post-weld heat treatment has been proved as an effective approach to minimise the residual stress in Ni-based IFWs [25]. Similarly, it is reasonable to assume PWHT is a way to reduce the residual stress in Ni-based LFWs.

3.3.4. Classification of Weld Zones

Several reports provided a classification of the weld zone for LFWed Ni-based superalloys, either based on microstructural or microhardness development.

Vishwakarma *et al.* [43] classified the 718 Plus LFWs into three regions: weld centre, thermo-mechanically affected zone (TMAZ), and base metal, based on optical microscopy (Fig. 3.31). The weld centre contains ultrafine recrystallised grains and precipitate-free grain boundaries, whereas, in the TMAZ, the grains are partially recrystallised, with partially dissolved precipitates at grain boundaries. Optical microscopy is convenient to roughly reveal the different weld zones, but due to its limited spatial resolution, the variation of small particles cannot be observed.

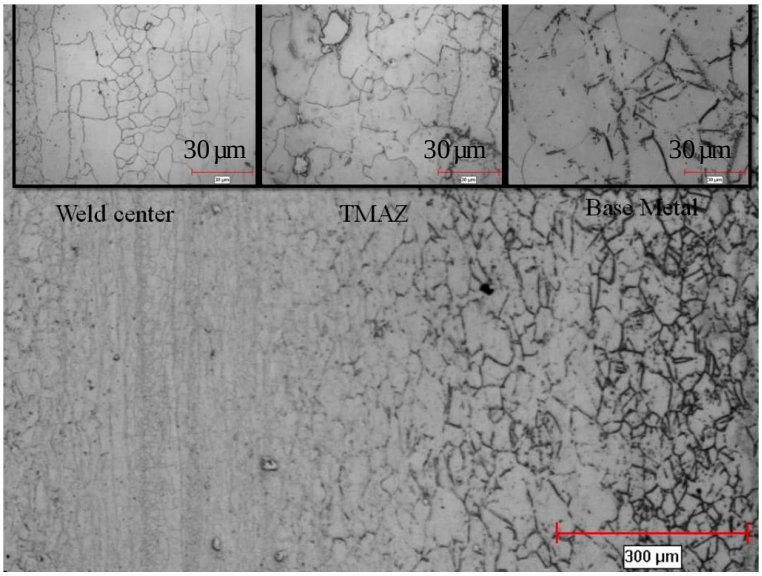

Fig. 3.31. Optical micrograph showing weld zone of 718 Plus LFWs by grain size change [43]

Mary and Jahazi [35] defined the weld zones of IN718 LFWs by hardness profile, where the TMAZ is the trough of hardness and the weld centre is the region (±0.5 mm) close to the weld interface (Fig. 3.32). This method provides a better detection of the outer boundary of TMAZ, where the reversion of γ′ and γ″ is hardly resolved in optical microscopy. It can be inferred that optical microscopy may underestimate TMAZ region. Nevertheless, the hardness approach does not reflect the interface between the weld centre and TMAZ, because of the lack of grain size information.

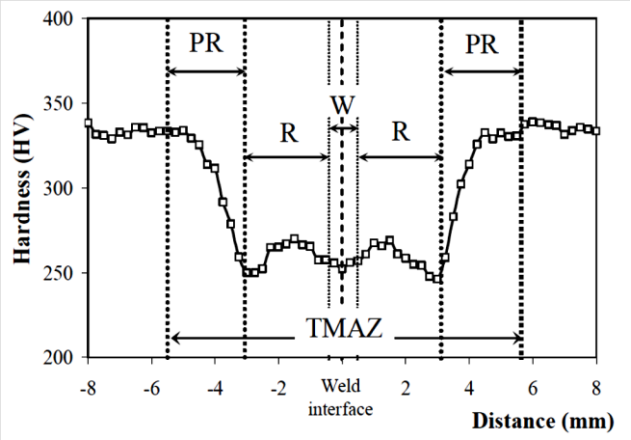

Fig. 3.32. Classification of IN718 LFWs using the microhardness distribution, W: weld centre, PR: partial reversion of γ′ and γ″, R: recrystallised area [35]

Chamanfar [41] divided the weld zone of Waspaloy LFWs into four regions: weld interface, TMAZ, HAZ and BM by optical and electron microscopy (Fig. 3.33). TMAZ is the region where dynamic recrystallisation and γ′ dissolution occur, while the HAZ only involves γ′ dissolution. The same classification method was also used in IN738 LFWs [44]. This four region definition is more precise than the three region definition, because it considers all the possible variation of microstructure in LFWs. A combination method of hardness and microstructural development for weld zone determination may improve the division of the boundary between neighbouring zones.

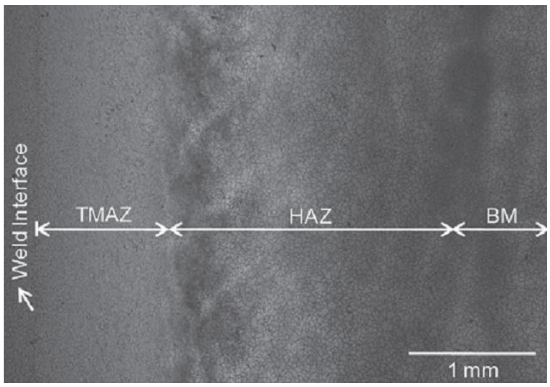

Fig. 3.33. Optical micrograph illustrating the weld zones of Waspaloy LFWs [41]

3.3.5. Weld Integrity and Defects

Studies of weld integrity and defects are used to assess the weldability and to optimise welding process parameters. The common techniques for weld assessment include optical microscopy, scanning electron microscopy, and energy-dispersive X-ray spectroscopy, which are effective to reveal the macrostructure, microstructure and chemical composition of welds.

3.3.5.a. Weld Integrity

The assessment of weld integrity is usually based on macroscopic examination and microstructural analysis. Mary and Jahazi [42] revealed that a dark layer of oxides formed near the extremities of the weld interface in IN718 LFWs (Fig. 3.34).

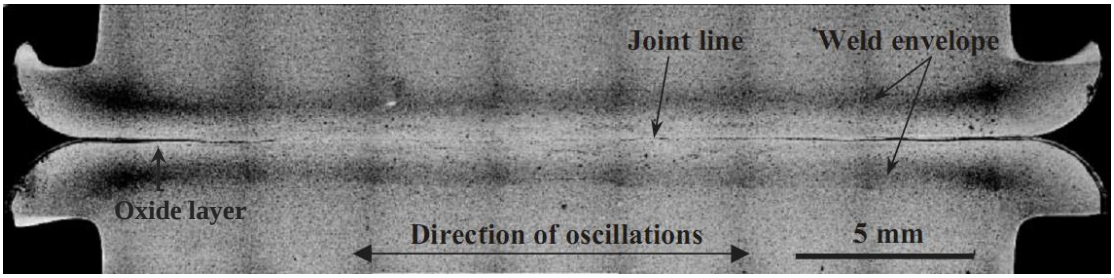

Fig. 3.34. Optical macrograph showing oxide layer at the extremities of weld interface [42]

The SEM/EDX results demonstrated that a number of Nb nitrides and Al, Fe, Ni, Nb oxide particles are located at the weld interface (Fig. 3.35). The chemical analyses of smaller particles are not accurate because of the limited spatial resolution of SEM/EDX (several microns). The formation of oxide residues is believed to originate from either the initial oxide film on the welding surface or oxidation during the friction stage.

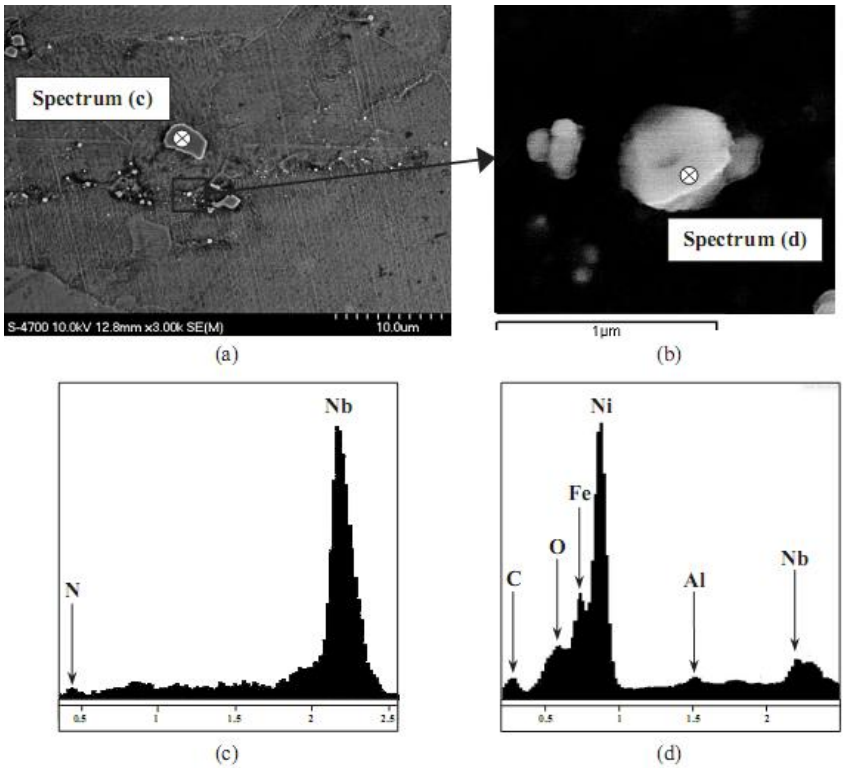

Fig. 3.35. (a) SEM SE micrograph showing Nb nitrides and small oxides at weld interface and (b) SEM BSE micrograph showing the oxides at high magnification, (c) EDX of big particle in image (a) showing Nb and N rich, and (d) EDX of small particles in image (a) showing Ni, Al, Fe, O rich particles [42]

Other weld integrity work from Chamanfar *et al.* [31] reported insufficient power input caused unsuccessful joints due to the incomplete extrusion in LFW of Waspaloy (Fig. 3.36).

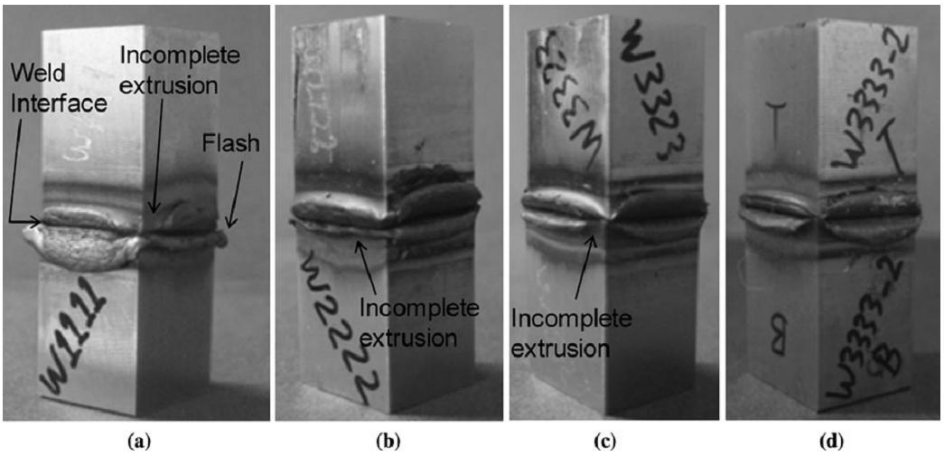

Fig. 3.36. Macroscopic examination for weld integrity of Waspaloy LFWs under different weld pressure, amplitude, frequency (a) 50 MPa, 2 mm, 40 Hz, (b) 70 MPa, 2.5 mm, 40 Hz, (c) 70 MPa, 3 mm, 80 Hz, and (d) 90 MPa, 3 mm, 80 MPa [31]

In later work, Chamanfar *et al.* [40] revealed the lack of bonding (Figs. 3.37.a-b) and Cr and Ti oxide layer at the weld interface by SEM (Fig. 3.37.c). Meanwhile, Chamanfar *et al.* concluded that an axial shortening of 2 mm is critical to eliminate the lack of bonding and extrude all the oxides from the interface (self-cleaning process).

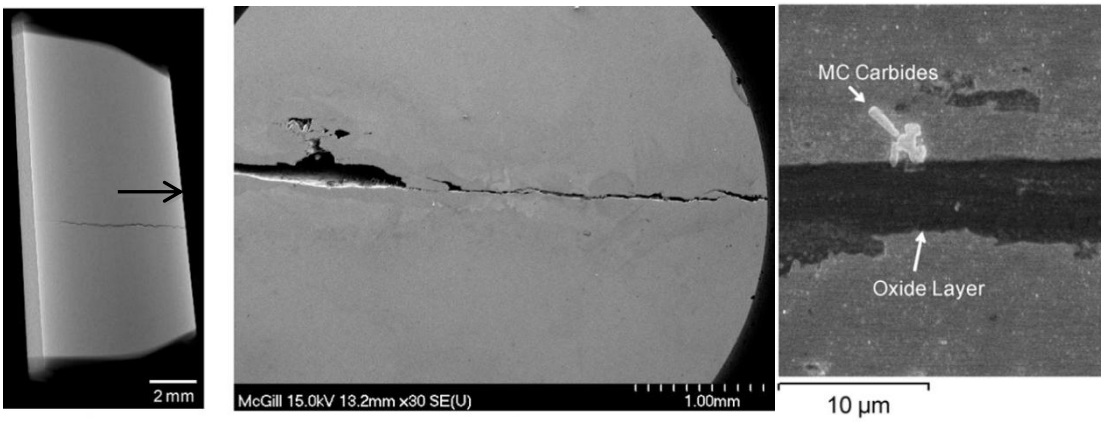

Fig. 3.37. SEM micrographs showing (a-b) the lack of bonding (SE micrographs), (c) oxide layer and MC carbides at the weld interface of Waspaloy LFWs (BSE micrograph) [40]

3.3.5.b. Weld Defects

Understanding the formation mechanisms of weld defects is the key to developing and optimising the welding process. Some weld defects were illustrated in Sections 3.3.3 and 3.3.5.a, such as high tensile residual stresses, lack of bonding, and oxide inclusions. However, several imperfections have also been reported in other Ni-superalloy LFWs.

The high temperatures experienced in the weld regions induced grain boundary liquation, which was observed in 718 Plus LFWs [43]. The liquid phase resolidified as a brittle Laves/γ eutectic (Fig. 3.38), which is detrimental to weld properties and cannot be eliminated by PWHT. In addition, high temperature can also cause intergranular constitutional liquation of second phase particles (γ′, NbC, TiC, TiN and δ phase).

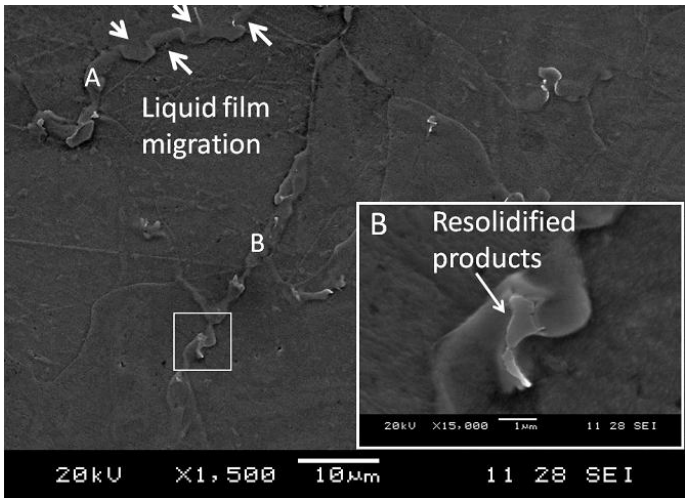

Fig. 3.38. SEM SE micrographs showing (a) the grain boundary liquation, and (b) the resolidified Laves/γ eutectic in 718 Plus LFWs [43]

Ola *et al.* [44] indicated that the phenomena of intergranular and intragranular liquation are found in the TMAZ of IN738 LFWs, while the γ-γ′ eutectics are formed as a result of

resolidification of liquid phases (Fig. 3.39). The occurrence of resolidified eutectics would reduce the mechanical properties of the joints, which need to be avoided or eliminated.

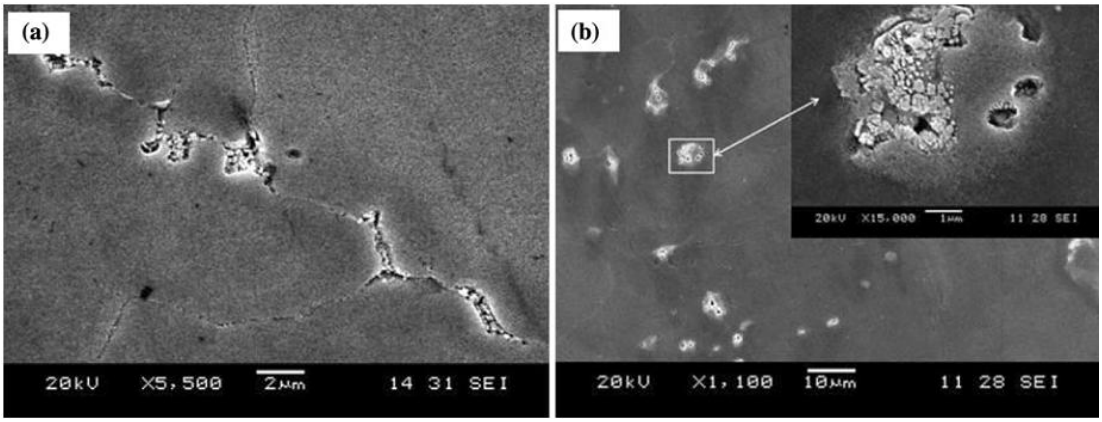

Fig. 3.39. SEM SE micrographs of the TMAZ of IN738 LFWs showing the presence of γ-γ′ eutectics that formed during cooling from (a) intergranular and (b) intragranular liquation [44]

3.3.5.c. Welding Dissimilar Ni-based Superalloys

Uneven hardness distribution is common in many metal welds due to the hardness differences of the parent metal [23, 59-61]. As can be seen in Fig. 3.26, there is around 200 HV difference between the two alloys in the as-welded condition, which could be reduced to 70 HV by post-weld heat treatment. It is reasonable to assume that the hardness trough may give rise to low tensile strength.

Because of the variety of Ni-based superalloys, there are many possibilities of dissimilar Ni-superalloys LFWs or IFWs. But so far most work has involved LFW or IFW of similar Ni-superalloys, and limited work about welding dissimilar Ni-superalloys has been published.

Karadge *et al.* [47] investigated the influence of crystal orientation on LFW of single crystal CMSX-4 to polycrystalline RR1000. The schematic diagrams of crystal orientation are shown in Fig. 3.40, in which the <001> direction is always perpendicular to the friction (oscillation/reciprocation) direction, while κ=0° and κ=45° correspond to <100> and <110> parallel to the friction direction, respectively.

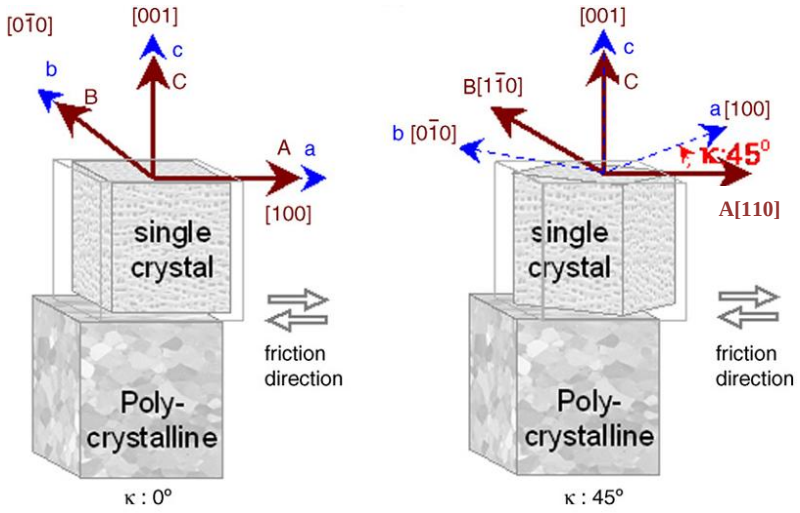

Fig. 3.40. Schematic diagrams of orientation of LFW single crystal CMSX-4 to polycrystalline RR1000. κ is the angle that the <001> direction makes with the friction direction in the sense towards the <110> at 45 °[47]

The weldability presents a remarkable correlation with angle κ, which reveals that κ must be between 35 ° to 60 ° to obtain sound welds (Fig. 3.41). The explanation put forward for this phenomenon, is that a favourable orientation is required for FCC slip systems {110}<110> to allow sufficient plasticity. The plastic deformation occurs when the resolved shear stress (τ_r) applying in the slip direction on the slip plane exceeds the critical resolved shear stress (τ_c). The applied shear stress follows the Schmid's Law, which can be expressed as (Fig. 3.42):

$$\tau_r = \sigma \cos\psi \cos\lambda \tag{3.4}$$

where σ is the applied stress induced by the force (F) on the sample with cross-sectional area A_0, ψ is the angle between slip direction and applied stress, λ is the angle between the slip plane normal and applied stress. The Schmid Factor is the maximum value of $\cos\psi \cos\lambda$ for slip planes.

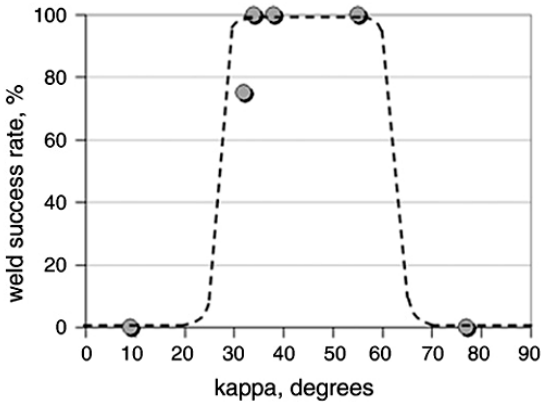

Fig. 3.41. Effect of crystal orientation on the weldability for the geometry shown in Fig. 3.40, in which spots represent experimental data and the dotted line is the best fit line [47]

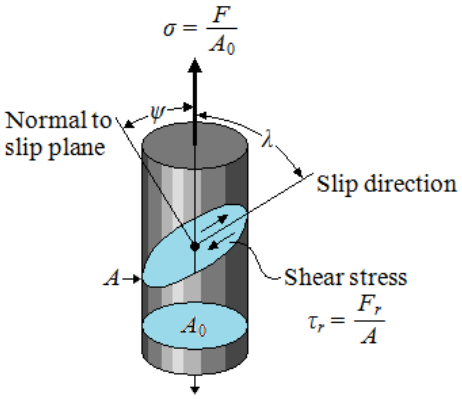

Fig. 3.42. Schematic diagram of the Schmid's law [62]

When the applied stress direction is <110> (while κ=45°), the maximum Schmid Factor reaches the value of $2/\sqrt{6}$. Whereas, the maximum Schmid Factor is $1/\sqrt{6}$ when the applied stress is in <100> direction (while κ=0° or 90°). This means under the same applied stress (σ), single crystal Ni-based superalloys are more easily be deformed when the applied stress direction is close to κ=45°. In this case, κ between 35° to 60° can provide enough

thermo-mechanical deformation under this specified weld parameters, whereas other κ angles cannot generate sufficient deformation.

In fusion welding, chemical composition variation is a common phenomenon, whereas in friction welding the compositional change is very limited although large plastic deformation occurs in friction welding. Huang *et al.* [23] investigated the chemical composition of 720Li-IN718 IFWs by SEM/EDX spot analyses, which revealed that a small compositional change occurred from one to the other alloy in a range of less than 15 μm (Fig. 3.43).

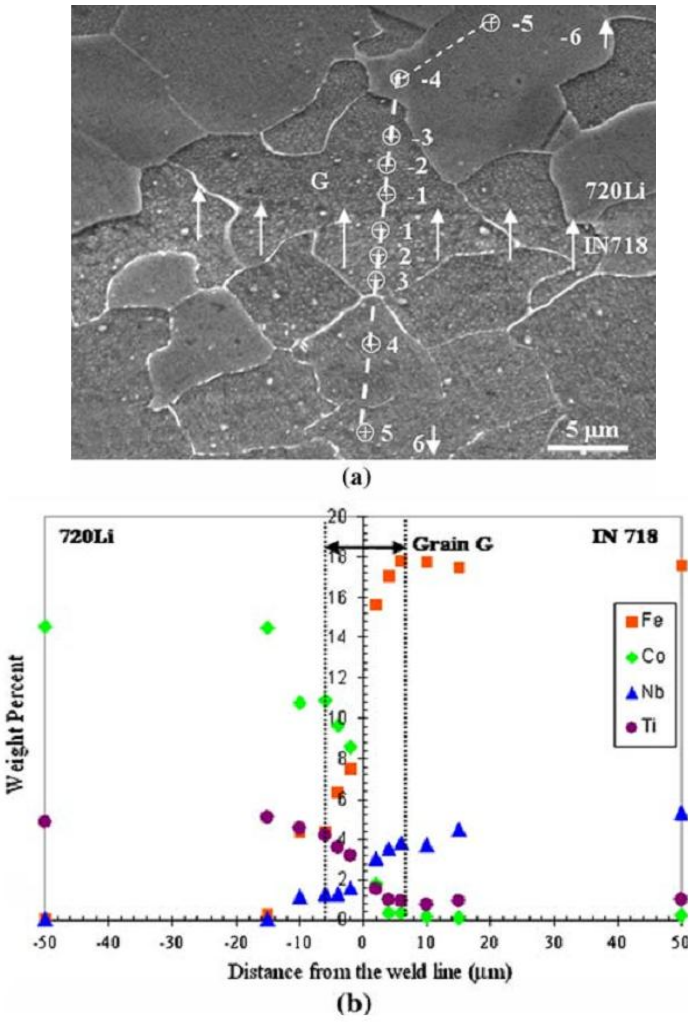

Fig. 3.43. (a) SEM/EDX spot analyses across the weld line (arrowed) in 720Li-IN718 LFWs. The first three spots were conducted inside the G grain at 2 μm, 4 μm, and 6 μm from the weld line. The fourth to sixth spots were at 10 μm, 15 μm and 50 μm towards the weld line. (b) The corresponding element profiles across the weld line [23]

3.4. Summary: Key Findings and Areas of Research

This chapter summarises the microstructure-property development associated with welding Ni-based superalloys using LFW and IFW. Very limited work has been done on welding dissimilar Ni-based superalloys, and most studies are about similar alloys. The key findings are listed below:

1. LFW of Ni-based superalloys is a solid-state welding process in which frictional heat is generated by reciprocating two work pieces, which are in contact. The frictional heat raises the temperature very rapidly to a maximum temperature below the solidus of the alloy, coupled with a compressive pressure, which mitigates the susceptibility for cracking in fusion welding. However, LFW may induce constitutional liquation or grain boundary liquation, with resolidified Laves/γ brittle phase in some Ni-superalloys.
2. The temperature development of LFW Ni-superalloys has been studied by experiments and modelling. Results reflect the same trend of temperature development at different locations on the weld piece, and the alloy type does not influence this trend. However, accurate in-situ measurement of the temperature at the weld interface is rather difficult due to the thermo-mechanical deformation of material during LFW.
3. The LFW weldability strongly depends on the heat input and axial shortening. In general, low heat input and insufficient axial shortening can induce incomplete bonding and residue of oxides at the weld line. However, due to the difference in the flow behaviour of materials, the geometry of weld pieces, and the weld systems, the optimised weld parameters in other works are not relevant to this dissertation.
4. During LFW, the high temperature and thermo-mechanical deformation induce drastic microstructural variation (in particles and grains) and large residual stress. The particles dissolve and may re-precipitate during cooling. DRX occurs near the weld interface generating fine grains, but the DRX mechanisms are still in dispute. Additionally, studies

on the microstructural and residual stress development of LFW Ni-based superalloys are limited.

5. The hardness variation in the weld zone is due to the effect of particles, grain size, γ/γ' misfit, and work hardening. In addition, PWHT is an effective method to develop or homogenise the hardness. Qualitative studies have been done relating microstructure to hardness in LFW Ni-based superalloys, as well as investigating the influence of PWHT on the microstructural and hardness development. But quantitative analyses are limited.

The scope of this thesis, LFW of IN718-IN713LC, is a novel area, as no relevant publication has been reported. LFW may provide a convenient way to manufacture high performance IN718-IN713LC gas turbine blisks, and would improve the performance of aeroengines if the research is successful. The areas that will be investigated include:

- Investigation of the potential defects in IN718-IN713LC LFWs, such as incomplete bonding, residual stress, cracks, pores, oxides and liquation.
- Influence of process parameters (pressure, amplitude, and frequency) on microstructural, hardness and residual stress development of LFW IN718-IN713LC.
- Effect of PWHT on the microstructure-hardness development of LFW IN718-IN713LC.

3.5. References

[1] Q. Wang, D. L. Sun, Y. Na, Y. Zhou, X. L. Han, and J. Wang, "Effects of TIG welding parameters on morphology and mechanical properties of welded joint of Ni-base superalloy," *11th International Conference on the Mechanical Behavior of Materials (ICM11),* vol. 10, 2011.

[2] P. Wangyao, W. Homkrajai, and S. Asavavisithchai, "Effect of postweld heat treatments on TIG-welded microstructures of superalloy, IN-738," *Chiang Mai Journal of Science,* vol. 36, pp. 320-330, 2009.

[3] H. L. Lin, "Optimization of Inconel 718 alloy welds in an activated GTA welding via Taguchi method, gray relational analysis, and a neural network," *International Journal of Advanced Manufacturing Technology,* vol. 67, pp. 939-950, 2013.

[4] D. Dye, K. T. Conlon, P. D. Lee, R. B. Rogge, and R. C. Reed, "Welding of single crystal superalloy CMSX-4: experiments and modelling," *Superalloys,* vol. 2004, pp. 485-491, 2004.

[5] M. B. Henderson, D. Arrell, R. Larsson, M. Heobel, and G. Marchant, "Nickel based superalloy welding practices for industrial gas turbine applications," *Science and Technology of Welding & Joining,* vol. 9, pp. 13-21, 2004.

[6] C. Y. Su, C. P. Chou, B. C. Wu, and W. C. Lih, "Plasma transferred arc repair welding of the nickel-base superalloy IN-738LC," *Journal of Materials Engineering and Performance,* vol. 6, pp. 619-627, 1997.

[7] A. Lingenfelter, "Welding of Inconel alloy 718: A historical overview," *Superalloy,* pp. 673-683, 1989.

[8] O. A. Ojo, N. L. Richards, and M. C. Chaturvedi, "Study of the fusion zone and heat-affected zone microstructures in tungsten inert gas-welded Inconel 738LC superalloy," *Metallurgical and Materials Transactions A-Physical Metallurgy and Materials Science,* vol. 37A, pp. 421-433, 2006.

[9] R. K. Sidhu, N. L. Richards, and M. C. Chaturvedi, "Effect of aluminium concentration in filler alloys on HAZ cracking in TIG welded cast Inconel 738LC superalloy," *Materials Science and Technology,* vol. 21, pp. 1119-1131, 2005.

[10] H. A. Shahsavari, A. H. Kokabi, and S. Nategh, "Effect of preweld microstructure on HAZ liquation cracking of Rene 80 superalloy," *Materials Science and Technology,* vol. 23, pp. 547-555, 2007.

[11] M. T. Rush, P. A. Colegrove, Z. Zhang, and B. Courtot, "An investigation into cracking in nickel-base superalloy repair welds," *Advanced Materials Research*, vol. 89, pp. 467-472, 2010.

[12] H. Guo, M. C. Chaturvedi, N. L. Richards, and G. S. Mcmahon, "Interdependence of character of grain boundaries, intergranular segregation of boron and grain boundary liquation in simulated weld heat-affected zone in Inconel 718," *Scripta Materialia,* vol. 40, pp. 383-388, 1999.

[13] X. Huang, M. C. Chaturvedi, and N. L. Richards, "Effect of homogenization heat treatment on the microstructure and heat-affected zone microfissuring in welded cast alloy 718," *Metallurgical and Materials Transactions A,* vol. 27, pp. 785-790, 1996.

[14] W. Chen, M. C. Chaturvedi, and N. L. Richards, "Effect of boron segregation at grain boundaries on heat-affected zone cracking in wrought Inconel 718," *Metallurgical and Materials Transactions A,* vol. 32, pp. 931-939, 2001.

[15] M. C. Chaturvedi, W. Chen, A. Saranchuk, and N. L. Richards, "The effect of B segregation on heat-affected zone micro-fissuring in EB welded Inconel 718," in *Superalloys 718, 625, 706 and Various Derivatives*, Pittsburgh, USA, pp. 743-751, 1997.

[16] Y. Ahn, B. Yoon, H. Kim, and C. Lee, "Effect of dilution on the behavior of solidification cracking in PTAW overlay deposit on Ni-base superalloys," *Metals and Materials International,* vol. 8, pp. 469-477, 2002.

[17] "http://dc193.4shared.com/doc/2egtQlq2/preview.html"

[18] L. O. Osoba, A. K. Khan, and S. O. Adeosun, "Cracking susceptibility after post-weld heat treatment in Haynes 282 nickel based superalloy," *Acta Metallurgica Sinica (English Letters),* vol. 26, pp. 747-753, 2013.

[19] S. Kou, *Welding Metallurgy*, 2nd ed. Hoboken, New Jersey, Wiley-Interscience, 2003.

[20] B. G. Muralidharan, V. Shankar, and T. P. S. Gill, *Weldability of Inconel 718 - A Review*. Indira Gandhi Centre for Atomic Research, Kalpakkam, 1996.

[21] G. Cam and M. Kocak, "Progress in joining of advanced materials," *International Materials Reviews,* vol. 43, pp. 1-44, 1998.

[22] A. W. Society, *Standard Welding Terms and Definitions Including Terms for Adhesive Bonding, Brazing, Soldering, Thermal Cutting, and Thermal Spraying*, 12th ed., 2010.

[23] Z. W. Huang, H. Y. Li, M. Preuss, M. Karadge, P. Bowen, S. Bray, and G. Baxter, "Inertia friction welding dissimilar nickel-based superalloys alloy 720Li to IN718," *Metallurgical and Materials Transactions A,* vol. 38, pp. 1608-1620, 2007.

[24] M. M. Attallah and M. Preuss, "Inertia friction welding (IFW) for aerospace applications," in *Welding and Joining of Aerospace Materials*, M. C. Chaturvedi, Ed., ed: Woodhead Publishing, 2012, pp. 25-74.

[25] M. Preuss, P. J. Withers, and G. J. Baxter, "A comparison of inertia friction welds in three nickel base superalloys," *Materials Science and Engineering A,* vol. 437, pp. 38-45, 2006.

[26] M. Bußmann and E. Bayer, "Market-oriented blisk manufacturing: a challenge for production engineering," in *The 1st CEAS European Air and Space Conference*, Berlin, Germany, 2007.

[27] P. Rombaut, "Joining of dissimilar materials through rotary friction welding," *Master Thesis, Mechanical Construction and Production, University of Gent,* 2011.

[28] K. Mucic, F. Fuchs, and N. Enzinger, "Linear friction welding of high strength chains," in *Trends in Welding Research 2012: Proceedings of the 9th International Conference*, Chicago, USA, pp. 752-756, 2013.

[29] I. Bhamji, M. Preuss, P. L. Threadgill, and A. C. Addison, "Solid state joining of metals by linear friction welding: a literature review," *Materials Science and Technology,* vol. 27, pp. 2-12, 2011.

[30] S. Alessi, N. Daly, and L. A. Polen, "Linear friction welding apparatus using counter load actuators," ed: Google Patents, 2011.

[31] A. Chamanfar, M. Jahazi, J. Gholipour, P. Wanjara, and S. Yue, "Mechanical property and microstructure of linear friction welded Waspaloy," *Metallurgical and Materials Transactions A,* vol. 42, pp. 729-744, 2011.

[32] S. Bray, "Linear Friction Welding," 2007.

[33] A. Vairis and M. Frost, "High frequency linear friction welding of a titanium alloy," *Wear,* vol. 217, pp. 117-131, 1998.

[34] F. Schröder, R. M. Ward, A. R. Walpole, R. P. Turner, M. M. Attallah, J. C. Gebelin, and R. C. Reed, "Linear friction welding of Ti6Al4V: experiments and modelling," *Materials Science and Technology,* 2014.

[35] C. Mary and M. Jahazi, "Linear friction welding of IN-718 process optimization and microstructure evolution," *Advanced Materials Research,* vol. 15, pp. 357-362, 2007.

[36] R. Damodaram, S. G. S. Raman, and K. P. Rao, "Microstructure and mechanical properties of friction welded alloy 718," *Materials Science and Engineering A,* vol. 560, pp. 781-786, 2013.

[37] A. Vairis, "Superplasticity effects and strain rate dependency in a material joining process," *Journal of Engineering Science and Technology Review,* vol. 1, pp. 28-32, 2008.

[38] R. Turner, J. C. Gebelin, R. M. Ward, and R. C. Reed, "Linear friction welding of Ti-6Al-4V: Modelling and validation," *Acta Materialia,* vol. 59, pp. 3792-3803, 2011.

[39] A. Chamanfar, M. Jahazi, J. Gholipour, P. Wanjara, and S. Yue, "Modeling grain size and strain rate in linear friction welded Waspaloy," *Metallurgical and Materials Transactions A,* vol. 44A, pp. 4230-4238, 2013.

[40] A. Chamanfar, M. Jahazi, J. Gholipour, P. Wanjara, and S. Yue, "Maximizing the integrity of linear friction welded Waspaloy," *Materials Science and Engineering A,* vol. 555, pp. 117-130, 2012.

[41] A. Chamanfar, M. Jahazi, J. Gholipour, P. Wanjara, and S. Yue, "Suppressed liquation and microcracking in linear friction welded WASPALOY," *Materials & Design,* vol. 36, pp. 113-122, 2012.

[42] C. Mary and M. Jahazi, "Multi-scale analysis of IN-718 microstructure evolution during linear friction welding," *Advanced Engineering Materials,* vol. 10, pp. 573-578, 2008.

[43] K. R. Vishwakarma, O. A. Ojo, P. Wanjara, and M. C. Chaturvedi, "Linear friction welding of Allvac 718 plus superalloy," in *Superalloy 718 and Derivatives,* ed. Pittsburgh, USA, 2010, pp. 413-426.

[44] O. T. Ola, O. A. Ojo, P. Wanjara, and M. C. Chaturvedi, "Analysis of microstructural changes induced by linear friction welding in a nickel-base superalloy," *Metallurgical and Materials Transactions A,* vol. 42, pp. 3761-3777, 2011.

[45] M. Y. Amegadzie, "Effect of forging pressure on the microstructure of linear friction welded Inconel 738 superalloy," *Master Thesis, Mechanical and Manufacturing Engineering, University of Manitoba, Winnipeg,* 2012.

[46] O. T. Ola, O. A. Ojo, P. Wanjara, and M. C. Chaturvedi, "A study of linear friction weld microstructure in single crystal CMSX-486 superalloy," *Metallurgical and Materials Transactions A,* vol. 43, pp. 921-933, 2012.

[47] M. Karadge, M. Preuss, P. J. Withers, and S. Bray, "Importance of crystal orientation in linear friction joining of single crystal to polycrystalline nickel-based superalloys," *Materials Science and Engineering A*, vol. 491, pp. 446-453, 2008.

[48] P. G. Frankel, "Residual Stresses in Aerospace Components," *EngD Thesis, Metallurgy and Materials, University of Birmingham*, 2008.

[49] M. Preuss, P. J. Withers, J. W. L. Pang, and G. J. Baxter, "Inertia welding nickel-based superalloy: Part I. Metallurgical characterization," *Metallurgical and Materials Transactions A*, vol. 33, pp. 3215-3225, 2002.

[50] M. Preuss, P. J. Withers, J. W. L. Pang, and G. J. Baxter, "Inertia welding nickel-based superalloy: Part II. Residual stress characterization," *Metallurgical and Materials Transactions A*, vol. 33, pp. 3227-3234, 2002.

[51] R. Damodaram, S. Ganesh Sundara Raman, and K. Prasad Rao, "Effect of post-weld heat treatments on microstructure and mechanical properties of friction welded alloy 718 joints," *Materials & Design*, vol. 53, pp. 954-961, 2014.

[52] O. T. Ola, O. A. Ojo, P. Wanjara, and M. C. Chaturvedi, "Crack-free welding of IN 738 by linear friction welding," *Euro Superalloys 2010*, vol. 278, pp. 446-453, 2011.

[53] F. J. Humphreys, "Characterisation of fine-scale microstructures by electron backscatter diffraction (EBSD)," *Scripta Materialia*, vol. 51, pp. 771-776, 2004.

[54] M. M. Attallah, "Microstructure property development in friction stir welds of aluminim based alloys," *PhD Thesis, Metallurgy and Materials, University of Birmingham*, 2008.

[55] P. J. Withers and H. K. D. H. Bhadeshia, "Overview - residual stress part 2 - nature and origins," *Materials Science and Technology*, vol. 17, pp. 366-375, 2001.

[56] P. J. Withers, "Mapping residual and internal stress in materials by neutron diffraction," *Comptes Rendus Physique*, vol. 8, pp. 806-820, 2007.

[57] K. Sköld and D. L. Price, *Neutron Scattering*. Orlando, Academic Press, 1986.

[58] A. G. Youtsos and C. Ohms, "European standardization activities on residual stress analysis by neutron diffraction," *Applied Physics A-Materials Science & Processing*, vol. 74, pp. 1716-1718, 2002.

[59] Y. S. Sato, S. H. C. Park, M. Michiuchi, and H. Kokawa, "Constitutional liquation during dissimilar friction stir welding of Al and Mg alloys," *Scripta Materialia*, vol. 50, pp. 1233-1236, 2004.

[60] W. B. Lee, Y. M. Yeon, and S. B. Jung, "The joint properties of dissimilar formed Al alloys by friction stir welding according to the fixed location of materials," *Scripta Materialia,* vol. 49, pp. 423-428, 2003.

[61] H. Uzun, C. D. Donne, A. Argagnotto, T. Ghidini, and C. Gambaro, "Friction stir welding of dissimilar Al 6013-T4 To X5CrNi18-10 stainless steel," *Materials & Design,* vol. 26, pp. 41-46, 2005.

[62] "http://www.engineeringarchives.com/les_matsci_schmidslaw.html"

Chapter 4. Materials and Experimental

This chapter describes the details of the materials and experimental methods carried out in the project, including sample preparation, heat treatment, Gleeble simulations, microstructural, hardness and residual stress characterisation.

4.1. Materials

IN718 and IN713LC (provided by Rolls-Royce plc.) were the two materials investigated in this study. They were chosen to be the disc (IN718) and blade (IN713LC) materials for low pressure turbine due to their high fatigue, creep and yield strength, and corrosion resistance at high temperature. The chemical composition is listed in Table 4.1. Their similar alloy elements limit the atomic diffusion at the weld interface to reduce the likelyhood of forming unexpected detrimental phases. The IN718 samples used for LFW were machined from large-scale forgings. A sub-δ solvus heat treatment at 980 ℃ for 1 h was carried out on IN718, followed by aging at 720 ℃ for 8 h and controlled cooling at 50 ℃/min to 620 ℃, held 8 h before air cooling (AC). In order to homogenise the microstructure of IN713LC, the casting bar was given a γ′ solution treatment at 1190 ℃ for 1 h/vacuum followed by furnace cooling. IN713LC used for LFW were extracted with the same orientation within the bar.

Table 4.1. Chemical composition of IN718 and IN713LC (wt.%)

Alloy	Ni	Cr	Al	Mo	Nb	Ti	Fe	C
IN718	52.16	19.0	0.6	3.0	5.3	0.9	19.0	0.04
IN713LC	74.75	12.0	6.0	4.5	2.0	0.7	-	0.05

4.2. Linear Friction Welding

In total, sixteen welds were welded using the MTS Process Development System (MTS-PDS) at Rolls-Royce plc., Derby. A high-speed camera recorded the deformation at the weld interface during the welding process. The process parameters are shown in Table 4.2. These welds can be divided into two groups.

Table 4.2. The welding process parameters of LFWed IN718-713LC

Weldment (number)	Pressure (MPa)	Amplitude (mm)	Frequency (Hz)	Upset (mm)	Oscillation Cycles	Shielding Gas
W1	275	2	45	2.8	Full cycles	No
W2	400	2	45	2.8	Full cycles	No
W3	600	2	45	2.8	Full cycles	No
W4	400	3	45	2.8	Full cycles	No
W5	400	3	60	2.8	Full cycles	No
W6	400	1.5	30	2.8	Full cycles	No
W7	400	1.5	60	2.8	Full cycles	No
W8	400	3	45	2.8	Full cycles	No
W9	400	3	45	1.83	60 cycles	No
W10	400	3	45	1	48 cycles	No
W11	400	3	45	0.43	32 cycles	No
W12	400	3	45	0.11	22 cycles	No
W13	400	2	45	0.37	32 cycles	No
W14	400	2	45	0.05	22 cycles	No
W15	400	3	45	2.1	60 cycles	Argon
W16	400	3	45	0.34	32 cycles	Argon

The first group includes W1 to W7, which was designed to study the influence of the process parameters (welding pressure, amplitude and frequency) on the microstructure-property of the welds. W1 to W3 used a constant nominal amplitude (2 mm) and frequency (45 Hz) with

three different pressures (275 MPa, 400 MPa, 600 MPa) to study the effect of pressure. W4 and W5, also W6 and W7, were two pairs of welds used to investigate the impact of frequency. W4 and W2, W7 and W5, were used to investigate the influence of amplitude. Other parameters were kept the same, such as axial upset (2.8 mm), oscillation ramp-down time (0.001 s), forging force and holding time (10 s).

The second group (W8 to W16) aimed at investigating the Al oxides formation mechanisms in LFWed IN718-IN713LC. W8 was used to verify the repeatability of Al oxides formation under this particular parameter (400 MPa, 3 mm, 45 Hz). W9 to W12 were welded at high amplitude (3 mm), with different cycles before reaching 2.8 mm upset, in order to catch the oxide formation period. W13 and W14 were used for comparing with W11 and W12, to study the effect of amplitude on oxide formation. W15 and W16 were welded in an argon protection environment to identify the influence of argon shielding on the oxide formation.

There are some other parameters that affect weld quality, such as component geometry, surface condition, stub height, component clamping force. These parameters were consistent in all welds to eliminate their influences. The geometry of weld blocks is illustrated in Fig. 4.1. IN718 and IN713LC blocks were 29.0×13.0×10.0 mm^3 and 36.4×13.0×10.0 mm^3, respectively. The weld interface was 6.0×10.0 mm^2, which was the surface of stub. During welding, the interface material became soft and got ejected as the form of flash. The geometry of the weld is displayed in Fig. 4.2. The *z*-axis of the IN713LC was the same as the casting direction.

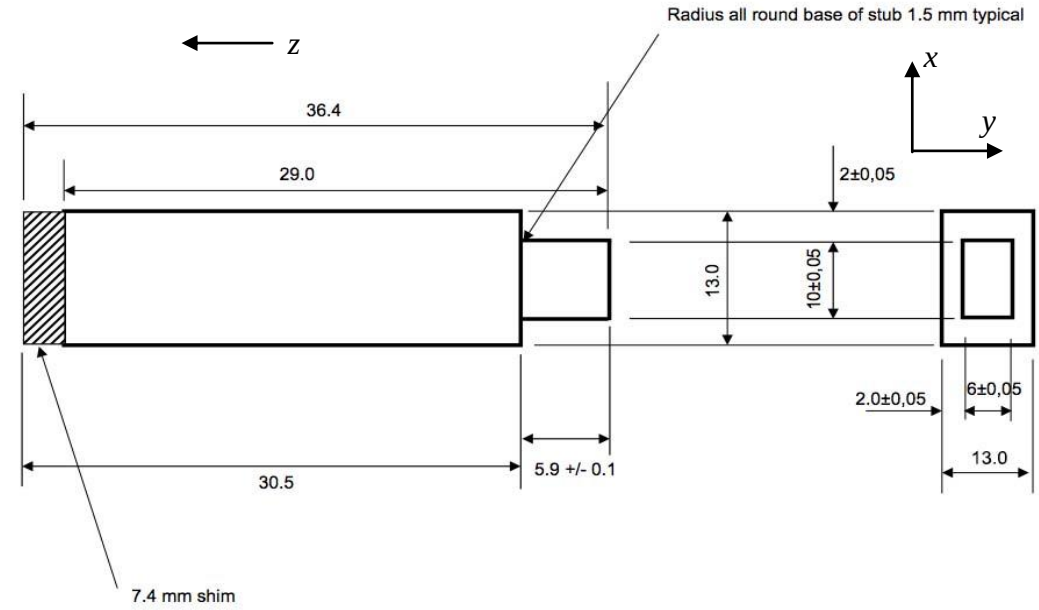

(a)

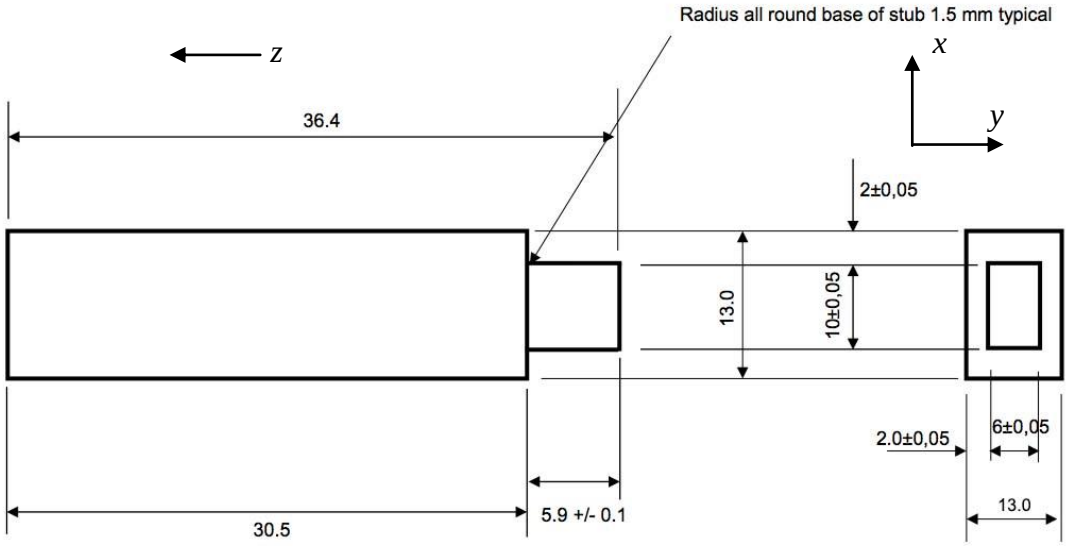

(b)

Fig. 4.1. The weld geometry of (a) IN718 and (b) IN713LC blocks with the stub

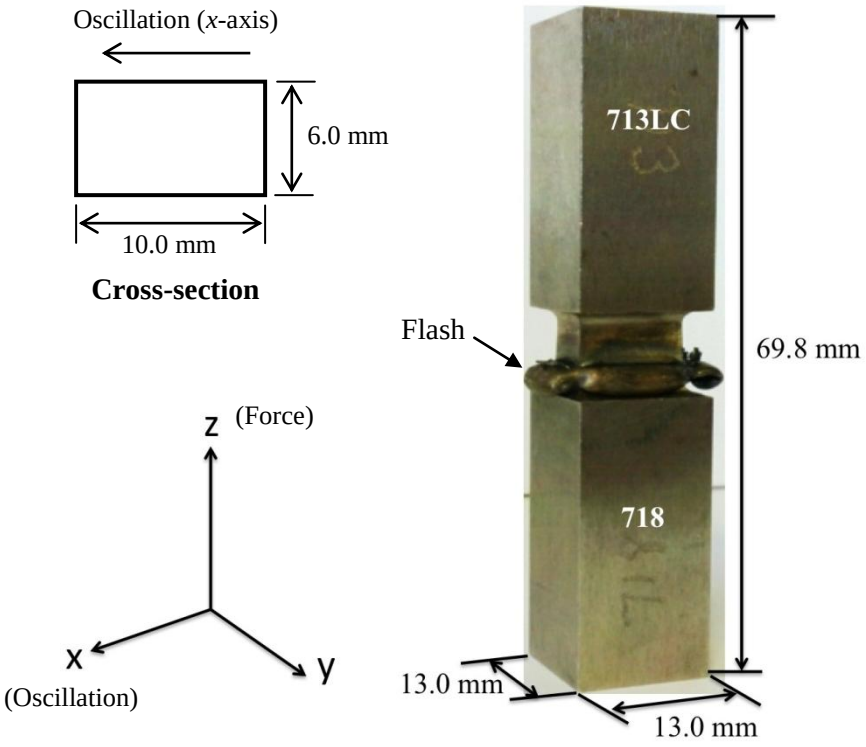

Fig. 4.2. The geometry of the IN718-IN713LC LFWs

4.3. Sample Preparation

The sample preparation can be divided into four steps: cutting, mounting, grinding & polishing, and etching. The detailed information is described below:

(1) Cutting

The welds were cut by silicon carbide cutting wheel on a Struers Accutom-5 cutting machine at a 3000 rpm rotation speed and 0.015 mm/s feed rate. The surface of interest is the cross-section of these pieces, which contains the whole weld area. The welds were cut at around 15 mm from the weld interface in each side (*x*-*y* plane, see Fig. 4.2), and halved the section along *x*-*z* plane.

(2) Mounting

The sectioned specimens were then mounted in bakelite using an OPAL-400 mounting machine, with 8 minutes heating at 170 ℃, followed by water cooling.

(3) Grinding & Polishing

The mounted samples were ground by a grinding disc MD Piano 120 under 10 N with running water. After grinding, samples were polished under 10 N using polishing discs MD Plan, MD Dac, MD Nap, combined with 9 μm, 6-3 μm, 1 μm diamond polishing suspension, respectively. Final polishing was done using a 0.05 μm alumina polishing suspension (OP-A) on a polishing disc MD Chem. In each step, samples were ground and polished for 2-3 minutes and cleaned by washing between two steps in order to obtain a fine polished sample with a mirror-like surface. For EBSD samples, the final polishing was under 5 N for 10 minutes to remove the deformed layer or the surface stress created during grinding/polishing. Acetone and a hot air dryer were used for final cleaning.

(4) Etching

In this study, Kalling's chemical etching and phosphoric electrolytic etching were employed for different purposes. In chemical etching, samples were immersed in Kalling's reagent (100 ml HCl, 100 ml ethanol, 5 g $CuCl_2$) for 3 seconds to etch away all the precipitated particles (γ', γ'', δ and carbides) on the surface of the γ matrix, clearly revealing the grain structure under the optical microscope. For SEM/EDX analyses, electrolytic etching was performed in fresh 10% phosphoric acid (10% phosphoric acid, 90% water by volume fraction) with a steel cathode for 3 seconds at 3.5 V, in order to reveal particles by etching away the γ matrix.

4.4. Post-Weld Heat Treatment

The post-weld heat treatment (PWHT) was performed in a laboratory furnace (in air), followed by water quenching. Three PWHT methods were applied on W2_400-2-45. The schematic diagram of three PWHTs was shown in Fig. 4.3.

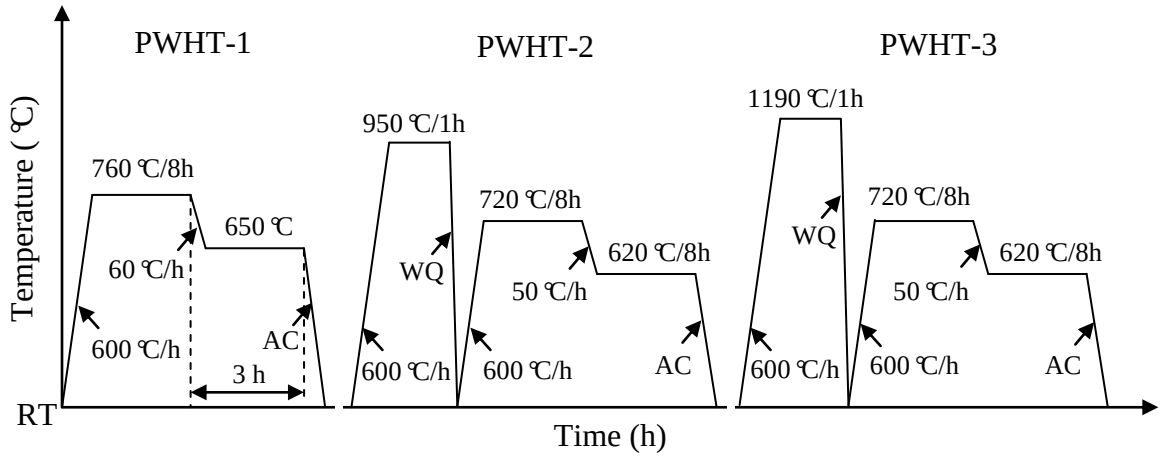

RT: room temperature, AC: air cooling, WQ: water quenching

Fig. 4.3. Schematic diagram of three PWHT procedures

PWHT-1 procedure (two-stage IN718 aging heat treatment)

Sample was heated to 760 ℃ at a rate of 600 ℃/h and held 8 h, followed by cooling to 650 ℃ at a rate of 60 ℃/h, and then held for 3 h including the cooling time, and then air cooled [1].

PWHT-2 procedure (IN718 solution treatment followed by a two-stage IN718 aging treatment)

Sample was heated to 950 ℃ at a rate of 600 ℃/h and held 1 h, followed by WQ. Subsequently, the sample was aged at 720 ℃ for 8 h (heating rate of 600 ℃/h), and cooled to 620 ℃ at a rate of 50 ℃/h, held 8 h, and then air cooled [2].

PWHT-3 procedure (IN713LC solution heat treatment followed by 2-stage IN718 aging treatment)

Sample was solution treated at 1190 ℃ for 1 h (heating rate of 600 ℃/h), followed by WQ. Subsequently, the sample was aged at 720 ℃ for 8 h (heating rate of 600 ℃/h), and then cooled at 50 ℃/h to 620 ℃, held 8 h, and then air cooled [2, 3].

4.5. Differential Scanning Calorimetry

In this work, a Netzsch 404C Pegasus heat-flux differential scanning calorimeter, equipped with Proteus-NETZSCH software, was used to determine the phase transformations in IN718 and IN713LC (solvus of γ′/γ″, δ, carbides, solidus and liquidus). A schematic diagram of the heat-flux differential scanning calorimetry (DSC) cell is shown in Fig. 4.4. Two fully recrystallised Al_2O_3 crucibles are placed on a constantan heat-flux plate with a layer of chromel disc in between. The chromel-constantan thermocouples are connected to the chromel disc to measure the temperature difference (ΔT) of interest. Before testing, a cubic sample of IN718 or IN713LC (2 ×2 ×2 mm^3, ~70 mg) was put into the sample crucible and the reference crucible was left empty using a purging atmosphere of argon gas, the preset heating program was applied, as shown in Fig. 4.5. Samples were heated to 1400 ℃ and held 10 minutes before cooling. The heating and cooling rates were 20 ℃/min.

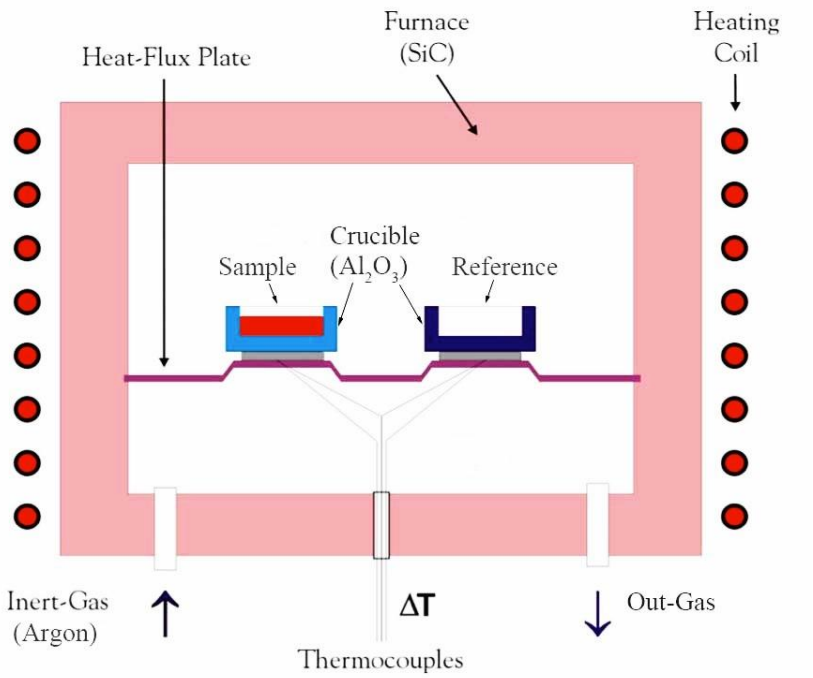

Fig. 4.4. Schematic diagram of heat-flux DSC 404C Pagasus [4]

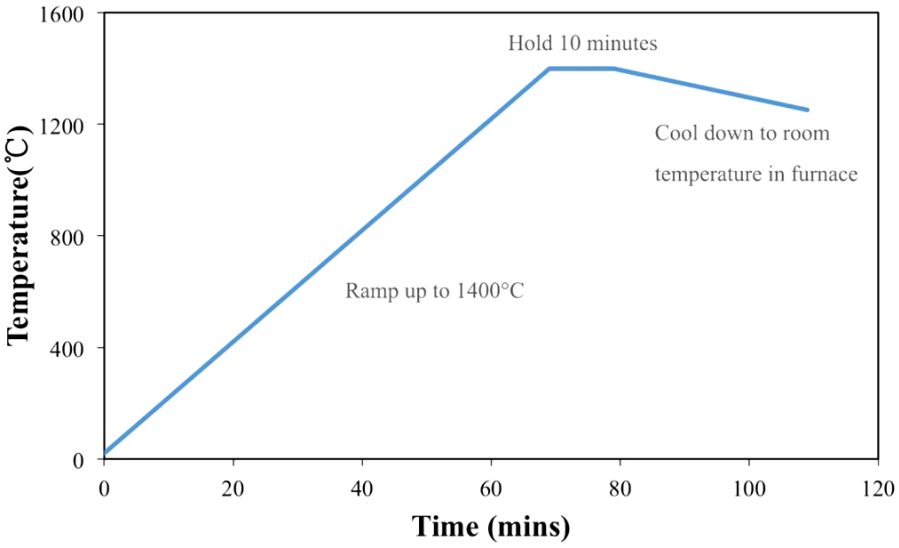

Fig. 4.5. Procedure of DSC thermal cycle for IN718 and IN713LC

4.6. Furnace Heat Treatment

A lab furnace was used to study the dissolution of γ′ in IN713LC and δ in IN718 at equilibrium heating condition. Both alloys were heat treated in as-received conditions. Samples were 6×6×6 mm^3 cube. Table 4.3 lists the heat treatment data performed. IN718 was heated to 970-1070 °C at a rate of 10 ℃/min, held 5 minutes and then water quenched. IN713LC was heated to 920-1190 °C at a rate of 10 ℃/min, held 1 h at peak temperature before WQ.

Table 4.3. Heat treatment data for as-received IN713LC and IN718

Alloy	Temperature (°C)	Holding Time (min)
IN718	970, 1010, 1035, 1060, 1070	5
IN713LC	920, 1020, 1130, 1170, 1180, 1190	60

4.7. Gleeble Thermo-Mechanical Simulation

The Gleeble 3500 (Dynamic Systems Inc.) is an advanced physical simulation and thermo-mechanical testing machine, which has been widely used for simulating the microstructural development in alloys during thermo-mechanical processing [5-8]. The Gleeble has a fully integrated digital control system to control the thermal and mechanical testing system, which provides a user-friendly interface to run programs and analyse data using computer software. The direct resistance heating systems plus the high thermal conductivity sample-holding grips can heat specimens at rates up to 10,000 °C/s, and cooling rate can achieve higher than 10,000 °C/s at the specimen surface using the quench system. The hydraulic servo system exerts up to 10 tons of static force in tension or compression with various control modes

(stroke displacement, various extensometers, force, engineering stress, engineering strain, true stress, and true strain).

In this work, a Gleeble 3500 was used to simulate the precipitates dissolution and hardness development in IN718 and IN713LC during rapid thermal cycling, in order to study the effect of the heating rate on microstructural development in LFWed IN718-IN713LC welds.

The IN718 and IN713LC bars were shaped to Φ 12 mm × L 12 mm cylinders by electric discharge wire cutting machine (EDM), followed by grinding off the recast layer. 0.25 mm K-type thermocouples were spot welded to the middle surface of the specimen and were connected to the thermal system to control and measure the temperature during testing (Fig. 4.6.a). After that, the specimen was clamped by four copper grips under 1 kN compressive force to improve the heat transfer (Fig. 4.6.b).

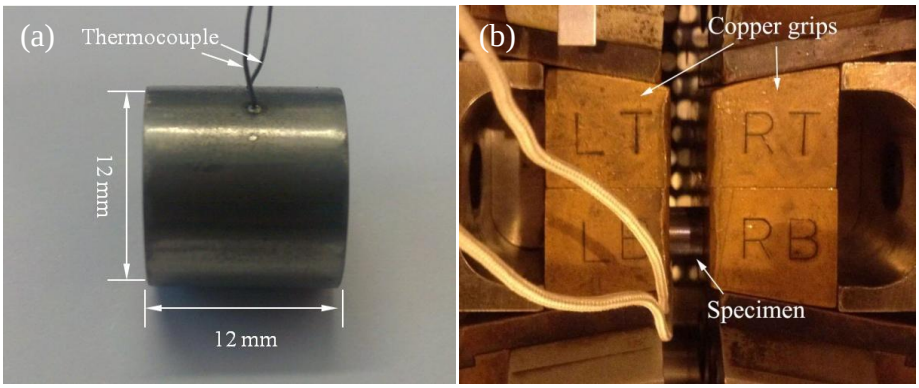

Fig. 4.6. Set-up of the GTMS: (a) the geometry of cylindrical specimen, (b) four copper grips clamping specimen before operating in the compression mode

A series of thermal cycles were employed as listed in Table 4.4. IN718 specimens were cycled at a heating rate 1-1000 °C/s to a maximum temperature between 700-1230 °C. IN713LC specimens were heated up to 900-1280 °C at 1-1000 °C/s. When the peak temperature was reached the heat was shut off which was followed by air cooling.

Table 4.4. The thermal cycles of IN718 and IN713LC performed in the GTMS

Alloy	Peak Temperature (°C)	Heating Rate (°C/s)
IN718	700, 750, 775, 780, 790, 820, 910, 1020, 1075, 1080, 1090, 1095, 1105, 1110, 1195, 1200, 1215, 1230	1, 300, 700
IN713LC	900, 1000, 1100, 1160, 1190, 1200, 1205, 1210, 1220, 1230, 1235, 1240, 1250, 1260, 1270, 1280	1, 10, 25, 50, 100, 300, 500, 1000

4.8. Microstructural Characterisation

4.8.1. Optical Microscopy

A Zeiss Akioskop-2 optical microscope equipped with Axio Vision image analysis software, was used to investigate the microstructure of the base metal and welds. This microscope covers the magnification range from 50 to 1000 in both manual and motorised modes. The software can automatically map a large area by adding separate images together. Recording and assessing the microstructure of welds are thus straightforward.

4.8.2. Scanning Electron Microscopy

Two SEMs were employed to investigate the microstructure of samples: the field emission gun scanning electron microscope (FEG-SEM) JEOL-7000 and the Philips XL-30 (using LaB_6 filament), both equipped with Oxford INCA energy dispersive X-ray (EDX) for chemical composition analysis. The operating voltage was 20 kV for imaging and EDX.

4.8.3. Transmission Electron Microscopy

A TECNAI F20 transmission electron microscope (TEM) (operated at 200 kV) was used to study the chemical composition of the small phases. IN718 and IN713LC base metals were cut to 300 μm thick slices by EDM, punched to 3 mm discs, and then ground to around 100 μm thickness, followed by using a Tenupol twinjet electro-polishing machine to create an electron transparent sample at a voltage of 20 V in an electrolyte of 20% perchloric acid and 80% methanol at -35 ℃ (a thin area in the middle of discs for characterisation.)

4.8.4. Electron Backscattered Diffraction

In this study, microstructural investigations were carried out on the welds using a XL-30 SEM, with equipped Channel-5 electron backscattered diffraction (EBSD) analysis system, with an accelerating voltage of 20 kV and working distance of 15 mm. These investigations provided information on the grain size, grain boundary, recrystallisation and microtexture, in order to understand the deformation regimes, microstructural and microhardness development in the LFWs.

4.8.5. Stereological Methods

Stereological methods were used to quantify the grain size and particle size and fraction [9].

If the average grain area is *A*, the equivalent circle diameter is defined as:

$$D = (4A/\pi)^{1/2} \tag{4.1}$$

If the average particle area is *S*, the equivalent circle radius is,

Cubic particle: $$r = (3/4\pi)^{1/3} \cdot S^{1/2} \quad (4.2)$$

Spherical particle: $$r = (S/\pi)^{1/2} \quad (4.3)$$

and if the particle surface fraction is f_s, the volume fraction is equal to:

$$f_v = {f_s}^{3/2} \quad (4.4)$$

4.9. Microhardness

Microhardness was performed on a Struers DuraScan-70 Vickers hardness tester loading 200 g for 10 seconds on each test point. This machine can automatically calculate the hardness value by the equation:

$$HV = 1.854F/d^2 \quad (4.5)$$

where F is the loading force (kg), and d is the average of indentation diagonals (mm).

Two different paths were employed for different purposes. The first path aimed to measure the microhardness distribution of the whole cross-section of the welds. Fig. 4.7 illustrates the mapping indentations of this path. C is the middle point of the weld line AB. The AB is equally divided into 11 parts, with interval 0.95 mm, and each part uses the same indentations as that on AF. On AD (1.8 mm) and DF (2.7 mm), the indentation interval is 0.1 mm and 0.3 mm, respectively. The IN713LC has the same indentation locations. In total, 605 points were measured in an area of 9×9.5 mm^2 for each sample, which provided precise hardness contour mapping. The second path was simplified to precisely measure the microhardness values for quantitative analyses. Measurement was focused on the centre of the welds. Smaller intervals (0.03 mm - 0.3 mm) were used and all the values were averaged over 3 measurements.

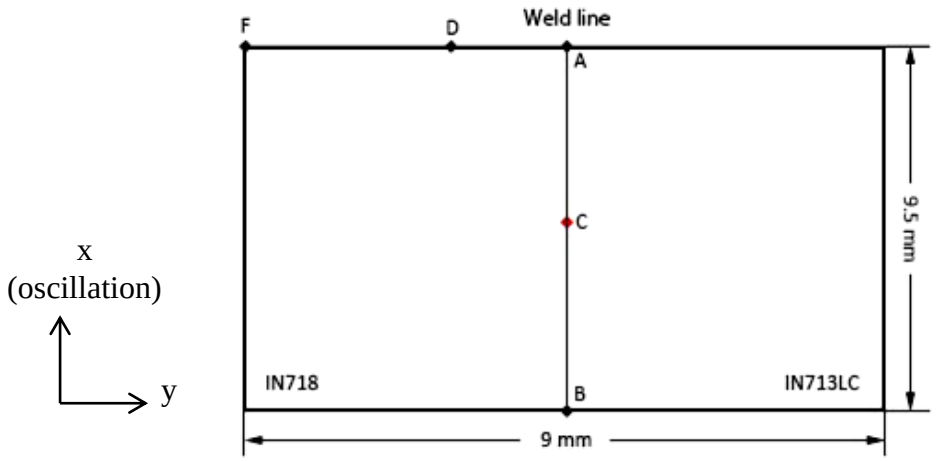

Fig. 4.7. Schematic diagram of indentations for hardness contour mapping of as-welded IN718-IN713LC

4.10. Residual Stresses

Residual stress characterisation was carried out using the Strain Analyser for Large and Small scale engineering Application (SALSA) in the Institute of Laue-Langevin (ILL) in Grenoble, France. SALSA was equipped with a hexapod-mounted sample stage, which provided high-precision manipulation for heavy samples (positioning error is less than 50 μm) [10]. The measurement was performed along the three principal axes, (*x, y* and *z* directions), as shown in Fig. 4.2. Figure 4.8 shows the experimental set-up for in-situ neutron diffraction studies of residual stresses. The incident beam was diffracted by the sample before being collected by the detector. The corresponding *x, y* and *z* strains were calculated by:

$$\varepsilon = (d - d_0)/d_0 \tag{4.6}$$

where d, d_0 correspond to deformed lattice spacing and strain-free lattice spacing. The d_0 values were taken from far-field measurements. The measured positions are far from the weld line, which can be assumed as strain-free areas.

The residual stresses were calculated from the strains using [11]:

$$\sigma_x = \frac{E}{(1+\nu)(1-2\nu)}\left[(1-\nu)\varepsilon_x + \nu\left(\varepsilon_y + \varepsilon_z\right)\right] \quad (4.7.a)$$

$$\sigma_y = \frac{E}{(1+\nu)(1-2\nu)}\left[(1-\nu)\varepsilon_y + \nu(\varepsilon_x + \varepsilon_z)\right] \quad (4.7.b)$$

$$\sigma_z = \frac{E}{(1+\nu)(1-2\nu)}\left[(1-\nu)\varepsilon_z + \nu\left(\varepsilon_x + \varepsilon_y\right)\right] \quad (4.7.c)$$

where E is Young's modulus of material, and υ is the Poisson's ratio . The Young's modulus and Poisson's ratio of IN718 and IN713LC are listed in Table 4.5.

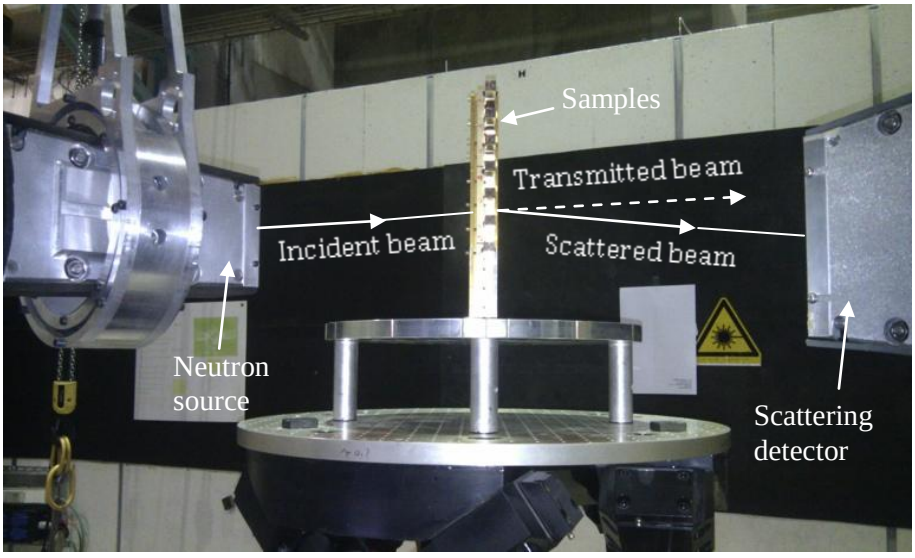

(a)

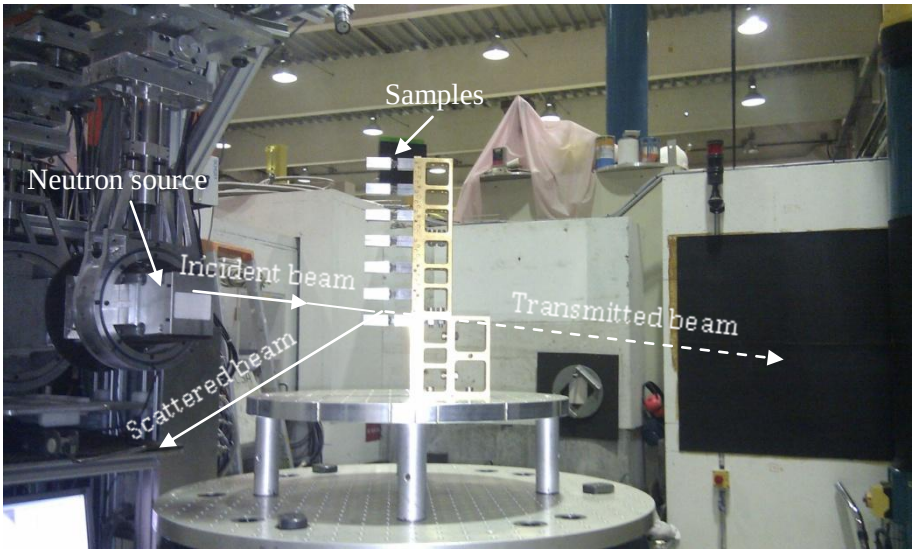

(b)

Fig. 4.8. Set-up of the neutron diffraction residual stress measurement on SALSA

Table 4.5. The Young's modulus and Poisson's ratio of the (311) plane of IN718 [12] and IN713LC [13]

Material	Young's modulus (E)	Poisson's ratio (v)
IN718	208 GPa	0.29
IN713LC	200 GPa	0.30

A wavelength of 1.648 Å was used to study the (311) plane, to obtain the most suitable reflections for strain measurements [10]. The strain-free lattice spacing d_0 values are from far field measurements. The gauge volume of beam is $2 \times 2 \times 2$ mm^3. In the process, 15 detection points (7 points in IN718, 7 points in IN713LC, 1 point at the weld line) placed on a single central line trace was measured in the three directions, which gave a total of 45 points per sample and 270 points for 6 welds (W6 did not finish due to time limitation). The counting time was 10 minutes for each point. Because the coarse grain microstructure of cast IN713LC could not provide sufficient scattered grains in gauge volume, the diffracted signal was poor in IN713LC. In order to improve the diffracted signal, the samples were rocked ± 2 mm perpendicular to the scattering vector while detecting IN713LC. The measured 2θ datum were analysed by LAMP software to convert to strain and residual stresses datum [14].

4.11. Data Analysis and Errors

The main error with indentation hardness testing comes from the strain hardening effect of the process. Generally, smaller indentation tends to minimise the error induced by strain hardening. A loading force was kept at 200 g to create small indentations with diagonals in

the range of 26-38 μm and also to avoid the error caused by the variation of loading force. The standard deviation of Vickers hardness was calculated from three measurements.

For EBSD grain size measurement, the step size was 0.3-1 μm, and each grain was identified from a minimum of 8 detected points. The errors came from the size with step size chosen, the poorly indexed rate and the quality of data. The standard deviation of grain size was presented in data analysis.

The main source of error in precipitate fraction measurement was from determining the threshold values of the precipitate boundary while analysing data using Image-J. The fraction values were averaged by three measurements, and the standard deviation was presented in results.

For residual stress measurements, The d_0 values were taken from far-field measurements (strain-free) which could make the stress values inaccurate. However, the d_0 values in the weld zone might change with variations in composition, thus the residual stress can be overestimated by more than a factor of two (as discussed in Section 3.3.3).

The main source of error with Gleeble tests is the temperature measured by the K-type thermocouple, which typical has an error of 2-5 ℃. The error in temperature would induce an error in the measured precipitate volume fraction.

4.12. References

[1] R. E. Schafrik, D. D. Ward, and J. R. Groh, "Application of alloy 718 in GE aircraft engines: past, present and next five years," in *Superalloys 718, 625, 706 and Various Derivates*, Pittsburgh, USA, pp. 1-11, 2001.

[2] R. A. Mayor, "Selected mechanical properties of Inconel 718 and 706 weldments," *American Welding Society*, pp. 269-275, 1976.

[3] S.-H. Chang, "Effects of γ′ precipitation on the structure and properties of 713LC superalloy via HIP treatment," *Materials Transactions*, vol. 53, pp. 446-451, 2012.

[4] R. Nicula, "Introduction to Differential Scanning Calorimetry," ed. Rostock University: Physics Department, 2002.

[5] S. S. Babu, J. Livingston, and J. C. Lippold, "Physical simulation of deformation and microstructure evolution during friction stir processing of Ti-6Al-4V alloy," *Metallurgical and Materials Transactions A*, vol. 44, pp. 3577-3591, 2013.

[6] M. M. Attallah, M. Strangwood, and C. L. Davis, "Influence of the heating rate on the initiation of primary recrystallization in a deformed Al–Mg alloy," *Scripta Materialia*, vol. 63, pp. 371-374, 2010.

[7] G. A. Knorovsky, M. J. Cieslak, T. J. Headley, A. D. Romig, and W. F. Hammetter, "Inconel 718: a solidification diagram," *Metallurgical Transactions A*, vol. 20, pp. 2149-2158, 1989.

[8] S. G. R. Brown, J. D. James, and J. A. Spittle, "A 3D numerical model of the temperature-time characteristics of specimens tested on a Gleeble thermomechanical simulator," *Modelling and Simulation in Materials Science and Engineering*, vol. 5, pp. 539-548, 1997.

[9] E. E. Underwood, *Quantitative Stereology*. Reading, USA, Addison-Wesley Publishing, 1970.

[10] T. Pirling, G. Bruno, and P. J. Withers, "SALSA - a new instrument for strain imaging in engineering materials and components," *Materials Science and Engineering A*, vol. 437, pp. 139-144, 2006.

[11] P. J. Withers, "Mapping residual and internal stress in materials by neutron diffraction," *Comptes Rendus Physique*, vol. 8, pp. 806-820, 2007.

[12] M. Preuss, P. J. Withers, and G. J. Baxter, "A comparison of inertia friction welds in three nickel base superalloys," *Materials Science and Engineering A,* vol. 437, pp. 38-45, 2006.

[13] W. V. Rooyen and A. Walpole, "Assessing the metallurgical effects associated with the linear friction welding of IN713LC to IN718," Rolls-Royce plc., UK, MTL50577, 2010.

[14] "http://www.ill.eu/instruments-support/computing-for-science/cs-software/all-software/lamp/"

Chapter 5. Microstructure-Property Development of Linear Friction Welded IN718-IN713LC

The severe thermo-mechanical deformation that occurs during LFW can result in complex microstructural development, and thus influences the mechanical properties. This chapter focuses on the effect of thermo-mechanical deformation associated with different LFW process parameters on the microstructure-property development of LFWed IN718-IN713LC, with respect to the microstructure, microtexture, microhardness, and residual stress development. Microstructural characterisation includes the investigation of the grain and precipitate structures, involving grain size, grain boundary angle, sizes and volume fraction of particles. Microhardness testing was used to correlate the hardness development after LFW with the microstructure. Residual stress characterisation addressed the effect of LFW process parameters on the residual stress development. Further analyses were carried out on the chemical composition, microtexture analysis, formation mechanism of weld interface defects (Al oxide), and prediction of the strain rate during LFW.

5.1. Base Metal Characterisation

It is important to investigate the base metal microstructure by investigating the grain, precipitates, structures, and hardness. In this study, a combination of OM, SEM, EDX and EBSD techniques were used to assess the base metal microstructure, to clearly identify later the microstructural changes caused by the process.

5.1.1. Alloy Chemical Composition

The chemical composition of IN718 and IN713LC was analysed using SEM/EDX. And the data was the average of 10 measurements (Tables 5.1 and 5.2). Current results are similar to the Rolls-Royce plc. provided data. The SEM/EDX data was used in the development of precipitate dissolution models in Chapter 7.

Table 5. 1. Chemical composition of IN718

Alloy	Ni	Cr	Al	Mo	Nb	Ti	Fe	C
Rolls-Royce plc. (wt.%)	52.16	19.0	0.6	3.0	5.3	0.9	19.0	0.04
Rolls-Royce plc. (at.%)	51.4	21.2	1.3	1.8	3.3	1.1	19.7	0.2
Current work (wt.%)	51.9	18.8	0.6	3.2	5.7	0.9	18.9	-
Current work (at.%)	51.4	21.0	1.3	1.9	3.6	1.1	19.7	-

Table 5. 2. Chemical composition of IN713LC

Alloy	Ni	Cr	Al	Mo	Nb	Ti	C
Rolls-Royce plc. (wt.%)	74.75	12.0	6.0	4.5	2.0	0.7	0.05
Rolls-Royce plc. (at.%)	70.17	12.7	12.3	2.6	1.2	0.8	0.23
Current work (wt.%)	74.3	12.2	6.0	4.5	2.4	0.6	-
Current work (at.%)	70	13	12.3	2.6	1.4	0.7	-

5.1.2. Grain Structure and Texture

5.1.2.a. IN718 Base Metal

EBSD mapping shows an equiaxed grain structure, with frequently observed annealing twins in the IN718 matrix (Fig. 5.1). The grain boundaries can be classified into: low angle grain boundaries (LAGBs, $3° <$ misorientation $< 5°$), moderately misoriented grain boundaries

(MMGBs, 5° ≤ misorientation < 15°), and high angle grain boundaries (HAGBs, misorientation ≥ 15°). Any misorientation less than 3° is typically ignored due to the spatial resolution of the EBSD system [1].

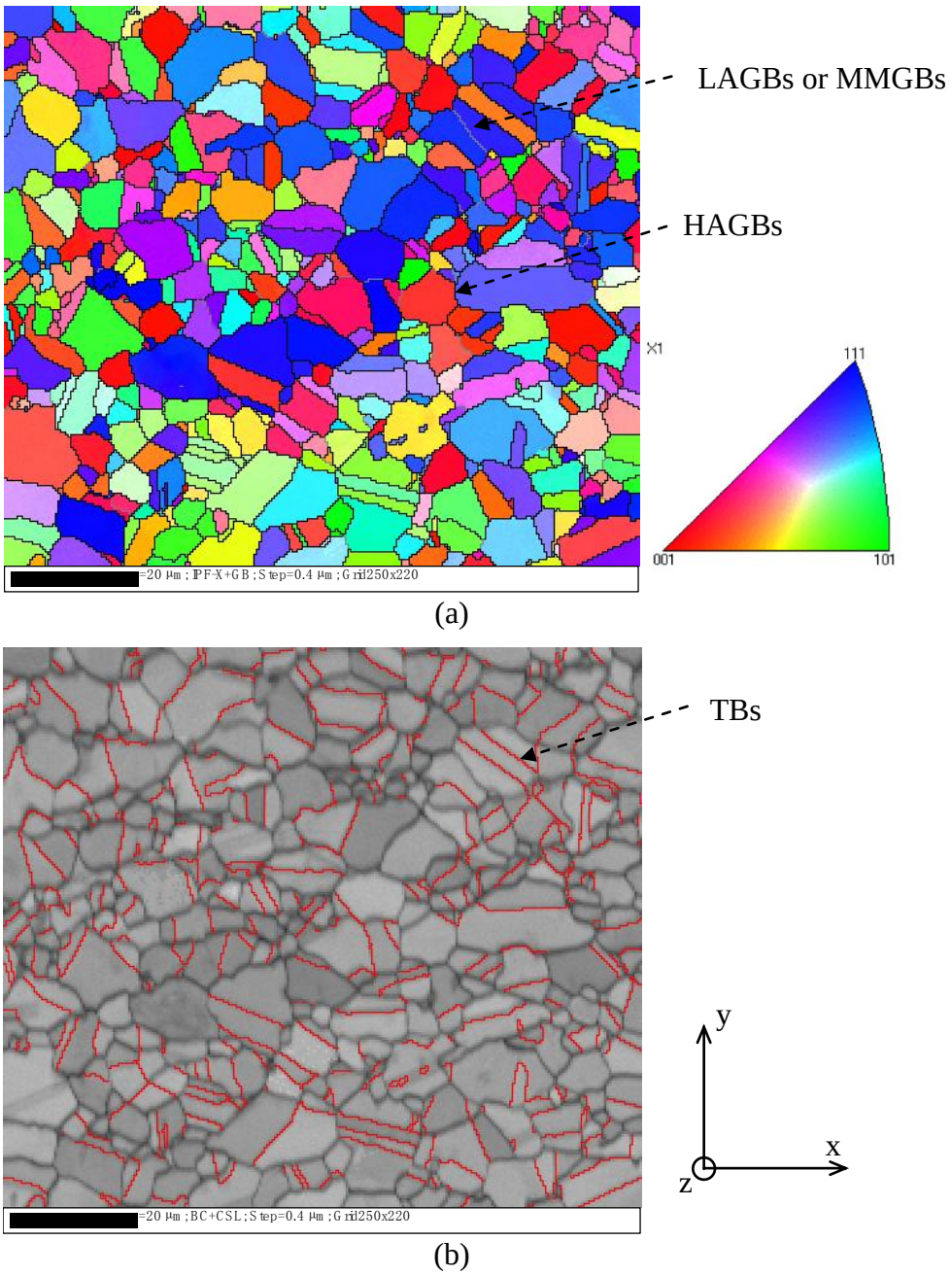

Fig. 5.1. EBSD maps for the forged IN718 showing (a) equiaxed grains by IPF-x map coupled with grain boundary (GB) map, in which grey lines represent both LAGBs and MMGBs, black lines represent HAGBs, and (b) band contrast (BC) image coupled with twin boundaries (TBs, highlighted in red line)

The pole figures reveal a general random texture of IN718 (Fig. 5.2). The mean grain size is about 7.5 µm in equivalent diameter.

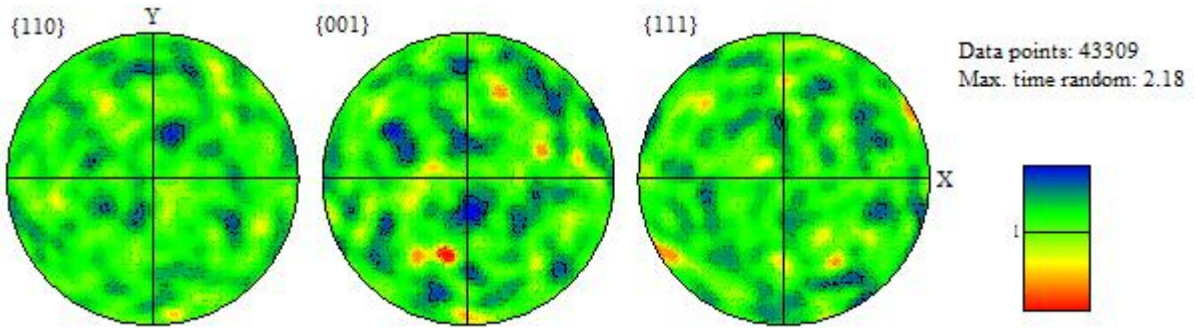

Fig. 5.2. Pole figures showing the random texture of forged IN718

Figure 5.3 illustrates the grain boundary misorientation distribution in IN718. The misorientation angles are in the range of 3-62 °, and almost all of them are HAGBs in which twin boundaries (misorientation = 60 °) account for 36.3%. All of these data indicate a conventional grain structure of forged IN718, as discussed in Fig. 3.23(a) [2].

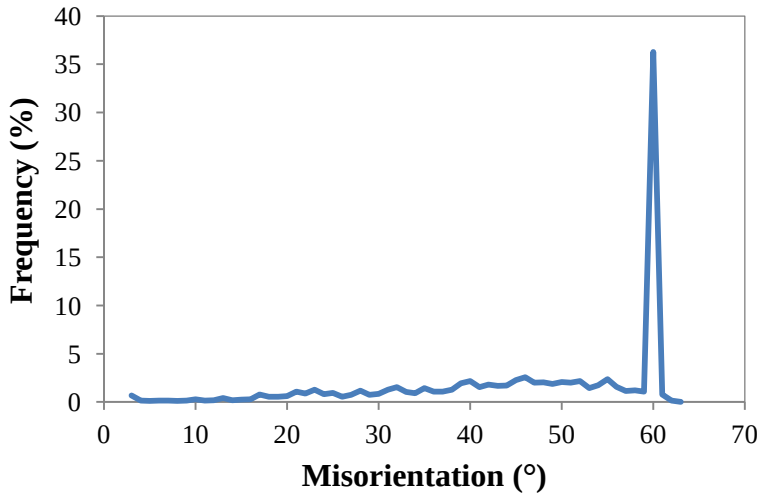

Fig. 5.3. Grain boundary misorientation distribution of forged IN718

5.1.2.b. IN713LC Base Metal

IN713LC consists of coarse columnar grains, with a dendritic structure (Fig 5.4). The bright particles at the grain boundaries were identified as NbC.

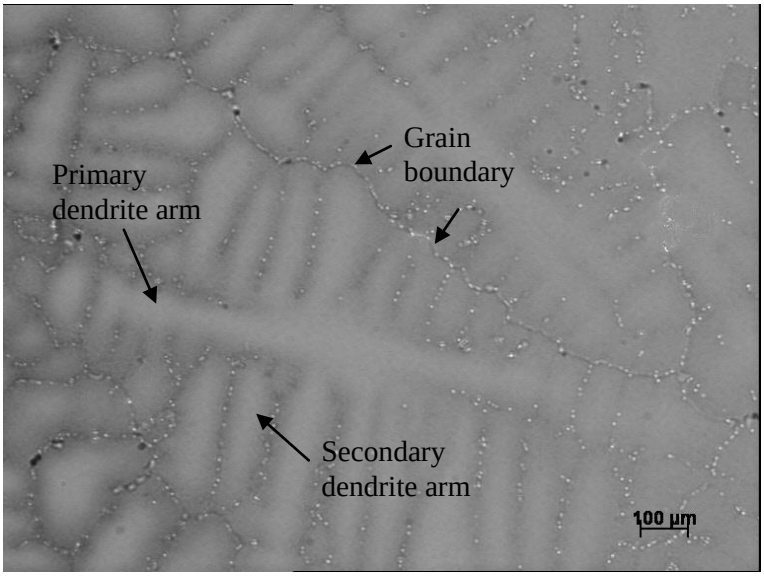

Fig. 5.4. Optical micrograph for IN713LC showing the coarse cast grain structure with dendrites

Figure 5.5 shows an EBSD inverse pole figure (IPF) map in the *x*-direction, coupled with grain boundary (GB) map showing the grain structure of cast IN713LC. It shows columnar crystal structure with a mean grain length ~1 mm and width ~0.3 mm. The pole figures indicate a {001}<100> texture in IN713LC (Fig. 5.6), which is expected since <100> is the preferred growth direction for FCC structures during casting. As the turbine blades are required to withstand enormous centrifugal loads at elevated temperature, the coarse grain of IN713LC can enhance the creep resistance by eliminating or reducing the number of grain boundaries [3].

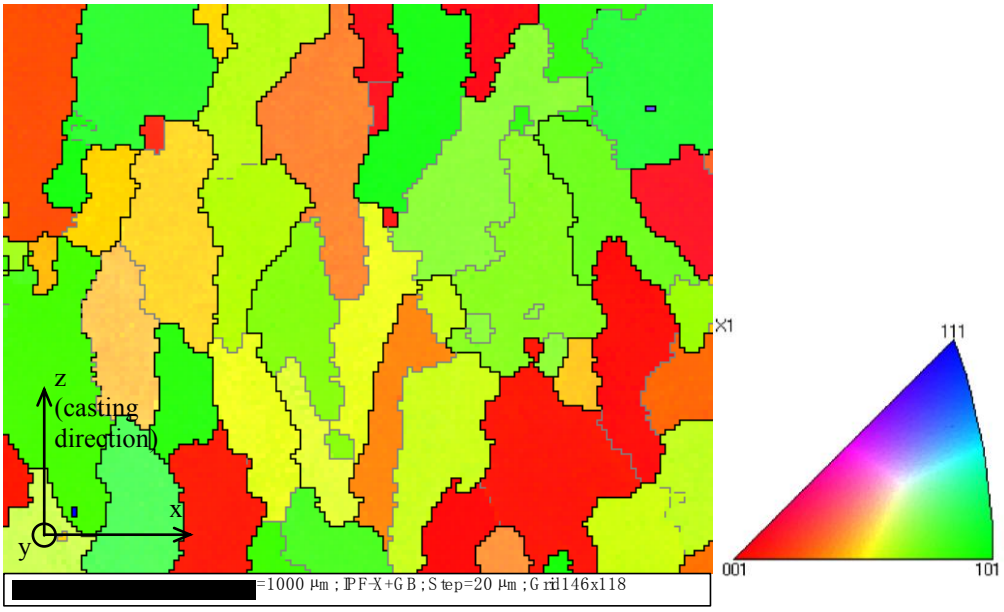

Fig. 5.5. EBSD (IPF-x + GB) map showing the grain structure of cast IN713LC, in which LAGBs and MMBs are indicated by grey lines and HAGBs are indicated by black lines

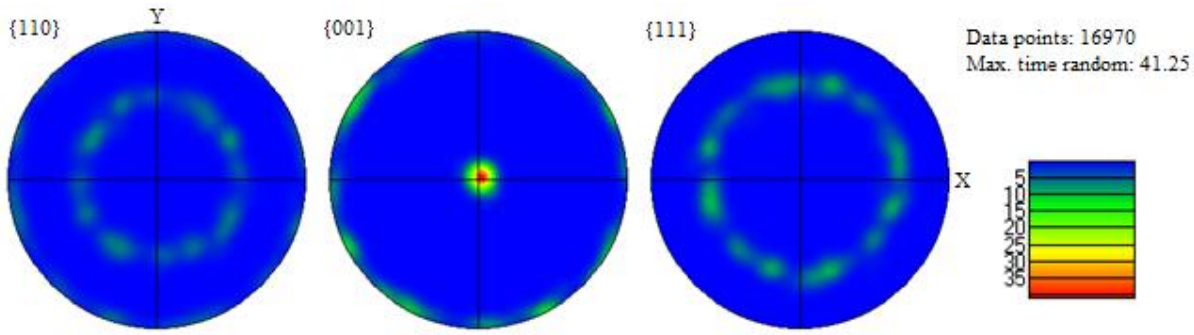

Fig. 5.6. Pole figures showing {001}<100> texture of cast IN713LC

The grain boundary misorientations are randomly distributed in the range of 3-46 °, as can be seen from Fig. 5.7. All of these results indicate that IN713LC possesses a traditional cast grain structure. During LFW, the IN713LC was aligned such that the <001> direction was perpendicular to the friction (oscillation) direction.

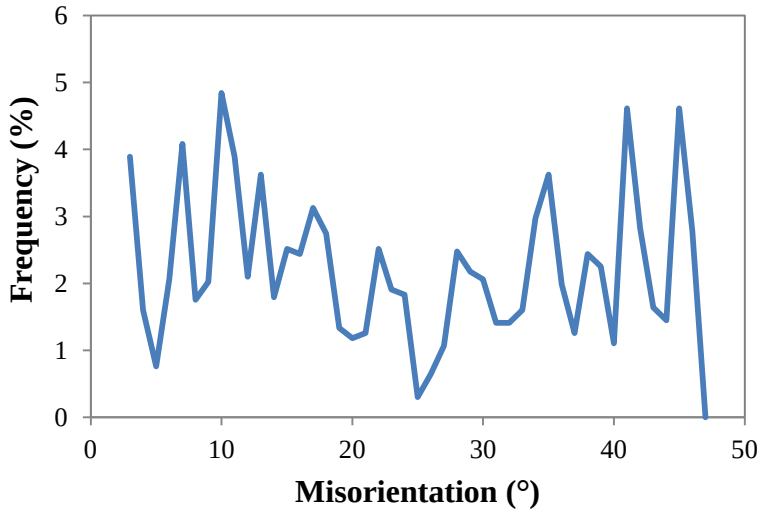

Fig. 5.7. Grain boundary misorientation distribution of cast IN713LC

5.1.3. Constituent Particles

Figure 5.8 is an optical micrograph showing the microstructure of IN718 base metal. δ phase particles are located at the grain boundaries, and inside grains. Additionally, carbides (volume fraction < 1%) are infrequently located at the grain boundaries. At high magnification, the carbides are irregularly shaped, with sizes around 3-6 µm, whereas the rod-like δ phases are 0.5-2 µm in length and 0.3-0.5 µm in width (Fig. 5.9.a). SEM/EDX found the carbides to contain high C, Nb, and Ti, which agrees with the literature [4], indicating that they are MC type (Nb,Ti)C (Fig. 5.9.b). Additionally, SEM/EDX measured data from the black particle in Fig. 5.10.a, shows it is probably TiN in view of its high Ti and N contents, with an atomic percent ratio of 1:1. The volume fraction of TiN in IN718 is less than 0.5%.

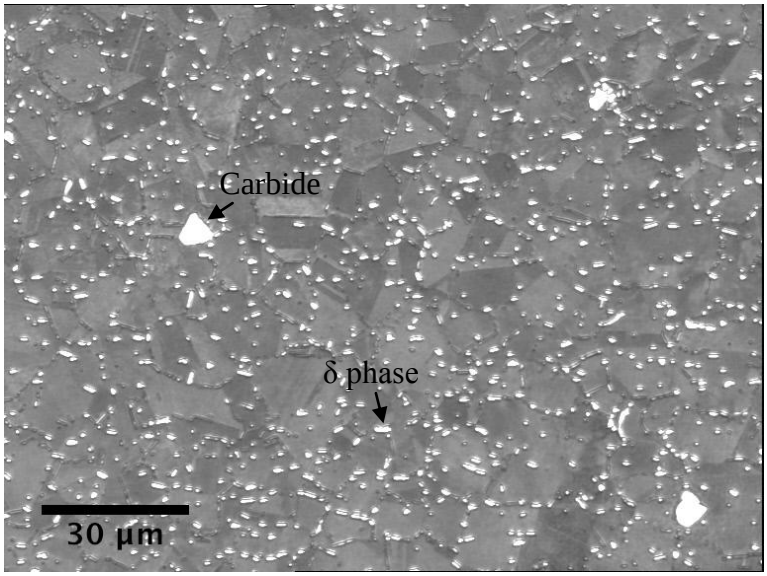

Fig. 5.8. Optical micrograph showing the δ phase and MC carbide distribution in forged IN718

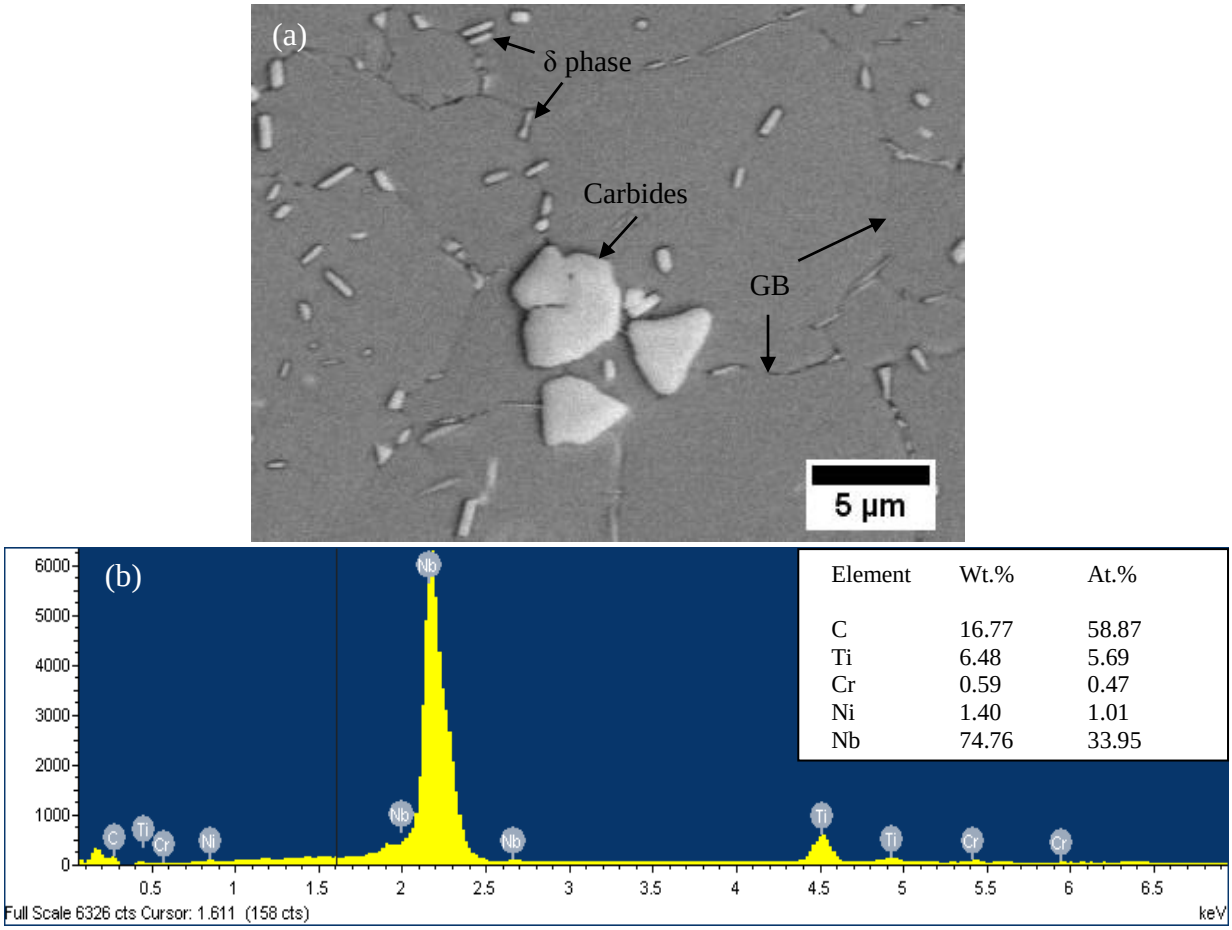

Fig. 5.9. (a) SEM SE micrograph showing the microstructure of IN718, containing δ phase and carbides (b) EDX spectrum showing the carbides are rich in Nb and C

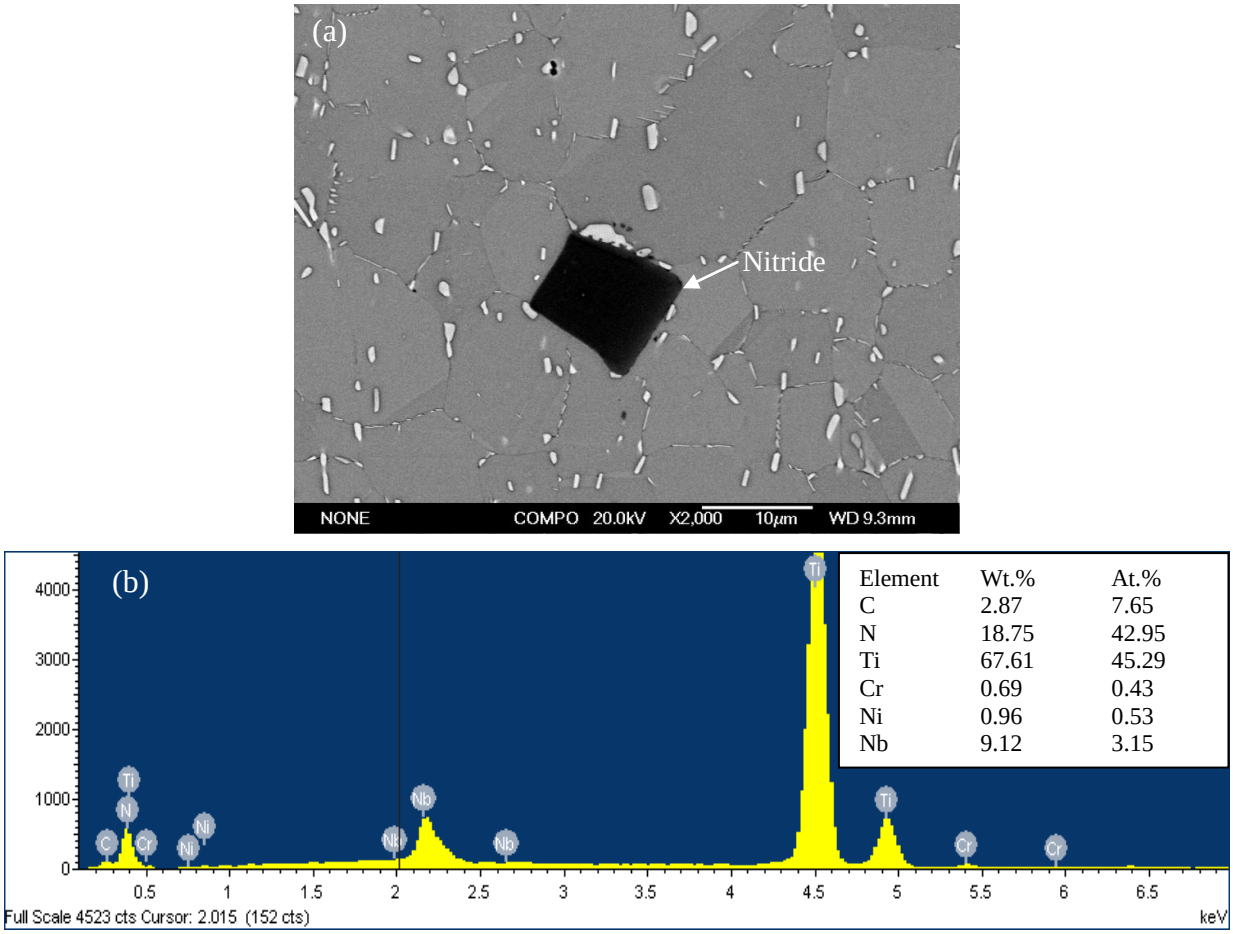

Fig. 5.10. (a) SEM BSE micrograph showing the cubic nitride in IN718, (b) corresponding EDX spectrum identifying the particle is rich in Ti and N

Figure 5.11.a shows a backscattered SEM micrograph of IN713LC, showing a large volume fraction of cubic γ′ inside the grains, as well as, small numbers of irregularly shaped carbides and γ-γ′ eutectic at the grain boundaries. The volume fraction of γ-γ′ eutectic in the matrix is less than 0.2%. The size of γ′ in the matrix is around 300 nm. The EDX measurement (Fig. 5.11.b) identified that the carbide is (Nb,Ti)C in view of its high Nb, Ti, C contents.

Because the spatial resolution of SEM/EDX is limited by beam spreading, chemical composition analyses of small particles (γ′ and δ phase) were also carried out by TEM/EDX, and will be discussed in Chapter 7, alongside the dissolution model.

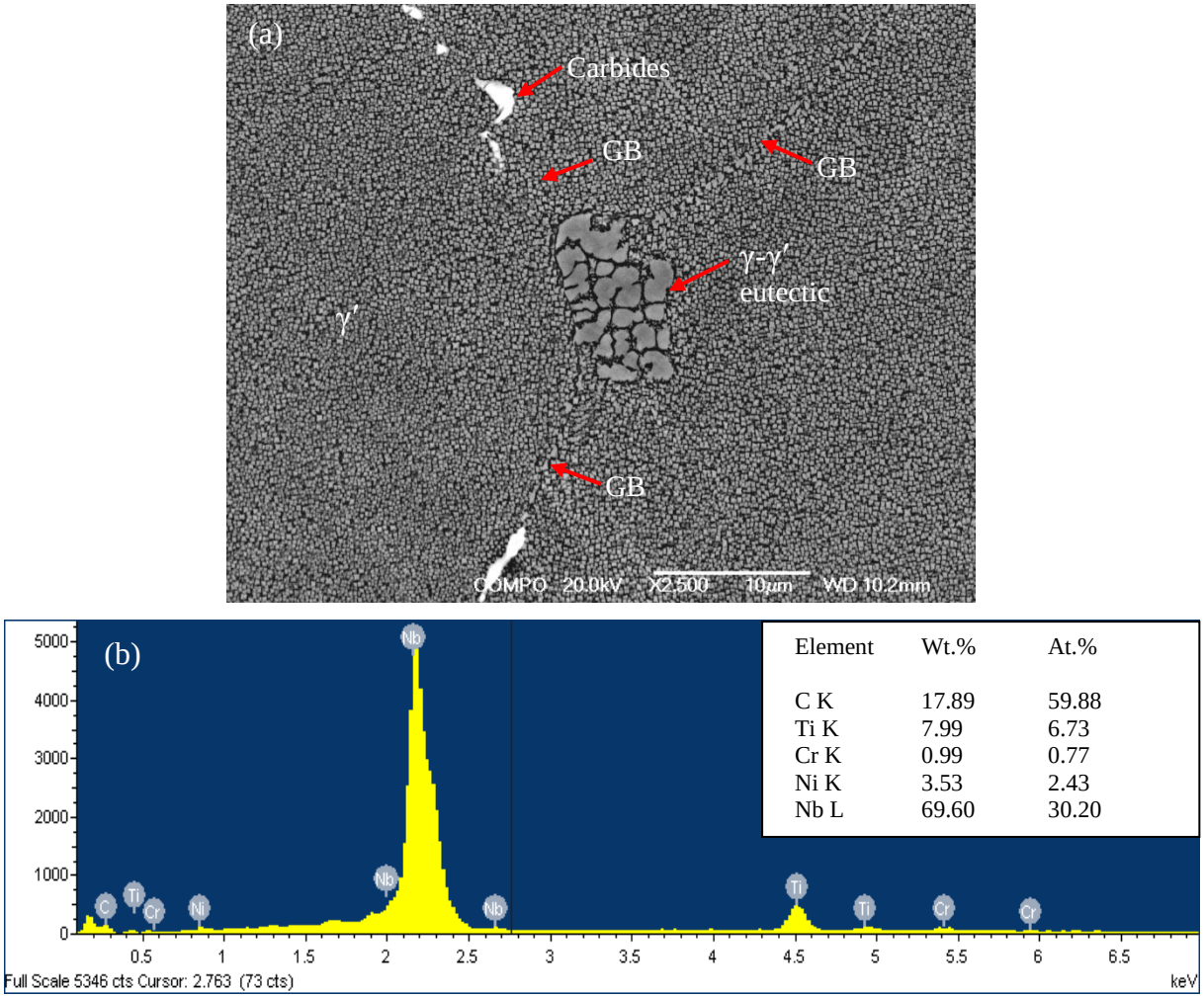

Fig. 5.11. (a) SEM BSE micrograph of the microstructure of IN713LC showing irregular NbC and γ-γ′ eutectic at grain boundaries, and large amount of intragranular γ′ particles, (b) EDX spectrum of carbides

5.2. Weld Macrostructure and Microstructure

The purpose of this section is to investigate the influence of LFW process parameters on the microstructural development. Qualitative and quantitative analyses of the microstructural development of LFWed IN718-IN713LC are presented. Samples W1, W2, and W3 demonstrated the impact of the forging pressure (275 MPa, 400 MPa, and 600 MPa). W2 and

W4 (2 mm and 3 mm), also W5 and W7 (3 mm and 1.5 mm), investigated the effect of the amplitude. W4 and W5 (45 Hz and 60 Hz), also W6 and W7 (30 Hz and 60 Hz), demonstrated the influence of the frequency. The parameters of welds were described in the form of weld number_pressure-amplitude-frequency, indicated as W1_275-2-45, W2_400-2-45, W3_600-2-45, W4_400-3-45, W5_400-3-60, W6_400-1.5-30, and W7_400-1.5-60.

5.2.1. Weld Integrity

The configuration of W2_400-2-45 has been presented in Fig. 4.2. Other weldment configurations are similar to W2, displaying a completely connected weld line with extruded flashes. For more details of weld line, optical micrographs are presented in Fig. 5.12 showing the cross-sections of W1 to W7. The weld line is bonded without obvious cracks and pores. Large amounts of flash are located near IN718, whereas limited flash appears in IN713LC since most of the expelled IN713LC drops off during welding. Under higher weld pressure, the weldments suffer larger distortion in IN713LC (Figs. 5.12.a-c). However, there is no apparent distortion in IN718. The extruded flash in IN718 is located closer to the weld under lower pressure (W1_275-2-45), than in samples welded at higher pressure (W2_400-2-45, W3_600-2-45). Comparing W2_400-2-45 with W4_400-3-45 and W7_400-1.5-60 with W5_400-3-60, suggests that small amplitude tends to expel the ejected material away from the weld line to form thin long flash layers. Unlike the pressure and amplitude, the frequency does not show an obvious effect on the flash. These phenomena demonstrate that the friction heat dissipates more easily into surroundings with increase of the weld pressure or reduction in the amplitude. Moreover, the distortion of IN713LC mainly depends on weld pressure.

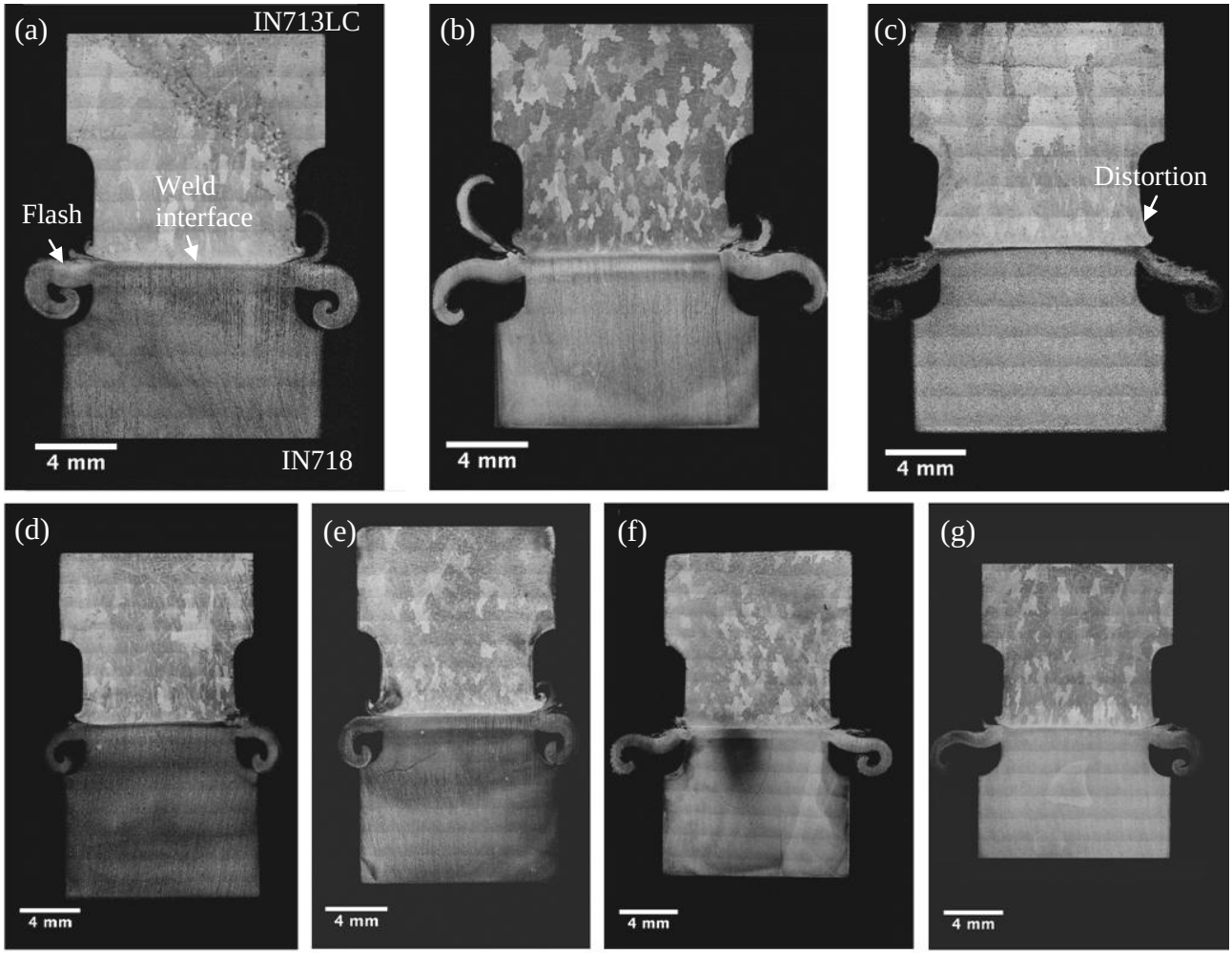

Fig. 5.12. Cross-section of IN718-IN713LC LFWs showing weld interface, flash, and distortion, (a) to (g) stand for W1 to W7

As introduced in Section 3.3.5.c, unsuccessful joints may occur on LFW of Ni-superalloys with large grain sizes with special crystal orientation [5]. In this study, the <100> directions of IN713LC was perpendicular to the friction (oscillation) direction just like the case of CMSX-4 [5]. All the welds were fully bonded, the large grain structure of IN713LC with strong {001}<100> texture did not influence the weld integrity. This is because of the difference of the grain structure of CMSX-4 and IN713LC. CMSX-4 is a single crystal alloy, which possesses anisotropic properties due to a geometrical necessity, with a preferential

welding friction direction (Fig. 3.40 and Fig. 3.41). In comparison, IN713LC is a polycrystalline cast alloy, which has a strong texture in <100> directions (*z*-direction of sample), but with random texture in the *x* and *y*-directions (Fig. 5.6). This means that IN713LC has anisotropic properties in <100> direction (*z*-direction of sample) and isotropic properties in *x* and *y*-directions. The κ value of each grain in IN713LC is randomly distributed in the range of 0-90 °, which enables successful welding (Fig. 3.41).

Figure 5.13 consists of SEM BSE micrographs showing the microstructural development near the weld line of W1_275-2-45. The weld interface is fairly straight. No evidence for local melting was found in the weld, which further confirms the weld integrity. Recrystallised grains were found near the weld line in IN713LC. In IN718, δ phase is fully dissolved in area A and partially dissolved in area B, due to the high temperature during welding. But in lower temperature area C, the δ phase shows the same morphology and fraction as in the base metal. More quantitative analyses of δ phase will be presented in Section 5.2.2.b.

Similar microstructural studies were also carried out on all the welds to assess whether or not that they were fully bonded. During analysis, some oxide inclusions were found in W4_400-3-45 and W5_400-3-60, and will be discussed in Chapter 8.

Figure 5.14 shows a group of NbC particles located near the weld interface in W2_400-2-45, but this phenomenon is not found in every specimen. The reason for their existence may be attributed to the fact that NbC enrichment region (like the area marked with dashed line in Fig. 5.13) moves to the weld interface when the weld reaches the preset upset. The presence of the NbC near the weld interface indicates that the peak temperature during welding is below the NbC solvus temperature (1280 ℃) [6]. The NbC rich zone may degrade the fatigue

life of welds, as presented by Alexandre *et al.* [7], who showed that cracking tends to occur at NbC particles in ultrafine grained IN718 (~5 μm).

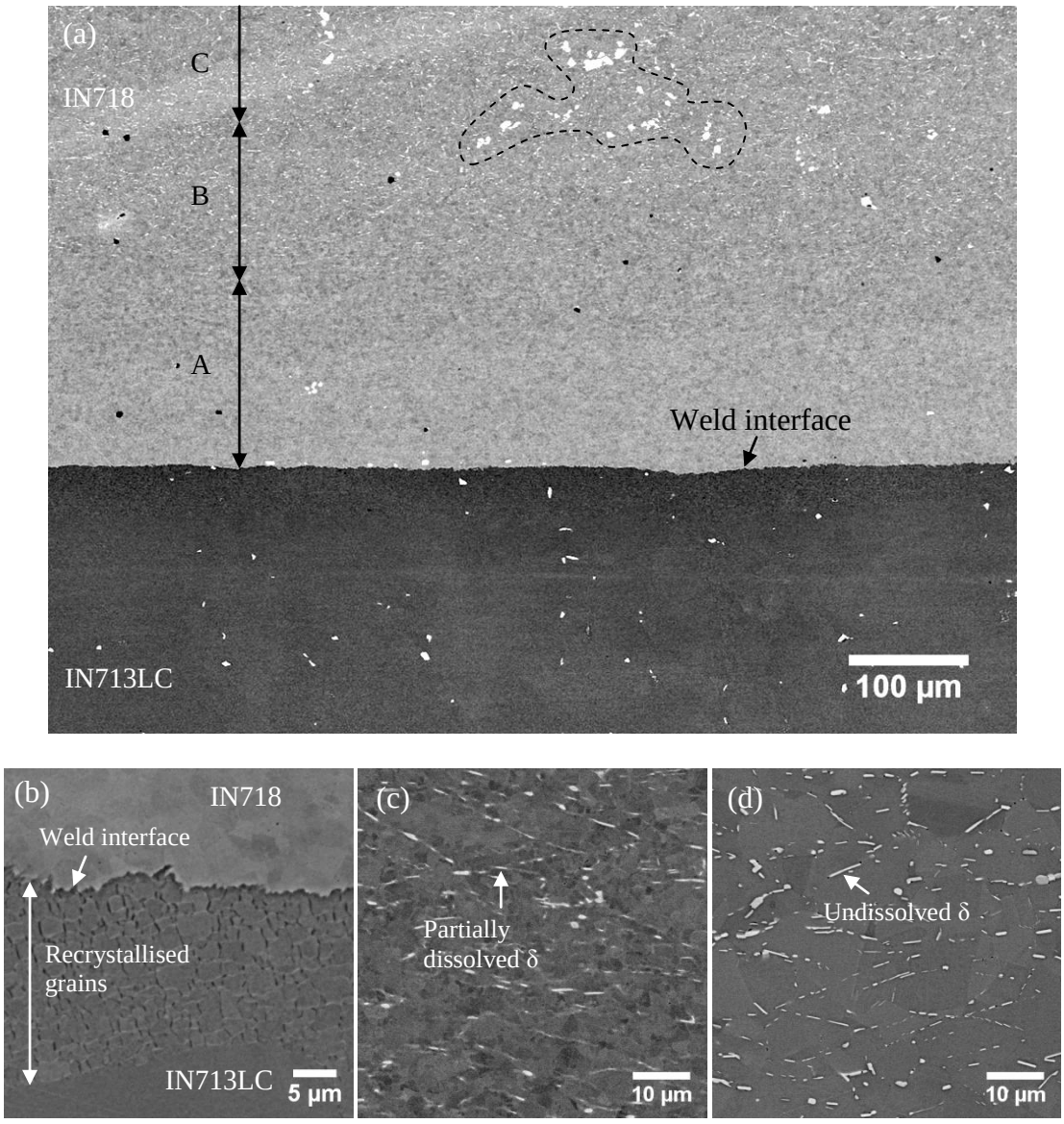

Fig. 5.13. SEM BSE micrographs of W1_275-2-45 near weld line showing (a) the microstructural development near the weld line, (a) low magnification micrograph of the near weld line area, (b) high magnification micrograph of the weld interface and area A, (c) high magnification micrograph of the area B, and (d) high magnification micrograph of the area C

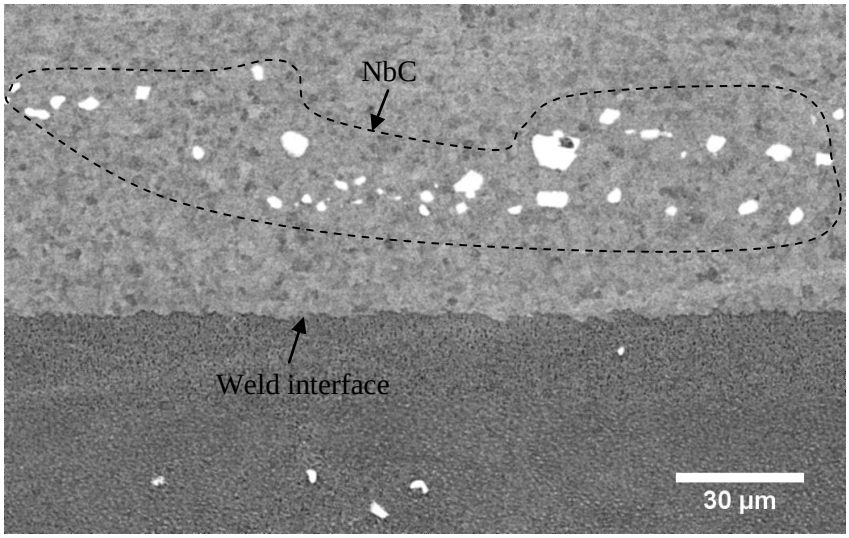

Fig. 5.14. SEM BSE micrograph of W2_400-2-45 near weld line showing numbers of NbC (in dashed line) located in IN718 close to weld interface

5.2.2. Precipitate Development

5.2.2.a. Qualitative Analyses

In LFW, some precipitates can be dissolved by the elevated temperature, and may re-precipitate in the matrix during cooling. Quantitative analyses of the development of precipitates contribute to understanding the relationship between the process parameters and the microstructure.

Figure 5.15 is SEM BSE micrographs of IN718 showing the extent of δ phase variation in W1_275-2-45. At 60 µm, δ phase is completely dissolved, but some NbC still remain. The δ phase free zone extends to 120 µm, which is the start of δ phase partial dissolution zone. The partial dissolution zone extends to 500 µm, and then reaches the same δ content as it is in base metal.

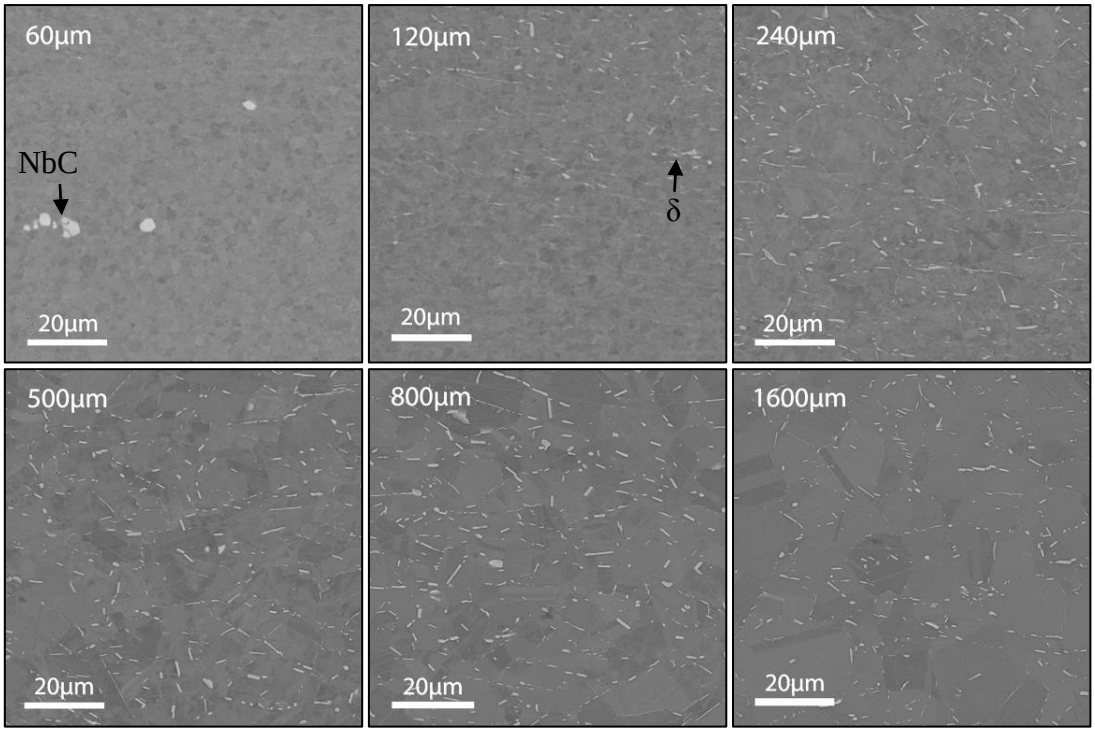

Fig. 5.15. SEM BSE micrographs showing the δ phase variation at different distances indicated from the weld interface in IN718 of W1_275-2-45

At higher magnification, ultrafine particles γ′ and γ″ were observed in IN718 (Fig. 5.16). γ′/γ″ are fully dissolved at 600 µm and partially dissolved at 750 µm. However, due to the limited spatial resolution, it is not possible to quantify the variation of their volume fraction.

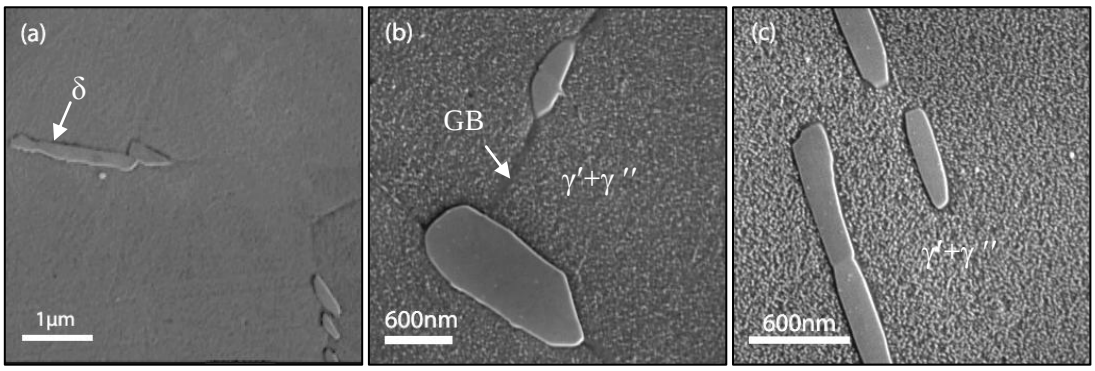

Fig. 5.16. SEM SE micrographs showing γ′/γ″ variation in IN718 of W2_400-2-45, (a) γ′/γ″ full-dissolution at 600 µm from the weld interface, (b) γ′/γ″ (white ultrafine particles) partial dissolution at 750 µm from the weld interface, and (c) γ′/γ″ precipitates in base metal

The variation of γ′ in IN713LC is shown in Fig. 5.17. At 2000 μm from the weld interface, the morphology and volume fraction of γ′ are the same as that in base metal (~300 nm, 60%). While moving towards the weld interface, the volume fraction of γ′ gradually decreases until it reaches zero because of the temperature increase. The morphology of γ′ varies from cube to sphere, which is caused by the variation in misfit [8]. In addition, ultrafine dynamic recrystallised (DRXed) equiaxed grains (1-3 μm) are observed at 10 μm from the weld line, and this DRX zone is very narrow (10-30 μm).

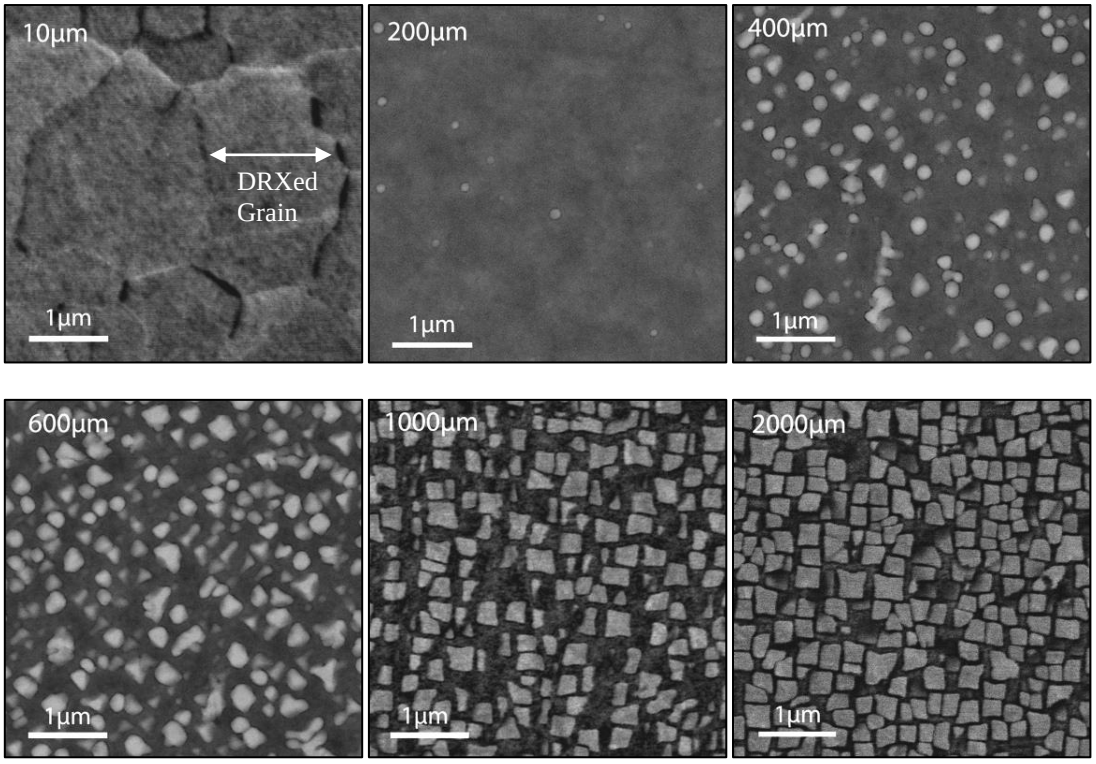

Fig. 5.17. SEM BSE micrographs showing the γ′ particles variation at the different positions indicated from the weld interface in IN713LC of W1_275-2-45

At high magnification, re-precipitated γ′ particles were observed in IN713LC near the weld line (Fig. 5.18). Large amounts of ultrafine spherical γ′ (~20 nm) particles are re-precipitated at 300 μm from weld interface. The γ′ re-precipitation, in the form of ultra-fine particles, is

attributed to the high content of γ′ forming elements which cannot be completely retained in solution in the supersaturated matrix during air cooling. This phenomenon has been evident in another high volume fraction γ′ alloy CMSX-2 [9].

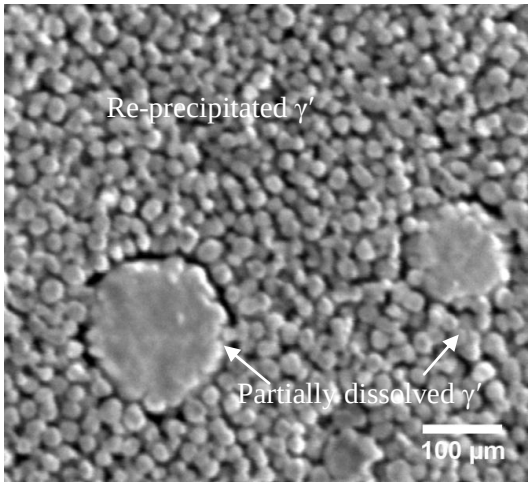

Fig. 5.18. SEM SE micrograph showing partially dissolved γ′ and re-precipitated γ′ in IN713LC at 300 µm from the weld interface in W1_275-2-45

5.2.2.b. Quantitative Analyses

Quantitative analyses have been carried out on δ phase in IN718 and γ′ in IN713LC to study the influence of process parameters on precipitate development. The datum were measured and analysed by ImageJ. However, due to the difficulty of quantifying ultra-fine re-precipitated γ′ (~20 nm) in IN713LC, the quantitative analysis is only for pre-existing γ′.

Figure 5.19 shows the variation in δ phase area fraction for different conditions. In general, the δ phase area fraction is reduced in the region near the weld line, which is attributed to the high temperature leading to the δ phase dissolution.

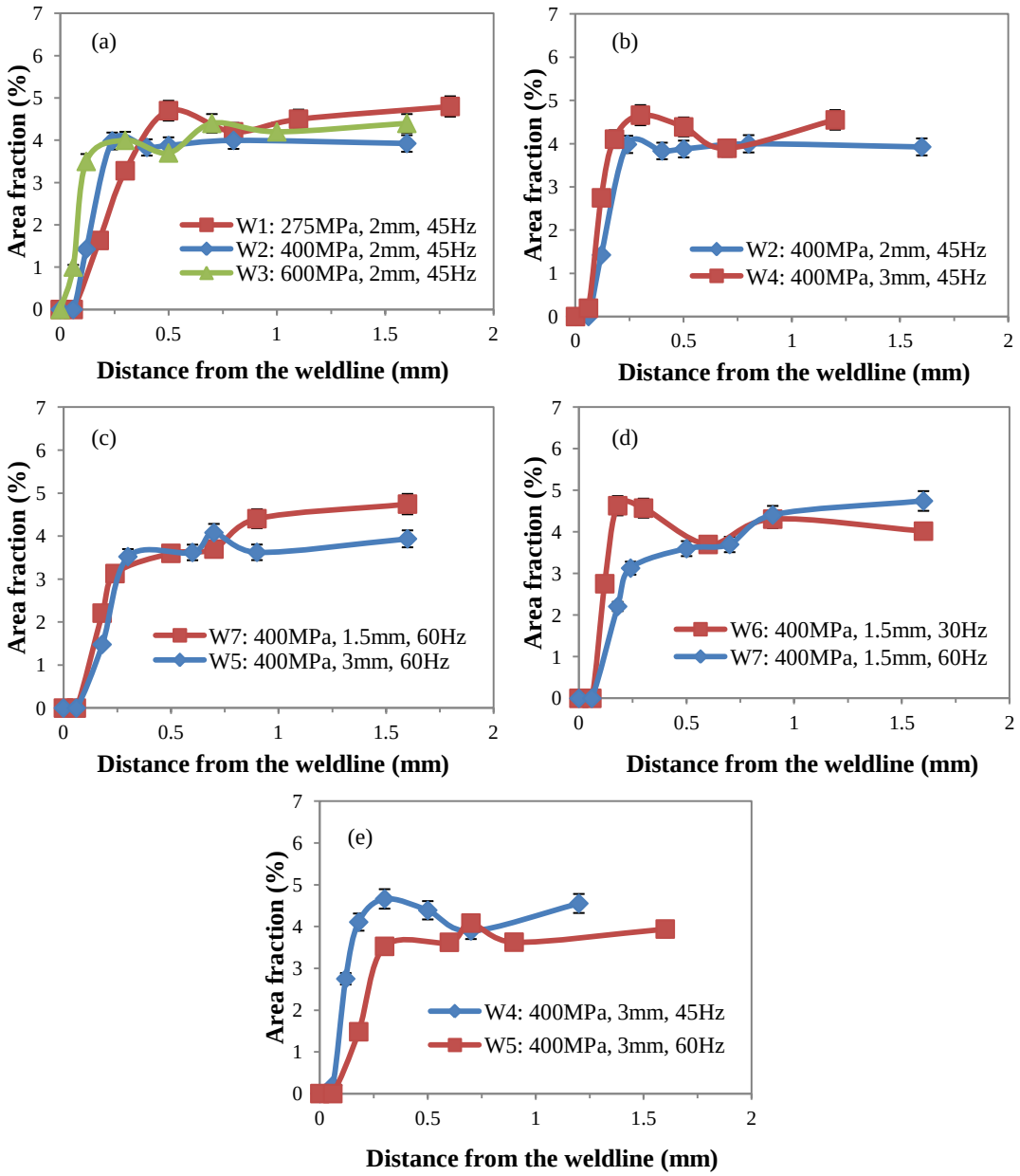

Fig. 5.19. Variation in δ phase area fraction in IN718-IN713LC LFWs under different (a) pressure, (b-c) amplitude, (d-e) frequency, and dashed lines are the δ phase area fraction range in base metal

Figure 5.20 quantifies the δ dissolution zone for the different parameters used. It is found that the extent of the δ dissolution zone is proportional to frequency and inversely proportional to pressure and amplitude, and it is more sensitive to the pressure and frequency than the amplitude as can be seen by comparing the absolute values of the gradients. The δ dissolution

zones are 0.30, 0.21, 0.12, 0.15, 0.28, 0.14, and 0.32 mm for W1-7, respectively. It should be noted that the small numbers of samples may be not valid to reflect the true tendency.

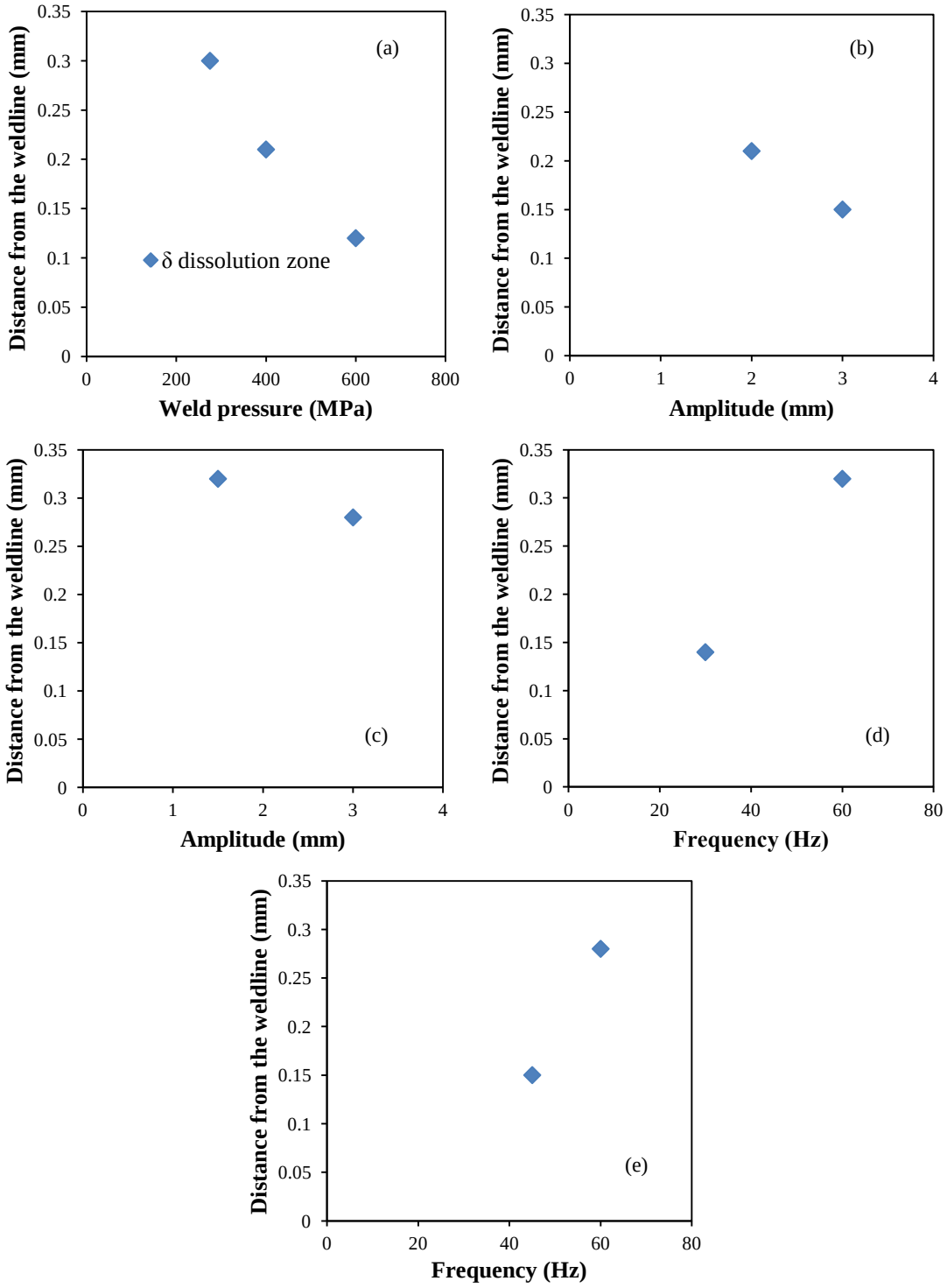

Fig. 5.20. δ phase dissolution zone in IN718-IN713LC LFWs under different (a) pressure, (b-c) amplitude, and (d-e) frequency

Figure 5.21 shows the volume fraction development of γ′ in IN713LC. In Fig. 5.21.a, the γ′ dissolution zones are 0.9, 1.4 and 1.8 mm for W1 to W3, and the γ′ dissolves in a linear manner towards the weld line. While the pressure is 400 MPa, changing the amplitude and frequency in the range of 1.5-3 mm and 30-60 Hz induces a γ′ dissolution zone ~1.2-1.4 mm (Figs. 5.21.b-e). Generally, by observing the trend in γ′ volume fraction, it was found that the weld pressure is the dominant parameter, which markedly influences γ′ development, whereas the influence of both amplitude and frequency are limited.

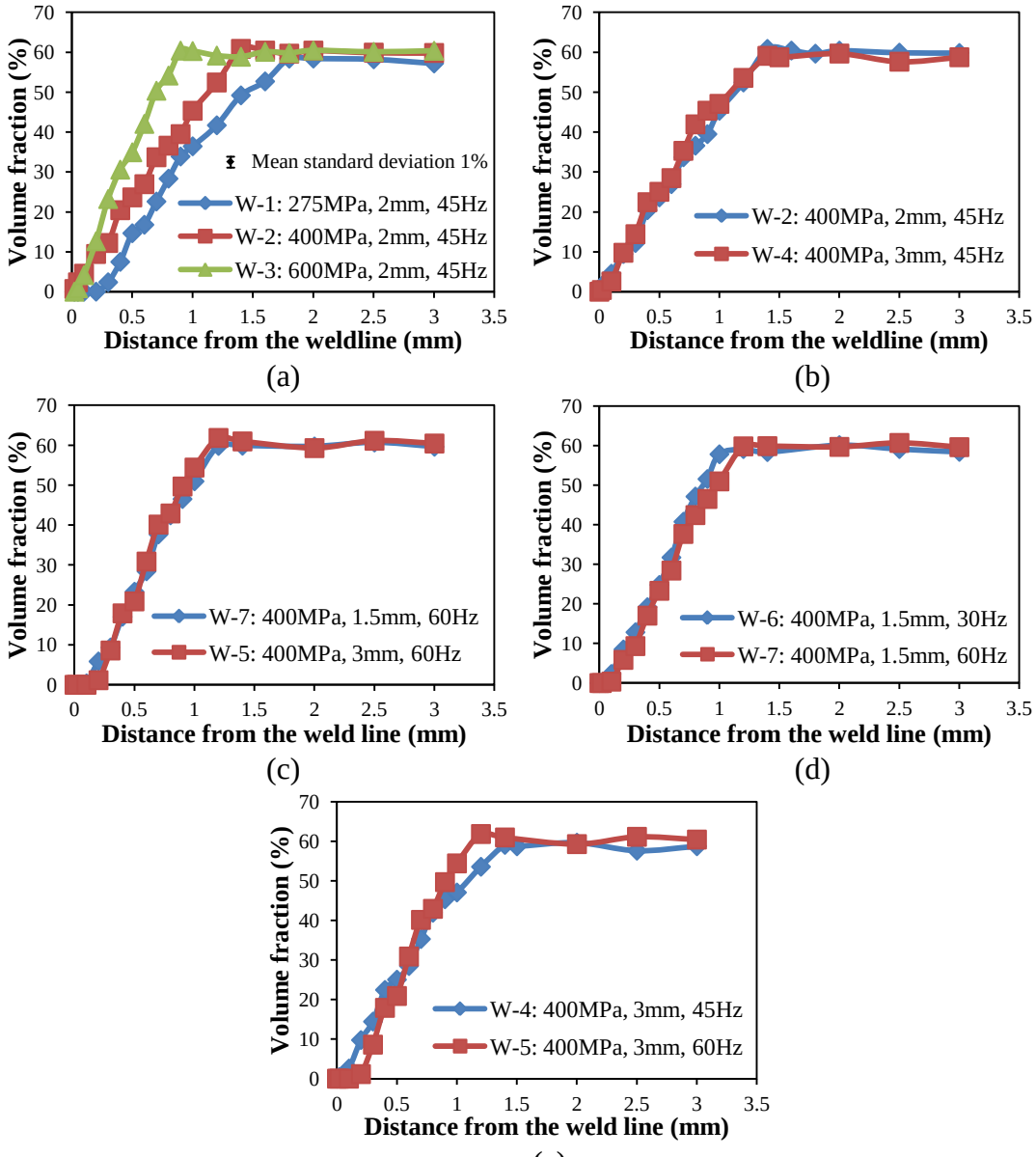

Fig. 5.21. Variation in γ′ precipitate volume fraction of IN713LC in IN718-IN713LC LFWs under different (a) pressure, (b-c) amplitude, and (d-e) frequency

The investigations of δ and γ′ fraction variations in IN718-IN713LC LFWs indicate that the weld pressure dominates the area over which the dissolution of particles occurs and the size of the HAZ. In comparison, the amplitude and the frequency play minor role in the HAZ range. Accordingly, increasing the weld pressure can avoid the excessive loss of strengthening particles, and thus contribute to the maintenance of hardness. This point of view is consistent with the studies of microhardness development, which will be presented in Section 5.4.

5.2.3. Grain Development

5.2.3.a. Grain Structure

It was mentioned in Section 5.2.2.a that the grain size variation of IN713LC is very limited. Therefore, the grain variation study was mainly focused on IN718. As seen in Fig. 5.22.a, the EBSD map of IN718 is divided into three main zones: thermo-mechanically affected zone (TMAZ), heat affected zone (HAZ), and base metal (BM), in which the TMAZ plus the HAZ is called weld affected zone (WAZ).

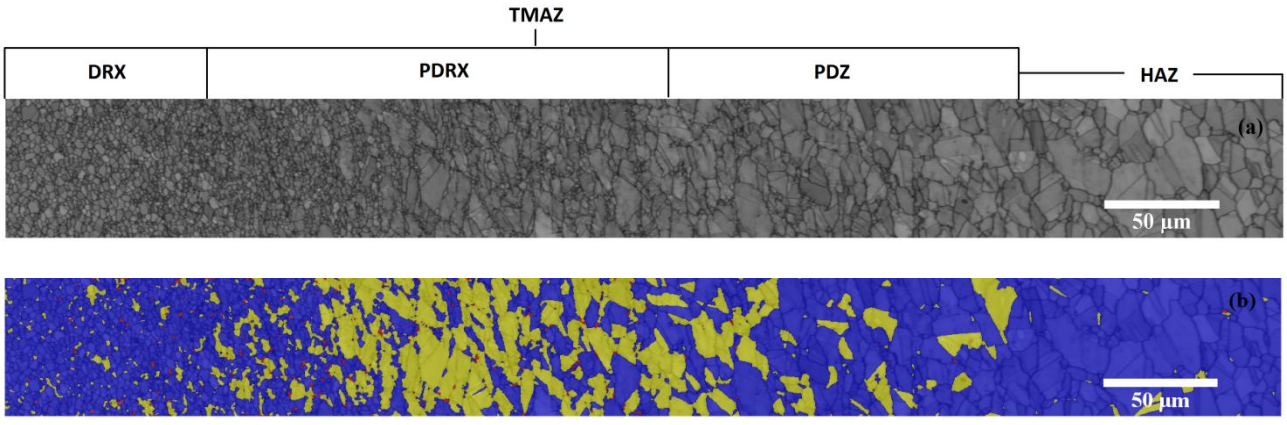

Fig. 5.22. (a) EBSD BC map showing the grain development of IN718 in W1_275-2-45, (b) BC+RF map showing grain types variation, blue: recrystallised grain, yellow: substructure, red: deformed grain

The TMAZ can be classified into three subgroups: dynamic recrystallised zone (DRX), partially dynamic recrystallised zone (PDRX), and plastically deformed zone (PDZ). The DRX is close to the weld interface where original grains were fully recrystallised into fine equiaxed grains as the result of high temperature and plastic deformation. The DRX zone consists of 95% recrystallised grains and 5% substructure and deformed grains. In PDRX zone, the temperature and plastic deformation does not lead to full recrystallisation, so that the microstructure shows a lower fraction of recrystallised grains (30%) and a higher fraction of substructure and deformed grains (70%) than that of DRX zone. The recrystallised grains are mainly located at prior grain boundaries, which is in agreement with the observation of DRX in IN718 IFWs [10]. In PDZ, the grains are elongated by the large compressive stress during welding. Compared with DRX and PDRX zones, the temperature and deformation in PDZ is lower, and therefore cannot provide enough driving force to initiate recrystallisation, but may induce dynamic recovery. The PDZ consists of 80% recrystallised grains and 20% substructure and deformed grains. In addition, HAZ only includes precipitate dissolution, therefore it shows a similar grain structure and recrystallised grain fraction (>95%) as that of the base metal. The BM is next to HAZ, which is not labelled in Fig. 5.22.

Figure 5.22.b consists of band contrast (BC) and recrystallised fraction (RF), showing grain structure variation. The grains are classified into three structures: recrystallised structure, substructure (structure contains subgrains), and deformed structure. The DRX zone mainly consists of recrystallised grains, with only a small amount of substructure and deformed grains. This is because the large plastic deformation and high temperature lead to recrystallisation forming dislocation-free grains close to the weld line. Meanwhile, the forging pressure applies force on recrystallised grains, which induces new dislocations inside grains. However, the influence of forging pressure is limited, as most of grains are still

recrystallised and contain a low dislocation density. PDRX contains a large volume fraction of recrystallised grains and grains showing a recovered substructure, coupled with a small quantity of deformed grains. In the region of PDRX close to DRX, more than half of the grains are recrystallised, since the plastic deformation and temperature are still high enough to drive recrystallisation. While the plastic deformation and temperature gradually decrease towards the base metal, the number of recrystallised grains decreases and leaves large numbers of subgrains in initial grains as substructure (to be shown in Fig. 5.25). In PDZ, there are no new recrystallised grains, but this region still includes substructure. HAZ shows the same recrystallised structure as the base metal, since no deformation occurs here.

5.2.3.b. Grain Size

Figure 5.23 shows the grain size development in welds, based on EBSD results. It shows that grains are recrystallised to fine grains (1-2.5 μm) near the weld line, and the sizes of grains gradually increase towards the base metal. Since the weld blocks are cut from different places in forged bulk materials, there may have been slight differences in the grain size of the base metal. The matrix grain size of W7_400-1.5-60 is 3 μm smaller than other welds, and W7 shows the smallest grain variation zone (0.23 mm) among all the welds. The possible explanation was given by Zhao and Chaudhury [11] that smaller initial grain size makes recrystallisation more difficult, because a fine grained alloy can accommodate more strain by grain boundary sliding than a coarse grained alloy, resulting in lower stored strain energy and less dynamic recrystallisation.

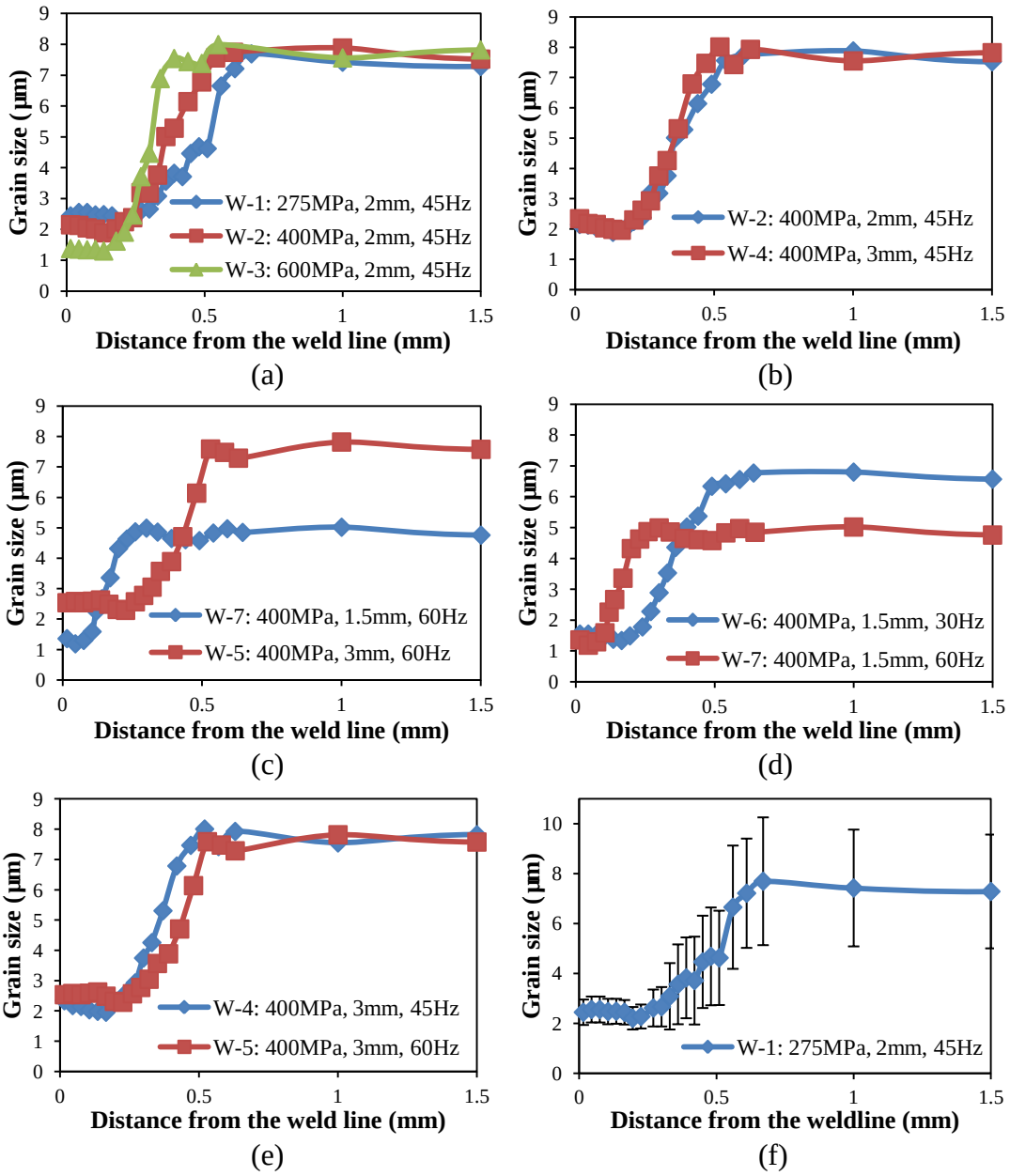

Fig. 5.23. Grain size variation of IN718 in IN718-IN713LC LFWs under different (a) pressure, (b-c) amplitude, (d-e) frequency, (f) typical standard deviation in W1

Samples W1 through W5 have a grain size around 7.5 μm, which allows the influence of process parameters on grain size to be studied. Figures 5.23.a, b, and e show the effect of pressure, amplitude, and frequency on grain size. It indicates that increased pressure can slightly reduce recrystallised grain size and the extent of the grain size variation zone.

However, any influence of amplitude and frequency was not observed. As the pressure is increased from 275 MPa to 600 MPa, the recrystallised grain size decreases from 2.5 μm to 1.3 μm, and the grain size variation zone reduces from 0.61 mm to 0.39 mm. This change can be explained because higher pressure tends to generate larger strain rates, and as is known from Equation 2.17, the recrystallised grain size is inversely proportional to strain rate.

In general, the grain size variation zone in IN718 is very narrow. Correlating grain size variation with δ phase variation (Fig. 5.19), suggests that the small grain size variation zone is due to the impediment of grain boundary movement by δ phases.

5.2.3.c. Strain Rate

Figure 5.24 is an EBSD BC map showing the grain development in the DRX of IN718 in W1_275-2-45. The grains are generally fine, but the grains near the weld interface are coarser than those grains near PDRX. This is because the temperature near the weld interface is higher than in the PDRX, which causes recrystallised grains near the weld interface to grow faster than in other places during cooling. As the cooling rate after welding is rapid, it is reasonable to assume that there is no growth of recrystallised grain near the PDRX, and the grain size in this area can be used to predict the strain rate in the DRX of welds during welding, based on Equation 5.1 [12]:

$$\boldsymbol{d_{DRX} = 3 \times 10^{5}\left(\dot{\varepsilon} exp(Q/RT)\right)^{-0.27}} \quad (5.1)$$

where d_{DRX} is recrystallised grain size, Q is 443.2 kJmol^{-1}, R is 8.3145 Jmol^{-1}K^{-1}, T is ~1200 ℃ approximately based on the microstructural development (Section 7.4.4).

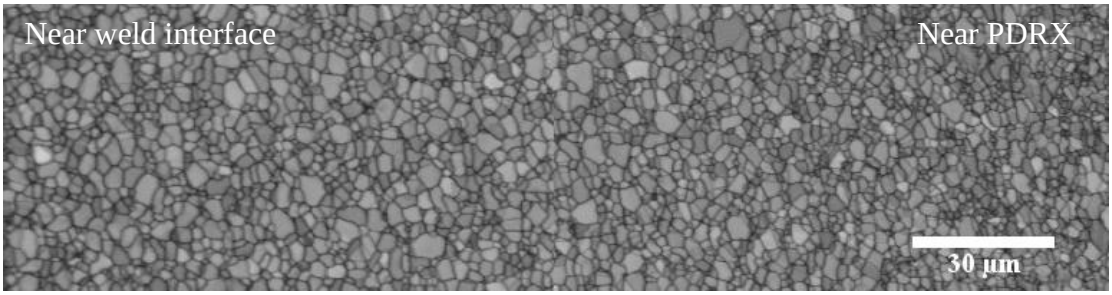

Fig. 5.24. EBSD BC map showing the grain development in DRX of IN718 in W1_275-2-45

For W1 (recrystallised grain size is 2.2 µm), the calculated strain rate 1859 s^{-1} is of the same order of magnitude as Chamanfar *et al.* [13] reported value of 1325 s^{-1} in LFWed Waspaloy, and is in the range of Turner et al [14] predicted value 500-2500 s^{-1} in LFWed Ti-6Al-4V, However, the calculated strain rate in W1_275-2-45 is much larger than the value (9 s^{-1}) calculated by Vairis' expression [15],

$$\dot{\varepsilon} = af/L \tag{5.2}$$

where a is the amplitude of oscillation, f is the frequency and L is the length of specimen in the oscillating direction. This is because that Vairis' expression is a simple model, which assumes that the deformation is homogeneous and ignores the important effect of pressure. In general, higher weld pressure generates a larger force at the weld line, which tends to induce a larger strain rate. The current study proves that the strain rate of IN718 is sensitive to the pressure in IN718-IN713LC LFWs, as the pressure increases from 275 MPa to 600 MPa, the strain rate rises from 1859 s^{-1} to 13045 s^{-1}.

5.2.3.d. Mechanism of Recrystallisation

Figure 5.25 is EBSD (IPF-x + GB) map showing the microstructure of PDRX in IN718. The initial grains (like grain A) show serrated grain boundaries, and the grain boundaries are

surrounded by recrystallised fine grains (like grain B). Subgrains (arrowed grain boundary misorientation > 3 °) are formed at the original grain boundaries in sizes around 1 μm (like grain C). The variation of colours within original grains indicates that hot deformation induces the difference of misorientation. The formation of serrated grain boundaries and subgrains indicates that the DRX mechanism of LFW IN718 is continuous dynamic recrystallisation (CDRX), which involves the coalescence of dislocations, and reconfiguration of subgrains form along the original grain boundaries, rather than by grain boundaries bulging in discontinuous dynamic recrystallisation mechanism (DDRX). The findings in this study are in line with the proposed mechanism of Wang *et al.* [16] that CDRX is the main DRX mechanism in IN718 at high Zener-Hollomon Parameter (*Z*) (1000 °C and 0.1 s^{-1}). In the current study, *Z* is 6 times larger than that of the Wang *et al.* study, and thus further confirms that CDRX is the main DRX mechanism in LFW IN718.

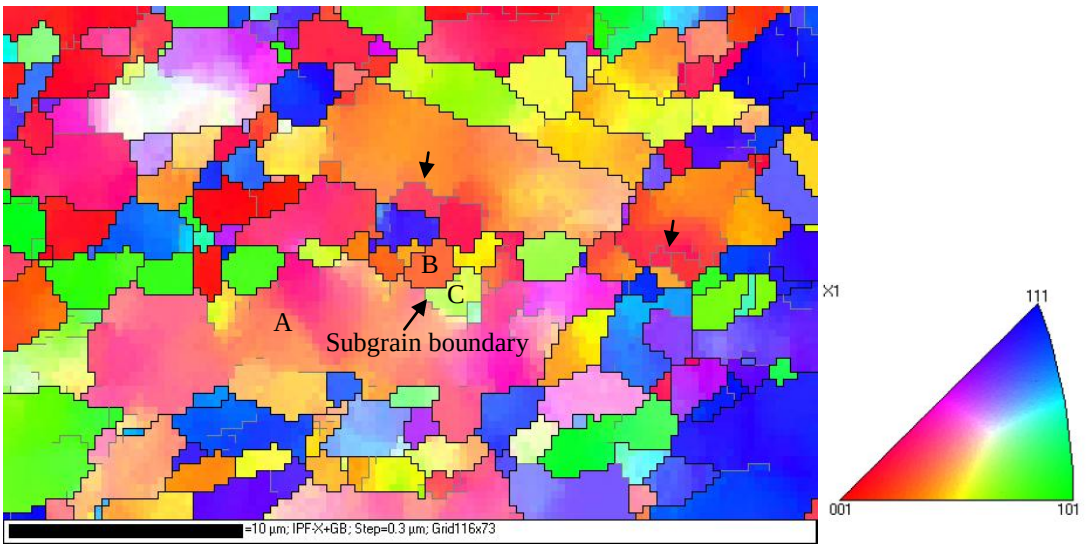

Fig. 5.25. EBSD (IPF-x + GB) map showing the grain development in PDRX of IN718 in W1_275-2-45, A is the initial grain, B is recrystallised grain, C is subgrain, grey lines represent subgrain boundaries (3 ° < misorientation < 15 °) and black lines represent HAGB (misorientation ≥ 15 °), arrows point to subgrain boundaries

5.3. Microtexture

Figures 5.26 and 5.27 are pole figures showing the microtexture development in the TMAZ of IN718. Since the numerical value of orientation indices are the same as that of crystal indices in FCC metal, it reflects a {111}<110> texture in the TMAZ of all the welds. This texture is in accord with the fcc slip system, in which {111} planes slip in <110> directions. The maximum times random indicates that {110} and {111} planes tend to be parallel to the *x*-direction (oscillation direction) and *z*-direction (forging pressure direction) respectively, with increase of weld pressure. In other words, microtexture becomes sharper as the pressure increases. This is because the magnitude of texture relates to the plastic deformation. In this study, larger pressure tends to drive more {111} slip planes towards the oscillation direction <110> thus generating a sharper microtexture.

Comparing Fig. 5.26 with Fig. 5.27, it can be noticed that the microtexture in PDRX+PDZ is 1.5 times higher than that in DRX. This is because the majority of grains in PDRX and PDZ are deformed, whereas fewer grains suffer deformation in DRX. However, in contrast to the microtexture (Max. times random is 33) in LFWed Ti-based alloy [17], the measured texture in this study of LFWed Ni-based superalloys is relatively weak. Moreover, the influence of pressure on the magnitude of microtexture in Ti-based alloy LFWs is opposite to that in Ni-based superalloys LFWs, in which lower pressure causes sharper microtexture in Ti LFWs. This is due to the difference in texture formation mechanism. LFW of Ti involves α-β phase transformation and plastic deformation, whereas LFW of Ni-superalloys only involves plastic deformation.

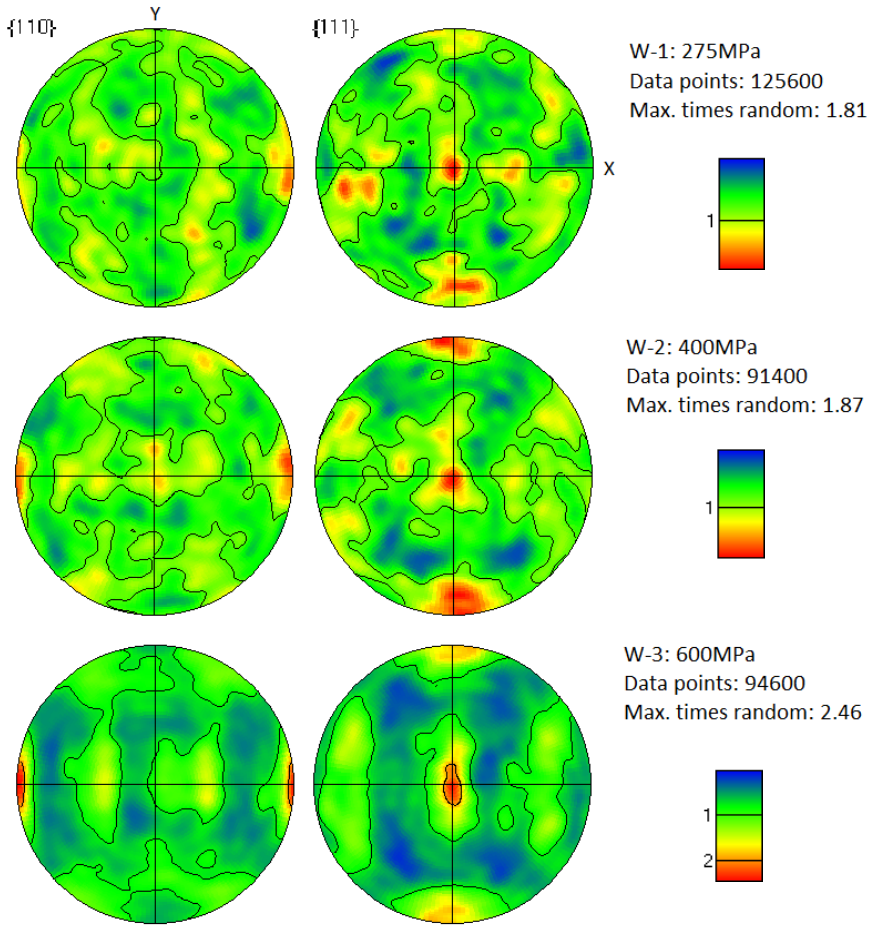

Fig. 5.26. Pole figures in the DRX of IN718 showing a {111}<110> texture, *z*-direction is normal to *x*-*y* plane, which is the point of intersection of *x*-*y* axes

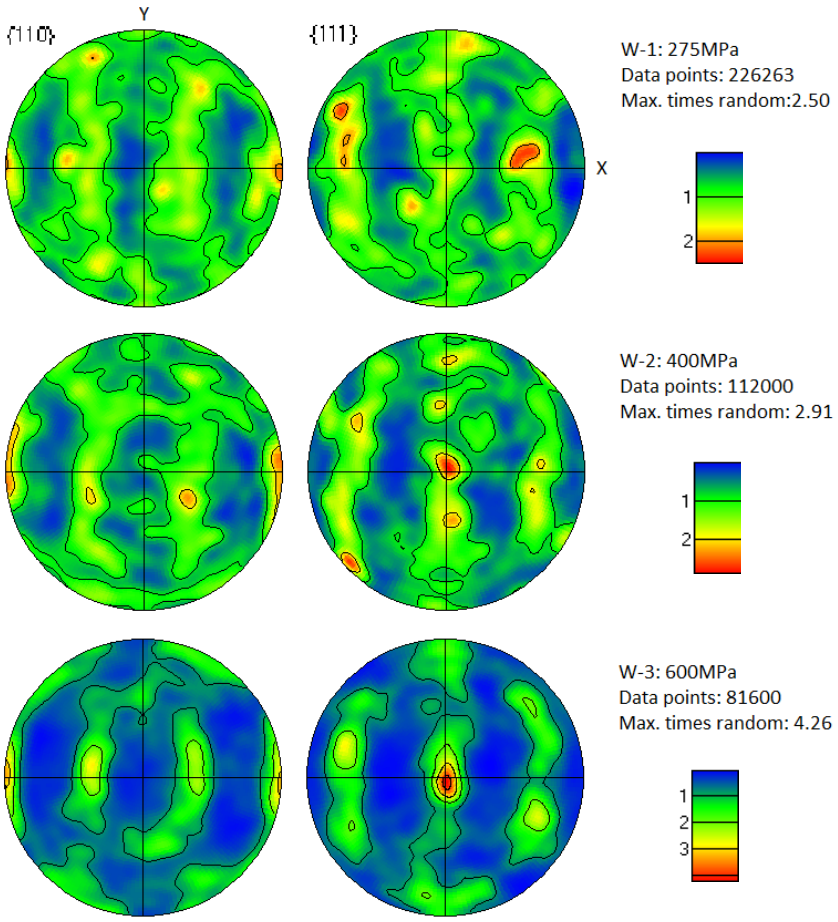

Fig. 5.27. Pole figures in the PDRX and PDZ of IN718 showing a {111}<110> texture

5.4. Microhardness

5.4.1. Microhardness Mapping

Figure 5.28.a is a microhardness map showing the microhardness development across the whole cross-section of W1_275-2-45. It reveals a dramatic hardness trough in IN718 and a slight increase of hardness in IN713LC, both in the region near the weld line. The reason for the hardness decrease in IN718 is the dissolution of strengthening precipitates γ′/γ″ during welding. The hardness increase in IN713LC is attributed to the strengthening from the

re-precipitated very fine γ′ during cooling. Both of these have been confirmed by SEM images of Fig. 5.16 and Fig. 5.18. The hardness of IN718 matrix is relatively even about 461 HV (with 8 HV standard deviation), since it is a homogenous forged alloy. In comparison with IN718, the hardness of IN713LC matrix is less even around 393 HV (standard deviation is 13 HV), as a result of the inhomogeneous cast microstructure.

Figure 5.28.b is a microhardness contour map of W1_275-2-45 showing from the top view of Fig. 5.28.a. It shows the hardness trough in IN718 and the hardness increase in IN713LC, which are both in the region of 1.4 mm towards the weld line. The lowest hardness present at 0.8 mm of IN718 towards the weld line is in a region of $7\times0.3\ mm^2$ (marked as A). The reason for the lower hardness in area A than in area C is assumed to be the difference of the volume fraction of γ′/γ″ induced by the different thermal cycles during LFW. The temperature at the middle of weld is always higher than that at the edge of weld [18], which induces larger loss of strengthening precipitates γ′/γ″ in A than in C, causing lower hardness in A. Additionally, it is notable that two hardness peaks in IN713LC (marked as B) are due to the grain boundary strengthening provided by the recrystallised fine grains. No hardness peak is detected in the middle of the weld, because the interval between hardness measurements (0.1 mm) is larger than the DRX zone in IN713LC (0.01-0.03 mm). In the later studies, this peak was detected by smaller intervals, which will be presented later. To simplify the measurements for quantitative analyses, hardness developments of other welds were only carried out in the middle of welds across the weld line by using smaller intervals. In addition, the values were averaged over 3 measurements.

In IN713LC, a hardness increase (40-70 HV) is observed near the weld line. It has been shown in Fig. 5.18, that this is a result of a large volume fraction of re-precipitated fine γ′

particles. In W3_600-2-45, dynamic recrystallised fine grains result in a hardness peak value of 478 HV in IN713LC at 30 µm from the weld. Since normally the DRX zone in the IN713LC side is very narrow (10-30 µm), no peak value was observed in W1_275-2-45 and W2_400-2-45.

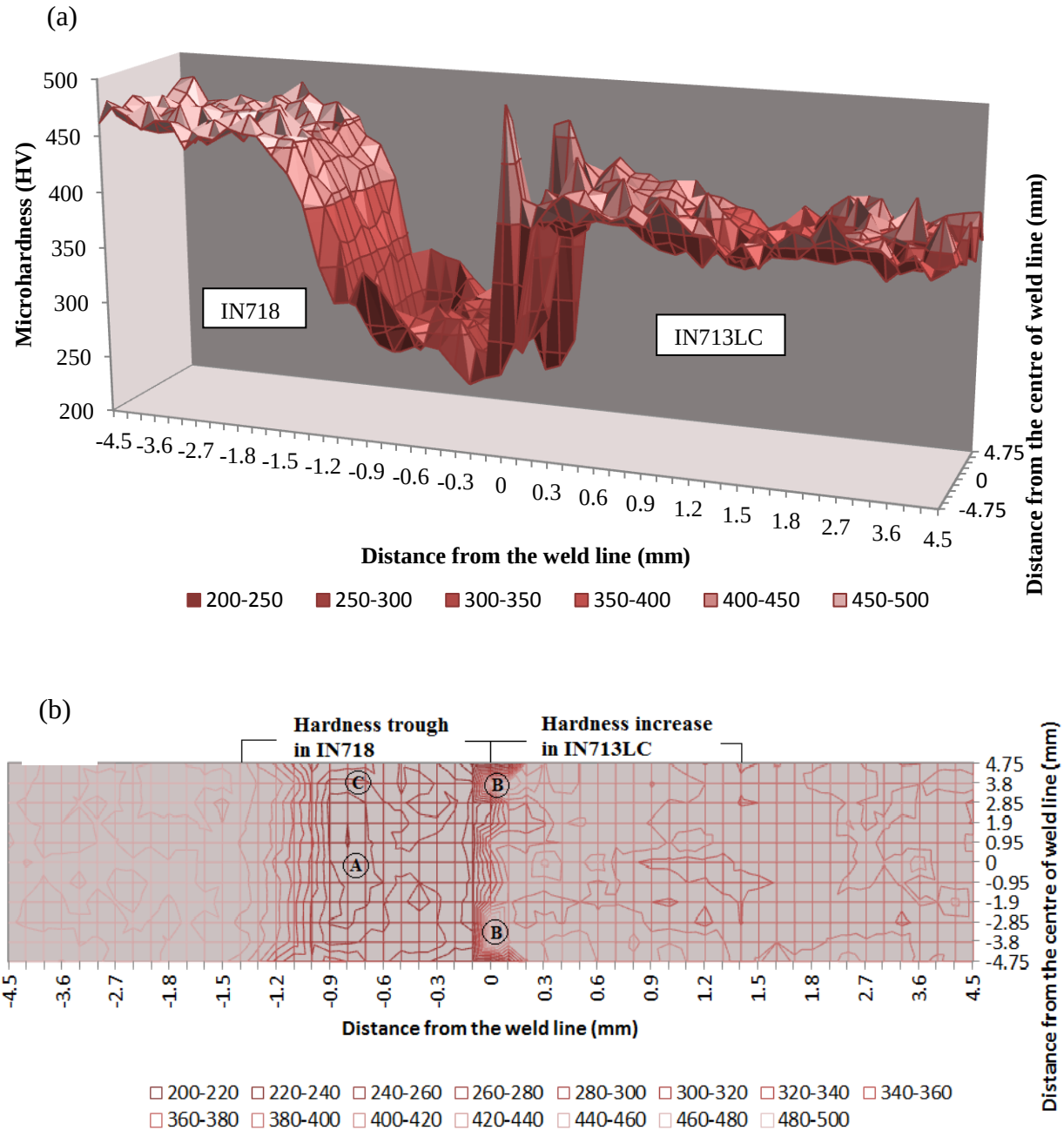

Fig. 5.28. Microhardness map showing microhardness development of W1_275-2-45

5.4.2. Influence of Pressure

Fig. 5.29.a shows the hardness development under different weld pressures. It shows that the weld pressure significantly influences the width of the weld affected zone (WAZ) of IN718. To achieve the same axial shortening, WAZ becomes narrower with increase in pressure. The length of WAZ is listed in Table 5.3. The zone caused by γ′/γ″ dissolution is referred to as the heat affected zone (HAZ), which is the zone with the lowest hardness (represented as Min. HV in Table 5.3) towards the base metal. The reason that the higher pressure induces smaller WAZ can be seen from the weld time (Table 5.3), which refers to the time of reaching the maximum axial displacement, as illustrated in Fig. 3.11. Higher pressure allows the material to be extruded faster under lower temperature, thus less weld time is required to achieve the same axial displacement. Therefore, WAZ and peak temperature reduce as the weld pressure increases.

In IN718, the dramatic hardness drop from the base metal to 260 HV in IN718 is due to the dissolution of γ′/γ″ during LFW. In W1_275-2-45 and W2_400-2-45, the slight hardness increase in IN718 is observed in the regions of 0.8 mm and 0.6 mm towards the weld line, with hardness peaking at 0.3 mm and 0.2 mm. This is consistent with the work of Mary and Jahazi [19] on IN718 LFWs and Daus *et al.* [20] on IN718 IFWs. The hardness increase is due to the grain boundary strengthening by DRXed fine grains. However, the strengthening by plastic deformation was not considered. In fact, plastic deformation generates large numbers of dislocations in PDRX and PDZ zones, and higher dislocation concentration, which results in a higher resistance to plastic deformation. This plastic deformation has been discussed in Fig. 5.22.b. The hardness peak is not observed in the high-pressure W3_600-2-45, due to its small DRX zone.

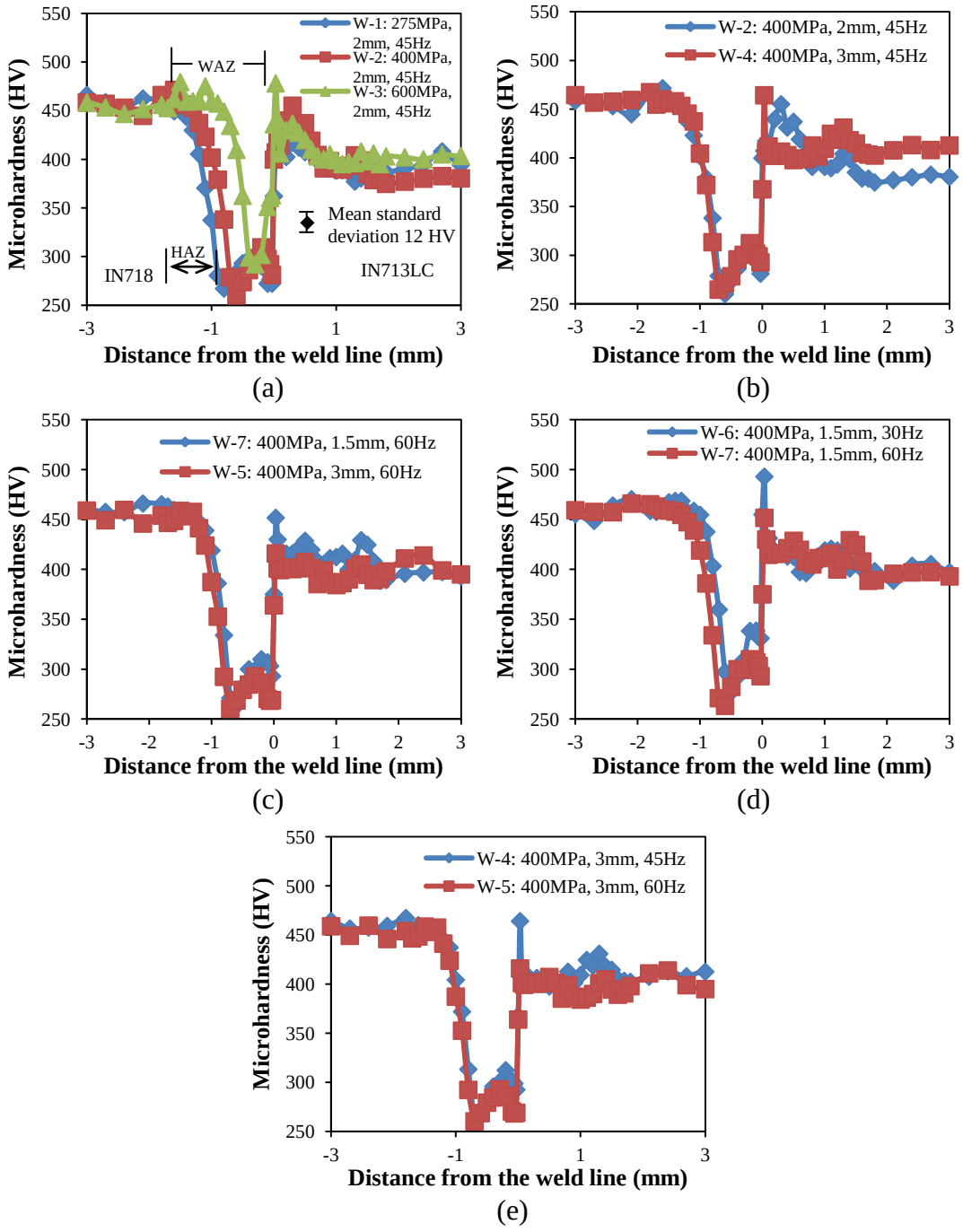

Fig. 5.29. Microhardness development of IN718-IN713LC LFWs under different (a) pressure, (b-c) amplitude, and (d-e) frequency

Table 5.3. The widths of WAZ and HAZ of IN718 in IN718-IN713LC LFWs defined by microhardness development and weld time

Weld Number	Parameters	WAZ (mm)	HAZ (mm)	HV Peak (mm)	Min. HV (mm)	Weld Time (s)
W1	275 MPa, 2 mm, 45 Hz	1.7	0.9	0.3	0.8	3.17
W2	400 MPa, 2 mm, 45 Hz	1.3	0.7	0.2	0.6	2.35
W3	600 MPa, 2 mm, 45 Hz	0.9	0.6	No	0.3	1.48
W4	400 MPa, 3 mm, 45 Hz	1.3	0.6	0.2	0.7	2.26
W5	400 MPa, 3 mm, 60 Hz	1.3	0.6	0.3	0.7	2.28
W6	400 MPa, 1.5 mm, 30 Hz	1.0	0.5	0.18	0.5	2.42
W7	400 MPa, 1.5 mm, 60 Hz	1.3	0.7	0.18	0.6	2.43

5.4.3. Influence of Amplitude and Frequency

As shown in Fig. 5.29.b-e, microhardness development seems to be affected to only a small extent by the variation in the amplitude and frequency. The length of the WAZ in IN718 slightly decreases along with the increase of hardness with reduction of the amplitude or frequency. Compared with the effect of pressure, the influence of the amplitude and frequency on hardness can be ignored.

5.5. Residual Stress

Analysis of the diffraction data by LAMP, IN718 showed an ideal diffracted signal as revealed by clear diffraction peaks. However, the method of rocking the sample did not result in an increase in the diffracted intensity in IN713LC. The residual stress data from IN713LC had generally a large scatter of 2θ, which made it difficult to define the position of the diffraction peak. Accordingly, the stresses of IN713LC were not very reliable. The other

issue, which made the stress values inaccurate, was that d_0 values were taken from far-field measurements. These measured positions were far from the weld line, which could be assumed as strain-free areas. However, the d_0 values in the weld zone would change with changes in composition. An increase in the dissolved Ti and Nb atoms increases the lattice spacing of matrix, thus the residual stress can be overestimated by more than a factor of two. Comparison work has been done on IN718-720Li LFWs by Frankel [21]. It is clear that the stress values might have been overestimated.

Figures 5.30 to 5.32 show the residual stress distributions in the *x*, *y*, *z*-directions of LFWed IN718-IN713LC under different weld pressure, amplitude and frequency. All the welds show asymmetric residual stress distribution. To simplify the analysis, welds are divided into two parts: IN718 and IN713LC. Due to the difference of d_0 values in two alloys can induce inaccurate calculation, the centre residual stress data was not calculated (within 1 mm from the weld line).

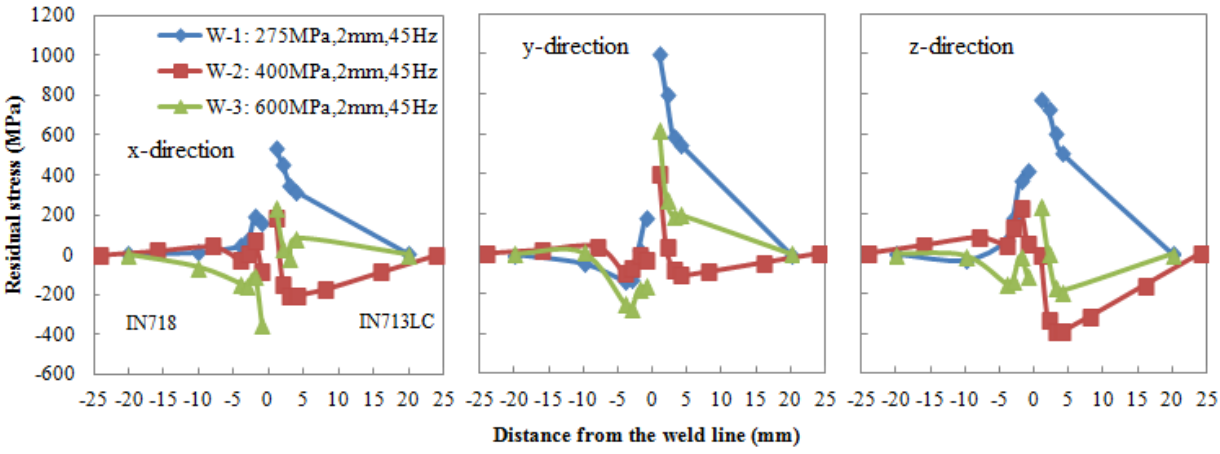

(a) (b) (c)

Fig. 5.30. Residual stress development of IN718-IN713LC LFWs under different weld pressure for (a) *x*, (b) *y*, and (c) *z*-directions

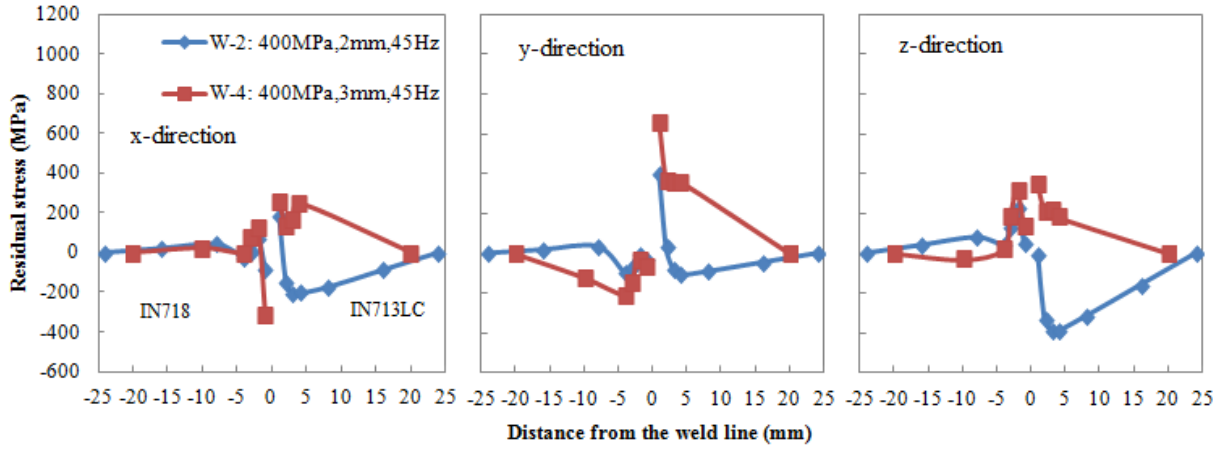

(a) (b) (c)

Fig. 5.31. Residual stress development of IN718-IN713LC LFWs under different amplitude for (a) *x*, (b) *y*, and (c) *z*-directions

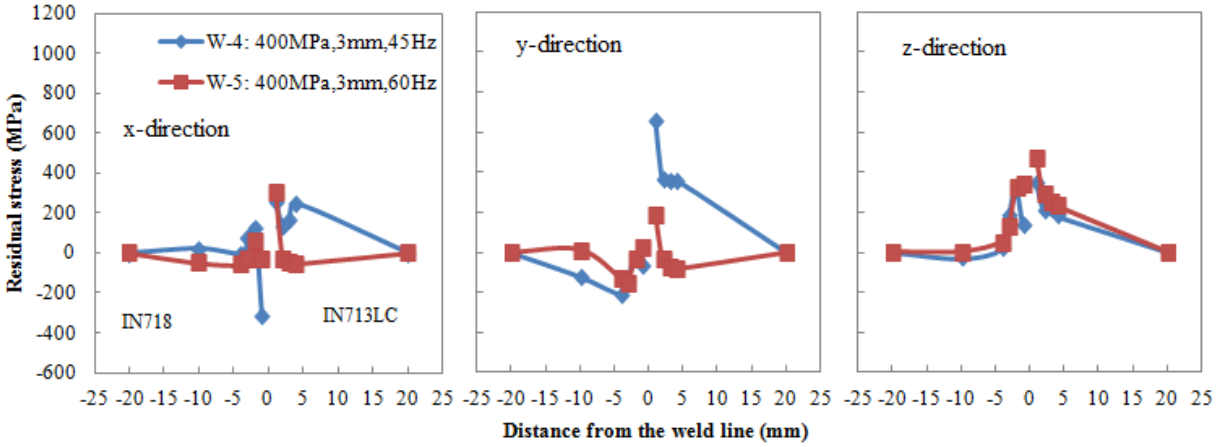

(a) (b) (c)

Fig. 5.32. Residual stress development of IN718-IN713LC LFWs under different frequency for (a) *x*, (b) *y*, and (c) *z*-directions

In IN718:

- The residual stress is in the region of 5 mm towards the weld line. The near weld line stress changes from tensile to compression, as the pressure increases. However, the amplitude and frequency do not show apparent correlation with residual stress.

- The largest tensile stress (420 MPa) arises in the *z*-direction near the weld line of the sample welded at 275 MPa (W1_275-2-45), which reaches 76% of the yield stress of solution treated IN718 (550 MPa). The lowest compressive stress (350 MPa) appears in the x-direction near the weld line of the sample welded at 600 MPa (W3_600-2-45).

In LFW, the residual stress is generated by the effect of temperature and welding force. In the oscillating process, the material in the weld zone is heated and expands. When the oscillation stops, temperature starts to decrease. The cool material near the weld affected zone restricts the hot material contraction, thus tending to leave a field of tensile stress in the weld zone. As discussed in Section 5.4.2, higher pressure allows the material to be welded at lower temperatures, which tends to generate smaller thermal expansion induced tensile stress. Meanwhile, a compressive stress is applied in the *z*-direction to consolidate the joining during cooling. This compressive stress can offset the thermal induced tensile stress, and finally results in a compressive stress in the *z*-direction at the weld line when it reaches a critical value. Moreover, the softened material is flowing out during oscillation and the welding pressure induced force is unlikely to be always parallel to *z*-direction, it may also generate stresses in the *x* and *y*-directions, which counteract the thermal induced tensile stress and leave compressive stresses while the pressure rises to a critical value. In this study, the critical value for creating compressive stresses in three directions near weld line is 600 MPa.

IN713LC:

- It shows a larger residual stress area (15 mm) and higher tensile stresses close to the weld line than that of IN718. Unlike IN718, the residual stress does not constantly decrease with increase of pressure, and the influence of amplitude and frequency on residual stress is not obvious.

- The largest tensile stress (1000 MPa) is in the *y*-direction of the sample welded at 275 MPa (W1_275-2-45), which is over the yield stress of the material (677 MPa). The lowest compressive stress (390 MPa) appears in the *z*-direction of the sample welded at 400 MPa (W2_400-2-45) at 4 mm from the weld line.

Since the diffraction pattern of IN713LC is poor, the stress values in IN713LC may be inaccurate. In addition, the lack of calculated strain free lattice spacing (d_0) may cause incorrect evaluation of the stress. These issues may cause the apparent different influence of weld pressure on residual stress development in IN713LC than IN718, but may also reflect high tensile stress in the sample welded at 275 MPa (W1_275-2-45). However, taken together with the IN718 results, it is reasonable to assume that the tensile stress in IN713LC reduces with increase of pressure. The work from Rooyen and Walpole [22] has proven that the residual stress distribution in IN713LC measured by the hole drilling method, is sensitive to weld pressure. The stress gauge was installed at 0.5 mm from the weld line. Results showed that increased pressure leads to smaller tensile stresses in the *x* and *y*-directions at 0.5 mm from the surface of IN713LC.

5.6. Conclusions

This chapter studied the microstructure-property development of LFWed IN718-IN713LC, focused on base metal and weld characterisation, including the investigations of macrostructure, microstructure, microtexture, microhardness, and residual stress.

- The base metal of IN718 and IN713LC showed very different microstructures. In forged IN718, equiaxed fine grains with random texture were observed, which

resulted in good flow behaviour during hot deformation. In comparison, coarse columnar grains with {001}<100> texture in cast IN713LC provided excellent creep resistance.

- During LFW, high temperature and large deformation induced dissolution of precipitates and recrystallisation. Compared with fusion welding, the HAZ in LFWs was relatively small. The area of the HAZ mainly depended on the weld pressure, with larger pressure producing a weld with a smaller HAZ. However, the influences of amplitude and frequency on the area of the weld zone were limited in extent.
- The strain rate in welding was very large, which allowed welds to be welded in a few seconds. The recrystallisation of IN718 was proved to be a CDRX mechanism by using EBSD.
- A weak texture was identified in the TMAZ of IN718. This microtexture could intensify with increase of weld pressure, but the enhancement is limited.
- LFWs showed uneven hardness distributions in the HAZ. It was found that there was a hardness trough in IN718 and a hardness increase in IN713LC. The different hardness distribution was attributed to the difference of strengthening particles, solid solution element, grain sizes, and stored dislocations across the weld.
- A large residual stress was detected in the weld zone. The residual stress could be changed from tensile to compressive while the weld pressure increases. It was assumed that large tensile stress would reduce the yield strength of the weld, whereas compressive stress could strengthen the material if the external force was applied in the opposite direction of compressive stress.

5.7. References

[1] M. M. Attallah, "Microstructure property development in friction stir welds of aluminim based alloys," *PhD Thesis, Metallurgy and Materials, University of Birmingham*, 2008.

[2] J. De Jaeger, D. Solas, T. Baudin, O. Fandeur, J.-H. Schmitt, and C. Rey, "Inconel 718 single and multipass modelling of hot forging," in *Superallloys 2012: 12th International Symposium on Superalloys*, Champion, USA, pp. 663-672, 2012.

[3] R. C. Reed, *The Superalloys: Fundamentals and Applications*. New York, Cambridge University Press, 2006.

[4] J. Zhou, V. Bushlya, and J. Stahl, "An investigation of surface damage in the high speed turning of Inconel 718 with use of whisker reinforced ceramic tools," *Journal of Materials Processing Technology*, vol. 212, pp. 372-384, 2012.

[5] M. Karadge, M. Preuss, P. J. Withers, and S. Bray, "Importance of crystal orientation in linear friction joining of single crystal to polycrystalline nickel-based superalloys," *Materials Science and Engineering A*, vol. 491, pp. 446-453, 2008.

[6] A. Mitchell, "The precipitation of primary carbides in IN718 and its relation to solidification conditions," in *Superalloys 718, 625, 706 and Derivatives*, Pittsburgh, pp. 299-310, 2005.

[7] F. Alexandre, S. Deyber, and A. Pineau, "Modelling the optimum grain size on the low cycle fatigue life of a Ni based superalloy in the presence of two possible crack initiation sites," *Scripta Materialia*, vol. 50, pp. 25-30, 2004.

[8] R. A. Ricks, A. J. Porter, and R. C. Ecob, "The growth of γ′ precipitates in nickel-base superalloys," *Acta Metallurgica*, vol. 31, pp. 43-53, 1983.

[9] T. Grosdidier, A. Hazotte, and A. Simon, "Precipitation and dissolution processes in γ/γ′ single crystal nickel-based superalloys," *Materials Science and Engineering A*, vol. 256, pp. 183-196, 1998.

[10] R. Damodaram, S. Ganesh Sundara Raman, and K. Prasad Rao, "Effect of post-weld heat treatments on microstructure and mechanical properties of friction welded alloy 718 joints," *Materials & Design*, vol. 53, pp. 954-961, 2014.

[11] D. Zhao and P. Chaudhury, "Effect of starting grain size on as-deformed microstructure in high temperature deformation of alloy 718," *Superalloys*, vol. 718, pp. 625-706, 1994.

[12] Y. Wang, W. Shao, L. Zhen, L. Yang, and X. Zhang, "Flow behavior and microstructures of superalloy 718 during high temperature deformation," *Materials Science and Engineering A*, vol. 497, pp. 479-486, 2008.

[13] A. Chamanfar, M. Jahazi, J. Gholipour, P. Wanjara, and S. Yue, "Modeling grain size and strain rate in linear friction welded Waspaloy," *Metallurgical and Materials Transactions A*, vol. 44A, pp. 4230-4238, 2013.

[14] R. Turner, J.-C. Gebelin, R. Ward, and R. Reed, "Linear friction welding of Ti–6Al–4V: modelling and validation," *Acta Materialia*, vol. 59, pp. 3792-3803, 2011.

[15] A. Vairis and M. Frost, "High frequency linear friction welding of a titanium alloy," *Wear*, vol. 217, pp. 117-131, 1998.

[16] S. Wang, L. Wang, and Y. Liu, "A novel approach to dynamic recrystallization nucleation for a nickel-base superalloy," *Acta Metallurgica Sinica (English letters)*, vol. 24, pp. 295-300, 2011.

[17] J. Romero, M. Attallah, M. Preuss, M. Karadge, and S. Bray, "Effect of the forging pressure on the microstructure and residual stress development in Ti–6Al–4V linear friction welds," *Acta Materialia*, vol. 57, pp. 5582-5592, 2009.

[18] W. Y. Li, T. j. Ma, and J. l. Li, "Numerical simulation of linear friction welding of titanium alloy: Effects of processing parameters," *Materials & Design*, vol. 31, pp. 1497-1507, 2010.

[19] C. Mary and M. Jahazi, "Linear friction welding of IN-718 process optimization and microstructure evolution," *Advanced Materials Research*, vol. 15, pp. 357-362, 2007.

[20] F. Daus, H. Y. Li, G. Baxter, S. Bray, and P. Bowen, "Mechanical and microstructural assessments of RR1000 to IN718 inertia welds - effects of welding parameters," *Materials Science & Technology*, vol. 23, pp. 1424-1432, 2007.

[21] P. G. Frankel, "Residual Stresses in Aerospace Components," *EngD Thesis, Metallurgy and Materials, University of Birmingham*, 2008.

[22] W. V. Rooyen and A. Walpole, "Assessing the metallurgical effects associated with the linear friction welding of IN713LC to IN718," Rolls-Royce plc., UK, MTL50577, 2010.

Chapter 6. Development of Post-Weld Heat Treatments for Linear Friction Welded IN718-IN713LC

The microstructural and microhardness development in as-welded IN718-IN713LC LFWs were discussed in Chapter 5. It was found that the grain size was refined towards the weld line, but the hardness decreased. This chapter aims to study the influence of the post-weld heat treatment (PWHT) on the microstructural and microhardness development in linear fraction welded IN718-IN713LC. The challenge in dissimilar welding is to develop a heat treatment that will homogenise the microstructure, recover the microhardness, and relieve the residual stresses, yet without negatively affecting either parent material.

6.1. Post-Weld Heat Treatment

Differential scanning calorimetry (DSC) was used to define the phase transformation temperatures of IN718 and IN713LC for determining the heat treatment temperatures. The phase transformation temperatures are listed in Tables 6.1 and 6.2, which are obtained from the DSC traces as shown in Fig. 7.1 and will be further discussed in Chapter 7. Three different PWHTs were applied to study their influence on the microstructural and microhardness development of W2_400-2-45, as introduced in Section 4.4, and the schematic diagram of PWHTs is shown in Fig. 6.1.

PWHT-1 is a two-stage aging treatment to precipitate γ″ at 760 ℃ and γ′ at 650 ℃, followed by air cooling (AC), which aims to strengthen IN718 and relieve the residual stresses [1]. PWHT-2 consists of a solution treatment of IN718 at 950 ℃ / 1 h to fully dissolve γ′/γ″, water quenching (WQ), followed by a two-stage aging at 720 ℃ / 8 h and 620 ℃ / 8 h for

precipitation of γ″ and γ′, and then AC. The purpose is to homogenise the microstructure and increase the hardness of IN718 [2]. PWHT-3 includes IN713LC γ′ and IN718 γ′/γ″ solution treatment at 1190 ℃ / 1 h, WQ, followed by a two-stage IN718 aging at 720 ℃ / 8 h and 620 ℃ / 8 h to precipitate γ″ and γ′, and then AC, in order to homogenise the microstructure of welds and improve the hardness of IN718.

Table 6.1. Phase transformation temperatures (℃) of IN718 at equilibrium based on the DSC measurements at heating/cooling rates 20 ℃/min

	Start of γ′/γ″ dissolution	γ′/γ″ solvus	Start of δ dissolution	δ solvus	MC solvus	Solidus	Liquidus
Current work	690	920	1010	1070	1290	1270	1345
Literature	670 [3]	910 [4]	980 [5]	1040 [6]	1294 [7]	1265 [7]	1348 [7]

Table 6.2. Phase transformation temperatures (℃) of IN713LC at equilibrium based on the DSC measurements at heating/cooling rates 20 ℃/min

	Start of γ′ dissolution	γ′ solvus	MC solvus	Solidus	Liquidus
Current work	900	1190	1325	1305	1359
Literature [8]	987	1205	1317	1250	1349

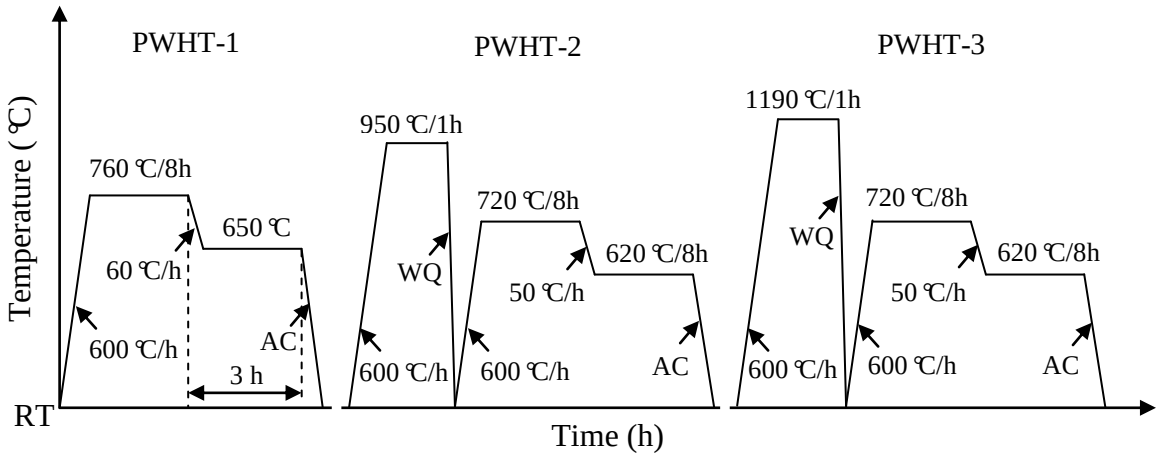

RT: room temperature, AC: air cooling, WQ: water quenching

Fig. 6.1. Schematic diagrams of three PWHT procedures

6.2. Microstructure

6.2.1. Precipitate Development

Figure 6.2 shows the microstructure of W2 after PWHT-1. When aging at 760 ℃ for 8 h and then cooling to 650 °C at rate 60 °C/h and holding for 1.5 h, large amounts of γ′/γ″ precipitate in the weld affected zone (WAZ) of IN718, as illustrated in Fig. 6.2.a. The precipitated γ′/γ″ has a mean diameter of ~33 nm (TEM is required to make precisely measurement), as shown in a high magnification SEM micrograph in Fig. 6.2.b. At the low aging temperature, no precipitate change occurs in IN713LC.

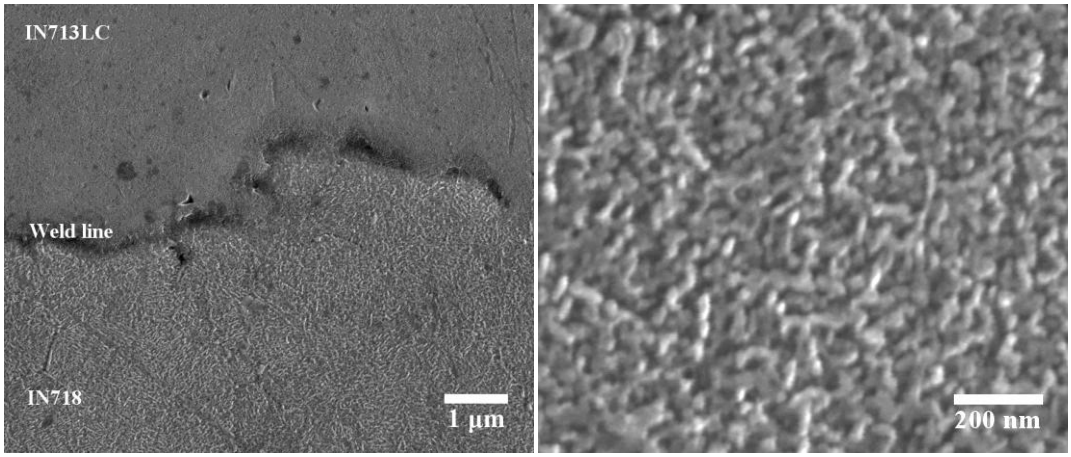

(a) (b)

Fig. 6.2. SEM SE micrographs showing the microstructure of (a) the weld line and (b) the precipitated γ′/γ″ in the WAZ of IN718 after PWHT-1

Figure 6.3 shows the microstructure of W2 after PWHT-2. δ precipitates were found near the weld line at the grain boundaries of IN718 (Fig. 6.3.a), as a result of solution treatment at 950 ℃ for 1 h, which can be explained by the TTT diagram in Fig. 6.4 [9]. The area percentage of precipitated δ in grain boundaries was found to be 6.3%, which is larger than that in the base metal (4.5%). Since the δ phase is incoherent with γ matrix, the increased δ phase does not confer hardening to the alloy. On the contrary, it may reduce the hardenability

due to the depletion of γ″. The presence of δ phase at grain boundaries can help to control the grain size, and therefore optimises the tensile and fatigue properties [10-12]. The precipitated δ is needle-shaped around 0.8-1.5 μm length and 0.2-0.5 μm width (Fig. 6.3.b), which is smaller than the size of δ in the base metal. At high magnification (Fig. 6.3.c), large amounts of γ′/γ″ are observed in the γ matrix, with an average size of ~20 nm. The γ′/γ″ in PWHT-2 is smaller than that in PWHT-1. This is because the aging temperatures of PWHT-2 (720 ℃ and 620 ℃) are lower than those of PWHT-1 (760 ℃ and 650 ℃), which causes a lower nucleation rate and lower growth rate for the γ′/γ″ precipitate in PWHT-2 [13], as shown in Fig. 6.4. As observed in PWHT-1 and PWHT-2, no apparent microstructure variation was observed in IN713LC.

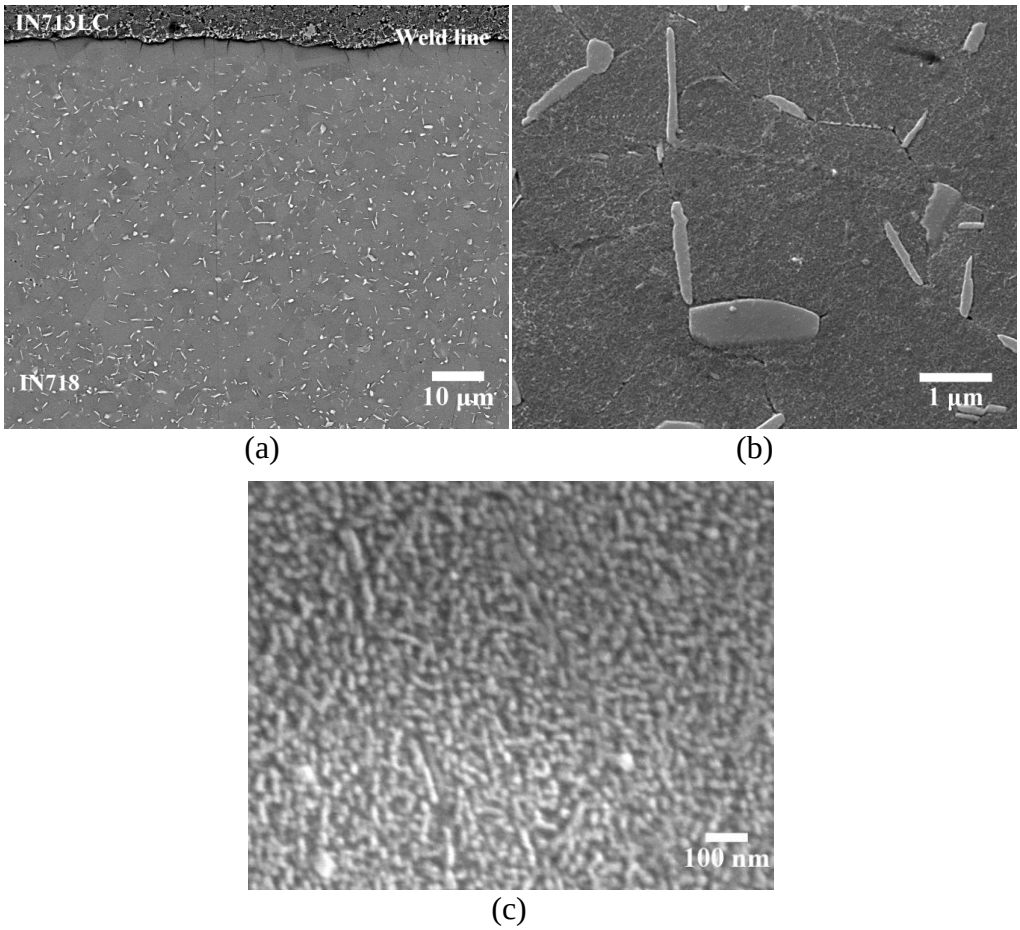

(a) (b)

(c)

Fig. 6.3. SEM micrographs showing the microstructure of (a) the weld line (BSE micrograph), (b) the precipitated δ (SE micrograph) and (c) γ′/γ″ in the WAZ of IN718 after PWHT-2 (SE micrograph)

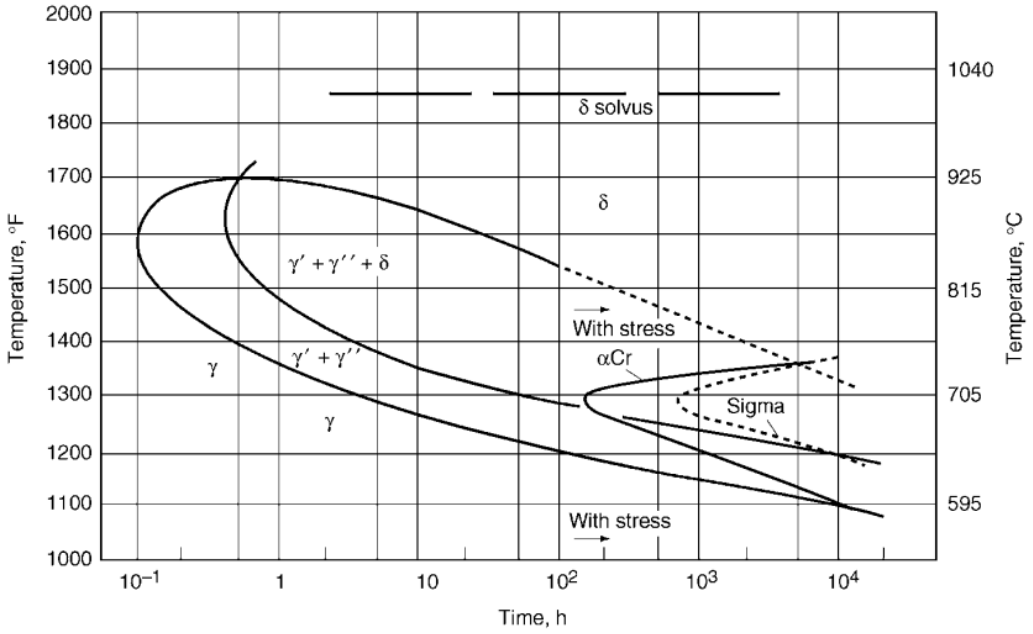

Fig. 6.4. TTT diagram of forged IN718 [9]

Figure 6.5 shows the microstructure of W2 after PWHT-3. As the sample was heated to 1190 °C, δ and γ′/γ″ in IN718 and γ′ in IN713LC were fully dissolved. The δ phase no longer pins the grain boundaries in IN718, and the grain size near the weld line dramatically increases (Fig. 6.5.a). Further analysis of the grain size will be discussed in Section 6.2.2. The precipitated γ′ in IN713LC is cubic, with a mean size of 94 nm, which is smaller than the γ′ before PWHT (260 nm). This is because the precipitated γ′ forms during the water quenching from 1190°C, and there is not enough time for growth. The precipitated γ′/γ″ in IN718 is similar in size to that formed in PWHT-2 (~22 nm), since the aging conditions are the same.

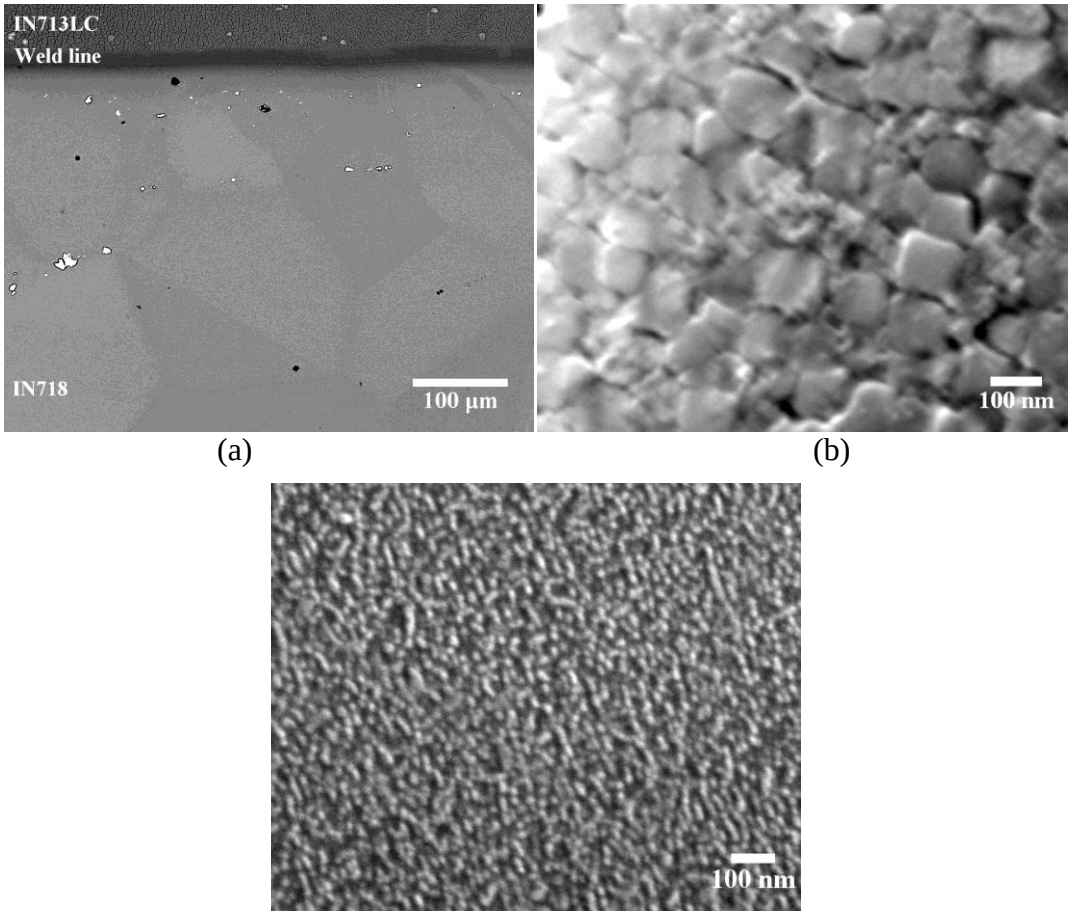

(a) (b)

(c)

Fig. 6.5. SEM micrographs showing the microstructure of (a) the weld line (BSE micrograph), (b) the precipitated γ′ in IN713LC (SE micrograph) and (c) γ′/γ″ in the WAZ of IN718 after PWHT-3 (SE micrograph)

6.2.2. Grain Structure Development

EBSD was used to analyse the influence of PWHT on the grain morphology, as shown in Figs. 6.6-6.9, and the grain size is illustrated in Fig. 6.10 (error <0.2 µm). It was expected that the PWHT might result in grain growth, which would consequently affect the mechanical properties.

Figure 6.6 shows the grain development of the as-welded W2. It shows equiaxed recrystallised grains (~2.1 μm) near the weld line of IN718 and a part of a coarse IN713LC grain. The deviation of colours in IN713LC reflects the local misorientation, which occurs due to the subgrain rotation during welding. The subgrains are formed through the accumulation and rearrangement of the dislocations during deformation. As a metal with low or intermediate stacking fault energy, Ni has slow recovery during dynamic recrystallisation, therefore high density of dislocations is assumed to remain in the as-welded condition. The TEM work on the friction welded IN718 by Damodaram *et al.* [14] has confirmed this.

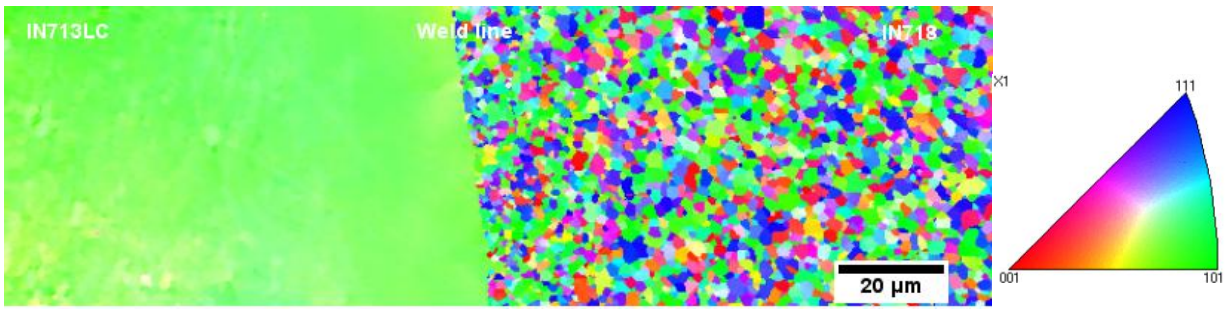

Fig. 6.6. EBSD IPF map showing the grain development of the as-welded W2

Due to the low heat treatment temperatures in PWHT-1, no grain growth was observed in the heat treatment process (Fig. 6.7). The grain size of PWHT-1 (~2.2 μm) is almost the same as that of the as-welded sample (~2.1 μm). No grain variation was found in IN713LC.

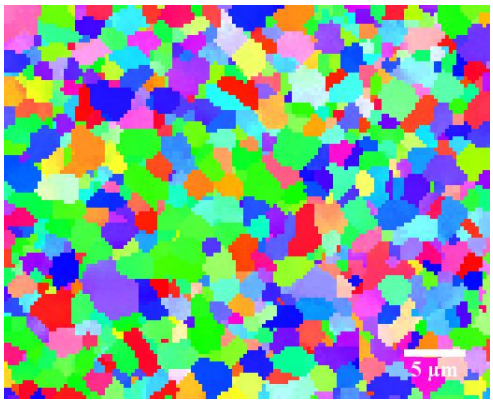

Fig. 6.7. EBSD IPF map showing the IN718 grains near the weld line after PWHT-1

During PWHT-2, sample is exposed at a higher temperature (950 ℃ for 1 h) than PWHT-1, which would be expected to cause grain growth. However, grain growth was hampered by the precipitated δ at grain boundaries during aging at 950 ℃, and only a slight grain growth occurred in PWHT-2 to 2.9 μm (Fig. 6.8), and some annealing twins were found in the PWHT-2 sample. No change of grain morphology was observed in IN713LC.

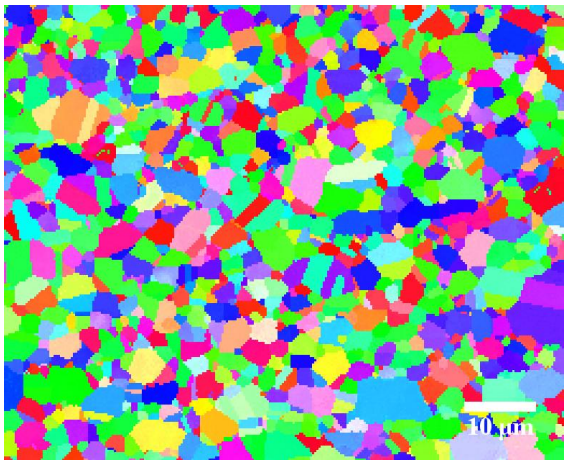

Fig. 6.8. EBSD IPF map showing the IN718 grains near the weld line after PWHT-2

In comparison with PWHT-1 and PWHT-2 samples, the grain morphology in PWHT-3 sample changes dramatically (Fig. 6.9). As the solution treatment temperature (1190 ℃/1 h) completely dissolves the δ phase, the grain size of IN718 dramatically increases to 150 μm, and a large volume fraction of annealing twins was observed. More changes occurred in IN713LC. The columnar grains of IN713LC recrystallised and generated equiaxed grains. It is believed that this is a static recrystallisation process and the recrystallisation driving force is attributed to the high dislocation density accumulated during LFW [15]. After recrystallisation, the recrystallised grains in IN713LC continuously grow in the solution treatment process to an average diameter of 157 μm, which is almost the same size as in IN718.

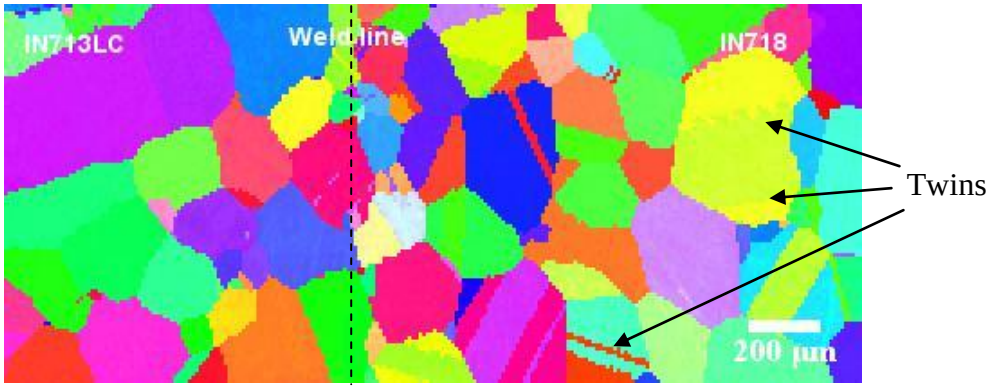

Fig. 6.9. EBSD IPF map showing the grain development across the weld line after PWHT-3

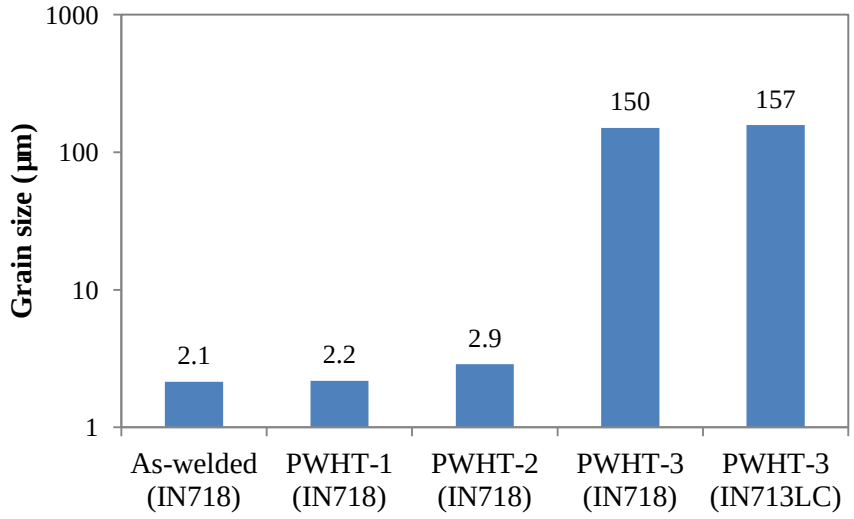

Fig. 6.10. Grain size variation in the as-welded and the PWHTed conditions

6.3. Microhardness

Figure 6.11 shows the microhardness development across the weld line in the as-welded and the PWHTed samples. An obvious hardness increase occurs in the WAZ of IN718. This is because that γ′/γ″ precipitation during the aging treatment, as shown in Figs. 6.2.b, 6.3.c and 6.5.c.

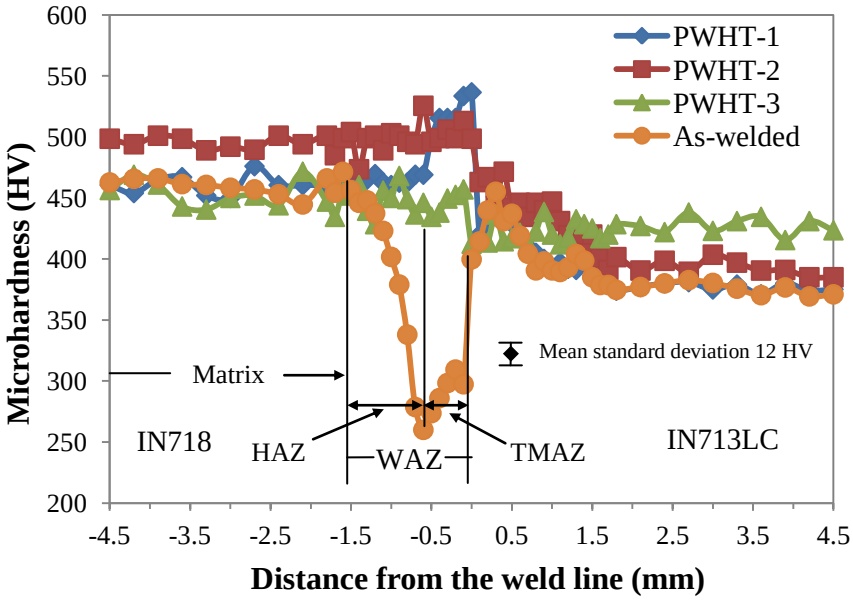

Fig. 6.11. Microhardness development in the as-welded and the PWHTed conditions

In the HAZ of IN718 of PWHT-1 sample (0.6-1.4 mm), the hardness recovers to the same value as that of the matrix (~460 HV), and then rapidly increases in the thermo-mechanically affected zone (TMAZ) from 0.6 mm to reach the maximum value (536 HV) at the weld line. The hardness peak in TMAZ is attributed to the grain boundary strengthening from the fine grains (Fig. 6.7), known as the Hall-Petch relation [16]. Also, the dissolved δ phase during welding provides more γ′/γ″ forming elements which cause more γ′/γ″ precipitating during aging treatment, therefore the hardness increases in TMAZ of IN718. No hardness change occurred in the IN718 matrix and IN713LC of PWHT-1 sample.

Comparing with PWHT-1 and the as-welded samples, the hardness of IN718 (500 HV) in PWHT-2 sample is relatively homogenous, which is 50 HV higher than the matrix hardness of the as-welded and PWHT-1 samples. This is attributed to the difference of heat treatment processes. PWHT-2 sample was solution treated to fully dissolve the γ′/γ″ phases, and the two-stage aging treatment induced precipitation of γ′/γ″ uniformly distributed in IN718. As

discussed in Section 6.2.1, the size of the precipitated γ′/γ″ in PWHT-2 (~20 nm) is finer than that of PWHT-1 (~33 nm), which can generate more precipitation strengthening to the material [17]. It is expected that the grain boundary strengthening obtained from the fine grains in the TMAZ of IN718 (Fig. 6.8) could generate a slight hardness increase similar to that which occurs in PWHT-1 sample. However, no hardness peak is shown in the TMAZ of the PWHT-2 sample. This is because that the reprecipitated δ in the TMAZ of PWHT-2 (Fig. 6.3.a) consumes more γ′/γ″ forming elements than that of δ in matrix, as the higher area percentage of reprecipitated δ (6.3%) than the δ in base metal (4.5%). The reprecipitated γ′/γ″ in the TMAZ might be slightly less than that in other places of IN718 and therefore the precipitation strengthening obtained from γ′/γ″ in the TMAZ is lower than that in base metal, which counteracts the grain boundary strengthening. A slight increase of hardness (20-40 HV) was found in IN713LC of PWHT-2 sample, which could be attributed to the precipitation strengthening obtained from the growth of γ′ during heat treatment.

PWHT-3 sample shows the most homogenous hardness distribution across the welds, in which the IN718 hardness is about 30 HV higher than the hardness of IN713LC. The hardness of IN718 in PWHT-3 (~440 HV) is lower than that in PWHT-2 (~500 HV). It is believed that the severe grain growth of IN718 (Fig. 6.9) reduced the grain boundary strengthening. Compared with other samples, the IN713LC of PWHT-3 has the most uniform hardness distribution, as the result of its homogenous morphology of grains and γ′ precipitates. However, PWHT-3 may not be suitable from application viewpoint. This is because the creep resistance of IN713LC is the limiting factor in high temperature application. The recrystallisation of IN713LC could significantly reduce its high temperature creep property, and the grain growth in IN718 is detrimental to its performance as a disc alloy.

6.4. Conclusions

This chapter studied the influence of three different PWHTs on the microstructural and microhardness development of LFWed IN718-IN713LC. SEM was used to investigate the precipitate development after heat treatment, along with micrograph analysis to quantify the percentage and size of precipitates. The study of grain development was carried out by EBSD, including the variation of grain size and morphology. Additionally, Vickers hardness was applied to measure the hardness across the welds. The following conclusions can be drawn:

- All the three PWHT methods have successfully recovered the hardness of the welds to reach or exceed the hardness of the as-welded sample. Simple aging treatment (PWHT-1) is the easiest way to strengthen the WAZ of IN718 by reprecipitating γ′/γ″ without forming other phases and changing grain morphology. A hardness peak is left near the weld line after PWHT-1 and the difference of the hardness of IN718 and IN713LC is around 170 HV.
- PWHT-2 develops a homogenous hardness in IN718 with the highest value 500 HV among all the PWHTed samples. The reprecipitated δ in TMAZ can prevent grain boundary migration at high temperatures [18]. A slight hardness increase occurs in IN713LC and the difference of the hardness of IN718 and IN713LC is ~110 HV. Similar to PWHT-1, this method does not cause much change of the grain morphology.
- PWHT-3 sample shows the most homogenous hardness distribution among these three PWHT methods. The hardness difference between IN718 and IN713LC is reduced to 30 HV. However, dramatic grain growth occurs in the welds since the sample is solution treated at high temperature (1190 ℃) [19]. The grain size of IN718 increased to 150 μm and the columnar grains of cast IN713LC recrystallised to

equiaxed grains, with an average size of 157 μm. Because the IN713LC is used as turbine blades, which requires the large columnar grains to maintain an excellent creep resistance at high temperature, PWHT-3 is not suitable to be applied in real production.

- In conclusion, PWHT-1 and PWHT-2 can be used to reinforce the strength of as-welded IN718-IN713LC in actual production, in which PWHT-1 is more efficient and PWHT-2 might produce higher mechanical properties.

6.5. References

[1] M. Preuss, P. J. Withers, and G. J. Baxter, "A comparison of inertia friction welds in three nickel base superalloys," *Materials Science and Engineering A,* vol. 437, pp. 38-45, 2006.

[2] Z. W. Huang, H. Y. Li, M. Preuss, M. Karadge, P. Bowen, S. Bray, and G. Baxter, "Inertia friction welding dissimilar nickel-based superalloys alloy 720Li to IN718," *Metallurgical and Materials Transactions A,* vol. 38, pp. 1608-1620, 2007.

[3] N. B. Dahotre, M. H. McCay, T. D. McCay, C. R. Hubbard, W. D. Porter, and O. B. Cavin, "Effect of grain structure on phase transformation events in the Inconel 718," *Scripta Metallurgica et Materialia,* vol. 28, pp. 1359-1364, 1993.

[4] J. R. Davis, *Heat-resistant Materials*. Ohio, ASM International, 1997.

[5] D. Y. Cai, W. H. Zhang, P. L. Nie, W. C. Liu, and M. Yao, "Dissolution kinetics and behavior of δ phase in Inconel 718," *Transactions Nonferrous Metals Society of China,* vol. 13, pp. 1338-1341, 2003.

[6] A. Niang, B. Viguier, and J. Lacaze, "Some features of anisothermal solid-state transformations in alloy 718," *Materials Characterization,* vol. 61, pp. 525-534, 2010.

[7] W. D. Cao, R. L. Kennedy, M. P. Willis, and T. Allvac, "Differential thermal analysis (DTA) study of the homogenization process in alloy 718," in *Superalloys 718, 625 and Various Derivatives*, Pittsburgh, USA, pp. 147-160, 1991.

[8] S. Zlá, B. Smetana, M. Žaludová, J. Dobrovská, V. Vodárek, K. Konečná, V. Matějka, and H. Francová, "Determination of thermophysical properties of high temperature alloy IN713LC by thermal analysis," *Journal of Thermal Analysis and Calorimetry,* vol. 110, pp. 211-219, 2012.

[9] M. J. Donachie, *Superalloys: A Technical Guide*, American Welding Society International, 2002.

[10] G. Sjoberg and N. G. Ingesten, "Grain boundary δ-phase morphologies, carbides and notch rupture sensitivity of cast alloy 718," in *Superalloys 718, 625 and Various Derivatives*, Pittsburgh, USA, pp. 603-620, 1991.

[11] R. C. Reed, *The Superalloys: Fundamentals and Applications*. New York, Cambridge University Press, 2006.

[12] S. Azadian, L. Y. Wei, and R. Warren, "Delta phase precipitation in Inconel 718," *Materials Characterization,* vol. 53, pp. 7-16, 2004.

[13] Y. F. Han, P. Deb, and M. C. Chaturvedi, "Coarsening behaviour of γ″- and γ′-particles in Inconel alloy 718," *Metal Science,* vol. 16, pp. 555-562, 1982.

[14] R. Damodaram, S. Ganesh Sundara Raman, and K. Prasad Rao, "Effect of post-weld heat treatments on microstructure and mechanical properties of friction welded alloy 718 joints," *Materials & Design,* vol. 53, pp. 954-961, 2014.

[15] X. Lin, M. H. Song, W. W. Zhao, and J. Chen, "Effect of intermediate heat treatment temperature on microstructure and notch sensitivity of laser solid formed Inconel 718 superalloy," *Journal of Wuhan University of Technology-Materials Science Edition,* vol. 26, pp. 908-913, 2011.

[16] L. L. Shaw, A. L. Ortiz, and J. C. Villegas, "Hall–Petch relationship in a nanotwinned nickel alloy," *Scripta materialia,* vol. 58, pp. 951-954, 2008.

[17] M. Sundararaman, P. Mukhopadhyay, and S. Banerjee, "Deformation behaviour of γ" strengthened Inconel 718," *Acta Metallurgica,* vol. 36, pp. 847-864, 1988.

[18] S. Patel and G. Smith, "The role of niobium in wrought superalloys," in *International Symposium on Niobium 2001,* Orlando, USA, pp. 1081-1108, 2001.

[19] L. Chen, F. Sui, and X. Liu, "Grain growth model of Inconel 718 alloy forged slab in reheating process prior to rough rolling," *Acta Metall. Sin,* vol. 45, p. 1242, 2009.

Chapter 7. Influence of the Heating Rate on Precipitate Dissolution during Welding of Ni-based Superalloys

The rapid heating to high temperatures in LFW can induce drastic microstructural changes in the welds. For instance, δ and γ′ precipitates can be dissolved if the temperature approaches the solvus temperature. The dissolution of these precipitates can affect the mechanical properties of the weld. Since dissolution is a diffusion-controlled process, the rapid heating during welding may result in a different evolution of precipitates from those in isothermal or equilibrium heating. In this chapter, the dissolution of γ′ phase in IN713LC and δ phase in IN718 due to rapid heating is discussed. Gleeble thermal simulations were performed, combined with analytical modelling, to study the kinetic effects of rapid heating, followed by air cooling (AC), in order to simulate welding dissolution phenomena.

7.1. Precipitates Dissolution

Differential scanning calorimetry (DSC) and furnace heat treatments were used to determine the equilibrium phase transformation temperatures, including dissolution and melting in IN718 and IN713LC. The IN718 and IN713LC were provided by Rolls-Royce plc. All the tests were carried out on the alloys in the as-received condition. The IN718 underwent a sub-δ solvus heat treatment at 980 ℃ for 1 h, followed by aging treatment at 720 ℃ for 8 h, and controlled cooling at 50 ℃/min to 620 ℃, held 8 h before AC. IN713LC casting bar underwent a γ′ solution treatment at 1190 ℃ for 1 h/vacuum followed by furnace cooling, in order to obtain a homogenous microstructure of IN713LC.

7.1.1. Phase Transformation Temperatures

Phase transformation temperatures of IN713LC and IN718 were determined using DSC at heating/cooling rates of 20 ℃/min to a peak temperature of 1400 ℃. Figure 7.1 shows DSC traces for the endothermic/exothermic peaks corresponding to the phase transformations in IN713LC and IN718. For IN713LC, γ′ starts dissolving at 900 °C, and completely dissolves at 1190 ℃. The γ′ solvus temperature is estimated by averaging the end temperature of the γ′ dissolution on heating and the start temperature of the γ′ precipitation on cooling, and it is within the range of 1180-1200 ℃, as expected from the literature [1]. Tables 7.1 and 7.2 list the phase transformation temperatures of IN713LC and IN718, respectively.

It can be difficult to precisely identify the dissolution temperatures only based on thermal analysis. Microstructural characterisation was also carried out to study the dissolution of precipitates.

Table 7.1. Phase transformation temperatures (℃) of IN713LC at equilibrium based on the DSC measurements

	Start of γ′ dissolution	γ′ solvus	MC solvus	Solidus	Liquidus
Current work	900	1190	1325	1305	1359
Literature [2]	987	1205	1317	1250	1349

Table 7.2. Phase transformation temperatures (℃) of IN718 at equilibrium based on the DSC measurements

	Start of γ′/γ″ dissolution	γ′/γ″ solvus	Start of δ dissolution	δ solvus	MC solvus	Solidus	Liquidus
Current work	690	920	1010	1070	1290	1270	1345
Literature	670 [3]	910 [4]	980 [5]	1040 [6]	1294 [7]	1265 [7]	1348 [7]

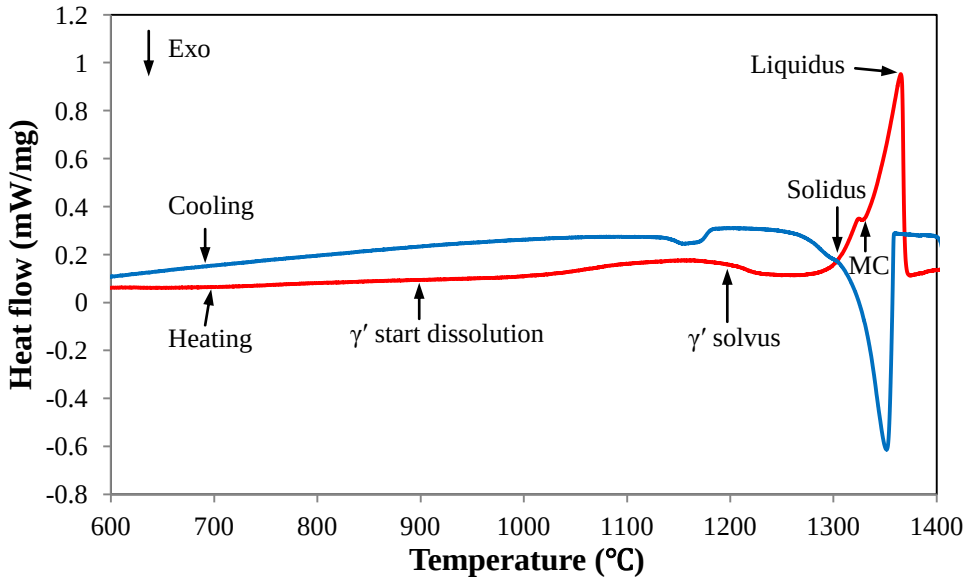

(a)

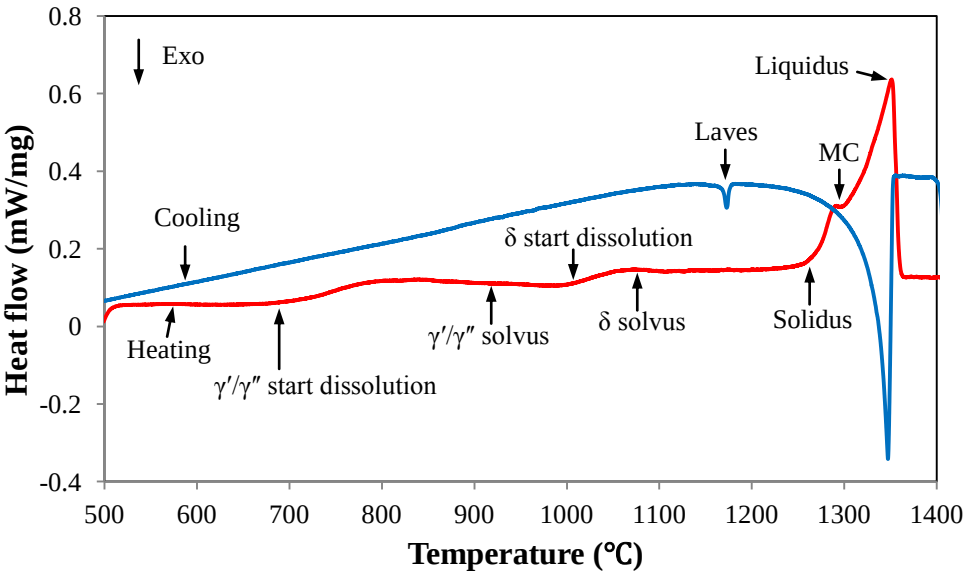

(b)

Fig. 7.1. DSC traces for (a) IN713LC and (b) IN718 base metal

7.1.2. γ′ Dissolution in IN713LC at Equilibrium Heating

Further studies of γ′ dissolution in IN713LC at equilibrium were performed using furnace heat treatments and quantitative microscopy. Small cubic samples were heated to peak temperatures between 920 ℃ to 1190 ℃, and held for 1 h to enable the extent of γ′

dissolution to approach equilibrium [8, 9], followed by water quenching, as described in Section 4.6. Heat treatment temperatures were chosen from the γ′ dissolution range identified for IN713LC using DSC, as illustrated in Fig.7.1.a. The γ′ volume fraction was measured using ImageJ, as shown in Fig. 7.2. It shows the secondary γ′ precipitates are uniformly distributed with the γ matrix, with size ~0.13 μm. The volume fraction of γ′ in IN713LC base metal is 60%.

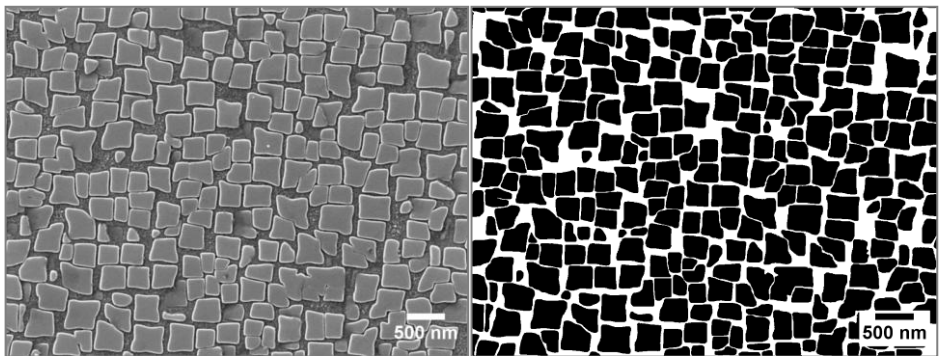

(a) (b)

Fig. 7.2. Microstructure of γ′ phase in IN713LC base metal, (a) SEM micrograph used for ImageJ analysis, and (b) threshold image obtained using ImageJ

Figure 7.3 shows the volume fraction of γ′ in IN713LC as a function of the heat treatment temperature at equilibrium, following water quenching. The measured γ′ volume fraction was consistent with the DSC data, in which γ′ starts dissolving at ~900 °C, and completely dissolves at 1190 ℃. Reprecipitated γ′ formed during cooling. It is interesting to note that the volume fraction presents an exponential decay along with the rising temperature. Initially, γ′ dissolves slowly when the temperature is low. However, the dissolution rate increases rapidly when the temperature approaches the solvus temperature.

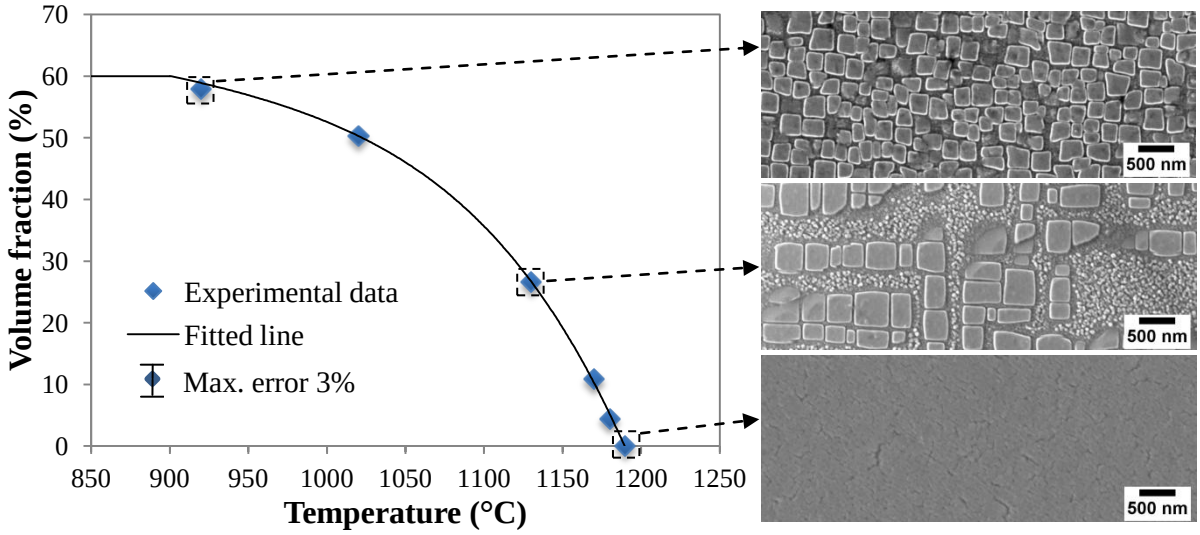

Fig. 7.3. Variation in the γ′ volume fraction in IN713LC following equilibrium heating and water quenching

7.1.3. δ Dissolution in IN718 at Equilibrium Heating

As shown in Table 7.2, the δ phase dissolves in a temperature range between 1010 °C and 1070 ℃, which is a similar temperature range to other data in the literature, between 950 ℃ and 1010 ℃ by Azadian *et al.* [10]. However, the measured δ solvus temperature 1070 °C in the current study is slightly higher than Azadian's data ~1010 °C. This is due to the difference of the Nb content (current study: 5.7 wt.%, Azadian *et al*: 5.3 wt.%), as shown in Fig. 7.4. As reported by Niang *et al.* [6], the δ solvus temperature is proportional to the Nb content. Based on Niang's results, the δ solvus at Nb 5.7 wt.% (in this study) predicted by extrapolation is ~1074 ℃, which is in a good agreement with the DSC measured solvus temperature (1070 ℃).

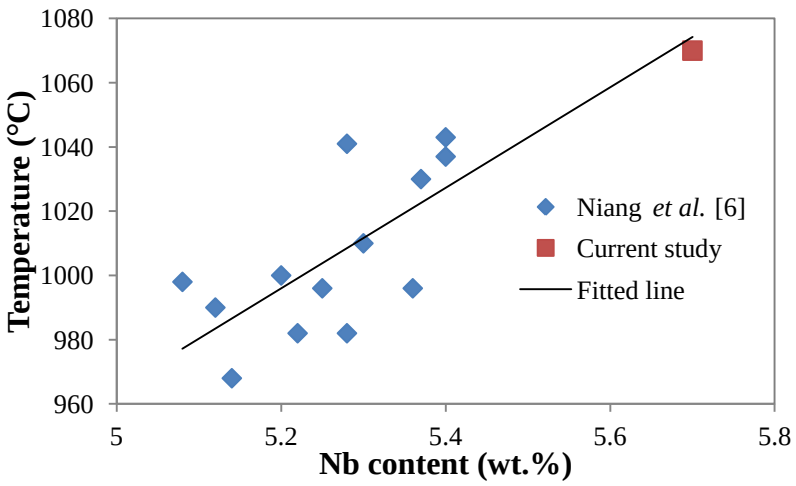

Fig. 7.4. δ phase solvus temperature for different Nb contents of IN718 showing the data from this study and the literature

Figure 7.5 shows the microstructure of δ in IN718 base metal. The δ volume fraction was measured using ImageJ. It shows the δ precipitates are mainly located at grain boundaries, and are occasionally intragranular. The size and volume fraction of δ phase in IN718 is ~0.54 μm and 0.95%, respectively.

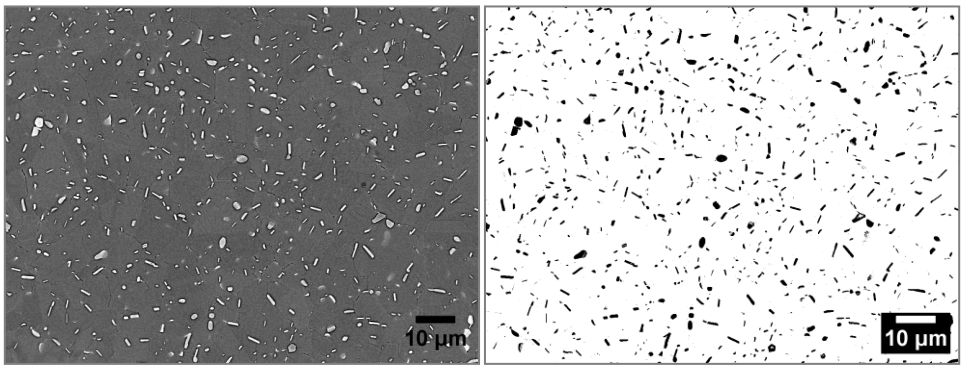

Fig. 7.5. Microstructure of δ phase in IN718 base metal, (a) SEM BSE micrograph used for ImageJ analysis, and (b) threshold image obtained using ImageJ

Figure 7.6 shows the development of the equilibrium volume fraction of δ phase in IN718 as a function of the heat treatment temperature. Similar to γ′ dissolution in IN713LC, the

volume fraction of δ phase in IN718 also presents an exponential decay along with the increasing temperature. The δ phase starts to dissolve at ~1010 ℃, and completely dissolves at ~1070 ℃.

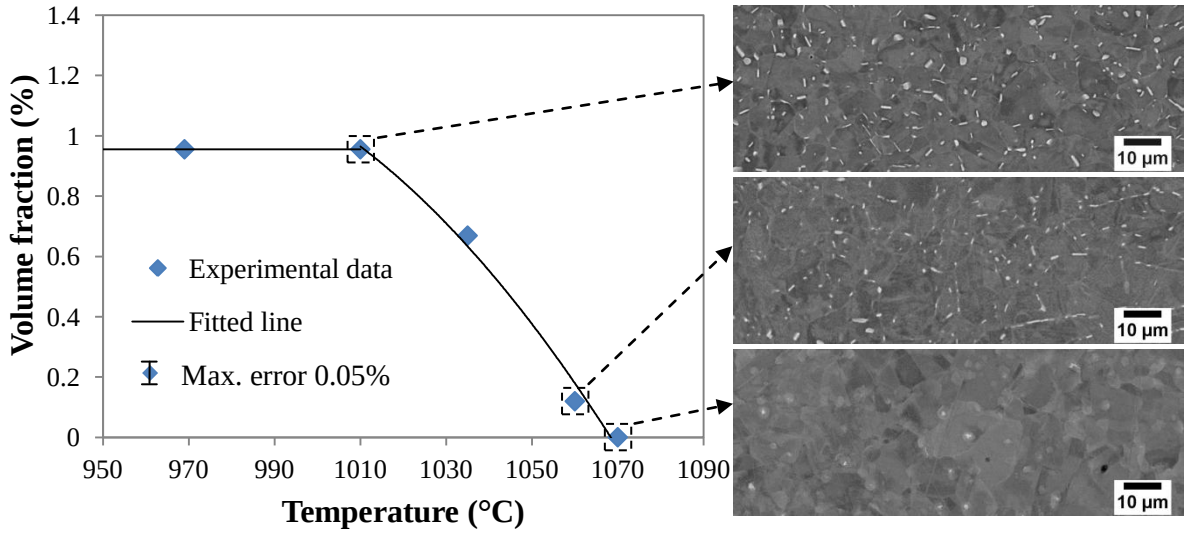

Fig. 7.6. Variation in δ phase volume fraction in IN718 following equilibrium heating and water quenching

7.2. Precipitate Dissolution due to Rapid Heating

During welding, the material is rapidly heated to elevated temperature and then cooled rapidly in air. In this case, the precipitates dissolve under a non-isothermal process, and the equilibrium phase transformations are no longer applicable. In the current study, the dissolution behaviour of γ′ and δ under rapid heating was investigated. The sample heat treatment process was described in Section 4.7. After thermal cycling using the Gleeble thermal simulator, the SEM micrographs were taken for microstructural analysis from the area near the thermocouples.

7.2.1. γ′ Dissolution in IN713LC due to Rapid Heating

Figure 7.7 shows the development in the γ′ volume fraction in IN713LC under different heating rates (1 ℃/s to 1000 ℃/s). The dissolution of γ′ shifts to higher temperature with increase of heating rate, as expected from the literature [2].

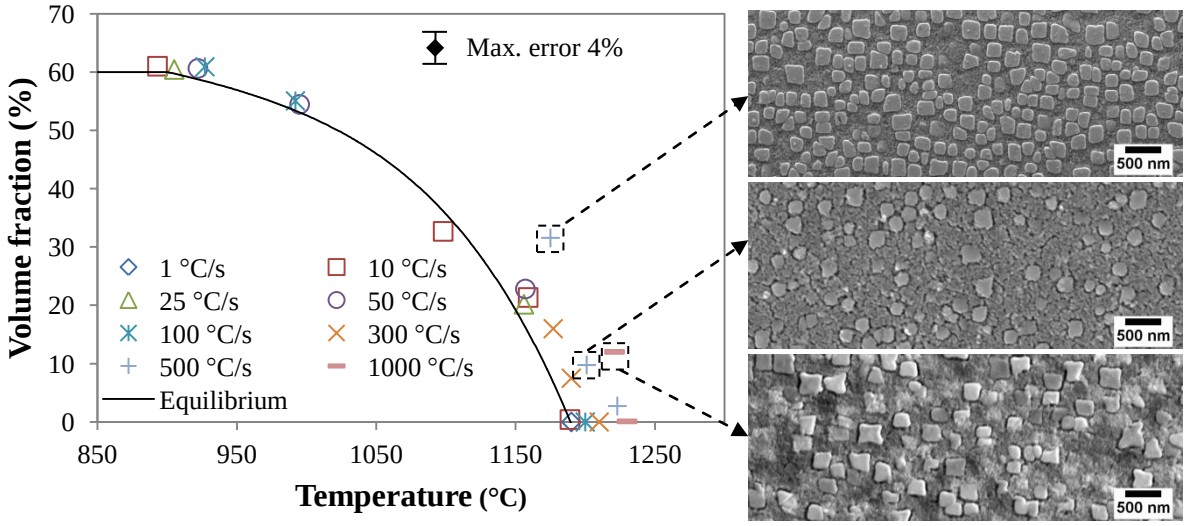

Fig. 7.7. Variation of the volume fraction of γ′ phase in IN713LC at different heating rates

The temperature at which the γ′ dissolves completely (γ′ solvus temperature) was found to rise with the increase in the heating rate, as shown in Fig. 7.8. The γ′ solvus increased 40 ℃ from 1190 ℃ at equilibrium to 1230 ℃ at a heating rate of 1000 ℃/s. No constitutional liquation phenomenon was observed (the concept of constitutional liquation was discussed in Section 2.5.1), which can be explained using Fig. 7.9. When rapidly heating an alloy with a composition X, the γ′ precipitates may not have enough time to completely dissolve when the temperature reaches the γ′ equilibrium solvus (T_{solvus}). As such, the γ′ solvus (T_1) will exceed the equilibrium T_{solvus}. If the heating rate becomes very rapidly, the γ′ precipitates cannot completely dissolve before reaching the γ-γ′ eutectic temperature T_E, which will cause the

local constitutional liquation due to the inverse γ-γ′ eutectic reaction. There is another factor which affects constitutional liquation, which is the size of γ′ precipitates. If the alloy presents primary γ′ precipitates (1-10 μm), there is no chance for them to be dissolved before T_E under rapid heating, and liquation will occur [11-13]. In the present study, the size of γ′ is uniformly distributed ~0.13 μm. The γ′ solvus temperature rises to 1230 ℃ at 1000 ℃/s heating rate, which is still below the γ-γ′ eutectic temperature T_E (1250 ℃) proposed by Zlá *et al.* [2]. Hence, when the temperature reaches T_E, γ′ precipitates have already completely dissolved, and there will be no residual γ′ precipitate to react with the γ matrix to give rise to the eutectic reaction to form a liquid phase (constitutional liquation). More investigations on the modelling of the γ′ dissolution will be discussed in Section 7.3.

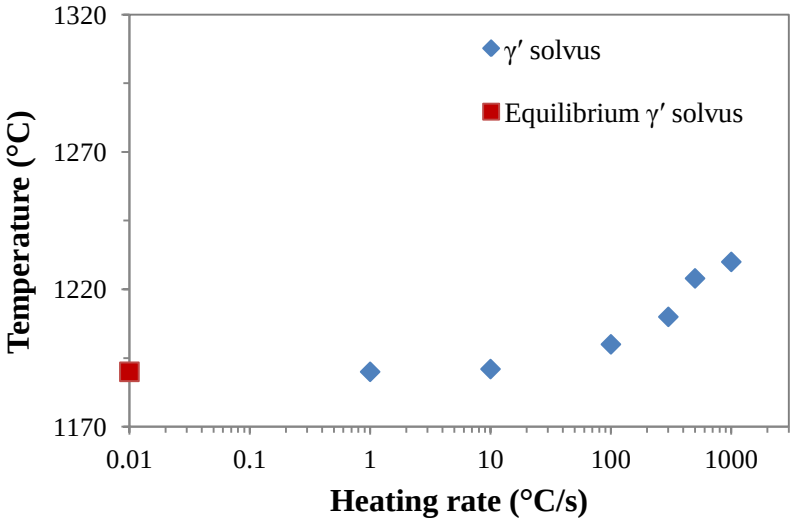

Fig. 7.8. Variation of the γ′ solvus in IN713LC at different heating rates

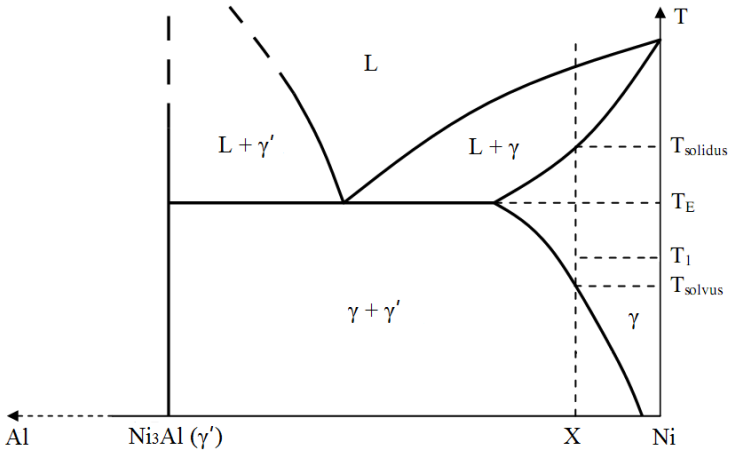

Fig. 7.9. Ni-Al phase diagram illustrating the γ-γ′constitutional liquation

7.2.2. δ Dissolution in IN718 due to Rapid Heating

Figure 7.10 shows the development of the δ volume fraction in IN718 at heating rates 1 ℃/s, 300 ℃/s, and 700 ℃/s. In comparison with equilibrium heating, the dissolution of δ phase shifts to higher temperature with the increase in the heating rate. The reason is similar to γ′ dissolution which has been discussed in Section 7.2.1, the higher heating rate allows less time for precipitate dissolution when samples are heated to the same temperature.

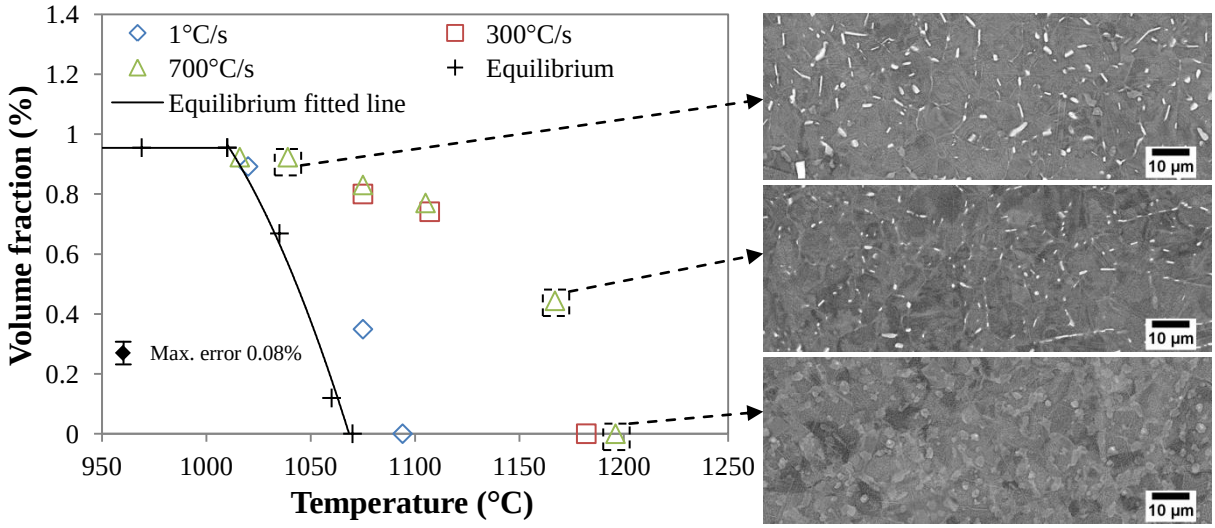

Fig. 7.10. Variation of the volume fraction of δ phase at different heating rates followed by air cooling

Figure 7.11 shows the variation in the δ solvus with the heating rate. The solvus temperature increases from 1070 ℃ at equilibrium to 1196 ℃ at 700 ℃/s heating rate. The heating rate shows a bigger effect on the δ dissolution than in the case of γ′ in IN713LC. This is because the size of δ (0.54 μm) is larger than that of γ′ (0.13 μm), so that δ phase is more difficult to dissolve. More investigations on the modelling of the δ dissolution will be discussed in Section 7.3.

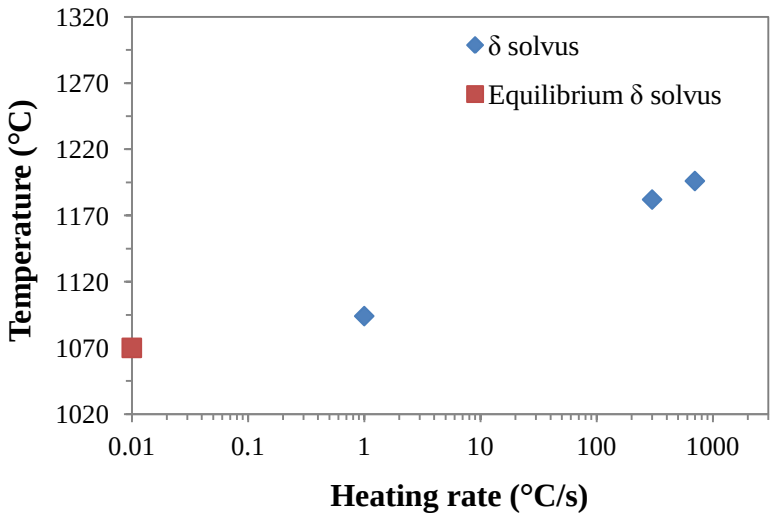

Fig. 7.11. Variation of the δ solvus at different heating rates followed by air cooling

7.3. Mathematical Modelling of Precipitate Dissolution

In the current study, a mathematical model to predict γ′ and δ dissolution due to transient thermal cycling in IN713LC and IN718 was established, which can be used to predict the development of the γ′ and δ volume fraction during rapid thermal cycles, as well as to calculate the variation in the γ′ and δ solvus. The model is based on the work of γ′ dissolution

in Astroloy by Soucail and Bienvenu [14], and the model by Ashby and Easterling [15] for the dissolution of carbides in steel welds.

7.3.1. Modelling of Precipitate Dissolution at Equilibrium

In IN713LC, Al is present mainly in γ′ precipitates and the γ matrix. Similarly for IN718, Nb can be assumed to be primarily in δ and γ when the material is heated above the γ′/γ″ solvus (920 ℃). The equation for Al content in IN713LC can be expressed as:

$$X_{Al} = f_{\gamma'}(T) \cdot X_{Al,\gamma'} + \left(1 - f_{\gamma'}(T)\right) \cdot X_{Al,\gamma}(T) \tag{7.1}$$

where $f_{\gamma'}(T)$ is the volume fraction of γ′ at temperature *T*, X_{Al} is the atomic fraction of Al in the alloy, $X_{Al,\gamma}(T)$ is the atomic fraction of Al in the γ at temperature *T*, $X_{Al,\gamma'}$ is the atomic fraction of Al in γ′ phase. Equation 7.1 can be rearranged to:

$$f_{\gamma'}(T) = \frac{X_{Al} - X_{Al,\gamma}(T)}{X_{Al,\gamma'} - X_{Al,\gamma}(T)} \tag{7.2}$$

Similarly for IN718, the equilibrium volume fraction of δ phase is given by:

$$f_{\delta}(T) = \frac{X_{Nb} - X_{Nb,\gamma}(T)}{X_{Nb,\delta} - X_{Nb,\gamma}(T)} \tag{7.3}$$

where $f_{\delta}(T)$ is the volume fraction of δ at temperature *T*, X_{Nb} is the atomic fraction of Nb in the alloy, $X_{Nb,\gamma}(T)$ is the atomic fraction of Nb in the γ at temperature *T*, and $X_{Nb,\delta}$ is the atomic fraction of Nb in δ phase.

X_{Al} and X_{Nb} are 0.123 and 0.036, as shown in Table 5.2 and Table 5.1. $X_{Al,\gamma'}$ and $X_{Nb,\delta}$ are considered independent of temperature, are 0.178 and 0.177, obtained from the averaged value of ten measurements by EDX using TEM for the base metal, as listed in Table 7.3. Thus, $X_{Al,\gamma}(T)$ and $X_{Nb,\gamma}(T)$ can be calculated from the experimental data of $f_{\gamma'}(T)$ and

$f_\delta(T)$, as illustrated in Figs. 7.3 and 7.6. The logarithm of $X_{Al,\gamma}(T)$ and $X_{Nb,\gamma}(T)$ versus $1/T$ are plotted in Figs. 7.12 and 7.13.

Table 7.3. Chemical composition of γ′ and δ phase measured by EDX/TEM

Phase	Al	Nb	Ti	Cr	Mo	Ni	Fe
γ′ (at.%) in IN713LC	17.84	1.99	1.50	4.89	1.37	72.41	-
δ (at.%) in IN718	0.29	17.66	3.73	2.33	0.85	71.14	4.00

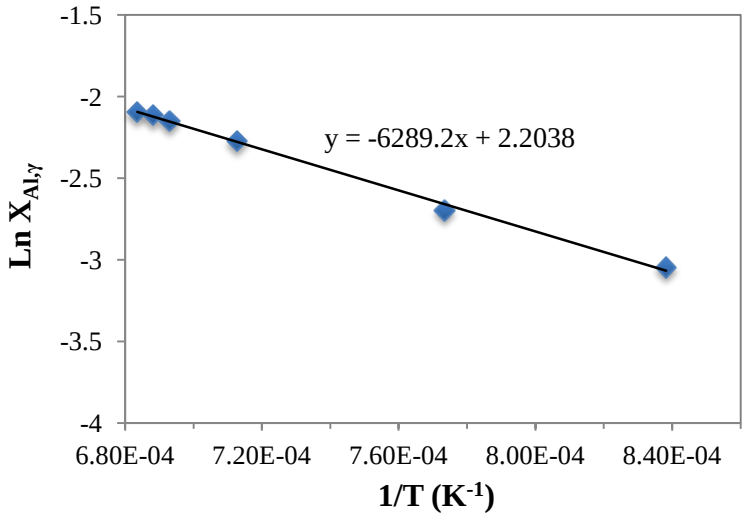

Fig. 7.12. Logarithm of $X_{Al,\gamma}(T)$ versus $1/T$ with their least squares fitted line

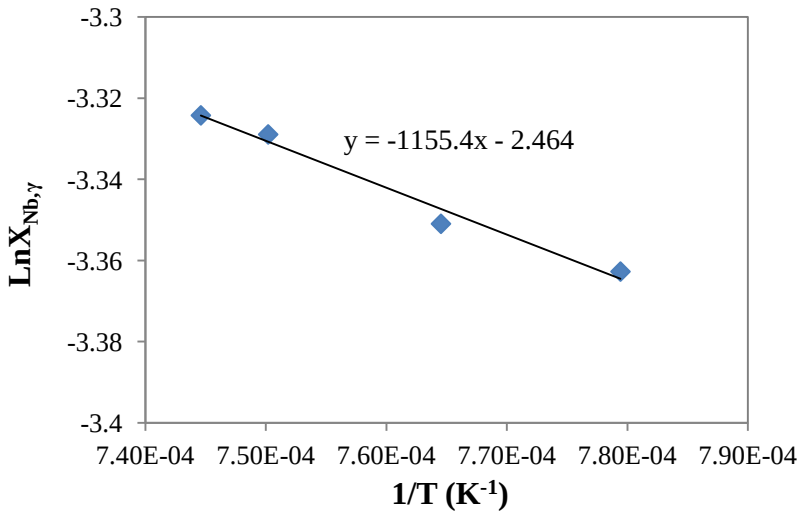

Fig. 7. 13. Logarithm of $X_{Nb,\gamma}(T)$ versus $1/T$ with their least squares fitted line

The relationship between the logarithm of $X_{Al,\gamma}(T)$, $X_{Nb,\gamma}(T)$ and T are given by the least squares fitted lines as:

$$\ln X_{Al,\gamma} = 2.2 - \frac{6289.2}{T+273}\ ,T\ in\ °C \tag{7.4}$$

$$\ln X_{Nb,\gamma} = -2.46 - \frac{1155.4}{T+273}\ ,T\ in\ °C \tag{7.5}$$

Substituting Equations 7.4 and 7.5 into Equations 7.2 and 7.3 respectively, the development of the volume fraction of γ′ and δ at equilibrium are obtained:

$$\begin{cases} T < 900°C: & f_{\gamma'}(T) = 0.6 \\ 900 \le T \le 1190°C: & f_{\gamma'}(T) = \frac{0.123 - exp\left(2.2 - \frac{6289.2}{T+273}\right)}{0.178 - exp\left(2.2 - \frac{6289.2}{T+273}\right)} \end{cases} \tag{7.6}$$

$$\begin{cases} T < 1010°C: & f_{\delta}(T) = 0.0095 \\ 1010 \le T \le 1070°C: & f_{\delta}(T) = \frac{0.036 - exp\left(-2.46 - \frac{1155.4}{T+273}\right)}{0.177 - exp\left(-2.46 - \frac{1155.4}{T+273}\right)} \end{cases} \tag{7.7}$$

Figures 7.14 and 7.15 show the model of the equilibrium γ′ and δ volume fraction in IN713LC and IN718 generated by Equations 7.6 and 7.7, respectively. The models match well the experimental data, which proves the practical validity of the simple models.

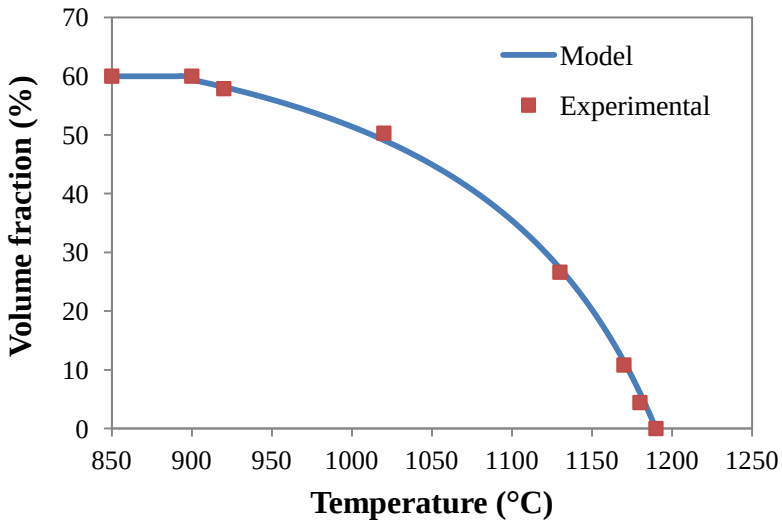

Fig. 7.14. The prediction of the mathematical model and the experimental data of the γ′ volume fraction variation IN713LC due to equilibrium heating and water quenching

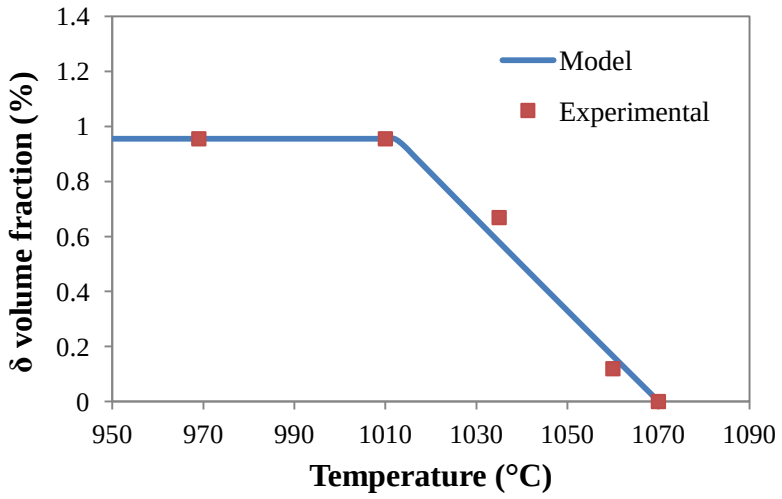

Fig. 7.15. The prediction of the mathematical model and the experimental data of the δ volume fraction variation in IN718 due to equilibrium heating and water quenching

7.3.2. Modelling of Precipitate Dissolution during Rapid Thermal Cycling

7.3.2.a. Concept of the Time-Temperature Equivalence

Figure 7.16 shows the recorded temperature when heating IN713LC using the Gleeble to 1200 ℃ at a heating rate of 300 ℃/s, followed by air cooling. The temperature shows an exponential decay during cooling, but it shows a linear decay from the peak temperature to the temperature (900 ℃) within the dissolution range of γ′. The linear decay of temperature was also observed over the dissolution range of temperatures in other thermal cycles at various heating rates. Therefore, the thermal cycles can be simplified to a heat treatment process with constant heating and cooling rates. The programmed and measured thermal data of IN713LC is listed in Table 7.4. Similarly, the temperature shows a linear decay from the peak temperature to the temperature (1010 ℃) at which δ starts to dissolve for IN718. The thermal data of IN718 is listed in Table 7.5.

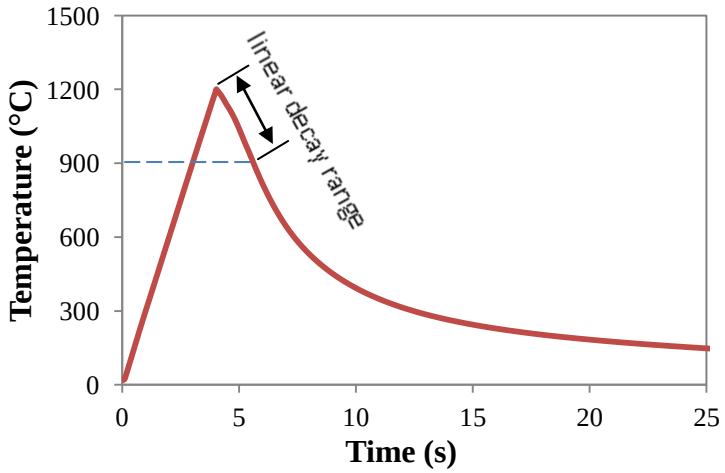

Fig. 7.16. Temperature development of IN713LC under heating rate 300 ℃/s to 1200 ℃ followed by air cooling

Table 7.4. Programmed and measured thermal data of Gleeble rapid thermal cycling of IN713LC

Programmed Heating rate-Peak temperature (℃/s-℃)	Measured Heating rate-Cooling rate-Peak temperature (℃/s-℃/s-℃)	Programmed Heating rate-Peak temperature (℃/s-℃)	Measured Heating rate-Cooling rate-Peak temperature (℃/s-℃/s-℃)
1-1190	1-125-1190	100-1000	100-92-992
10-900	10-N/A-893	100-1200	100-188-1198
10-1100	10-50-1098	300-1190	300-125-1177
10-1160	10-98-1159	300-1200	300-244-1190
10-1190	10-215-1189	300-1210	300-189-1210
25-900	25-40-905	500-1190	500-279-1175
25-1160	25-57-1156	500-1220	500-237-1201
50-900	50-42-922	500-1260	500-176-1223
50-1000	50-101-995	1000-1270	1000-218-1221
50-1160	50-74-1157	1000-1280	1000-261-1230
100-900	100-43-927		

Table 7.5. Programmed and measured thermal data of Gleeble rapid thermal cycling of IN718

Programmed Heating rate-Peak temperature (℃/s-℃)	Measured Heating rate-Cooling rate-Peak temperature (℃/s-℃/s-℃)	Programmed Heating rate-Peak temperature (℃/s-℃)	Measured Heating rate-Cooling rate-Peak temperature (℃/s-℃/s-℃)
1-1020	1-150-1020	700-1020	700-150-1020
1-1075	1-200-1075	700-1075	700-125-1039
1-1095	1-215-1095	700-1095	700-204-1075
300-1080	300-215-1075	700-1105	700-179-1105
300-1110	300-267-1107	700-1195	700-214-1167
300-1190	300-228-1182	700-1215	700-223-1196

To solve the precipitate dissolution during rapid thermal cycling, a concept of time-temperature equivalence was adopted, as discussed in Section 2.5.1. Figure 7.17 shows the time-temperature equivalence used in the current study. The thermal cycle with heating rate V_h from the initial temperature T_0 at time t_0 to the peak temperature T_p at time t_p, and with cooling rate V_c to T_0 at t_f, was replaced by an equivalent hold time t_e at peak temperature T_p. The t_e is sum of the equivalent heating time t_{eh} and the equivalent cooling time t_{ec}. The t_{eh} is defined as:

$$t_{eh} = \int_{t_0}^{t_p} \exp\left(-\frac{Q}{R}\left(\frac{1}{T} - \frac{1}{T_p}\right)\right) dt \tag{7.8}$$

where Q is the activation energy for the dissolution of the γ′ or δ precipitates. The T can be replaced by $V_h(t - t_p) + T_p$ representing the heating ramp before T_p. So the Equation 7.8 becomes:

$$t_{eh} = \int_{t_0}^{t_p} \exp\left(\frac{Q}{RT_p}\left(1 - \frac{1}{\frac{V_h(t-t_p)}{T_p}+1}\right)\right) dt \tag{7.9}$$

Because $\left|\frac{V_h(t-t_p)}{T_p}\right| = \left|\frac{T-T_p}{T_p}\right|$ and $\left|\frac{T-T_p}{T_p}\right| \ll 1$, so $1 - \frac{1}{\frac{V_h(t-t_p)}{T_p}+1}$ is approximated to $\frac{V_h(t-t_p)}{T_p}$.

Equation 7.9 is simplified as:

$$t_{eh} \approx \int_{t_0}^{t_p} \exp\left(\frac{QV_h(t-t_p)}{RT_p^2}\right) dt \approx \frac{RT_p^2}{QV_h} \tag{7.10}$$

Similarly,

$$t_{ec} \approx \frac{RT_p^2}{QV_c} \tag{7.11}$$

Therefore,

$$t_e = t_{eh} + t_{ec} = \frac{RT_p^2}{Q}\left(\frac{1}{V_h} + \frac{1}{V_c}\right) \tag{7.12}$$

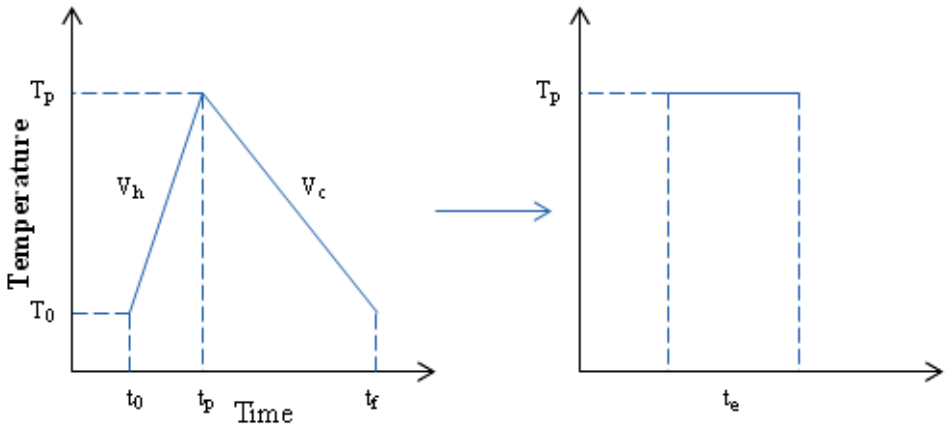

Fig. 7.17. Time-temperature equivalence for replacing a rapid thermal cycle with a hold time t_e at the equivalent temperature T_p

According to the time-temperature equivalence, the non-isothermal dissolution process is transformed into a diffusion-controlled isothermal dissolution. As known from Fick's second law, the diffusion length *y* is expressed as:

$$y = \sqrt{D_p t_e} \tag{7.13}$$

where D_p is the diffusion coefficient of Al in Ni or Nb in Ni at temperature T_p. In the current study, the diffusion coefficient of Al in Ni was chosen from the literature as [16]:

$$D_{(\mu m^2 s^{-1})} = D_0 exp\left(-\frac{Q}{RT}\right) = 9.03 \times 10^8 exp\left(-\frac{282680}{RT}\right)$$

where *D* is the diffusion coefficient at a specific temperature *T*, D_0 is the diffusion coefficient at a reference temperature, *Q* is the diffusion activation energy, and *R* is the gas constant.

For IN718, the diffusion coefficient of Nb in Ni was selected as [17]:

$$D_{(\mu m^2 s^{-1})} = 1.04 \times 10^8 exp\left(-\frac{200500}{RT}\right)$$

where *R* is the universal gas constant, 8.3145 J mol^{-1} K^{-1}.

7.3.2.b. Geometric Model

A one-dimensional dissolution model was also suggested (Fig. 7.18) to model the precipitate dissolution based on the following assumptions:

- Precipitates have a constant size and are uniformly distributed in the matrix.
- Each precipitate is considered as a spherical particle with a radius of *r*, surrounded by a spherical matrix of radius *l*.

The volume fraction of precipitates *f* is defined as [14]:

$$f = \frac{r^3}{l^3} \tag{7.14}$$

During rapid thermal cycling, the diffusive field of a precipitate extends a distance of $\sqrt{D_p t_e} + r$ into the matrix. The matrix volume fraction f_m affected by dissolution is defined as [14]:

$$\begin{cases} \sqrt{D_p t_e} + r < l: & f_m = \frac{\left(\sqrt{D_p t_e} + r\right)^3}{l^3} \\ \sqrt{D_p t_e} + r > l: & f_m = \frac{\left(\sqrt{D_p t_e} + r\right)^3}{\left(\sqrt{D_p t_e} + r\right)^3 + l^3} \end{cases} \tag{7.15}$$

For the boundary conditions, f_m is equal to $\frac{r^3}{l^3}$ when $\sqrt{D_p t_e}$ is small, and f_m is equal to 1 when $\sqrt{D_p t_e}$ is large. For $\sqrt{D_p t_e} + r \approx l$, Equation 7.15 is not accurate.

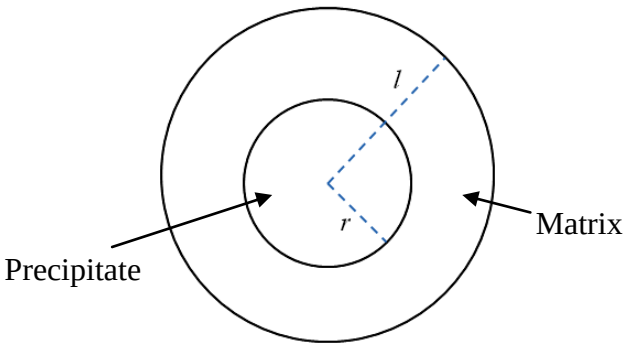

Fig. 7.18. Geometric model of precipitate dissolution

7.3.2.c. Calculation of the Solvus of γ′ in IN713LC and δ in IN718

At equilibrium dissolution, the atomic fraction of Al and Nb in the γ matrix follows Equations 7.4 and 7.5 for IN713LC and IN718, respectively. During rapid thermal cycles, the equations are changed to Equations 7.16 and 7.17 for γ′ and δ phase dissolve completely at temperature T_s in a time t_s less than that required at equilibrium.

$$\ln \frac{X_{Al,\gamma}}{f_m} = 2.2 - \frac{6289.2}{T+273}\ , T\ in\ °C \tag{7.16}$$

$$\ln \frac{X_{Nb,\gamma}}{f_m} = -2.46 - \frac{1155.4}{T+273}\ , T\ in\ °C \tag{7.17}$$

The solvus of γ′ and δ phase (T_s) can be calculated by substituting Equation 7.15 into Equations 7.16 and 7.17.

7.3.2.d. Calculation of the Volume Fraction of γ′ in IN713LC and δ in IN718

Prediction of the volume fraction of precipitates during a rapid thermal cycle is based on the equilibrium models, Equations 7.2 and 7.3. In rapid thermal cycling, the variation of the atomic fraction of Al in γ matrix $X_{Al,\gamma}(T)$ is substituted by a variable $X_{Al,\gamma}(T,t)$ related to the hold time *t* at temperature *T*, as [14]:

$$X_{Al,\gamma}(T,t) = k\left(\left(\sqrt{Dt} + r\right)^3 - r(T,t)^3\right) + X_{Al,\gamma} \tag{7.18}$$

where *k* is independent of *T* and *t* as a constant, $r(T,t)$ is the radius of precipitate at time *t* and temperature *T*. $X_{Al,\gamma}$ is the atomic fraction of Al in γ phase before γ′ dissolution. The variation of Al concentration in the γ matrix around the precipitates is not considered.

At the beginning of dissolution, $r(T,t)$ equals to r. When the γ′ phase is completely dissolved at T_c with an equivalent hold time t_c in a rapid thermal cycle A, $r(T,t)=0$. So k can be expressed as:

$$k = \frac{X_{Al,\gamma}(T_c,t_c) - X_{Al,\gamma}}{\left(\sqrt{D_c t_c}+r\right)^3} \tag{7.19}$$

By substituting Equation 7.19 into Equation 7.18:

$$X_{Al,\gamma}(T,t) = \frac{X_{Al,\gamma}(T_c,t_c) - X_{Al,\gamma}}{\left(\sqrt{D_c t_c}+r\right)^3}\left(\left(\sqrt{Dt}+r\right)^3 - r(T,t)^3\right) + X_{Al,\gamma} \tag{7.20}$$

where T_c and t_c can be calculated by the solvus model and the time-temperature equivalence method.

The volume fraction of γ′ in the rapid thermal cycle A can be calculated by inserting Equation 7.20 into Equation 7.2:

$$f_{\gamma'}(T) = \frac{X_{Al} - X_{Al,\gamma} - \frac{X_{Al,\gamma}(T_c,t_c) - X_{Al,\gamma}}{\left(\sqrt{D_c t_c}+r\right)^3}\left(\left(\sqrt{Dt}+r\right)^3 - r(T,t)^3\right)}{X_{Al,\gamma'} - X_{Al,\gamma} - \frac{X_{Al,\gamma}(T_c,t_c) - X_{Al,\gamma}}{\left(\sqrt{D_c t_c}+r\right)^3}\left(\left(\sqrt{Dt}+r\right)^3 - r(T,t)^3\right)} \tag{7.21}$$

Similarly, the volume fraction of δ in rapid thermal cycle is expressed as:

$$f_{\delta}(T) = \frac{X_{Nb} - X_{Nb,\gamma} - \frac{X_{Nb,\gamma}(T_c,t_c) - X_{Nb,\gamma}}{\left(\sqrt{D_c t_c}+r\right)^3}\left(\left(\sqrt{Dt}+r\right)^3 - r(T,t)^3\right)}{X_{Nb,\delta} - X_{Nb,\gamma} - \frac{X_{Nb,\gamma}(T_c,t_c) - X_{Nb,\gamma}}{\left(\sqrt{D_c t_c}+r\right)^3}\left(\left(\sqrt{Dt}+r\right)^3 - r(T,t)^3\right)} \tag{7.22}$$

where $X_{Nb,\gamma}$ is the atomic fraction of Nb in γ phase before δ dissolution.

7.4. Validation of the Models

7.4.1. Prediction of the Effect of Thermal Cycling Rate on the Solvus of the γ′ in IN713LC and δ in IN718

Prediction of the solvus temperatures of γ′ and δ phases is based on the model created in Section 7.3.2.c. The initial sizes of γ′ and δ precipitates are 0.13 μm and 0.54 μm, and the thermal cycles applied for the calculations are listed in Table 7.6.

Table 7.6. Thermal cycles applied using the models for predicting the volume fraction variation of γ′ phase in IN713LC and δ phase in IN718

Alloy	Heating rate (℃/s)	Cooling rate (℃/s)	Calculated solvus (℃)
IN713LC	1	125	1190
IN713LC	10	215	1192
IN713LC	100	188	1204
IN713LC	300	189	1213
IN713LC	500	176	1215
IN713LC	1000	261	1223
IN718	1	215	1090
IN718	300	228	1182
IN718	700	223	1200

The γ′ solvus in IN713LC at different thermal cycles was plotted in Fig. 7.19 by solving Equations 7.15 and 7.16. The calculated values match well with the experimental data at a heating rate under 10 ℃/s, and have less than 9 ℃ error for heating rates above 10 ℃/s.

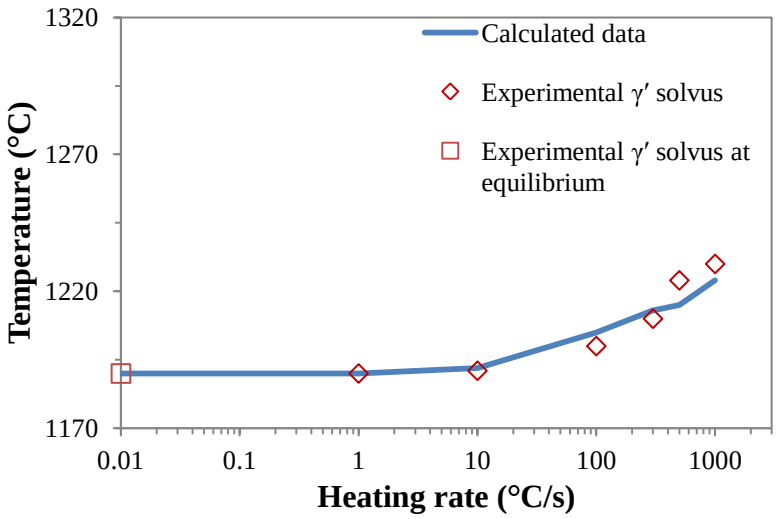

Fig. 7.19. Calculated and experimental determined γ′ solvus in IN713LC

Similarly, the solvus temperatures of the δ phase in IN718 under different thermal cycles were calculated from the Equations 7.15 and 7.17, as shown in Fig. 7.20. The calculated values match well with the measured data, with error less than 5 ℃.

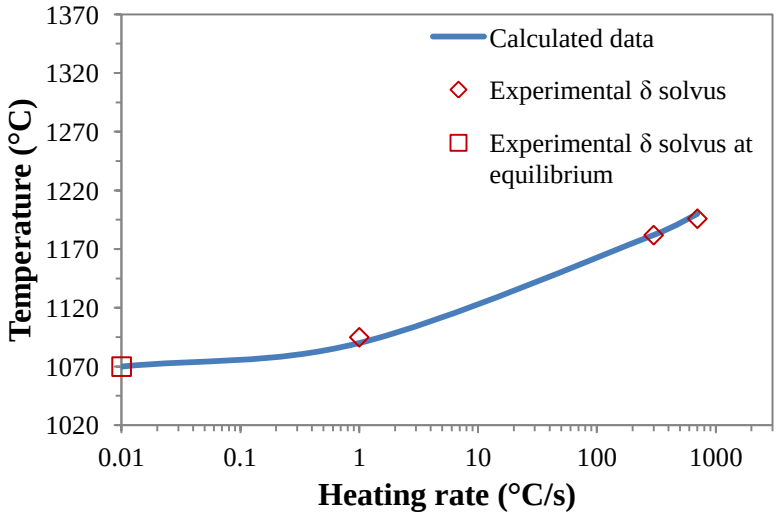

Fig. 7.20. Calculated and experimental determined δ solvus in IN718

The model is also valid in predicting both the solvus of high fraction γ′ phase in IN713LC and low fraction δ phase in IN718 under other different thermal cycles. It is reasonable to assume that the solvus model would be applicable to predict the phase solvus temperature for a wide range of alloys.

7.4.2. Prediction of the Effect of Thermal Cycling Rate on the Volume Fraction of the γ′ in IN713LC and δ in IN718

Prediction of the volume fraction of γ′ and δ phases was based on the equilibrium model and rapid thermal cycle model, as mentioned in Sections 7.3.1 and 7.3.2.d. The thermal cycles applied for prediction are listed in Table 7.6.

The calculated and experimental volume fractions of γ′ phase at different heating rates are plotted in Fig. 7.21. For the heating rate 10 ℃/s to 300 °C/s, the experimental γ′ volume fraction matches well with the values calculated by the equilibrium model. When the heating rate exceeds 500 ℃/s, the experimental values coincide with the curves computed using the rapid thermal cycle model.

Figure 7.22 shows the calculated and experimental volume fraction of δ phase at different heating rates. The rapid thermal cycle model calculated values show a generally good agreement with the experimental values. The deviation from the equilibrium rises with the increase in heating rate, which is similar to the γ′ dissolution as illustrated in Fig. 7.21.

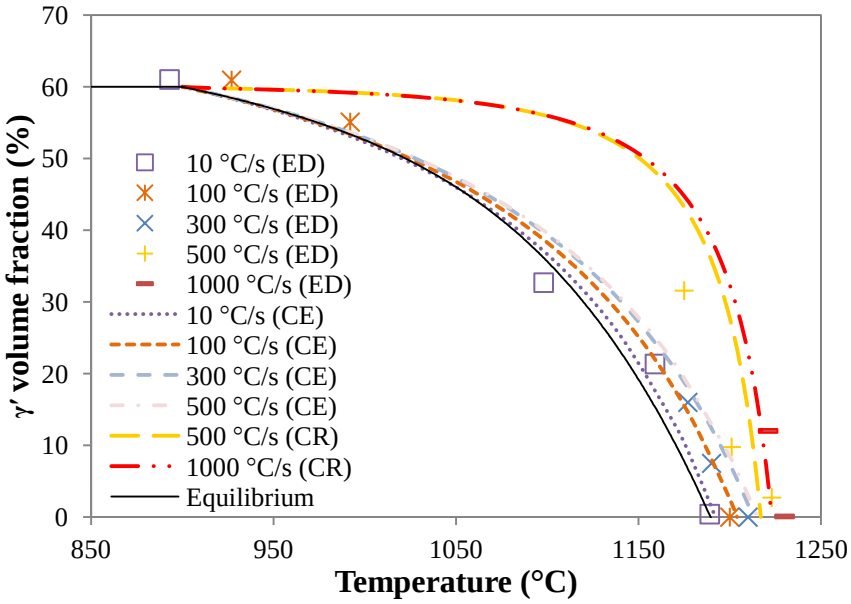

ED: experimental data, CE: calculated by equilibrium model, CR: calculated by rapid thermal cycle model

Fig. 7.21. Calculated and experimental determined γ′ volume fraction in IN713LC at various heating rates

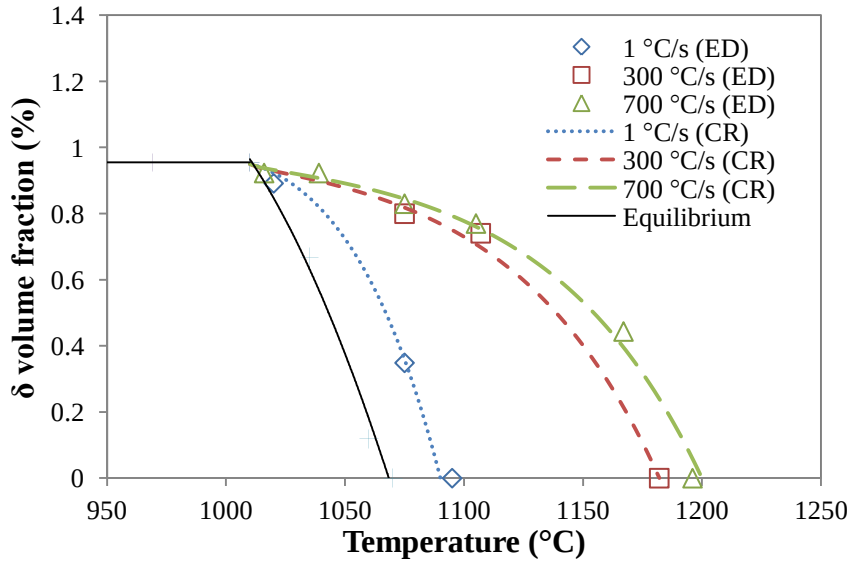

ED: experimental data, CR: calculated by rapid thermal cycle model

Fig. 7.22. Calculated and experimental determined δ volume fraction in IN718 at various heating rates

According to Equation 7.15, the results indicate that the rapid thermal cycle model is suitable for predicting the variation of a low fraction phase for a wide range of heating rates (when $\sqrt{D_p t_e} + r < l$) and the variation of high fraction of precipitates under high heating rates (when $\sqrt{D_p t_e} + r > l$). Whereas, the rapid model is not appropriate for calculating the fraction variation of high fraction of precipitates at low heating rates ($\sqrt{D_p t_e} + r \approx l$). In this case, the equilibrium model is suitable to predict the fraction of a high fraction phase at low heating rates.

7.4.3. Prediction of the Influence of Precipitate Size on the Dissolution of γ′ in IN713LC and δ in IN718 and the Occurrence of Constitutional Liquation

Thermal parameters of heating rate 500 ℃/s and cooling rate 200 ℃/s have been considered to study the influence of the precipitate size on the dissolution of γ′ and δ phase. The initial volume fraction of γ′ and δ phases are 60% and 0.95%, which are the same as the values in the present alloys. This section is only based on the developed models, with experimental corrections based on the literature.

Figure 7.23 shows the variation of the volume fraction of δ phase with three different sizes 0.4 μm, 0.54 μm, and 0.7 μm. It reveals that the dissolution of δ phase becomes more difficult when the particle size increases. The temperature at which δ fully dissolved rises from 1149 ℃ to 1226 ℃, when the particle size increases from 0.4 μm to 0.7 μm.

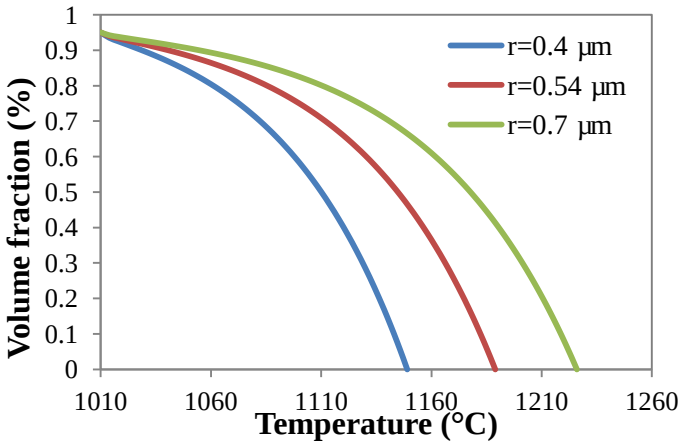

Fig. 7.23. Variation of the δ volume fraction during thermal cycle with heating rate 500 ℃/s and cooling rate 200 ℃/s for δ sizes 0.4 µm, 0.54 µm, and 0.7 µm

Figure 7.24 shows the evolution of the volume fraction of γ′ phase with three sizes 0.13 µm, 0.25 µm, and 0.5 µm and as for δ phase, the decrease of the γ′ volume fraction becomes slow with increase of γ′ size. For size 0.5 µm, γ′ phase cannot completely dissolve at 1250 °C (γ-γ′ eutectic temperature), which may cause constitutional liquation as discussed in Section 7.2.1. Because constitutional liquation should be avoided in welding, study of the relationship between the particle size and the critical heating rate is meaningful. Constitutional liquation occurs during heating, thus the cooling rate is not considered.

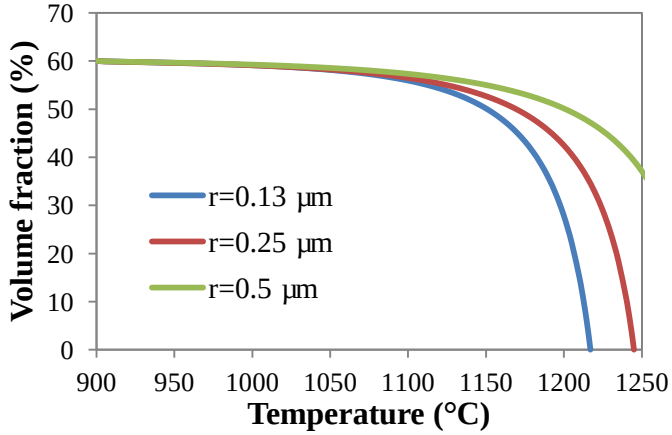

Fig. 7.24. Variation of the γ′ volume fraction during thermal cycle with heating rate 500 ℃/s and cooling rate 200 ℃/s for γ′ sizes 0.13 µm, 0.25 µm, and 0.5 µm

Figure 7.25 gives the relation of the initial particle size (r) and the critical heating rate (V) for inducing γ-γ′ constitutional liquation in IN713LC calculated by current model. The relation can be expressed as:

$$V = \frac{A}{r^2} \tag{7.23}$$

where A is a material-dependent parameter, which is 10.6 K ·μm^{2}s^{-1} for IN713LC. It reveals that the critical heating rate required is inversely proportional to the square of the initial particle size. Constitutional liquation occurs at a lower heating rate when the particle size increases. Therefore, the alloy with large particle size should be avoided to prevent constitutional liquation during welding. The safe heating rate for IN713LC to avoid constitutional liquation is below the line in Fig. 7.25.

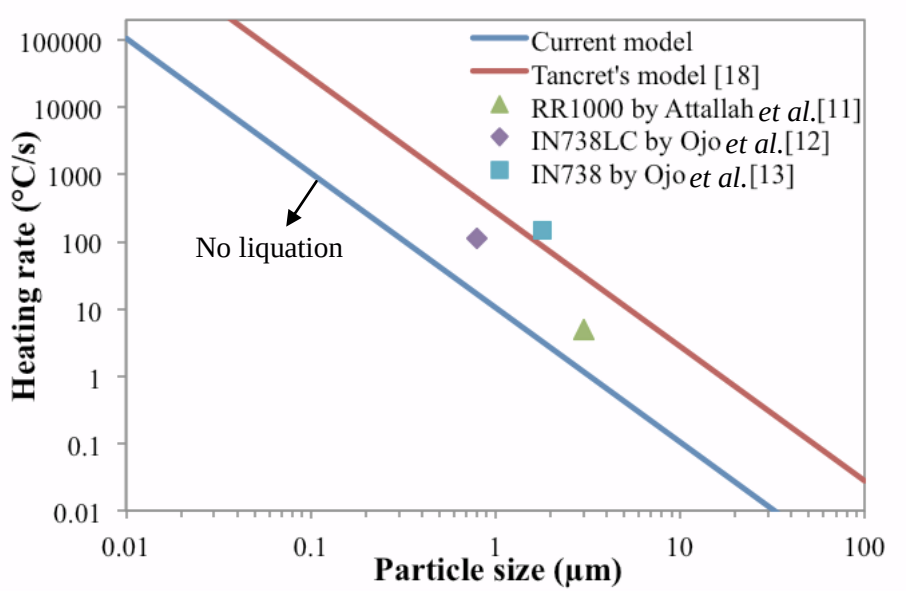

Fig. 7.25. Relation of the initial particle size and the critical heating rate for the γ-γ′ constitutional liquation in IN713LC

Equation 7.23 is also suitable for the alloys with similar composition (γ′ volume fraction ~60%). The work from Attallah *et al*. [11] observed constitutional liquation of the primary γ′ (3 μm) in RR1000 at a heating rate of 5 ℃/s using high-temperature confocal laser scanning

microscopy (HT-CLSM). The heating rate 5 ℃/s is above the Equation 7.23 calculated critical value 1.18 ℃/s, which explains the occurrence of constitutional liquation. Additionally, the current model has successfully indicated the occurrence of the constitutional liquation of γ′ (0.8 μm) in IN738LC [12] and γ′ (1.8 μm) in IN738 [13] at heating rates of 111 ℃/s and 150 ℃/s, respectively.

However, Tancret's model [18]:

$$V = \frac{280}{r^2} \tag{7.24}$$

which can only predict the constitutional liquation of IN738. It does not work for RR1000 and IN738LC, because Tancret overestimated the material-dependent parameter (*A*) to 280 $K\mu m^2 s^{-1}$, which is 26 times larger than the value calculated by the model in the current study (10.6 $K\mu m^2 s^{-1}$). Thus the current model works more widely than the Tancret's model for predicting the critical heating rate for the occurrence of constitutional liquation of γ′ in Ni-based superalloys.

7.4.4. Prediction of the Peak Temperature across Linear Friction Welds through Observing the Precipitate Volume Fraction

In the literature, three different approaches have been used to measure or estimate the temperature distribution in LFW: in-situ thermocouple measurement, infrared thermal imaging, and thermal modelling [19-22]. However, all of them have shortcomings. Thermocouple measurements are very difficult near the interface, due to the rapid movement of the sample and the ejection of the flash. Infrared thermal imaging can only measure the temperature on the surface of the samples, and the temperature calculated by thermal

modelling is not easy to verify. Current work has developed a new route of predicting the peak temperatures across linear fraction welds from the point of view of the phase transformation. The peak temperatures can be calculated by using the rapid thermal cycle models (Equations 7.21 and 7.22) once the γ′ and δ volume fractions are measured using quantitative microscopy.

Since the weld time for W1, 2, and 3 is 3.17 s, 2.35 s, and 1.48 s as listed in Table 5.3, and the maximum temperature and cooling rate close to the weld line of LFWed Ni-superalloys was around 1200 ℃ and 80 ℃/s, as reported in literature [19, 21]. The heating rate 400 ℃/s, 500 ℃/s, 800 ℃/s and cooling rate 80 ℃/s have been taken for the thermal cycles of W1, 2, and 3, respectively.

The maximum temperatures in the IN713LC across the LFWs were calculated by Equation 7.21, based on the γ′ volume fraction measurements obtained in Fig. 5.21.a, as shown in Fig. 7.26. It shows that the maximum temperature at the weld interface is around 1207 ℃ for samples welded under different parameters. The temperature gradient becomes steeper when the weld pressure increases, which means higher weld pressure can give rise to a smaller heat affected zone.

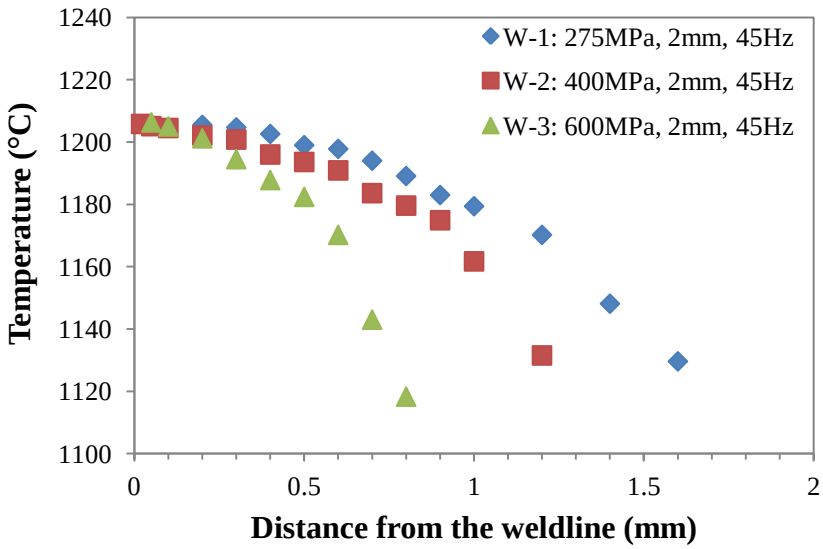

Fig. 7.26. Calculated maximum temperatures in the IN713LC across the LFWs under different weld parameters

The maximum temperatures in the IN718 across the LFWs were calculated by Equation 7.22 based on the δ phase volume fraction measurements obtained in Fig. 5.19.a, as shown in Fig. 7.27. The calculated maximum temperature (1197 ℃) is close to the extrapolated maximum temperature (1200 ℃) from the thermocouple measured values at the interface of LFWed IN718 [21]. The calculated maximum temperature in IN718 (1197 ℃) is 10 ℃ lower than that in IN713LC (1207 ℃), possibly because more heat losses occur in IN718 than IN713LC by the ejection of larger amount of IN718 flash during welding. Like IN713LC, higher weld pressure induces a narrower heat affected zone. The calculated maximum temperature has been used to predict the strain rate in the welding process, as discussed in Section 5.2.3.c.

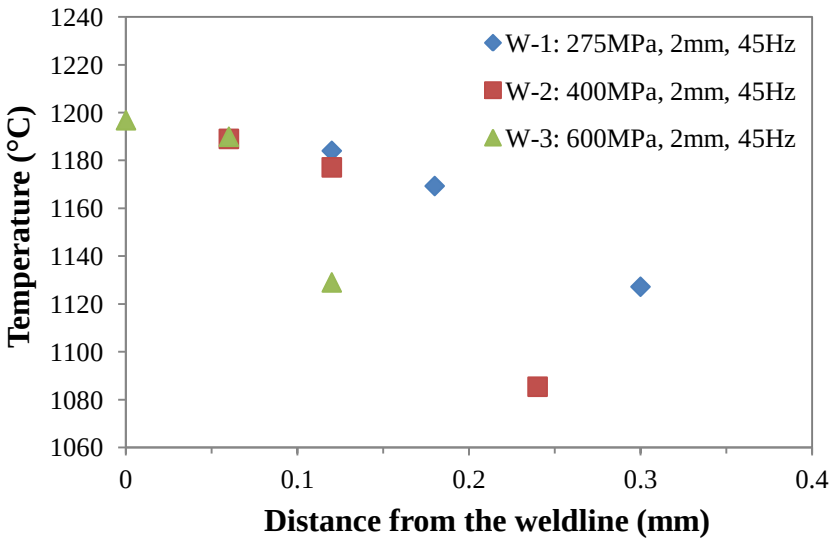

Fig. 7.27. Calculated maximum temperatures in the IN718 across the LFWs under different weld parameters

7.5. Conclusions

This chapter investigated the precipitate dissolution in IN713LC and IN718 at equilibrium and rapid thermal cycling. Dissolution occurs at higher temperatures during rapid thermal cycling, and the solvus temperature of precipitates rises with shortening of the thermal cycling. Mathematical models were established for the dissolution process, which were used to calculate the solvus and the volume fraction of γ′ and δ phase. The models were valid for the following applications:

- Solvus of γ′ and δ phase at different heating rates;
- Variation of the volume fraction of γ′ and δ phase at different heating rates;
- Influence of the initial precipitate size on the γ′ and δ phase dissolution;
- Relation of the initial precipitate size and the critical heating rate for inducing constitutional liquation of Ni-based superalloys;

- Maximum temperature across the welds during LFW of IN718-IN713LC.

Experimental and modelling work showed that the dissolution of precipitates is affected both by the thermal cycle and the precipitate size. Rapid thermal cycles can decrease the speed of the precipitate dissolution, which helps to maintain the mechanical properties of materials. However, the heating rate should be restricted within a critical value to avoid constitutional liquation of material. In addition, reducing the size of precipitates is another way to avoid constitutional liquation.

This chapter also verified the possibility of calculating the maximum temperature across welds from the analysis of the residual volume fraction of precipitates the reverse application of the rapid thermal cycle model using Equations 7.21 and 7.22. It provides a new route to obtain the temperature across the weld, especially for the area near the weld interface.

7.6. References

[1] M. J. Donachie, *Superalloys: A Technical Guide*, American Welding Society International, 2002.

[2] S. Zlá, B. Smetana, M. Žaludová, J. Dobrovská, V. Vodárek, K. Konečná, V. Matějka, and H. Francová, "Determination of thermophysical properties of high temperature alloy IN713LC by thermal analysis," *Journal of Thermal Analysis and Calorimetry*, vol. 110, pp. 211-219, 2012.

[3] N. B. Dahotre, M. H. McCay, T. D. McCay, C. R. Hubbard, W. D. Porter, and O. B. Cavin, "Effect of grain structure on phase transformation events in the Inconel 718," *Scripta Metallurgica et Materialia*, vol. 28, pp. 1359-1364, 1993.

[4] J. R. Davis, *Heat-resistant Materials*. Ohio, ASM International, 1997.

[5] D. Y. Cai, W. H. Zhang, P. L. Nie, W. C. Liu, and M. Yao, "Dissolution kinetics and behavior of δ phase in Inconel 718," *Transactions Nonferrous Metals Society of China*, vol. 13, pp. 1338-1341, 2003.

[6] A. Niang, B. Viguier, and J. Lacaze, "Some features of anisothermal solid-state transformations in alloy 718," *Materials Characterization*, vol. 61, pp. 525-534, 2010.

[7] W. D. Cao, R. L. Kennedy, M. P. Willis, and T. Allvac, "Differential thermal analysis (DTA) study of the homogenization process in alloy 718," in *Superalloys 718, 625 and Various Derivatives*, Pittsburgh, USA, pp. 147-160, 1991.

[8] E. Payton, T. Wynn, and M. Mills, "Experimental measurement of the kinetics of gamma prime dissolution during supersolvus heat treatment of powder metallurgical Ni-based disk superalloys," *Journal of Materials Science*, vol. 47, pp. 7305-7311, 2012.

[9] J. Cormier, X. Milhet, and J. Mendez, "Effect of very high temperature short exposures on the dissolution of the γ′ phase in single crystal MC2 superalloy," *Journal of Materials Science*, vol. 42, pp. 7780-7786, 2007.

[10] S. Azadian, L. Y. Wei, and R. Warren, "Delta phase precipitation in Inconel 718," *Materials Characterization*, vol. 53, pp. 7-16, 2004.

[11] M. M. Attallah, H. Terasaki, R. J. Moat, S. E. Bray, Y. Komizo, and M. Preuss, "In-Situ observation of primary γ′ melting in Ni-base superalloy using confocal laser scanning microscopy," *Materials Characterization*, vol. 62, pp. 760-767, 2011.

[12] O. A. Ojo and M. C. Chaturvedi, "On the role of liquated γ′ precipitates in weld heat affected zone microfissuring of a nickel-based superalloy," *Materials Science and Engineering A*, vol. 403, pp. 77-86, 2005.

[13] O. A. Ojo, N. L. Richards, and M. C. Chaturvedi, "Contribution of constitutional liquation of gamma prime precipitate to weld HAZ cracking of cast Inconel 738 superalloy," *Scripta Materialia*, vol. 50, pp. 641-646, 2004.

[14] M. Soucail and Y. Bienvenu, "Dissolution of the γ′ phase in a nickel base superalloy at equilibrium and under rapid heating," *Materials Science and Engineering A*, vol. 220, pp. 215-222, 1996.

[15] M. Ashby and K. Easterling, "A first report on diagrams for grain growth in welds," *Acta metallurgica*, vol. 30, pp. 1969-1978, 1982.

[16] Q. Wu, S. S. Li, Y. Ma, and S. K. Gong, "First principles calculations of alloying element diffusion coefficients in Ni using the five-frequency model," *Chinese Physics B*, vol. 21, p. 109102, 2012.

[17] R. Patil and G. Kale, "Chemical diffusion of niobium in nickel," *Journal of nuclear materials*, vol. 230, pp. 57-60, 1996.

[18] F. Tancret, "Thermo-Calc and Dictra simulation of constitutional liquation of gamma prime (γ′) during welding of Ni base superalloys," *Computational Materials Science*, vol. 41, pp. 13-19, 2007.

[19] A. Chamanfar, M. Jahazi, J. Gholipour, P. Wanjara, and S. Yue, "Mechanical property and microstructure of linear friction welded Waspaloy," *Metallurgical and Materials Transactions A*, vol. 42, pp. 729-744, 2011.

[20] A. Vairis and M. Frost, "High frequency linear friction welding of a titanium alloy," *Wear*, vol. 217, pp. 117-131, 1998.

[21] C. Mary and M. Jahazi, "Linear friction welding of IN-718 process optimization and microstructure evolution," *Advanced Materials Research*, vol. 15, pp. 357-362, 2007.

[22] R. Damodaram, S. Raman, and K. P. Rao, "Microstructure and mechanical properties of friction welded alloy 718," *Materials Science and Engineering: A*, vol. 560, pp. 781-786, 2013.

Chapter 8. Formation of Alumina Particles at the Weld Interface of Linear Friction Welded IN718-IN713LC

The occurrence of oxide inclusions is a common issue in fusion welding of Ni-based superalloys [1]. Linear friction welding has been considered as a better alternative technique for welding Ni-based superalloys due to its self-cleaning mechanism, whereby any surface contaminants will be expelled as flash due to the oscillating motion [2]. This chapter investigates the in-situ oxide formation during LFW, highlighting the impact of the process parameters, and assessing the need for argon shielding during LFW.

8.1. Formation of Al Oxides in Welds

In the few welds that were studied in this work, oxide inclusions were observed along the weld line in high amplitude (3 mm) welds (W4 and W5). Figure 8.1 shows SEM BSE micrographs for the morphology and location of these inclusions. EDX line scans identified these inclusions as Al-oxides (alumina), as they were found to be rich in Al and O (Fig. 8.2). Figures 8.1.a and 8.1.d illustrate a semi-continuous Al-oxide, located at the weld interface near the flash of W4 and W5. The trail of oxide inclusions extend up to 1 mm, with continuous layers up to 100 μm length. And Figs. 8.1.b and e show the oxide layers at high magnification. The oxides layers are ~2 μm thick, and are sometimes fragmented into a number of small oxide particles. Figures 8.1.c and f show some of the Al-oxide particles in the middle of the weld line. Because the Al-oxides were only found in high amplitude welds, and their formation was repeatable (also found in W8), it was reasonable to link the formation of the oxides to the influence of high amplitude. Based on this assumption, a series of welds were fabricated to explain the oxide formation mechanism in high amplitude LFWs.

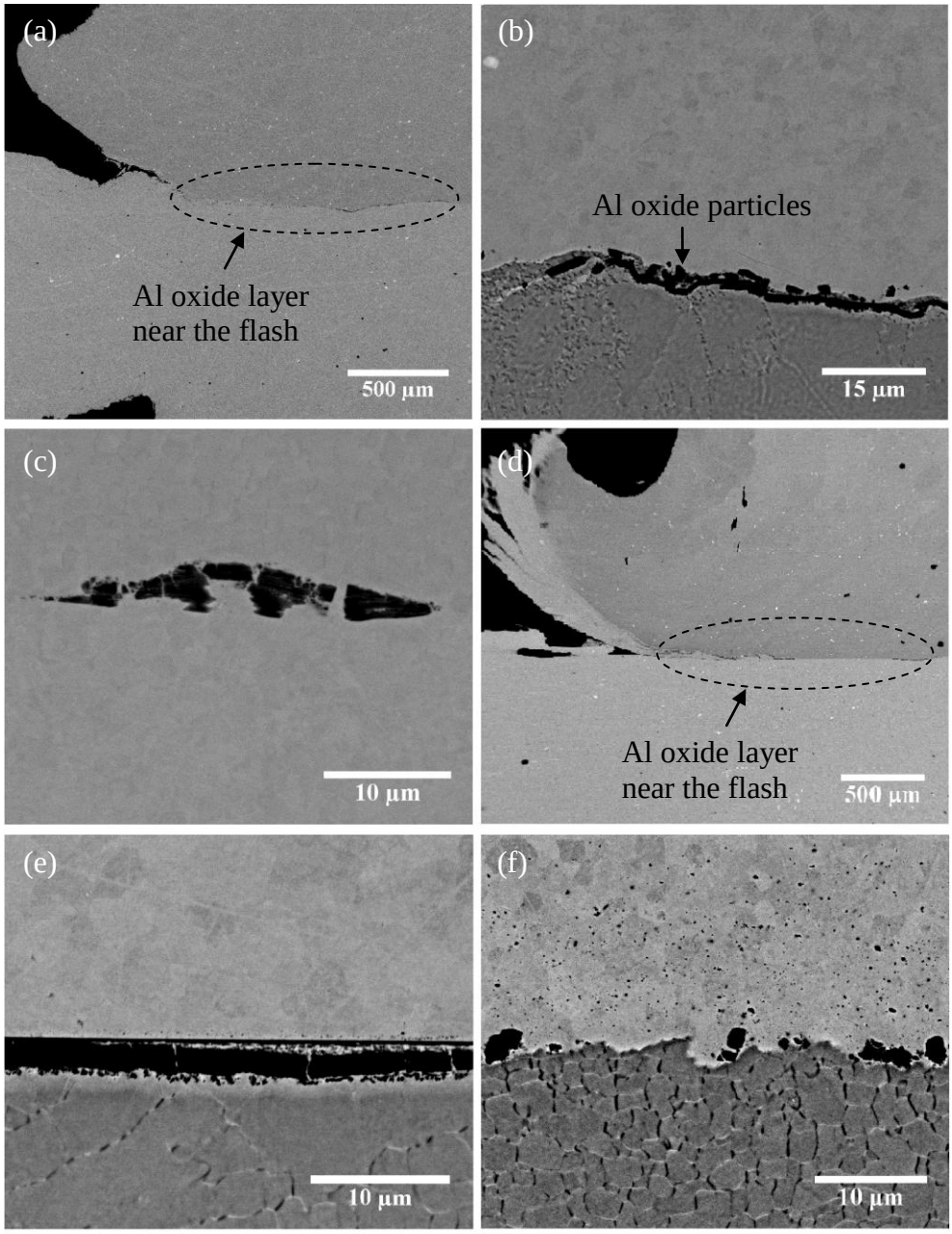

Fig. 8.1. SEM BSE micrographs showing Al oxide inclusions in (a-c) W4 and (d-f) W5, in which (a) and (d) show Al oxide layers near the flash, (b) and (e) show near flash Al oxide layers at high magnification, (c) and (f) show Al oxide particles in the middle of the weld line

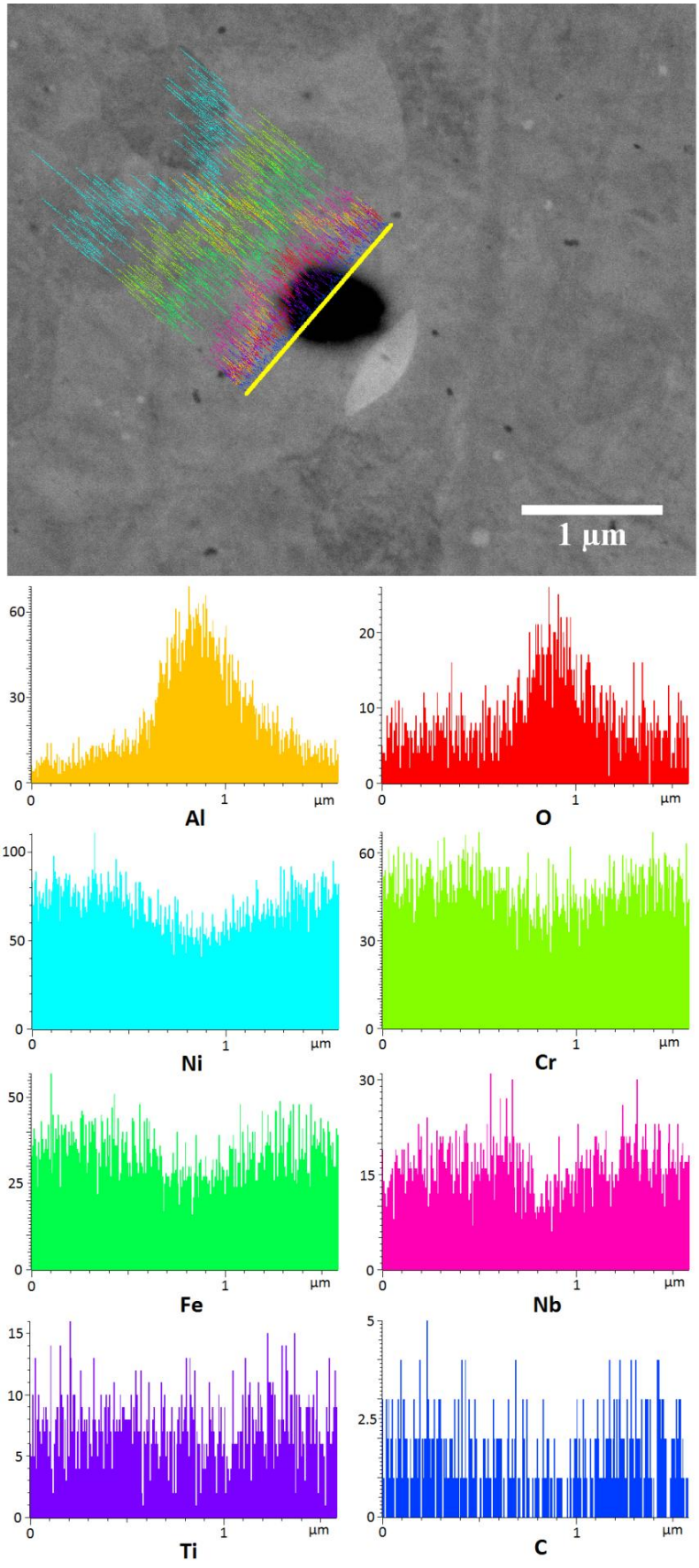

Fig. 8.2. EDX line scans of an oxide particle showing a high Al and O content

8.2. Formation Mechanisms of Al Oxides

As discussed in Section 3.3.5.a, oxide inclusions were previously found in IN718 and Waspaloy LFWs [3, 4]. However, the oxide formation mechanism was not developed. In the present study, a phenomenon of rapid expulsion of plasticised material was revealed using high speed imaging, at around 48 cycles during welding at high amplitude. This event was not discrete but lasted a number of cycles, and it did not take place simultaneously on both sides of the weld. This abnormal expulsion removed a large amount of flash on one side of the weld in a single oscillation cycle. Figure 8.3 shows high-speed images of the rapid expulsion process of W4. A few cycles before the rapid expulsion, the ejected materials did not fall off. They were accumulated at the edge of IN713LC as a large block of flash (Fig. 8.3.a). At 1/2 time of the rapid expulsion cycle, the flash was deflected upwards rather than normally downward before it fell off (Fig. 8.3.b). At 3/4 time of the expulsion cycle, the flash was pulled back, and a small amount of flash was drawn into the weld line (Fig. 8.3.c) before the whole flash fell off (Fig. 8.3.d). Since the flash was exposed in air under high temperature, oxides were very likely formed on the outer layer of the flash. This abnormal expulsion may provide a chance for part of those oxide contaminants to be drawn into the weld line, thus forming a layer of near flash oxides (Fig. 8.1.a). A few welds under different weld cycles were fabricated to observe the rapid expulsion to confirm this mechanism (Table 4.2).

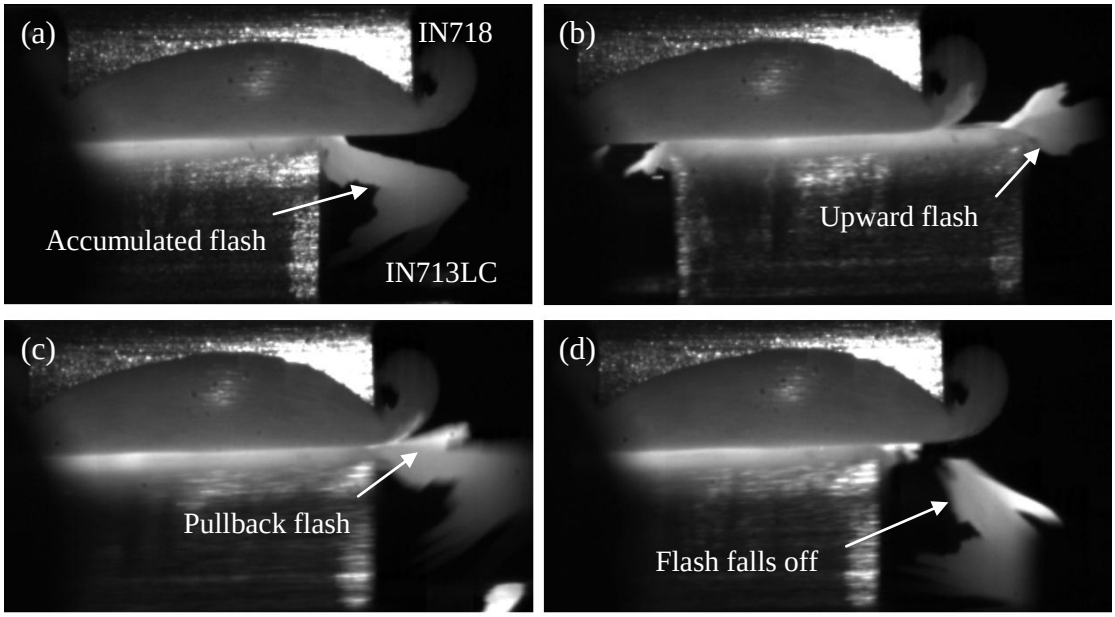

Fig. 8.3. High speed images showing the rapid expulsion of material in W4, (a) at the beginning of the cycle involving the accumulated flash falls off, (b) 1/2 cycle, (c) 3/4 cycle, and (d) at the end of this cycle

Figure 8.4 shows the Al-oxides from W9 to W14. At 3 mm amplitude, there was no near flash oxide layer before the abnormal expulsion, as confirmed by W11 and W12. When the oscillation reached above 48 cycles, the oxide layer appeared near the flash (Figs. 8.4.a & c). This phenomenon proves that the abnormal expulsion pulls a layer of Al oxides from the flash to the weld. No oxide layer was found in 2 mm amplitude welds, as no abnormal expulsion was involved, which further demonstrates that the formation of oxide layer was associated with the rapid expulsion. Near flash oxide layer, oxide particles were found in the middle of all the 3 mm amplitude welds (Figs. 8.4.b, d, e & g), and also appeared in 2 mm amplitude weld with 32 cycles (Fig. 8.4.h), but no oxide particles were observed in the 2 mm amplitude weld with 22 cycles (Fig. 8.4.j). This indicates that oxide particles are easier to form in higher amplitude welds, since higher amplitude leads to a larger area of material

being exposed in air, which increases the risk of oxidation. The oxides in a 2 mm amplitude weld can be removed by increasing the upset, as proved by W2. However, the oxides in a 3 mm amplitude weld were hardly removed by adding upset, which was likely to be because the oxides formation rate is faster than the extrusion speed of material. Incomplete joining at the edge of the weld interface was detected in low cycle welds (W12 and W14, with 22 cycles) (Figs. 8.4.f & i), which demonstrated that sufficient upset is essential to produce sound welds.

Since oxides cannot be removed during welding of high amplitude welds in air, argon shielding gas was used to eliminate the oxide layer formation. Figure 8.5 shows the microstructure of the weld line of W15 and W16 welded in argon atmosphere. Oxides have been observed in both the high cycle weld (60 cycles, W15) and low cycle weld (32 cycles, W16), but the quantity of oxides was significantly reduced compared to the high amplitude welds made in air. It is believed that the formation of oxides in W15 and W16 is due to a sub-optimum purge time with the argon flow, so the remnant oxide could be due to the presence of the residual oxygen in the argon atmosphere. Moreover, the low upset induced by insufficient oscillation cycles may not fully remove oxides away from the weld interface. In low cycle W16, oxides were observed both in the area of near the flash and in the middle of the weld line. However, in high cycle W15, oxide particles were only found near the flash and the amount of oxides was further reduced in W15. This indicates that welds are protected from further oxidation by the argon atmosphere, and the Al oxides formed from the remnant oxide can be reduced by increasing the number of oscillating cycles to effectively eject the oxides out of the weld.

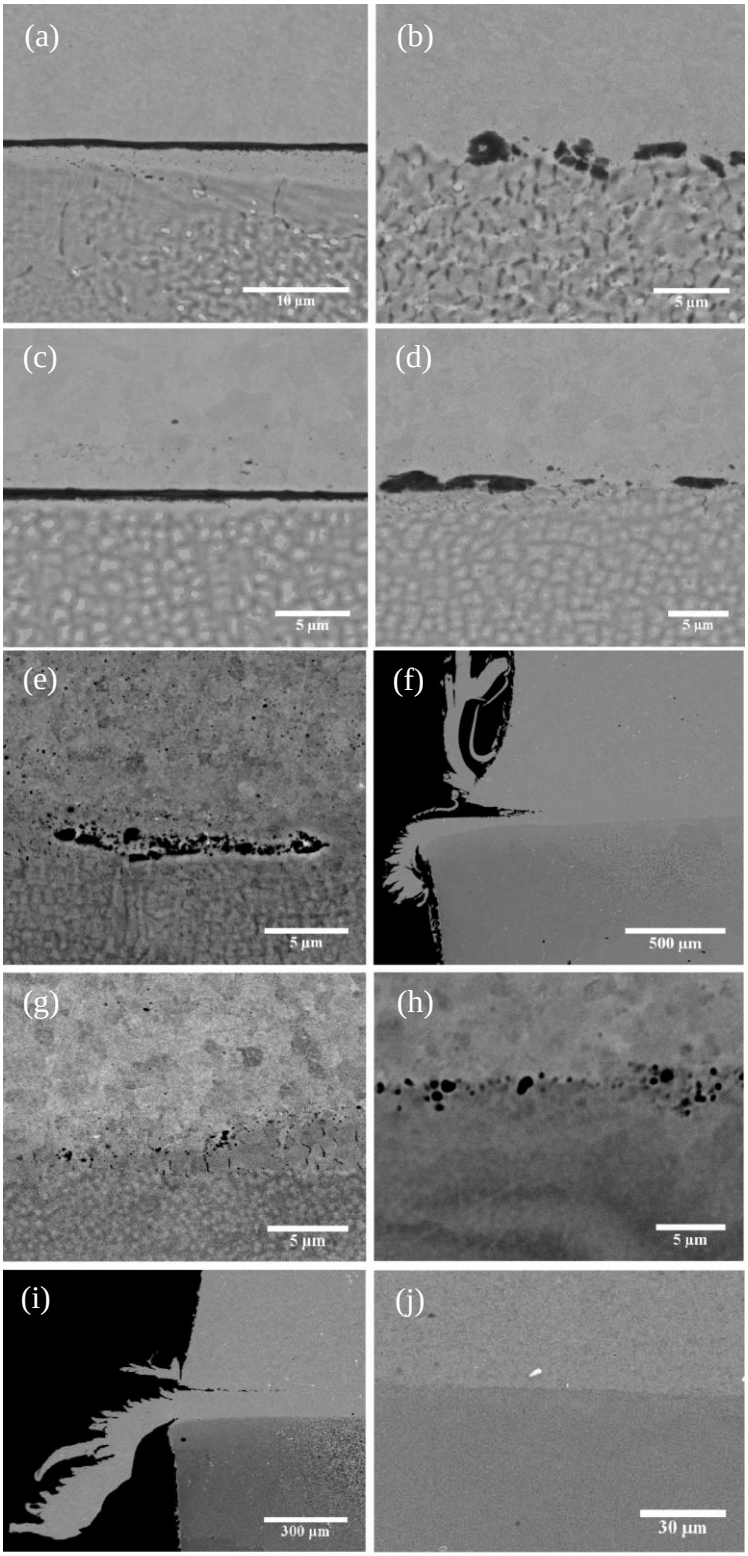

Fig. 8.4. SEM BSE micrographs showing Al-oxides variation (a) near the flash and (b) in the middle of W9, (c) near the flash and (d) in the middle of W10, (e) in the middle of W11, (f) near the flash and (g) in the middle of W12, (h) in the middle of W13, (i) near the flash and (j) in the middle of W14

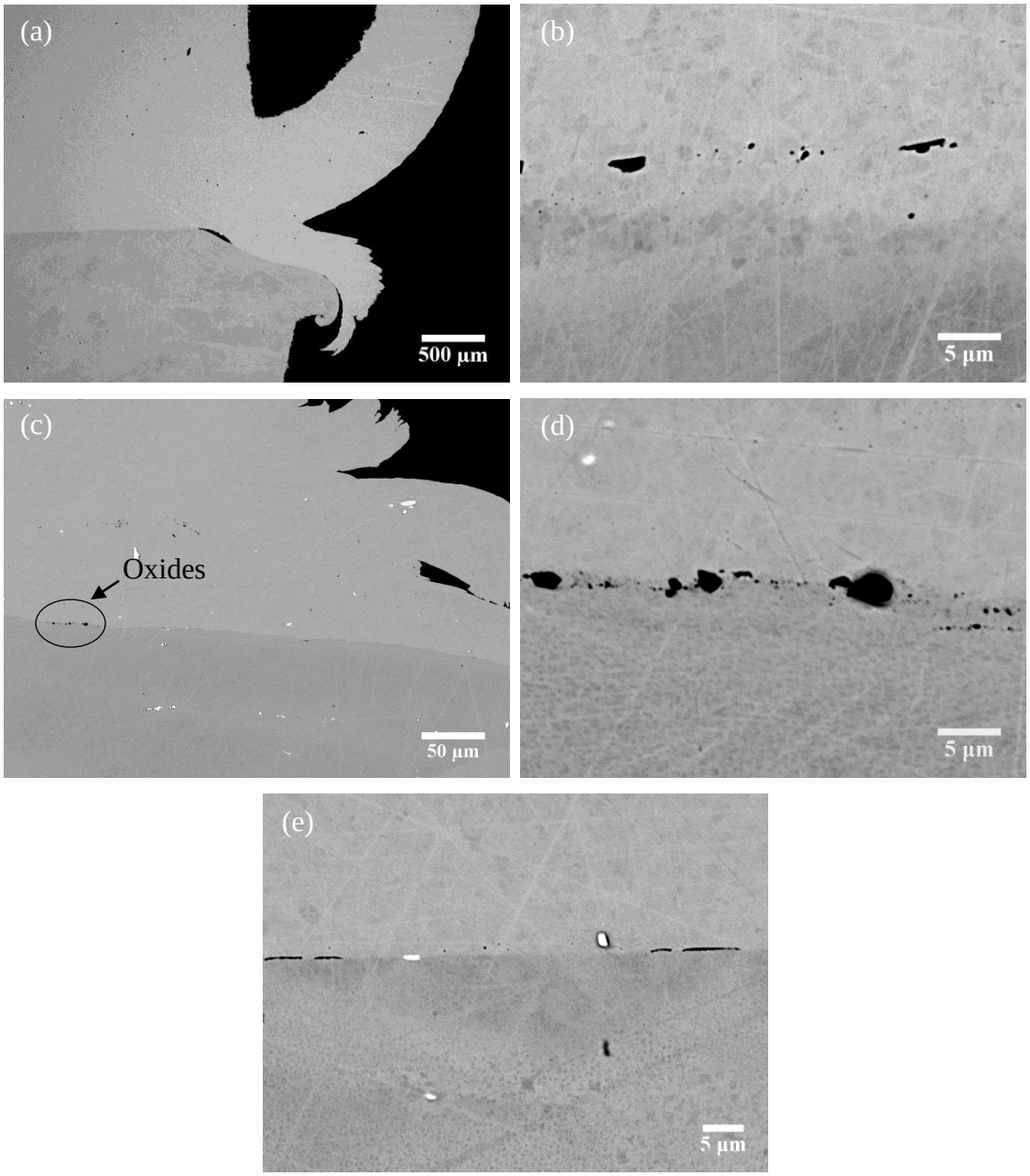

Fig. 8.5. SEM BSE micrographs showing Al-oxides in Ar purged welds in (a) near the flash of W15 (low magnification), (b) near the flash of W15 (high magnification), (c) near the flash of W16 (low magnification), (d) near the flash of W16 (high magnification image showing the circle in c), and (e) in the middle of W16

8.3. Conclusions

Al oxides were observed in high amplitude welds during welding in air. The formation of oxides was mainly due to the rapid expulsion of material induced by insufficient ejection of IN713LC flash during oscillation. Also, the larger exposed area in high amplitude welds was proved to be a minor factor in generating oxides. Smaller amplitude and larger pressure were found to produce oxide-free welds. The occurrence of oxidation can be reduced by argon shielding, but oxidation still occurs in high amplitude welds because of the presence of oxygen in the argon induced by insufficient purge time, and also due to insufficient upset. Therefore, enough argon gas purge time plus sufficient upset are required to produce sound high amplitude welds.

8.4. References

[1] A. Lingenfelter, "Welding of Inconel alloy 718: A historical overview," in *Superalloy 718 Metallurgy and Application*, Pittsburgh, USA, 1989.

[2] M. M. Attallah, *et al.*, "Microstructural development during linear friction welding of titanium alloys."

[3] C. Mary and M. Jahazi, "Mult-scale analysis of IN-718 microstructure evolution during linear friction welding," *Advanced Engineering Materials*, vol. 10, pp. 573-578, 2008.

[4] A. Chamanfar, *et al.*, "Maximizing the integrity of linear friction welded Waspaloy," *Materials Science and Engineering A*, vol. 555, pp. 117-130, 2012.

Chapter 9. Conclusions and Future Work

9.1. Summary and Conclusions

The work covered in the current study has demonstrated the structure-property development of linear friction welded IN718-IN713LC in as-welded and PWHTed conditions. In addition, the influence of thermal cycling rate on the precipitate dissolution is studied based on experiments and modelling to discover the difference of the precipitate dissolution behaviour between slow heating and rapid heating. The following conclusions can be drawn from the results presented.

9.1.1. Microstructure-Property Development in As-welded and PWHTed Samples

- The high temperature and large deformation generated in LFW process induce the dissolution of precipitates and recrystallisation in the weld affected zone (WAZ). Compared with fusion welding, the WAZ of LFWs is relatively small (several mm), and the area of the WAZ mainly depends on the weld pressure, where larger pressure tends to generate smaller WAZ.
- A weak texture is found in the TMAZ of IN718 by EBSD. The microtexture can intensify with increase of weld pressure, but the enhancement is limited. Therefore, this texture is not expected to affect the mechanical property of welds.
- An uneven hardness distribution is found across the as-welded samples, which is attributed mainly to the difference in the number and size of strengthening particles, with some contribution from solid solution strengthening, grain size differences, and stored dislocations across the weld. Due to the high temperature in LFW, γ'/γ''

precipitates are dissolved in the WAZ of IN718 and IN713LC which causes a hardness trough in IN718. However, the hardness increases in the WAZ of IN713LC are a result of the strengthening of reprecipitated fine γ′ during cooling.

- Rapid thermal cycling and large plastic deformation induce large residual stresses across the welds, in which the residual stresses in IN713LC are generally larger than those in IN718. The residual stress can be changed from tension to compression by increasing the weld pressure.
- Alumina oxides are observed in high amplitude welds. The formation of oxides is mainly due to the abnormal expulsion of material caused by insufficient ejection of IN713LC flash during oscillation. The larger exposed area in high amplitude welds is believed to be a minor factor in generating oxides. Smaller amplitude, larger pressure and higher upset are confirmed to produce a sound weld. Oxidation can be eliminated by using pure shielding gas plus sufficient purge time which produce a sound high amplitude weld.
- PWHT is an effective method to recover the hardness of the IN718-IN713LC LFWs. Among three PWHT methods, two-stage γ′/γ″ aging treatment is the most efficient way to reinforce the strength of welds without causing grain growth. Solution treatment plus two-stage aging treatment can generate a relatively homogenous hardness across the welds, but grain size might dramatically increase if the solution temperature is too high.

9.1.2. Influence of the Thermal Cycling Rate on Precipitate Dissolution

The volume fraction variation of γ′ and δ precipitates at different heating rates has been studied in this work. Dissolution occurs at higher temperatures during rapid thermal cycling, and the solvus temperature of precipitates rises with increases of heating rate. Mathematical

models are established for the dissolution process, for the calculation of the solvus and the volume fraction of γ′ and δ phase. The application of models includes the following aspects:

- Variation of the volume fraction and the solvus of γ′ and δ phase at different heating rates;
- Influence of the initial precipitate size on the γ′ and δ phase dissolution;
- Relation of the initial precipitate size and the critical heating rate for inducing constitutional liquation of Ni-based superalloys;
- Prediction of the maximum temperature across the IN718-IN713LC LFWs during linear friction welding process.

Both experiments and modelling work have shown that the dissolution of precipitates is affected both by the thermal cycle and the precipitate size. Rapid thermal cycles can decrease the rate of the precipitate dissolution, which helps to maintain the microstructure of materials. But the heating rate should be restricted within a critical value to avoid constitutional liquation of materials. In addition, reducing the size of precipitates is another way to avoid constitutional liquation. Current work also verifies the possibility of calculating the maximum temperature across the welds from the analysis of the volume fraction of remnant precipitates by the reverse application of the rapid thermal cycle model, which provides a new route to obtain the temperature across the weld, especially for the area near the weld interface.

9.2. Future Work

Current work has provided a wide understanding of the structure-property development of LFWed IN718-IN713LC in as-welded and PWHTed conditions, which includes WAZ

microstructural development, microhardness and residual stress development across the welds, the influence of rapid thermal cycle on precipitate dissolution, as well as the formation mechanisms of alumina oxides in high amplitude welds. Some possible areas of further investigations are listed as follows:

- To study the influence of PWHT on relieving the residual stresses in IN718-IN713LC LFWs, as well as measuring the strain-free lattice spacing value d_0 to amend the measured residual stresses in the present study. A model could be established for the residual stress development in as-welded and PWHTed welds.
- To investigate the recrystallisation of IN718 at rapid heating and high strain rate. And further assess the influence of temperature on recrystallised grain growth rate.
- Quantitatively analyse the relation between structure (precipitates, grain size, stored energy) and hardness to further develop a mathematical model for predicting hardness based on microstructure.
- To validate the constitutional liquation model by making predictions of the conditions required (critical heating rate and particle size) and then making the welds to demonstrate this.
- To establish models for the flash expulsion with the influence of weld parameters, especially the effect of weld amplitude, and further study the influence of weld parameters on the formation of alumina oxides in welds.